Statistical Model for the Prediction of Elastic Wave Scattering From Finite Complicated Shells

Hua He

M.S., Xi'an Jiaotong University, China (1988)
B.E., Xi'an Jiaotong University, China (1985)

Submitted to the Department of Ocean Engineering
in partial fulfillment of the requirements for the degree of

Doctor of Philosophy in Acoustics

at the

Massachusetts Institute of Technology

February 1997

Author .....

Department of Ocean Engineering
November, 1996

Certified by .....

Professor Ira Dyer
Weber-Shaughness Professor of Ocean Engineering
Thesis Supervisor

Accepted by ....

Professor J. Kim Vandiver
Chairman, Departmental Graduate Comittee

Statistical Model for the Prediction of Elastic Wave Scattering From Finite Complicated Shells

Hua He

Submitted to the Department of Ocean Engineeringon November, 1996,
in partial fulfillment of the requirements for the degree of
Doctor of Philosophy in Acoustics

Abstract

An elastic wave equipartition concept is formulated, tested, and used to predict the mid-frequency bistatic elastic wave scattering from finite complicated elastic shells in water. This statistical model is simple and insensitive to structural details, and provides a satisfactory alternative to extensive numerical approaches and to expensive scale-model measurements.

The elastic waves in shells (compressional, shear and flexural), if insonified, can convert and exchange energy with each other at shell discontinuities such as bulkheads and endcaps. Under extensive wave conversion, wave power, defined as energy density multiplied by axial group speed, is hypothesized to be equipartitioned among the elastic wave types, a concept analogous to modal energy equipartition in statistical energy analysis (SEA). The power equipartition hypothesis is tested through a finite element calculation of finite endcapped shells with four deep heavy rings (the ringed shell) and with no rings (the empty shell). Wave power equipartition is found plausible for the ringed shell, where the power difference among the elastic waves is within 3 dB during the second roundtrip time of the trace matched wave in the shell. For the empty shell, the power difference among the elastic waves is, however, typically 5-10 dB, indicating no power equipartition at least within the first 6 roundtrip periods of the trace matched wave in the shell.

Based on the elastic wave power equipartition hypothesis, sound radiation is predicted from the motion of the elastic waves with the finite shells treated as a finite array. The excitation is limited to within 30° of beam aspect, so that acoustic wave trace matching to supersonic compressional and shear waves is dominant. First, an infinitely long shell model is used to estimate acoustic wave power injected into the shells. Then, the power in each elastic wave type is obtained via the wave power equipartition hypothesis. Further, a radiation model is built to project the wave motion into sound pressure in the fluid. Finally, the predicted bistatic elastic scattering is displayed in the time domain, based on random phase realizations and a decay rate model which considers various dissipation mechanisms in the shells.

The predicted target strength is compared with MIT/NRL measured data for the ringed shell and the internalled shell with the internal structures resiliently mounted

to the rings. The mean target strength over the frequency region $3 < ka < 10$ and the observation region with within 30° of beam aspect is evaluated. The prediction differs from the measured data by no more than than 2.5 dB for the second and third roundtrip of the trace matched wave in the shells, as well as for a time integrated case. The consideration of the modified wave speeds in the prediction model does not yield a better agreement with the measured data. The unmodified wave speeds (from the infinitely long uniform shell) alone can provide acceptable prediction results.

The geometric scattering, much less sophisticated than the elastic scattering but important in the specular (forward) direction, is not considered in this study; its effect can be readily accounted for using methods in the literature. In doing so, a total estimate of scattering can be readily made.

Thesis Supervisor: Professor Ira Dyer
Title: Weber-Shaughness Professor of Ocean Engineering

Acknowledgements

First of all, I would like to thank my thesis supervisor, Professor Ira Dyer, who introduced me to this rich and fascinating project, guided me through the process and challenged me to make the most out of it. Ira, it is my great honor to work with you. I am equally grateful to the wisdom and guidance of my thesis committee members, Professor Henrik Schmidt, Professor Richard H. Lyon and Dr. Preston W. Smith. In addition, I appreciate many technical discussions with Dr. Yueping Guo. I also thank Dr. Joe Bondaryk, whose technical knowledge, critical comments and suggestions helped me a lot in documenting and presenting the thesis research.

To the acoustic group administrative staff, Sabina Rataj, Taci Darnell, Isela Cordova and Patrick Preston, thank you for keeping us all happy and for making the thesis process run smoothly. Sabina, you understand and care about students, and always try to provide a solution to any problem that comes along. Thank you very much. Thanks also goes to the administrative staff in the OE department headquarters and the OE student records office.

The research was supported by the Office of Naval Research under contracts #N00014-92-J-1076 and #N00014-95-I-0368. The experimental data was collected by the Physical Acoustics Branch at the Naval Research Laboratory (NRL) in Washington. Thanks to Dr. Liu and Dr. Vasudevan of the Navy Surface Warfare Center (NSWC) who provided valuable technical assistance in the finite element modeling of the shells using SARA-2D software. Thanks to Professor R. Fricke and Ron Frink at MIT for submitting the job runs. Financial support from the Department of Ocean Engineering for April and May of 1996 is deeply appreciated.

Life and study at MIT would be unimaginable without the company of the student colleagues. Many stimulating discussions in the office were rich experiences of learning and communicating ideas. During my recent thesis defense rehearsals, Vince, Peter, Brian, Dan, Pierre, Yevgeniy, Yuriy and Paeng provided valuable suggestions and comments. It was a very uplifting experience for me. Life outside the office (it does exist) is also memorable; activities with the student organizations MITCSSA and GSC, and activities in the MIT gym all made my time at MIT full of fun. I cherish the fantastic years at MIT and the friendships forged with you guys. I truly believe that the friendships will last for a very long time.

The draft of this thesis has been proofread in full by Joe Bondaryk and in part by several other people. I apprecite the help from Ken Rolt, Brian Tracey, Joo Thiam Goh, Rama Rao, Mark Hayner, and Peter Daly. I also thank Matt Conti and Chick Corrado for sharing their knowledge and understanding of the shell models and the measured scattering data.

Finally, I am extremely grateful to my wife for her great patience, encouragement and love. Juanhui, you have given so much to make this dream of mine possible. The love and support from Mom and Dad, from Ming He, and from Juanhui's family have been tremendous. I thank you all from the bottom of my heart.

Contents

Chapter 1

Introduction

1.1 Motivation and objectives

Sound is widely used for underwater detection because light can not travel very far in water. Sound scattering (echo) from an insonified elastic shell-like target in water contains both geometric and elastic scattering components. Elastic scattering, which usually occurs later in time than geometric scattering, is related to the resonance or elasticity of the shell-like target. Understanding and prediction of both geometric and elastic scattering is important for the detection of shell-like elastic targets submerged in water. Geometric scattering is reasonably well understood (Ref. [1]). This thesis therefore concentrates on the elastic part.

Elastic scattering can be related to coupling between the acoustic and elastic waves and coupling among the elastic waves in shells. Namely, elastic scattering involves the following processes.

- acoustic excitation of the elastic waves in shells
- coupling among the elastic waves in shells
- sound radiation from the elastic waves in shells

For submerged, cylindrical, thin shells in the mid-frequency range (acoustic wavelength comparable to the shell radius), one usually observes three elastic wave types:

(1) *compressional* (quasi-longitudinal) waves due to in-plane structural elongation and compression; (2) *shear* (quasi-shear) waves due to in-plane transverse motion; and (3) *flexural* waves due to out-of-plane bending. The first two wave types, together, are also called membrane waves. The membrane waves in shells, unlike those in flat plates, have substantial normal displacement components caused by shell curvature and therefore are capable of radiating sound strongly once their speeds exceed that of water. Although flexural waves have large radial motions, they are subsonic and generally unimportant for sound radiation in water (unless near shell discontinuities).

One important mechanism of acoustic excitation of the elastic waves is *trace matching.* The supersonic membrane waves can be trace matched when the trace speed of an incident sound equals or exceeds that of the membrane waves. Therefore, trace matching only occurs when sound is incident within a sonic cone region centered around beam aspect (normal to the shell axis).

Reciprocally, one important mechanism of sound radiation from the elastic waves is supersonic wave radiation. Once trace matched, the membrane waves can propagate forward in the shells and radiate in the specular direction (with respect to the incidence direction). The radiation in the backscatter direction (the reverse incident direction) does not occur until the forward trace matched elastic waves are reflected at shell discontinuities such as endcaps and bulkheads.

The shell discontinuities in finite complicated shells play roles in all the three processes of the elastic wave scattering. The most important one is that they cause elastic waves conversion and create extensive elastic wave coupling and energy sharing among the elastic waves. Apart from bulkheads and endcaps, there are a large number of other kinds of discontinuities in the real world submerged vehicles. For example, additional internal structures with many degrees-of-freedom might be attached to bulkheads. All those inhomogeneities create enormous elastic wave interactions. As a result, the elastic wave field in a shell is very complicated.

To determine scattering from finite complicated shells, one might use experimental means, but building a real model and performing intensive underwater measurements is extremely expensive and time consuming. One might also attempt numerical calculations, but a complete numerical modeling of a real world shell model is close to

impossible. Not only is it hard to model every structural complexity of a real world shell, but also one often lacks knowledge of the structural details. Even if one has the blue prints of a real world shell model, manufacturing inaccuracies can yield serious structural uncertainties as well.

Since shell details are largely uncertain or even unknown, I choose to explore a statistical approach to estimate the average scattering behavior of finite complicated shells. Instead of treating finite complicated shells as complicated systems with many degrees-of-freedom, I treat elastic wave types as subsystems of the shells. The energy sharing among elastic wave types is conceptually no different from the energy sharing among structural subsystems. If the wave coupling is extensive enough to cause equipartition of wave energy flux or wave power, it is possible to characterize the statistical power of the elastic waves and estimate sound radiation from them. This method of predicting elastic wave scattering should be rather insensitive to shell structural details.

This thesis is motivated by the desire to formulate and test the wave power equipartition concept to predict quantitatively the elastic scattering from complicated elastic shells in water. Although geometric scattering is not studied in this thesis, its effect (especially in the specular direction) can be easily accounted for using methods in the literature, e.g. [1]. In doing so, a total estimate of scattering can be readily made.

1.2 Previous work and related research

Literature review

Scattering from shells has been studied extensively especially in the last few decades. Scattering from empty spherical shells and infinitely long cylindrical shells are the most tractable because the shell geometry is separable and the scattering can be determined exactly by modal series. [2].

Resonance scattering theory (RST), is helpful to identify and classify mechanisms causing resonance scattering. Experimental techniques have been developed to iso-

late the resonance response from the geometrical scattering [3], [4]. The resonances considered in these studies, however, are mainly caused by the radiating elastic waves because the finite elastic shells presented have no discontinuity or only weak discontinuities. As a result, wave conversion among the elastic waves was ignored in these studies.

Generalized ray approaches have been intensively used to show resonance scattering from surface-guided elastic waves on smooth shells of various shapes [5], [6],[7] and [8]. Ray approaches provide clear physical pictures of coupling between sound and shell waves, but are generally limited to high frequencies. Although it has been successfully used in examining the effect of internal structures, it is generally difficult to apply ray theory as the level of shell complexity increases.

A modal-based method [9] was used to achieve considerable understanding of transient elastic wave propagation and sound radiation from submerged finite shells with bulkheads and endcaps. This study is, however, limited to the radiation case where the shells are excited by a point force. In addition, the endcaps considered have no slope discontinuities.

The approaches reviewed so far are predominantly deterministic. Yet, since elastic wave interactions and coupling at shell discontinuities create a reverberant field, statistical approaches should be feasible and helpful.

Weaver [10] estimated diffuse sound radiation from shells following concepts in traditional Statistical Energy Analysis (SEA). Elastic waves were treated as subsystems and modal energy equipartition was assumed. The study, however, did not test the plausibility of the modal energy equipartition in shells. Moreover, the assumption of diffuse sound field eliminates the angle dependence of radiation.

Treating a structure, such as an empty shell, as a deterministic master structure while treating the attached structures, such as bulkheads and internals, as a group of resonators with certain statistical properties, some authors [11], [12] have recently studied the structural acoustic problems of Fuzzy Structures (FS). It is interesting that some major findings in the FS study can be readily derived from traditional SEA methods.

Rybak [13], [14] conducted theoretical studies on longitudinal and flexural wave coupling in plates with random inhomogeneities. He calculated the 'mean-square modulus of the field' by means of the Dyson equation as well as the spatial distribution of average energy. The wave power equipartition concept in this thesis is influenced by his work.

Since phase is, together with amplitude or energy, a fundamental aspect of wave phenomena, a SEA counterpart of phase, statistical phase analysis (SPA), has been developed since the 1980s [15], [16] and [17]. The major development of the study of SPA is that the averaged phase slope of mobility transfer functions depends on modal density and modal overlap of the system, and is proportional to modal density of the structure by a factor of $\pi/2$ if modal overlap is much smaller than 1. The analysis of statistical phase provides a way of measuring modes of a structure and has the potential to be used in the sound scattering case. This potential has been explored by a recent study [18] which showed that the extension to resonant scattering is possible, in the case of a single structural or wave system. However, the problem in this thesis is mid-frequency transient scattering from shells with coupling among multiple elastic wave types, and thus does not seem to be amenable to the technique of SPA.

Shell scattering research at MIT

In the MIT structural acoustics program, experimental analysis of scattering of scaled shell models have been carried out over the past several years. Several Ph.D. and Master theses [19], [20], [21], [22], [23] and [24] reflect this research effort. This thesis work is part of the continuous research to further understand elastic wave scattering.

The essence of the MIT shell scattering study is to find out what *does* and what *does not* affect the shell scattering. Three shell models have been built that are acoustically representative of underwater vehicles but simple enough to treat with available techniques.

The shell models include a set of incrementally complicated shells of 90:1 scale [21]. The simplest is the *empty shell.* It is a cylindrical thin shell capped by a conical endcap that is connected by a fractional spherical shell. There are slope discontinuities at

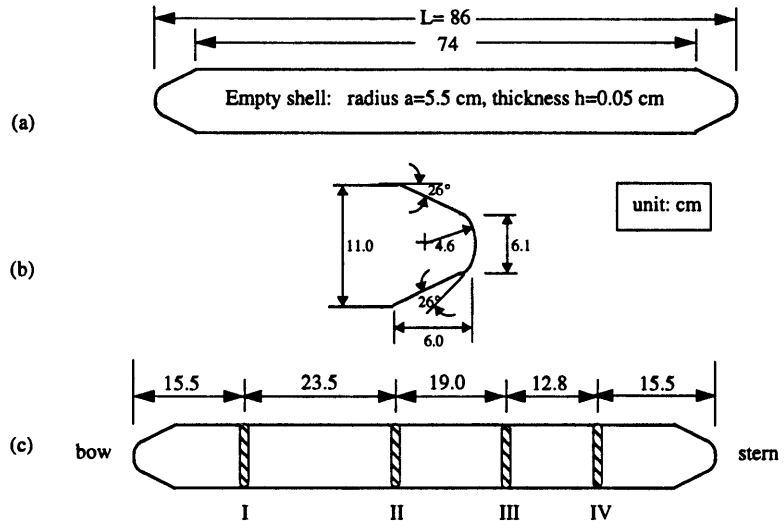

Figure 1-1: Dimensions and configurations of the MIT empty and ringed shells. Dimensions in *cm*. (a) the empty shell; (b) endcap; (c) the ringed shell with four rings.

both the cylindrical-conical shell junctions and the conical-spherical shell junctions. The slope discontinuities shown in (a) and (b) of Fig. 1-1, although small, can have strong influence on elastic wave conversion.

Two other shell models are studied. One is identical to the empty shell stiffened by four unequally spaced heavy elastic rings, and is called the *ringed shell.* The third shell, *internalled shell*, is distinguished from the ringed shell by additional sprung elastic internal structure resiliently mounted at the rings.

Fig. 1-1 shows the dimensions and configurations of the empty and the ringed shells; Fig. 1-2 shows the configurations of the internalled shell. The mass ratio of the three shell models are **1**(empty shell):**2** (ringed shell):**4**(internalled shell). The compressional wave speed is 5270 m/s in the shells and 1625 m/s in the delrin rods. The shells and the rings are nickel Ni-200. App. B lists the shell parameters in detail.

The frequency is in the mid range of the dimensionless product of the acoustic wavenumber in water and the shell radius, $2 < ka < 12$, where the acoustic wavelength $\lambda = 2\pi/k$ is comparable to the shell radius a. The lower bound is about one half the shell's ring frequency and the upper bound is about three times the shell's ring frequency.

The scattering measurement of the MIT shell models is reviewed in the following. The experiments were conducted in a water tank at the Naval Research Laboratory (NRL) and consisted of a series of measurements of scattered sound signals from the three shell models due to broadband ($2.3 < ka < 11.0$) plane sound pulse excitation. The transient sound pressure was measured in both the backscatter direction (monostatic) and in other directions (bistatic). As shown in Fig. 1-3 for the experiment configuration, the shells were excited by a $3m$ long 84-hydrophone line array source. The bistatic scattered pressure was measured at a $2m$ distance from the shell center, typically at 1° increments from 0° to 360°. The incidence angle θ is measured with respect to the shell axis, thus bow incidence is equivalent to $\theta = 0°$. The observation angle is also measured with respect to the shell axis. The incident pressure p_i is measured near the shell surface with the shell models removed. The scattered pressure is obtained by subtracting the incident pressure from the total measured pressure, $p_s = p_t - p_i$. The subtraction process provides a signal-to-noise ratio above 45 dB.

Corrado [19] discussed the evolution of membrane waves in shells and the measured radiation losses. He pointed out shear wave dominance in the backscattering of the empty shell. He also studied the monostatic and bistatic target strength and found that the target strength of the ringed shell and the internalled shell are very similar to each other, while clearly different from that of the empty shell. His studies provide basic knowledge that guides further investigation of transient backscatters in this work. Because Corrado focused more on the membrane waves, the flexural wave was not extensively discussed in his study.

Corrado [19], Bondaryk [20] and Conti [21] used a beamforming technique to project the nearfield sound pressure onto the shell surface, revealing details of forward- and backward-going elastic waves in the shells. In the special case of axial incidence,

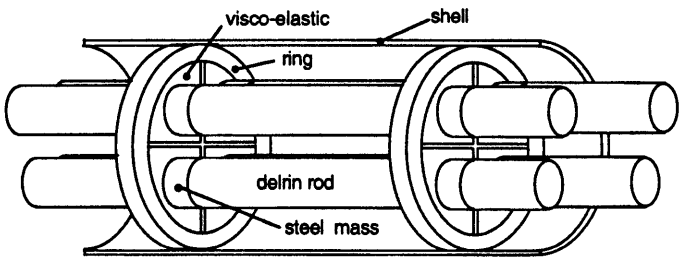

Figure 1-2: Illustration of the MIT internalled shell model. From Conti's thesis [21].

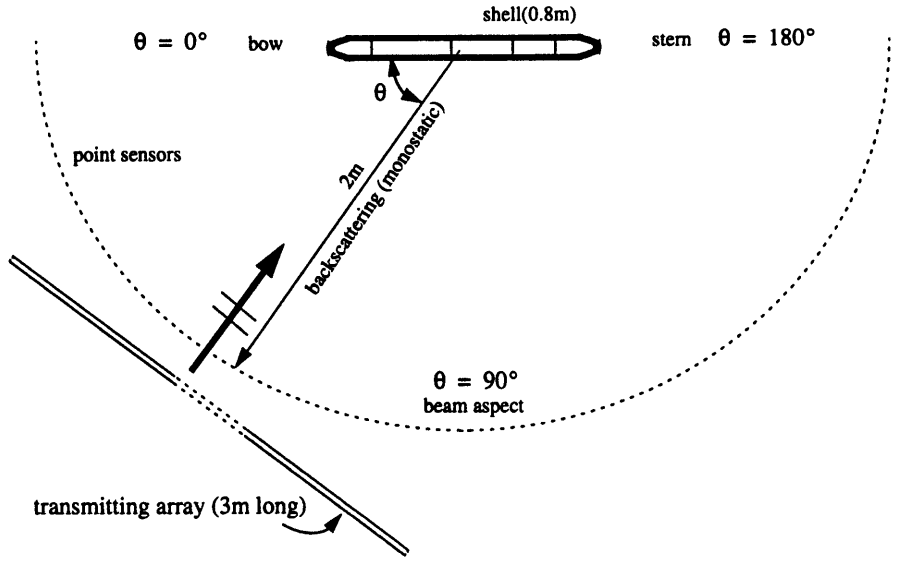

Figure 1-3: Sketch of the MIT/NRL shell scattering measurement configurations (not to scale).

Bondaryk found that approximately one tenth of the compressional wave amplitude of mode $n = 0$ is reflected at the endcaps. Although the beam focusing technique is powerful, the lack of circumferential measurement points prevents the analysis of waves of higher mode ($n > 0$) in the shells.

Conti [21] focused on scattering near the axial direction, where the length scale of the endcaps falls into the transition region between the low and high frequency approximations. Conti discussed rather extensively the flexural wave interaction with compressional waves at the endcap junctions and at the elastic rings for mode $n = 0$. He did not consider shear waves after demonstrating their unimportance at aspect angles close to axial incidence.

Machovjak [23] processed the bistatic experimental data with Maximum Likelihood beamforming to identify structural resonances in the data. His observation of the flexural wave influence in later arrivals for the ringed and the internalled shell demonstrated that flexural waves play a role in the scattering processes, even though they are subsonic.

Park [22] compared the decay rates of beam aspect monostatic scattering, in three frequency bands and two temporal regions. He found that by the time the flexural

waves transverse the average ring bay, the decay rate is generally smaller than that immediately after the initial return. His analysis did not consider shear waves because shear waves are not directly excited at beam incidence.

Apart from the experimental analysis, analytical and numerical studies have been carried out at MIT as well. Ricks [24] developed a Direct Global Matrix model for infinitely long cylindrical shells by using the full 3D elastic theory. Guo [25], [26] used asymptotic methods to analyze wave propagation in conical shells. He showed that shear and flexural waves cutoff in the conical shell, while the compressional wave does not when fluid loading is considered. What is more, compressional waves are found to dissipate heavily in the conical endcap. The amplitude of the compressional wave can attenuate by tens or even hundreds of decibels, after one roundtrip in the conical endcap. Guo's research on wave dissipation at the endcap provides direct guidance to the estimate of compressional wave decay in this study. In addition to the study of wave propagation at the endcaps, Guo also studied the effect of bulkheads and keels on shell scattering and radiation, see [27], [28] and [29].

1.3 Approach

The purpose of this thesis is to formulate and test statistical concepts in order to predict elastic wave scattering from finite complicated shells in water.

Excited by incoming sound, and converted at shell discontinuities, the elastic waves will exchange energy among themselves, possibly resulting in an equipartition of wave power provided the coupling among the wave types is strong. This wave power equipartition concept is similar to energy sharing processes among coupled structural subsystems. The classical SEA [30] predicts equipartition of modal energy if the coupling between the subsystems dominates the dissipation. In the case of wave types being treated as subsystems, wave power might be equipartitioned, if the decay of the average field because of elastic wave coupling is more rapid than the decay because of damping [13]. I hypothesize elastic wave power equipartition in this study and via the hypothesis, I expect to redistribute the injected sound power among the power in the elastic wave types, whether or not they are directly excited.

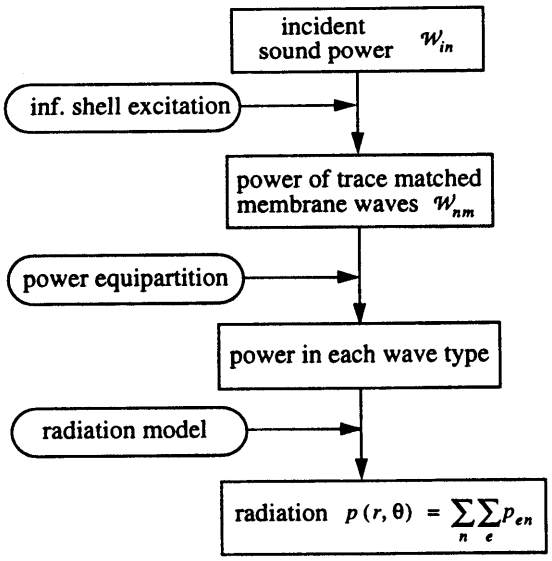

Figure 1-4: Illustration of the modeling procedure and the associated assumptions.

Fig. 1-4 illustrates the statistical scheme based on the elastic wave power equipartition hypothesis. The box 'Inf. shell excitation' is intended to estimate how much of the incident sound power is injected into the shells while the box 'radiation model' is intended to project the wave motion into sound pressure in the fluid. Before I discuss the two boxes further, I will discuss the test of the wave power equipartition hypothesis, which can be done through the following three possible approaches: measurements, theoretical analysis and numerical calculation.

The MIT/NRL measured data provide reliable transient scattered sound pressure from the three shell models. However, they do not contain direct vibration measurements on the shells. Even though it is possible to reconstruct the surface pressure and even the radial velocity on the shells by means of the beamforming technique, the in-plane wave motion is still missing. Thus the data can not be used directly to test the wave power equipartition hypothesis.

There does not seem to be an alternative theoretical approach. No analytical technique has been found in the literature to solve fluid-loaded finite complicated shells (such as the ringed shell) without making extra assumptions.

As a result, I use numerical approaches in this study. A finite element code

developed by BBN [31] (SARA-2D) allows the circumferential components of the shell response and scattered field to be compressed into Fourier modes (circumferential orders), as long as the shells are axially symmetric. This thesis uses a SARA-2D program that has been implemented by Liu and Vasudevan [32] to calculate the responses of both the empty shell and the ringed shell. The internalled shell can not be calculated by SARA-2D because it is not axially symmetric and has to be modeled as a 3D structure. There may be other FEM codes to solve 3D elastic shell scattering problems at mid frequencies, including viscoelastic internals, but huge computation cost prevents calculation of the internalled shell in this study. In fact, it is the general difficulty in computing complicated shells that motivates the development of a statistical scattering prediction model in this thesis.

In this study, the role of SARA-2D itself is mainly limited to generating shell surface responses. Independent post-processing is needed to transform the surface response into the wavenumber domain, in order to identify and evaluate the elastic wave motion and wave power. The coherent phase information is retained in the SARA-2D calculation so that it is possible to do transient analysis in post-processing by means of the inverse Fourier transform. The numerical analysis is intended to answer *if* and *when* the wave power hypothesis is plausible.

Based on the numerical inference of plausible wave power equipartition in the ringed shell model, I use the power equipartition hypothesis to predict sound scattering from the ringed and the internalled shells, using the flow chart shown in Fig. 1-4. As mentioned, there are two extra steps necessary: one is to estimate how much sound power is injected into the shells ('Inf. shell') and the other is to project the wave motion into sound pressure in the fluid ('radiation model'). Note that the two steps are not reciprocal, although they seem to be. The acoustic excitation involves an infinitely long shell while the radiation involves a finite shell. The reciprocity relation can not be readily applied and separate studies must be performed.

Sound power injected into a finite shell can not be readily calculated by rigorous theoretical means, but can be approximated. In this thesis, I limit sound incidence to the membrane wave trace matching region $60° < \theta < 120°$, where I expect the acoustic trace matching to dominate other excitation mechanisms, such as induction

at endcaps and excitation of the subsonic flexural wave at the rings. Trace matching not only provides much more efficient coupling between the sound pressure field and the shell motion, but also occurs over the whole shell length instead of at isolated shell discontinuities. It is thus reasonable to assume that the injected sound power is from trace matching alone. Based on this assumption, the injected power due to trace matching can be conveniently obtained from calculation of an infinitely long cylindrical shell. This assumption of 'trace matching only' is thus also expressed as the 'Inf. shell excitation' assumption in Fig. 1-4, which states that the acoustic trace matching injects the same amount of energy per unit shell length into the infinitely long shell as into the finite shell. The injected elastic wave power into an infinitely long shell can be calculated using conventional shell theories.

The radiation model box in Fig. 1-4 converts the elastic wave motion to sound radiation. Green's theorem can be used to compute sound pressure in the fluid if the surface pressure and velocity of each elastic wave type is known. In doing so, however, three issues have to be addressed. (1) Only radiation from the cylindrical shell section is considered while the endcap radiation is ignored. I expect the endcap radiation to be insignificant, if the sound observation angle is restricted to $60° < \theta < 120°$ as well, the same restriction as for sound incidence. (2) The wave power calculation does not provide a detailed pressure and velocity field, but the magnitude of total velocity. Thus, the phase field, surface pressure and radial velocity are missing and have to be estimated, mainly through calculation on the infinitely long shell. The phase field can be reconstructed from the axial phase speeds or axial wavenumbers, which might be estimated from the infinitely long shell calculation. The radial velocity component can be extracted from the total velocity following the wave motion polarization behavior in the infinitely long shell. The missing surface pressure can be estimated through the momentum equation. (3) The radiation model only gives magnitude of the scattered sound pressure. To extends the scattering prediction to the time domain, a decay rate model has to be developed that considers different wave dissipation mechanisms in the shell models.

In addition to its use in testing the wave power equipartition, SARA-2D is used to examine the assumptions and approximations in the acoustic excitation and radi-

ation modeling. For example, the rings might modify wave speeds and wave motion polarization behavior. Their effects need to be investigated before an infinitely long shell model can be used. The flow chart in Fig. 1-5 illustrates the post-processing steps. Parallel to the steps in Fig. 1-4, the numerical calculation provides detailed shell response.

The MIT/NRL data can be used to directly compare the prediction of the bistatic target strength from the statistical model. In addition, the data can be used to test the accuracy of the numerical calculations. Moreover, the data can be analyzed to derive understanding of the shell scattering behavior, such as decay rate and wave speed change due to the rings. Fig. 1-6 summarizes the relationship among the model, the measured data and the numerical calculation.

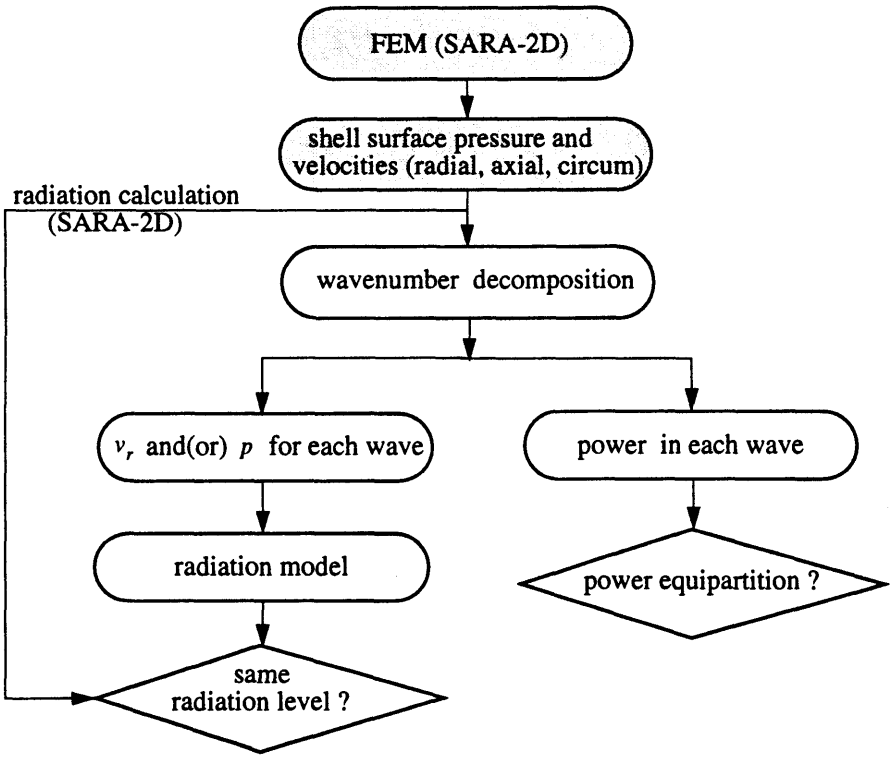

Figure 1-5: Illustration of numerical calculations based on SARA-2D shell response. The numerical calculation helps to test the hypotheses for the modeling. The shaded blocks represent straightforward implementation of finite element calculation while the remaining blocks are post-processing steps.

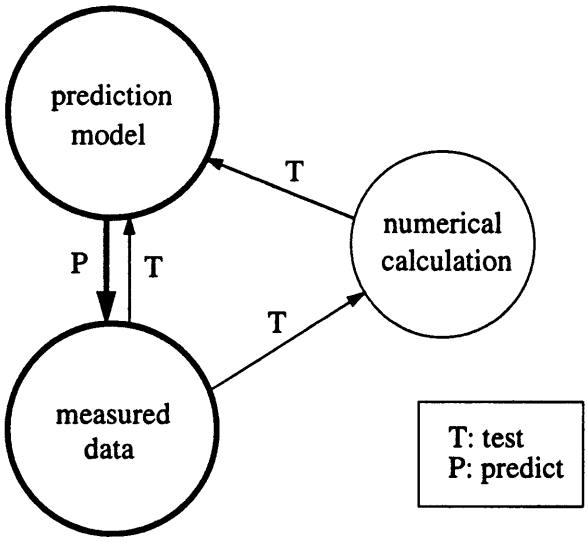

Figure 1-6: Interplay of model, measured data and numerical calculation.

1.4 Thesis overview

Without going into the mathematics, I outlined the statistical scheme in the previous section. This thesis is naturally organized as formulation and test of the wave power equipartition concept, in Chap.2 and in Chap.3 respectively, followed by the development of the radiation model in Chap.4. In Chap.5, the transient elastic scattering from the ringed and internalled shells is predicted based on elastic wave power equipartition, and is compared to the measured data.

The first part of Chap.2 discusses basic concepts and understanding of elastic wave excitation, propagation, radiation and coupling in cylindrical shells. A dispersion diagram in the frequency-wavenumber domain is projected to demonstrate the acoustic trace matching and elastic wave coupling processes. A semi-quantitative analyses on wave coupling strength and wave dissipation is performed. The significantly large coupling strength among the waves in comparison with the wave dissipation damping indicates that wave power equipartition is likely for the ringed shell and it is reasonable to hypothesize wave power equipartition. In the second part of Chap.2, I formulate mathematically the statistical scheme of computing the power in each elastic wave type for finite complicated shells, via the power equipartition hypothesis and

the infinitely long shell excitation assumption. I find that the power equipartitioned among the elastic waves equals the sound power injected into the shells scaled by the wave group speed ratios, and is approximately 20 dB lower than the incident sound power.

Chap.3 tests the wave power equipartition hypothesis through numerical calculations. First, the accuracy of the SARA-2D finite element modeling is verified. I show that the calculated scattering from the ringed shell is approximately 2 dB higher than the measured data within the membrane wave region. The detailed finite element analysis and wavenumber transform of the shell surface response are not presented in this chapter, but placed in App.C. Second, the power of the elastic wave types is calculated for the empty and the ringed shell, for both steady-state and time-windowed cases. The time windows are based on the integer number of roundtrip periods of the trace matched wave in the shells. The wave power difference is found to be within 3 dB for the ringed shell but typically within 5-10 dB for the empty shell. Thus, power equipartition is plausible for the ringed shell but not for the empty shell. In addition, wave power equipartition is found to occur during the second roundtrip period of the trace matched wave in the ringed shell. The calculation of finite shells with fewer rings indicates wave power equipartition is still approximately true, but more evident later in time.

Chap.4 builds a radiation model to convert wave motion to sound pressure in the fluid, based on Green's theorem. The model computes sound radiation from the cylindrical section while ignoring the endcap radiation. First, the effect of endcap radiation is tested, by comparing the radiation using decomposed surface responses from the SARA-2D calculation with the direct SARA-2D scattering calculation. I find that the radiation calculation without the endcaps is only 1-2 dB different from the direct SARA-2D calculation, as long as the observation angle is within $60° < \theta < 120°$. This observation is further supported by an examination of the MIT/NRL measured data. Second, I bridge the gap between the input of the radiation model and the output of the wave power calculation, by estimating the elastic wave speeds, surface pressure and radial velocity component of the total velocity due to each wave type. I find that the infinitely long shell calculation can be used as approximations which

underestimate the sound radiation to within 2 dB, in comparison with the direct SARA-2D calculation, and are thus acceptable for scattering prediction. In addition, I investigate the influence of the rings on the wave speeds. The rings can modify the membrane phase speeds considerably, but decrease the flexural phase speed only slightly. The membrane wave region, however, does not change significantly. The modified wave speeds will be used in Chap.5 for scattering prediction.

Chap.5 predicts elastic wave scattering in the time domain, based on the wave power calculation in Chap.2 and the radiation model in Chap.4. In order to convert the magnitude of the sound pressure into the time domain, a random phase realization concept is put forward. Further, the unified wave decay rate in the presence of strong wave coupling is formulated and estimated. The unified decay rate is found to be a weighted summation of individual decay rates of the elastic waves, with the weighting determined by the ratio of the axial group speeds of the elastic waves. Major decay mechanisms considered include radiation dissipation from the cylinder, coupling dissipation to compressional wave radiation from the endcaps, as well as energy loss into the internals. The second half of this chapter predicts the transient target strength for finite shells having the same dimensions and materials as the MIT ringed shell model but with unspecified internal details. The prediction is compared against the MIT/NRL measured data in windows defined as the integer number of roundtrip period of trace matched waves in the shells. The logarithmic means over the frequency region $3 < ka < 10$ and angular region $60° < \theta < 120°$ are rather close between the predictions and the measured data, with differences generally within $\pm 2.5dB$, for window 2 and 3 as well as for a time integrated case. The ring influence on membrane wave speeds is also considered. Inclusion of the random wavenumber realizations in the prediction model generally does not yield a better agreement with the measured data.

Chap.6 summarizes the results of this thesis and suggests for future research.

Chapter 2

Insonified elastic waves and their power

This chapter studies acoustic wave coupling to elastic waves and elastic wave propagation and coupling in shells. I discuss the basic concepts and understanding about elastic wave excitation, propagation, radiation and coupling in Sec.2.1. The discussion serves to facilitate the later modeling in the thesis. One focus is on trace matching, assumed as the dominant excitation mechanism within the membrane wave region, so that the infinite shell results can be used for the acoustic excitation of a finite shell. Another focus is on speculating elastic wave coupling strength against wave dissipation, to illustrate semi-quantitatively the likelihood of wave power equipartition in finite shells such as the ringed and the internalled shell. Based on the wave power equipartition hypothesis and the infinite shell excitation assumption, the elastic wave power is formulated in Sec.2.2 and calculated in Sec.2.3. The equipartitioned wave power is expressed as the injected sound power scaled by the group speed ratios of the elastic waves, and is approximately 20 dB lower than the incident sound power.

2.1 Elastic waves in shells, excitation, coupling, and dissipation

The problems of elastic waves in shells and their interaction with sound are unique on one hand and are commonly understandable on the other. The uniqueness is caused by the shell curvature. Because of curvature, any elastic wave has non-zero displacements both in-plane and out-of plane, although membrane waves are still predominately in-plane and the flexural waves are still predominantly out-of-plane. One implication of this is that the sound wave can couple to the supersonic membrane wave efficiently through their small, but very important radial motions. Such coupling would be much weaker in flat plates. Another implication is that the elastic waves in shells can be coupled with each other by essentially *any* kind of discontinuity, even at a single point.

Yet it is possible to understand the acoustic problems in a common sense. First, a sound wave can excite elastic waves by trace matching if the trace speed of the sound is larger than that of elastic waves. Trace matching, also called acoustic coincidence, is a fundamental concept that can be described by Snell's law. Second, elastic wave propagation in shells can be approximately viewed as wave propagation in a waveguide. The shells allow elastic waves to propagate in the axial direction, but confine them in the circumferential direction if the circumferential periodicity is regarded as a boundary.

2.1.1 Wave motion in an infinitely long shell

The equation of motion of an infinitely long cylindrical thin shell can be derived in many ways, well summarized in [33]. Donnell's equations of motion for thin shells, attached in App. A, is used in this study, since the shell thickness is 1/90 of the radius, and 1/120 of the shear wavelength at $ka = 12$.

For a time harmonic solution, the homogeneous part of Donnell's shell equation of motion yields a dispersion equation in the form

$$D(ka, k_x, n, \sigma, \rho_s, \rho...) = 0 \ , \tag{2.1}$$

where the dispersion relation D is determined by the product of acoustic wavenumber in the fluid and the shell radius, ka, and by circumferential mode n, axial wavenumber k_x and the material properties of the shell and the fluid. The integer n represents the circumferential resonances due to the periodic boundary condition of the uniform cylindrical shell. The relation between mode n and the circumferential wavenumber k_ϕ (ϕ denotes azimuthal angle as seen in Fig. 2-6) can be expressed as

$$k_\phi = \frac{n}{a} \ . \tag{2.2}$$

In the axial direction, the shell is boundless and the axial wavenumber k_x is therefore continuous. In fact, one can regard a shell as a waveguide, where waves of different mode n and wave types can propagate in the axial direction.

From Eq. 2.1, one can solve for three free elastic wave types: compressional, shear and flexural waves. The details of the mathematics are shown in App. A.

The compressional and the shear waves are also termed 'membrane waves'. They propagate faster in the shells than sound does in water and therefore are supersonic. This implies that they are able to radiate sound efficiently. Their propagation speeds generally do not vary with wave propagation directions because the in-plane membrane stiffness is basically isotropic for thin shells.

The flexural wave is caused by local bending motion of the shell and is predominantly out-of-plane. As frequency increases, the local bending stiffness increases and the flexural wave propagates faster, resulting in its dispersive nature. In the mid-frequency range, the flexural wave in the shell is subsonic. It might generate large surface pressure due to its large radial motion, but the field decays rapidly (55 dB per flexural wavelength away from the shell [34]). Since the local bending stiffness is generally anisotropic for a cylindrical shell, the flexural wave propagates faster in the shell axial direction than in the circumferential direction. Therefore, the flexural wave speed is in general determined by both frequency and direction of propagation. The anisotropic behavior of the flexural propagation, however, quickly reduces to isotropic

behavior above the shell ring frequency at $ka \simeq 3.5$ for a water-loaded nickel shell. At higher frequencies, the flexural waves in the shells behave more and more like that in the flat plate [35].

In the following, I study the dispersion of an infinitely long cylindrical shell submerged in water. An infinitely long shell is studied because its dispersion can be used to describe finite shells, at least to the first order approximation, for the elastic wave behavior away from shell discontinuities. Ref. [36] has shown that the wave field in the middle part of a finite empty shell is essentially no different from that of an infinitely long cylindrical shell.

Fig.2-1, 2-2 and 2-3 display respectively the axial wavenumber, phase speeds and group speeds for compressional, shear and flexural waves of different circumferential mode n. The material and circumferential geometry of the infinitely long shell is identical to that of the empty shell model shown in (a) of Fig. 1-1.

The results in Fig.2-1, 2-2 and 2-3 indicate that the shear waves have cutoffs near $ka = 2, 4, 6, 8$ for mode $n = 1$, 2, 3, 4 respectively, because the real part of the axial wavenumber vanishes. The compressional waves, on the other hand, do not really cutoff, although the real part of the axial wavenumber has minima near the *ad hoc* cutoffs at $ka = 3.5$, 7.0 and 10.5 for $n = 1$, 2 and 3 respectively. The axial wavenumber at those frequencies would vanish, however, if there were no fluid loading [2]. It is fluid loading that causes no real cutoffs, but only *ad hoc* cutoffs.

The behavior of the imaginary part of the axial wavenumber near the cutoffs is directly related to radiation dissipation of the waves. As shown in the upper-right plots of Figs. 2-1 and 2-2, the imaginary part of the shear wavenumber first increases as frequency is lowered towards the cutoffs, but quickly reduces to zero at the cutoffs. The compressional wave counterpart, however, increases as the frequency is lowered towards and even below the *ad hoc* cutoffs, indicating significant increase in radiation dissipation. This radiation damping is physically evident at endcaps as will be shown shortly in Sec.2.1.2. The loss factors of the membrane waves due to radiation damping can be calculated for each mode n in Eq. 2.3, and is displayed in Fig. 2-4.

$$\eta = 2\frac{imag(k_x)}{real(k_x)} \,. \tag{2.3}$$

The damping loss factors above the cutoff frequencies are not very different between the compressional waves and the shear waves, a phenomenon found in Ref. [37] for infinite cylindrical shells. Note that this radiation damping behavior will change in conical shells, where cutoffs become typical because of shell radius contraction. The issue will be further discussed in section 2.1.2.

The group speeds in Fig.2-1, 2-2 and 2-3 can be measured from the slopes of the wave loci. In the case of the membrane waves, the group speeds are smaller than the phase speeds. The flexural group speeds are smaller than the phase speeds below $ka = 3.2$ but increase to become twice the phase speeds at higher frequencies, a well known behavior of thin flat plates or thin beams. In general, the axial group speeds of the flexural waves are only a fraction of the membrane waves, except near cutoffs of the membrane waves. Since the energy speeds in the shell waveguide can be represented by axial group speeds [38], the flexural waves transport energy much more slowly than the membrane waves do.

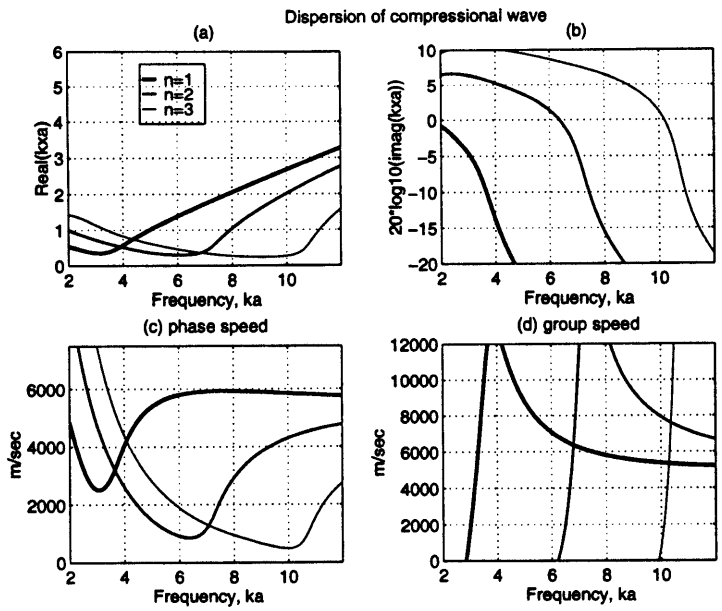

Figure 2-1: Compressional wave loci and speeds for n=1(solid), 2(dash) and 3(dash-dot). (a) Real k_x; (b) Imaginary k_x; (c) phase speed and (d) group speed. Compressional waves do not have real cutoffs because of fluid loading, but have *ad hoc* cutoffs near $ka = 3.5$, 7 and 10.5 for n=1, 2 and 3 respectively. From theoretical calculation of the fluid loaded infinitely long shell.

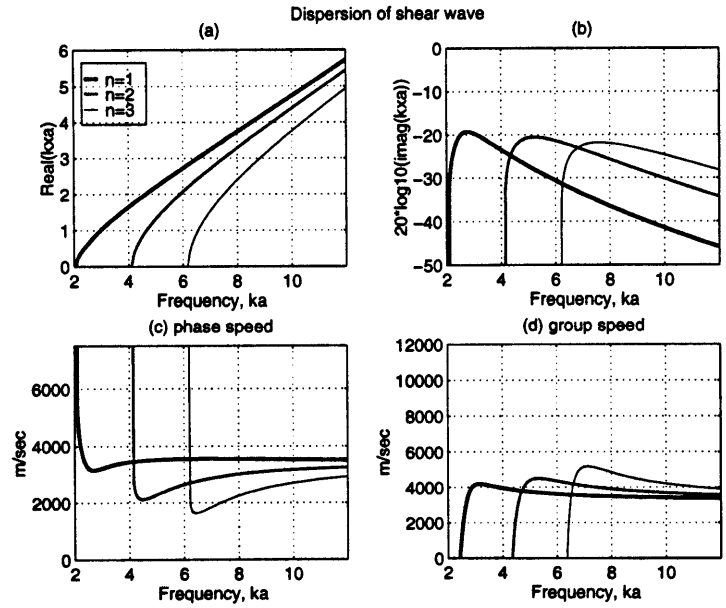

Figure 2-2: Shear wave loci and speeds for n=1(solid), 2(dash) and 3(dash-dot). (a) Real k_x; (b) Imaginary k_x; (c) phase speed and (d) group speed. Shear waves cutoffs can be observed near $ka = 2$, 4 and 6 for $n = 1$, 2 and 3 respectively. At cutoffs, phase speeds go to infinity while group speeds go to zero. From theoretical calculation of the fluid loaded infinitely long shell.

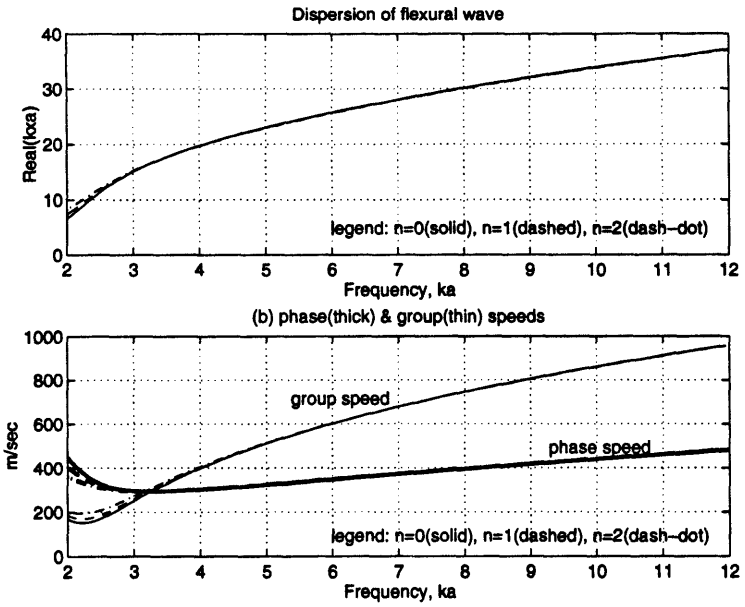

Figure 2-3: Flexural wave loci and speeds for n=1(solid), 2(dash) and 3(dash-dot). (a) Real k_x; (b) phase/group speeds. The Group speeds exceed the phase speeds at $ka = 3.5$, the ring frequency, and increase to becomes twice of the phase speeds as frequency becomes higher, a typical flat thin plate behavior. From theoretical calculation of the fluid loaded infinitely long shell.

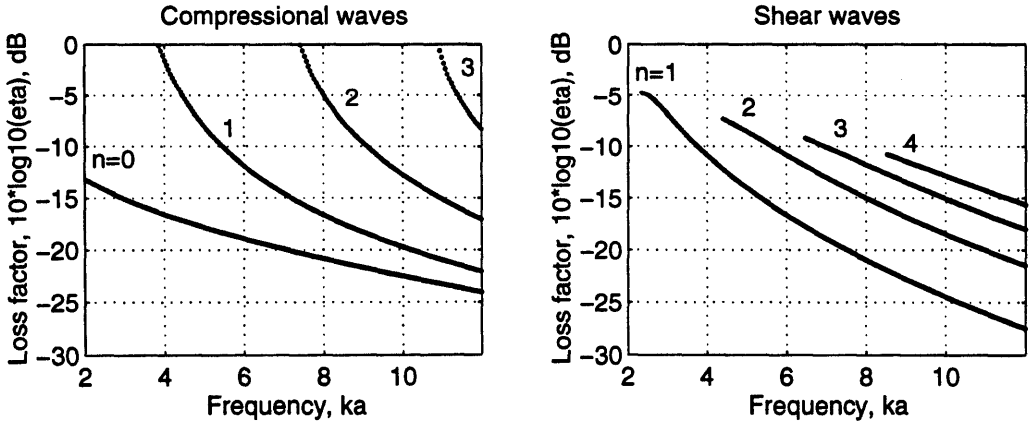

Figure 2-4: Loss factors of membrane waves. From theoretical calculation of the fluid loaded infinitely long shell.

2.1.2 Wave radiation from endcaps

Cylindrical shells in the real world are finite and terminated with endcaps. Endcaps contract the shell radius and cause many interesting acoustic phenomena. For example, endcaps might force elastic waves to cutoff because of the decrease of the local ka or $ka(x)$. Endcaps can also increase local flexural stiffness and thus flexural axial wave speeds. However, the major impact of endcaps on this study is the drastic increase of the radiation damping at the endcap, because compressional waves transmitted from the cylindrical shell, either from other wave types or from the compressional waves themselves, are forced to 'cutoff' due to the radius reduction. The waves thus become very dissipative since the imaginary axial wavenumber dominates the real axial wavenumber below the *ad hoc* cutoffs, see Fig. 2-1.

According to Guo's analytical study [26], the compressional wave amplitude might attenuate $10 \sim 100$ dB during a roundtrip into a conical endcap, the wave turning at a radius half the large radius. Fig. 2-5 shows his calculation of the compressional wave attenuation for each mode n at such an endcap. In the calculation, the wave attenuation is obtained from an integration over the endcap length. Typically, small n means small attenuation while large n indicates large attenuation. In comparison to the compressional waves, shear wave attenuation never exceeds 2.5 dB during such a round trip in the endcap, and can be regarded as relatively lossless at the endcaps.

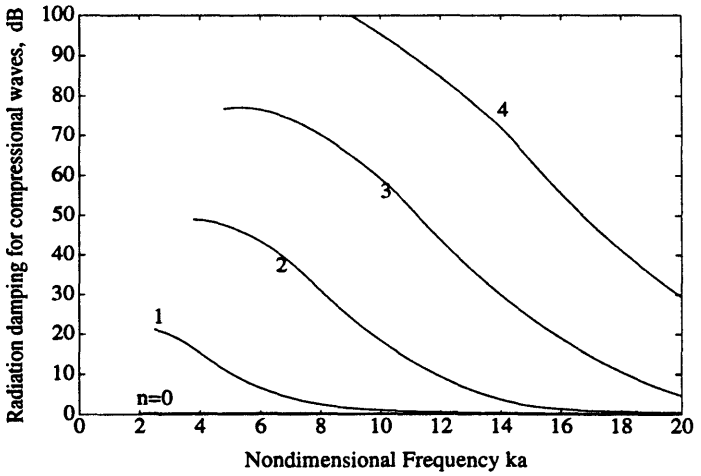

Figure 2-5: Attenuation of compressional waves during a round trip in a cone with small radius half the large radius and length equal to the diameter at the large end. From Guo [26].

2.1.3 Acoustic excitation of elastic waves in shells

Basic mechanisms

As mentioned in Sec.1.1, this thesis concentrates on elastic scattering. The following discussion is therefore focused on the elastic wave excitation; geometric scattering is not directly discussed.

Elastic waves in the finite shell models can be acoustically excited by at least the following three mechanisms:

- trace matching
- distributed forcing
- induced forcing.

Trace matching, or acoustic coincidence, occurs when the elastic wave speed exceeds sound speed in the fluid and when the acoustic wavelength is smaller than the characteristic shell dimensions. Taking the angle θ to be 0° in the bow axial direction and 90° in the beam direction, the axial trace matching of the shear and compressional waves occurs at $\theta \geq 61.3°$ and $\theta \geq 73.6°$ respectively, for a water-loaded nickel uniform shell (no rings) in this thesis. The angles are due to Snell's law in the form of $c_{mem} = c/cos\theta$ or Eq. 2.4. In other words, trace matching occurs only within a fan region (sonic cone) of about 60° around beam aspect ($\theta = 90°$). In this study, $60° < \theta < 120°$ is termed the membrane wave region because one, or both, membrane waves are susceptible to acoustic trace matching in the shell axial direction. It is true that the rings can affect the wave speeds and therefore the trace matching region. Sec.4.2.1. will show that four elastic heavy deep rings decrease the membrane wave speeds considerably above $ka = 5$. However, the minimum cutoff angle of the membrane wave region, which depends on the $n = 1$ shear wave speed, is not significantly affected by the rings. The minimum cutoff angle is shifted from 61.3° for the infinitely long shell to 59.7° for the ringed shell and to 58.7° for the internalled shell. Thus, I can still approximate the membrane wave region as $60° < \theta < 120°$ for the ringed and the internalled shells.

Fig. 2-6 sketches acoustic trace matching to membrane waves in a shell. An incident acoustic wave can trace match two helical elastic waves in the shell (two chiralities in opposite senses), but having the same axial wave speed. Two such opposite going waves in the circumferential direction lead to the circumferential resonances or mode n.

Distributed forcing occurs when the acoustic wavelength is many times larger than the shell dimension so that the fronts of the acoustic wave interacts with the shell in nearly the same phase like a unidirectional distributed force. Conti [21] demonstrated this forcing nature of the acoustic excitation of the endcap at low frequencies close to the axial direction ($\theta < 20°$).

Induced forcing is due to a local shell impedance change that induces internal coupling forces or moments, for example at ring attachments to the shell. These coupling forces or moments can be regarded as virtual sources that energize the shell to vibrate and radiate.

The above excitation mechanisms can be better understood if one considers the reciprocal process of excitation: radiation.

The reciprocal of acoustic trace matching of the supersonic elastic waves is supersonic sound radiation from the waves. If a plane sound is incident at $\theta = 75°$ where both shear and compressional waves are trace matched, the trace matched membrane waves will propagate forward in the shell and radiate in the specular direction $\theta = 105°$. The backward going membrane waves, if reflected at the shell end, will radiate in the backscatter direction $\theta = 75°$.

The reciprocal of distributed forcing is a piston pumping the fluid, as shown by Conti [21] for the axial endcap motion.

The reciprocal process of induced forcing is the power loss to the fluid during elastic wave interaction and conversion at shell discontinuities. Coupling among the elastic waves at shell discontinuities can create local displacement or stress disturbance to the surrounding fluid and can thus create sound radiation. In addition, even without flexural wave conversion to other wave types, the local shell impedance change would destroy the surface pressure canceling effect for the small-wavelength flexural waves

and create local flexural surface pressure that can indeed propagate far into the fluid. Such subsonic flexural wave radiation is commonly encountered in machinery noise control [35] in air.

The relative importance of the excitation mechanisms in the case of the MIT shell models can be discussed in the following angular regions.

- $60° < \theta < 85°$

  Rumerman [39] and Corrado [19] have given experimental and theoretical evidence that trace matching is the most important way of injecting sound energy into all three shell models. The trace matching dominance over other excitation mechanisms can be explained by its stronger coupling to fluid as well as the larger area of the coupling which occurs over the whole shell length.

- $85° < \theta < 90°$

  Corrado [19], Conti [21] and Klausbruckner [40] have shown that the geometric response dominates the scattering.

- $0° < \theta < 20°$

  In this region, Conti [21] has shown that the distributed forcing of the endcap is dominant for $ka < 6$.

- $20° < \theta < 60°$

  In this region, trace matching at the cylindrical shell is impossible. Geometric scattering is important, according to Dyer [34].

The focus of this work is the membrane wave trace matching region, $60° < \theta < 85°$. By removal of the geometric response from the MIT/NRL scattering data, and the SARA-2D numerical calculation, I extend the membrane region to $60° < \theta < 90°$. In fact I eventually extend the bistatic observation region to $60° < \theta < 120°$ after the geometric response, which dominates the forward (specular) scattering, is removed. Consequently, I take trace matching to dominate other excitation mechanisms in this region. The hypothesis that trace matching dominates the full elastic wave response will be tested in Sec.4.1 by a numerical calculation and by a reciprocity argument. Since an infinitely long cylindrical shell is excited only by trace matching

in $60° < \theta < 90°$ and the injected power can be calculated theoretically, I will use a uniform infinitely long cylindrical shell to study sound power injection into finite shells.

2.1.4 Acoustic trace matching and elastic wave coupling in the $ka - k_x$ domain

The concepts of trace matching and elastic wave coupling can be presented in the frequency - axial wavenumber domain or $ka - k_x$ domain. Such a presentation is expected to provide a clear and meaningful way of illustrating trace matching and elastic wave coupling concepts in an integrated way. The following results are obtained from the infinitely long shell calculation.

Fig. 2-7 displays the dispersion curve of the $n = 1$ shear wave (thick solid line, from Fig. 2-2) due to 66° sound incidence. The loci of the acoustic wave is represented by the thick dashed line governed by Snell's law

$$k_x = k\,cos\theta \quad . \tag{2.4}$$

Acoustic trace matching to the $n = 1$ shear wave is represented by point C where the two wave loci cross, because trace matching requires the same axial wavenumbers for the shear wave and the acoustic wave.

In the ideal case of no dissipation in the membrane waves, trace matching occurs at a point. However, the shell material damping, and more importantly, the radiation damping, can excite the membrane waves acoustically even if the trace wavenumber is slightly off the 'eigen' wavenumbers. This off-eigenvalue excitation is much like forced excitation of a damped resonator. The larger the damping, the wider the frequency (or wavenumber) response curve. As a result, the shear wave loci in Fig. 2-7 should be replaced by a narrow strip (two thin solid curves shown), the width of which is determined by half power bandwidth, which can be approximated by twice the imaginary part of the axial wavenumber,

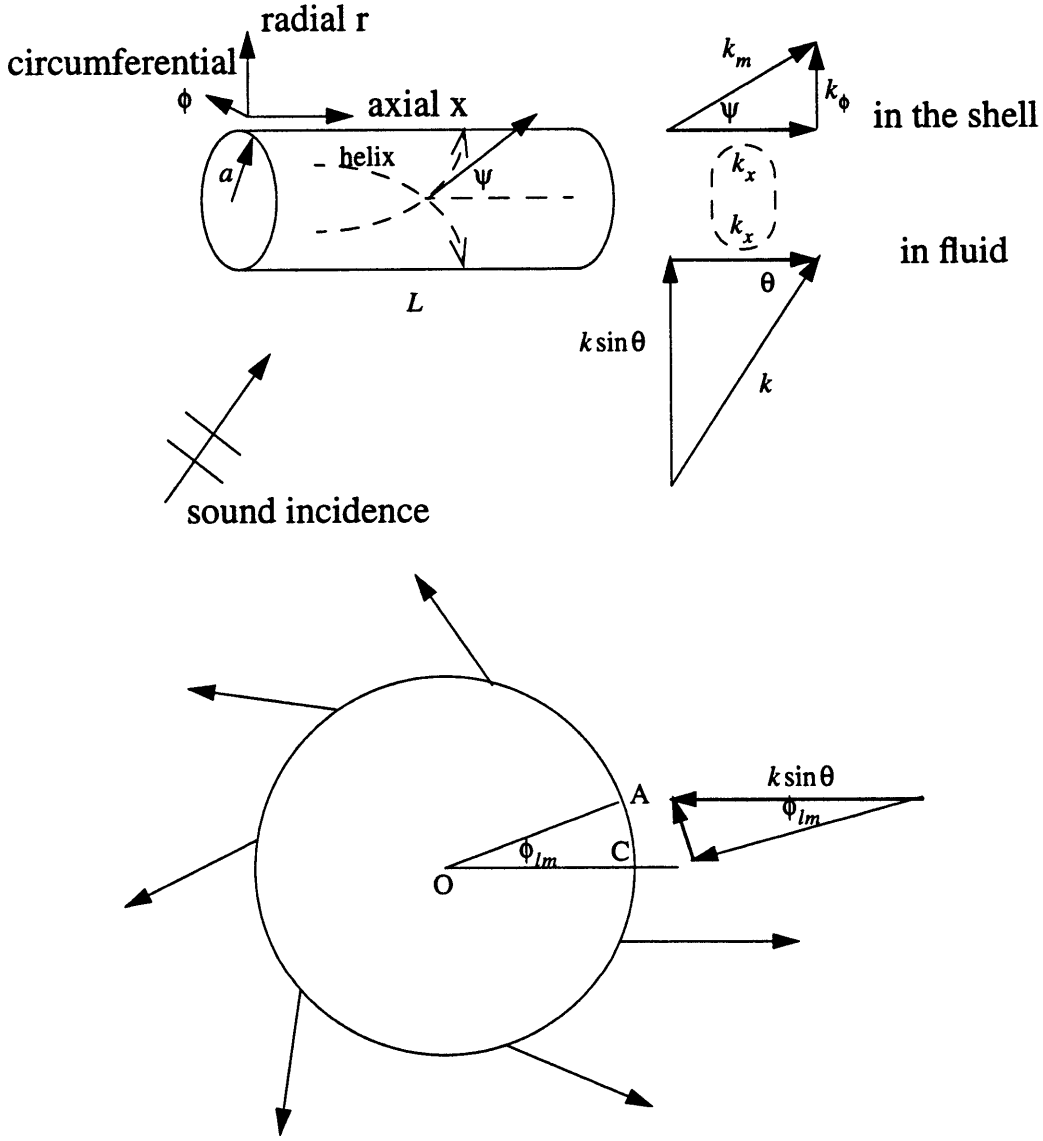

Figure 2-6: Sketch of acoustic trace matching in the shell.

$$\Delta_{1/2} \approx 2\, imag(k_x) \ . \tag{2.5}$$

The region of acoustic trace matching is where the acoustic line overlaps the shear wave 'strip', represented by line segment AB in Fig. 2-7. The finite trace matching region can be measured in both the frequency axis and the axial wavenumber axis.

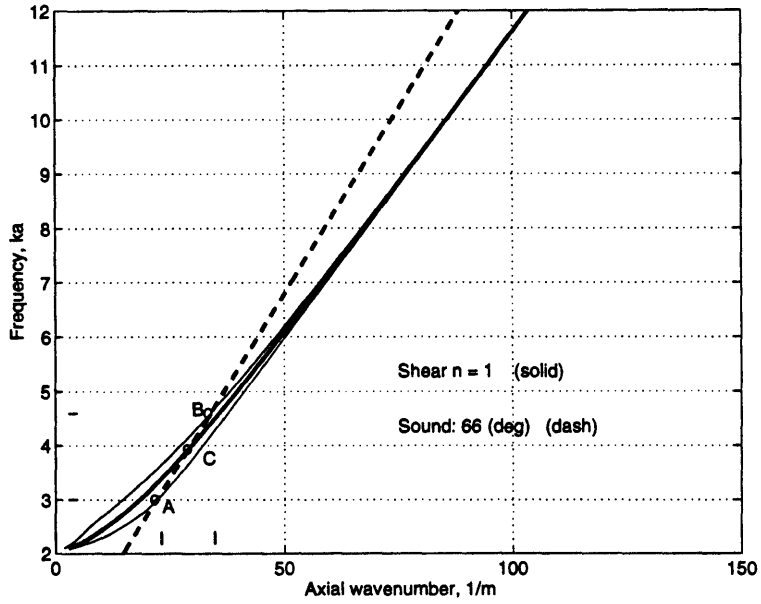

Figure 2-7: The $n = 1$ shear wave locus (thick solid line) and line of the incident acoustic wave (thick dash line), at 66° sound incidence. Trace matching occurs in a region, $\bar{AB}$, where the incident acoustic line and the shear wave strip (bounded by two thin solid lines) overlaps, instead of point C. The spread around the shear wave locus is determined by Eq. 2.5.

The trace matched membrane waves in the shells are able to convert to other wave types at shell discontinuities. Of course, there are no discontinuities in the calculation of a uniform infinitely long shell. The following discussion is intended to provide a physical rationale for cases in which such conversion is possible. Since the shell endcaps and ring discontinuities are commonly axially symmetric, an elastic wave type of mode n only couples to another one of the same mode n, but possibly of different wave type.

In addition, the elastic waves can only couple to each other if they share the same frequency band. For example, the trace matching region of the $n = 1$ compressional

wave due to 75° incidence occurs within the frequency band $3.6 < ka < 8.9$ (See Fig. 2-8). If the $n = 1$ shear wave is to be excited, it must be excited within the same frequency band, as if the trace matching region in the shell projects its image horizontally to the compressional wave. Fig. 2-8 demonstrates the coupling among the $n = 1$ elastic waves due to sound incidence at 75°. The finite trace matching region is not drawn but its effect has been considered.

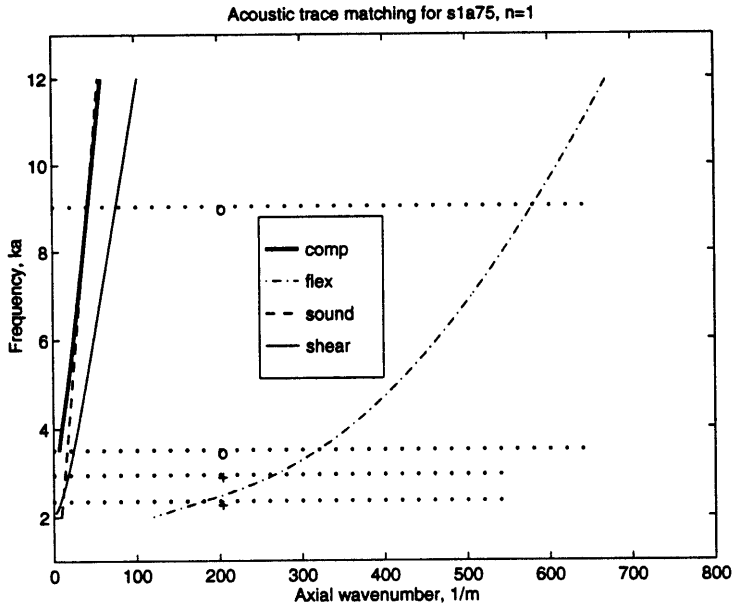

Figure 2-8: The $n = 1$ elastic wave loci due to sound incidence at 75°. The elastic waves can only couple if they share the same frequency band as well as the same circumferential mode n.

Fig. 2-9 provides an overview of trace matching due to acoustic wave incidence in an angular region $60° < \theta < 81°$. In the figure, the $n = 0$ shear wave is not shown because it has no radial motion component and can not be excited acoustically. Moreover, the finite trace matching region effect is ignored for clarity.

Fig. 2-9 is helpful in many ways. For shells without discontinuities, the figure not only indicates that no compressional wave can be excited below 72° incidence and no shear wave can be excited below 60°, but also shows which circumferential modes are excited at a fix incidence angle above the critical angles.

In addition, the figure can be used to check wave coupling if the shells have axial symmetrical discontinuities. In an example sound incidence at 75, the sound trace

matches the $n = 1$ compressional wave as well as the shear wave of mode $n = 1, 2$ and 3. The $n = 1$ compressional wave is trace matched at $ka = 8.5$ while the trace matching frequencies for the shear waves are $ka = 2.5$, 4.5, 7.5, for $n = 1$, 2, 3 respectively. The $n = 1$ compressional wave is able to convert to the $n = 1$ shear near $ka = 8.5$, but the $n = 1$ shear wave trace matched near $ka = 3.0$ is neither able to convert to the $n = 1$ compressional wave because the latter is cutoff at $ka = 2.5$, nor are the $n = 2$ and $n = 3$ shear waves able to convert to the corresponding $n = 2$ and $n = 3$ compressional waves for similar reasons.

Furthermore, Fig. 2-9 can be used to check sound radiation direction of the membrane waves, since trace matching and radiation are reciprocal. Given the fact the $n = 1$ shear can be trace matched by the $n = 1$ compressional wave, one can derive the radiation direction of the 'converted-reflected' $n = 1$ shear wave at $ka = 7.5$ to be close to 62° by interpolation from Fig. 2-9. This deviation from the coincident radiation is a very important characteristic of wave coupling. The wave coupling spreads the axial wavenumber and makes the radiation directivity complicated.

To summarize, Fig. 2-9 provides relations among trace matching, membrane wave coupling at axisymmetric discontinuities, and radiation directions of the converted waves. This diagram will be referenced frequently in this thesis.

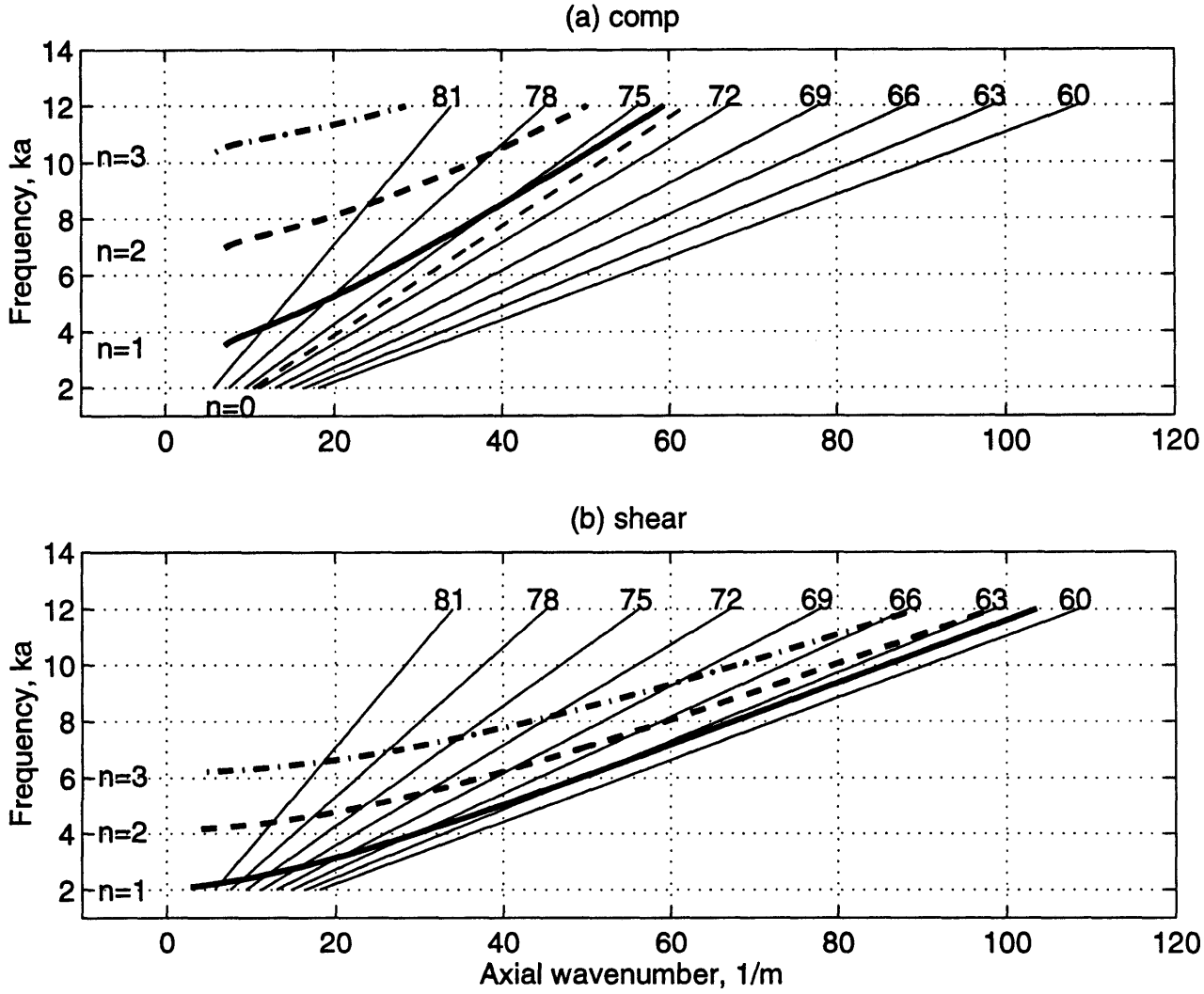

Figure 2-9: Diagram of acoustic wave coupling with (a) the compressional waves and (b) the shear waves, due to sound incidence $60° < \theta < 81°$. The straight lines correspond to the acoustic wave loci for different angles. For example, sound trace matches $n = 1$ compressional wave at $ka \approx 8.5$. The same frequency point for $n = 1$ shear, if converted from the compressional wave, lies between the 60° and 63° lines. Thus the converted $n = 1$ shear wave radiates at approximately 62°.

2.1.5 Speculations on wave coupling strength in the shell models

Elastic waves interact with each other at shell discontinuities and exchange energy among wave types. The energy sharing among wave types can be regarded as energy sharing among coupled subsystems, which has been described by traditional SEA approaches. It has been shown in SEA [30] that two coupled subsystem systems under steady-state broadband excitation can reach equipartition of modal energy if the coupling loss factor is significantly greater than the loss factor of the subsystem ($\eta_{coup} \gg \eta_{int}$). In the case of energy sharing among wave types, I expect a similar condition to be true: that is, the energy flux or wave power might be equipartitioned among the wave types if the wave coupling is much stronger than the wave dissipation. I will define energy flux or wave power later in subsequent section. I can, however, in a semi-quantitative way, evaluate the wave coupling relative to the wave dissipation in the case of the MIT shell models, and to make a quick estimate of the likelihood of wave power equipartition in finite complicated shells.

First, I discuss the concept of coupling loss factor, wave coupling and well as the relationship between the two. I use an example of two irregular plates coupled with a common boundary, which has been discussed in Ref. [30].

Fig. 2-10 illustrates coupling between two plates. Suppose plate 1 of area A_1 is coupled to another plate through a line-junction of length l_1. Plate 1 has vibrational energy E_1 within a frequency band centered at ω. The power flow out of plate 1, Π_{12}, depends on the wave transmissibility, τ_{12}, at the boundary and the collision rate, ν_1, of the wave incident on the boundary,

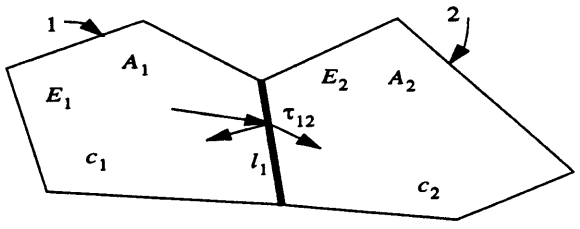

Figure 2-10: Illustration of two finite plates coupled by a line junction.

$$\Pi_{12} = E_1 \nu_1 \tau_{12} \ . \tag{2.6}$$

Let us assume a diffuse wave field in the plate, so that the collision rate, ν_1, can be conveniently expressed as

$$\nu_1 = c_1/d_1 \ , \tag{2.7}$$

where c_1 is the wave speed of plate 1 and d_1 is the mean free path of the diffuse field in plate 1 ($d_1 = \pi A_1/l_1$).

On the other hand, the power that flows out of plate 1 can be regarded as a sort of dissipation

$$\Pi_{12} = E_1 \omega \eta_{12} \ , \tag{2.8}$$

where η_{12} is termed coupling loss factor from plate 1 to 2.

Since Eq. 2.7 and Eq. 2.8 express the same physical quantity, the coupling loss factor of plate 1 to plate 2 is represented in a general form

$$\eta_{12} = \nu_1 \tau_{12}/\omega \ . \tag{2.9}$$

Thus the loss factor can be defined in wave terms to describe wave coupling strength, which is determined not only by how *strongly* different waves are converted at the structural discontinuities, but also by how *often* the waves interact with each other.

The interaction rate in this thesis is the same as the collision rate ν in the above example. The wave conversion coefficient includes wave mixing during both reflection and transmission processes.

The empty shell

For the empty shell, the interaction rate for a fixed circumferential mode n can

be estimated as

$$\nu_n = c_{nx}/L \,, \tag{2.10}$$

where c_{nx} is axial phase speed of a wave type of mode n, and L is the length of the shell. For the $n = 1$ mode, the flexural wave phase speed is approximately 400 m/s (at $ka = 7$). The trace matched speed at 75° sound incidence is 6000 m/s. The interaction rate of the flexural waves and the membrane waves are 500 $1/s$ and 7500 $1/s$ respectively.

Wave reflection and transmission coefficients at shell discontinuities such as endcaps are not generally known. However, it is possible to study the elastic conversion at a flat plate junction with the same bend angle as the cylindrical shell-conical shell junction discontinuity. Using the formulation and calculation in App. D, I estimate that compressional waves can convert more than one quarter of its wave power to flexural waves for $n = 0$, $n = 1$ and more than one quarter of its wave power to shear waves for $n = 2$, $n = 3$. Thus, endcaps are strong wave scatters.

Based on the above estimation of wave coupling, I suppose each elastic wave converts 1/5 of its power to other wave types every time an endcap is encountered. As a result, the coupling loss factors for the empty shell at $ka = 7$ are: 0.046 (compressional), 0.046 (shear) and 0.003 (flexural), according to Eq. 2.9.

The wave loss factor is approximately 0.035 for the compressional wave, and 0.02 for the shear wave, where I use the loss factor for mode $n = 1$ at $ka = 7$, as shown in Fig. 2-4.

The flexural wave damping includes two major mechanisms: material damping and subsonic radiation. I estimate that the loss factor due to material damping is 0.0004, by using a table in Ref. [41] for steel. I then estimate the loss factor due to subsonic radiation by considering flexural wave radiation from ribbed flat plates, with the endcap junctions in the empty shell treated as two ribs. The reason for the flat plate model is that the shell curvature effect on the flexural wave begins to fade above the ring frequency, $ka = 3.5$ in this study. I thus expect the flat plate model can be used as an approximation for $4 < ka < 10$. According to Lyon [30], the radiation

coefficient of the subsonic flexural waves from a ribbed flat plate is

$$\sigma_{rad} = \frac{\lambda_c}{\pi}\frac{\Gamma}{A_p}\frac{2}{\pi} arcsin(\frac{f}{f_c})\beta_{bc} \ , \tag{2.11}$$

where Γ represents the total length of the discontinuities or boundaries. A_p represents the equivalent area of the plate $2\pi aL$. λ_c is sound wavelength at coincidence frequency f_c. β_{bc} is a correction factor to represent boundary influence, ≈ 1 for a simply supported boundary and ≈ 2 for a clamped boundary. For boundary condition between the two, it can be approximated by $\sqrt{2}$. Note that Eq. 2.11 requires that the rib impedance should be much larger than the acoustic impedance of the surrounding fluid. The assumption is readily satisfied in air. In this study, the shell is submerged in water. However, the deep heavy rings still pose a stronger impedance to that of water within the frequency range of interest. Therefore, I expect Eq. 2.11 to be valid in this study as well.

The equivalent loss factor due to flexural wave radiation can be found from the following relation,

$$\eta = \frac{\rho c \sigma_{rad}}{\omega \rho_s h} \ . \tag{2.12}$$

The estimated flexural loss factor due to the subsonic radiation at the endcap junctions is approximately 0.002 using $\beta_{bc} \approx 1$.

This rough estimate indicates that coupling loss factors of the elastic waves for the empty shell are generally larger, but not significantly larger than the wave loss factors. The likelihood of wave power equipartition is limited.

The ringed shell

Wave reflection and transmission coefficients at the rings are not generally known either. I have to estimate them from results for some special cases. Conti [21] calculated flexural and compressional wave coupling in the MIT ringed shell model for the axisymmetric mode ($n = 0$). No shear waves were considered. I deduce from his calculation that the compressional wave power conversion ratio to the flexural wave

is approximately $2-3\%$. The compressional-shear wave power conversion ratio is not available, but is assumed to be roughly the same as the compressional-flexural power conversion ratio, $2-3\%$, likely a very conservative assumption. Thus, I speculate that each elastic wave converts at least $1/50$ of its power to other wave types every time a ring is encountered.

In the ringed shell, the interaction rate inside *each* bay is increased by 5 times on average. Since there are 5 such bays, the total wave interaction rate at the rings is increased by 25 times. In addition, wave reflections at the rings can cause significantly more interactions with the endcaps, and can increase the wave interaction rate at the endcaps by as high as 5 times.

Thus the total wave coupling loss factor for the ringed shell is increased drastically to yield: 0.343 (compressional), 0.343 (shear) and 0.021 (flexural).

The membrane wave dissipation for the ringed shell, dominated by supersonic radiation from the cylindrical shell, is likely to be no different from that for the empty shell. The same estimate of the dissipation loss factor is used as for the empty shell, that is, approximately 0.035 for the compressional wave and 0.02 for the shear wave for $n = 1$ at $ka = 7$. The flexural wave dissipation might increase because of subsonic radiation from the rings. With use of Eq. 2.11, I estimate the loss factor of the ringed shell due to sound radiation from the flexural wave to be 0.007.

This rough analysis suggests that the wave coupling loss factors in the ringed shell, at least for the membrane waves, are likely to be significantly larger than the corresponding loss factors, so that wave power equipartition is plausible.

The internalled shell

In comparison with the ringed shell, the internalled shell has a possibly larger wave interaction rate due to the internal structural discontinuities, but possibly larger wave dissipation as well due to mounting of the highly damped internalled structures at the rings. However, no experimental evidence is found that the internal structural damping is significant. Corrado [19] studied scattering decay rates of the two shells and showed that the internalled shell decays only at a slightly larger rate than than ringed shell. Therefore, power equipartition is also likely in the internalled shell.

Summary of the speculation on wave coupling strength

Wave coupling strength is determined by the product of interaction rate and wave conversion coefficient. If wave coupling strength is significantly larger than the wave dissipation, wave power equipartition is likely. In the case of the ringed shell and the internalled shell, the ratio η_{coup}/η_{diss} is likely to be significantly larger than 1, according to the semi-quantitative analysis. The above ratios of η_{coup}/η_{diss} for the three shells are listed in table 2.1.

Table 2.1: The ratio of coupling loss factor to wave damping loss factor in the empty shell and the ringed shell models, from the semi-qualitative analysis. ϖ is used to denote η_{coup}/η_{diss}.

Shells	ϖ_{comp}	ϖ_{shear}	ϖ_{flex}
empty shell	1.3	2.3	1.5
ringed shell	9.9	17.5	3.0

2.2 Formulation of wave power based on equipartition hypothesis

The formulation of elastic wave power in this section relies on the hypothesis of elastic wave power equipartition which states that power is equipartitioned among the compressional, shear and flexural wave types. In addition, the formulation relies on an infinite shell excitation assumption which states that acoustic trace matching dominates the excitation of the elastic waves within $60° < \theta < 120°$.

The semi-quantitative analysis in Sec.2.1.5 has suggested possible elastic wave power equipartition for the ringed shell. The detailed test of the hypothesis is left to a numerical analysis in Chap. 3. The infinite shell excitation assumption is to be studied in Sec.4.1, also by numerical calculation. The infinite shell excitation assumption allows the injected sound power into a finite shell to be derived from calculation of an infinite uniform cylindrical shell.

The power of the trace matched membrane wave per unit length, $\mathcal{W}_{nm}$, in an infinitely long cylindrical shell can be expressed as

$$\mathcal{W}_{nm} = 2\pi a h \rho < v_{nm}{}^2 > c_{g_{nm}} \ , \tag{2.13}$$

where subnote n represents circumferential mode and m represents the membrane wave type.

The term $\rho < v_{nm}{}^2 >$ in Eq. 2.13 represents energy density, including both kinetic and potential energy which are equal for elastic waves. $2\pi a h$ is the shell cross-section area and $c_{g_{nm}}$ is wave axial group speed representing energy transport speed along the shell axis. Therefore, the right hand side of Eq. 2.13 is termed wave power, which has dimension of $N \cdot m/s$ in MKS.

In Eq. 2.13, the wave velocity square $v_n{}^2$ (for a fixed wave type and mode n) is the summation of shell velocity squares in the radial, axial and circumferential directions, represented by subnote r, a and c respectively.

$$v_n{}^2 = v_{rn}{}^2 + v_{cn}{}^2 + v_{an}{}^2 \ . \tag{2.14}$$

Relative to the wave power, the injected wave energy per unit shell length is

$$\mathcal{E}_{nm} = \mathcal{W}_{nm}^{in}/c_{g_{nm}} \ . \tag{2.15}$$

Because of elastic wave coupling at shell discontinuities, the injected membrane wave energy will be redistributed to the other wave types, propagating in both forward and backward directions. The energy per unit length for each wave type after wave coupling has the form

$$\mathcal{E}_n \ = \ \mathcal{W}_{nm}/c_{g_{nm}} \ + \ \mathcal{W}_{nm'}/c_{g_{nm'}} \ + \ \mathcal{W}_{nf}/c_{g_{nf}} \ , \tag{2.16}$$

where subnote m represents the same membrane wave type that is trace matched and m' denotes the complementary membrane wave type (e.g. if one is shear wave, the other is compressional wave). Subnote f denotes the flexural wave. Note that I have fixed the incidence angle, frequency and mode n in Eq. 2.15, so that either the shear or compressional waves are trace matched, but not both.

In Eq. 2.16 the elastic waves travel both forward and backward. I have assumed that power in the forward wave should be no different, statistically, from the power in the backward wave. The assumption is valid if the elastic wave field in the shell is reverberant because of multiple wave interactions.

The wave power concept can be shown to be proportional to modal energy in traditional SEA [30]. In SEA, the number of axial modes (N_n) for each n over the frequency band $\Delta\omega = \omega_2 - \omega_1$ is

$$N_n = \frac{\Delta k}{\pi/L} = \frac{\Delta\omega/\bar{c_{gn}}}{\pi/L} = \frac{\Delta\omega L}{\pi \bar{c}_{gn}} \ , \tag{2.17}$$

where $\bar{c_{gn}}$ denotes the averaged group speed over the band $\Delta\omega$ and π/L is the average modal separation in wavenumber for a one-dimensional system.

The modal energy, similar to the derivation of Eq. 2.13, is

$$E_n/N_n = \frac{\pi}{\Delta\omega} 2\pi a h \rho < {v_n}^2 > \bar{c_{gn}} \ . \tag{2.18}$$

In comparison with Eq.2.13, Eq.2.18 shows that wave power is proportional to the modal energy. As a result, modal energy equipartition in SEA can be translated into wave power equipartition in this study. Wave power is used in this thesis because it describes forward and backward waves separately, which are important for computing directional sound radiation field.

In this chapter, I hypothesize wave power equipartition; but I will test the hypothesis in the next chapter, which shows that the wave equipartition hypothesis is indeed plausible in shells with multiple scatterers, such as rings.

The elastic wave power equipartition hypothesizes

$$\mathcal{W}_{nm} = \mathcal{W}_{nm'} = \mathcal{W}_{nf} = \mathcal{W}_n \ . \tag{2.19}$$

To determine the elastic wave power, energy conservation has to be considered. In the ideal case of no radiation damping and material damping, the sound energy injected into the shell is the sum of the elastic waves, for all time $t > 0$, but only restricted by the power equipartition condition of Eq. 2.19. Because of the damping, the wave energy will dissipate after the power is equipartitioned among the elastic waves. Indeed, the elastic waves can even dissipate energy before wave equipartition, which might not occur immediately after the trace matching. By the time wave power is equally partitioned, there is already a certain amount of energy dissipated into the fluid.

If wave conversion takes very long to reach power equipartition, radiation dissipation is almost the only thing important in the prediction of transient elastic wave scattering. Wave power equipartition becomes irrelevant in that case, and so is the statistical model set forth in this study.

In another extreme, if wave coupling and mixing is very active, wave power reaches equipartition almost instantly after the shell is excited. The elastic waves will then

radiate sound and decay at a unified rate that can be predicted statistically. In this case, sound radiation can be ignored until wave equipartition is reached.

Is it possible to estimate the amount of energy dissipated into the fluid before wave equipartition is reached? The possibility certainly exists, but only if the shell's structural details are known, because the early elastic wave coupling process is essentially *deterministic* and is highly dependent on particulars of the discontinuities. However, this study is to explore a simple statistical model for scattering prediction, I do not attempt to determine the early radiated energy. Instead, I assume that wave power mixing occurs in a short time so that the energy dissipation during the wave mixing (before equipartition) can be ignored. Subsequently, Eq.2.15 and Eq.2.16 becomes equal.

$$\mathcal{E}_{nm} \approx \mathcal{E}_n \ . \tag{2.20}$$

From Eq. 2.15, Eq. 2.16, Eq. 2.20 and Eq. 2.19, I derive the equipartitioned wave power as

$$\mathcal{W}_n = \frac{\mathcal{W}_{nm}^{in}}{1 + \frac{c_{g_{nm}}}{c_{g_{nm'}}} + \frac{c_{g_{nm}}}{c_{g_{nf}}}} \ . \tag{2.21}$$

Eq.2.21 shows that the equipartitioned elastic wave power is the injected wave power scaled by the ratios of the wave group speeds. Since the flexural wave has far smaller group speed (approximately 1/10 that of the membrane waves), the denominator in Eq.2.21 is typically $O(10)$.

2.3 Calculation of elastic wave power

Following the formulation of the elastic wave power in the previous section, this section calculates the elastic wave power in a finite shell, by using the infinitely long shell excitation assumption and the power equipartition hypothesis. I begin with the calculation of trace matched elastic wave power in the infinitely long cylindrical shell and then solve for the equipartitioned elastic wave in a finite shell, according to

Eq. 2.21.

In the calculation, I consider a finite cylindrical shell having the same material, radius and thickness as the cylindrical shell section of the MIT empty shell model. Correspondingly, an infinitely cylindrical long shell has the same cross-section dimensions and material as the empty shell model.

Under plane sound incidence, the shell displacements in the axial, circumferential and radial directions can be solved from linear equations in the transformed domain,

$$[\mathbf{L}][\mathbf{U}] = [\mathbf{F}] \ . \tag{2.22}$$

Eq. 2.22 is established by combining the Donnell's thin shell equations of motion of the fluid-loaded cylindrical shell and the momentum equation that relates the shell surface pressure to the shell radial displacement. In Eq. 2.22, matrix **U** contains the shell displacements in the axial, circumferential and radial directions, as well as the surface pressure. The forcing matrix **F** is determined by the strength of the incident sound. The first two elements of **F** are zero because the sound does not couple to the in-plane motions. The mathematical details can be found in App. A.

I first calculate the injected membrane wave power according to Eq. 2.13. To display the power, I use a scaling factor that represents sound power incident on the shell of unit length

$$\mathcal{W}_0 = 2\pi a \, sin\theta \, \frac{p_0^2}{\rho c} \ , \tag{2.23}$$

where p_0 is the incident sound pressure, ρc the characteristic acoustic impedance of water. θ is the angle measured from the shell axis. Within $60° < \theta < 90°$, this power reference varies no more than 11%. Fig. 2-11 shows the shell velocity (already summed in the square over three directions) and injected membrane wave power of mode $n = 1$ under sound incidence at 66°. At this angle, only shear waves are trace matched. The velocity curve has a peak near $ka = 4$ in (a) of Fig. 2-11 which corresponds to trace matching of the $n = 1$ shear wave, as seen from Fig. 2-9. The wave power in (b) of Fig. 2-11 is calculated according to Eq. 2.13, where the group speed of the shear wave

is used.

It is interesting to note that trace matching does not only occur at a single frequency, but necessarily in a finite frequency band, because of radiation dissipation. This frequency response demonstrates the resemblance to the excitation of a damped resonator discussed in Sec.2.1. For fixed frequency, the elastic wave is trace matched when the forcing wavenumber $kcos\theta$ is close to the eigen-wavenumber k_x of the membrane wave. If I allow frequency to change as well ($ka - k_x$ domain), the wave response has a resonator-like shape projection in the frequency axis as well. That shape is what is shown in Fig. 2-11. The wave power level falls off rapidly away from the trace matching frequency, by 20 dB at $ka = 8$ which is twice the trace matching frequency.

Near the trace matching frequency, $ka = 4$, the power injected into the shell is 10 dB less than the sound power projected on the shell. Most of the projected sound power is scattered to various directions, including the backscattering direction.

Fig. 2-12 shows the shell velocity response and injected membrane wave power of mode $n = 1$ under sound incidence at 75°. At this angle, both the shear and the compressional waves are trace matched. The power curve has two peaks, separated by almost two octaves and associated with the two wave types. I identify the peak at $ka = 2.6$ to be associated with the $n = 1$ shear wave and the peak at $ka = 9.2$ to be associated with the $n = 1$ compressional wave. The power in the middle of the two peaks is generally from the contribution of both the shear and the compressional waves. The rigorous separation of the wave components is difficult to because the eigen-wave-vectors are non-orthogonal. Instead of pursuing rigorous mathematics, I make an approximation by choosing an arbitrary middle frequency point ka_{mid} between the shear wave peak and the compressional wave peak. I then treat shell velocity within $2 < ka < ka_{mid}$ to be associated with the shear wave and shell motion within $ka_{mid} < ka < 12$ to be associated with the compressional wave. The rationale of doing so is that, first, the two peaks are generally far apart and fall off very quickly so that the exact choice of the middle point is not critical. Second, the shear and compressional waves have rather similar axial group speeds. Thus the wave power resulted from using either of the wave speeds only causes minor errors.

In the case shown in Fig. 2-12 (a), I choose $ka_{mid} = 4.7$. The power calculated in Fig. 2-12 (b) shows rather smooth transition from the shear wave power at $ka = 2.6$ to the compressional wave power at $ka = 9.2$, with only a small discontinuity near $ka = 4.7$.

Using the elastic wave power formulation in the previous section, I can calculate the power of each elastic wave type in a finite complicated shell, according to Eq. 2.21.

Fig. 2-13 and Fig. 2-14 display the equipartitioned elastic wave power for sound incidence at 66° and 75° respectively. The peak levels at 66° are approximately 20 dB lower than the incident power. The peak level 75° incidence, however, is somewhat less than 20 dB lower than the incident sound power. This difference in wave power between the two incidence cases is 3-4 dB, and is due to the lack of compressional wave trace matching at 66°. In addition, I observe that the wave power dominates at frequencies close to the trace matching frequencies for different circumferential modes.

In the foregoing wave power calculation, I use the wave group speeds and phase speeds on the infinitely long shell. It will be shown in Sec.4.2.1. that the shell discontinuities such as the rings not only create wave conversion and cause wave power equipartition, but also modify the wave loci, and therefore the wave group and phase speeds. However, the use of the modified wave speeds may not provide a better scattering prediction, as shown in Sec.5.2.

The power of the waves represents the strength of the waves. To predict scattering, a radiation model is needed to project the elastic wave motion to sound in the fluid. Before the radiation model is developed in Chap.4, however, I will first test the hypothesis of wave power equipartition as the topic of Chap.3.

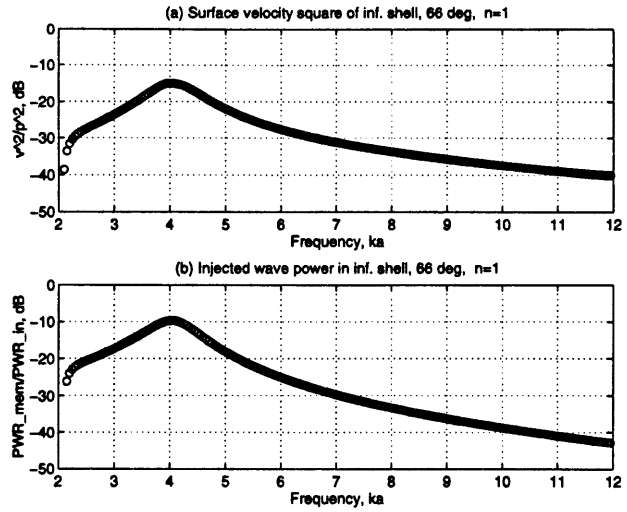

Figure 2-11: Shell velocity and wave power for n=1 mode. Sound incidence is at 66°. (a) Shell velocity scaled by incident sound pressure. (b) Injected wave power scaled by the incident sound power. The peak at ka=4 corresponds to the trace matching frequency of the n=1 shear wave.

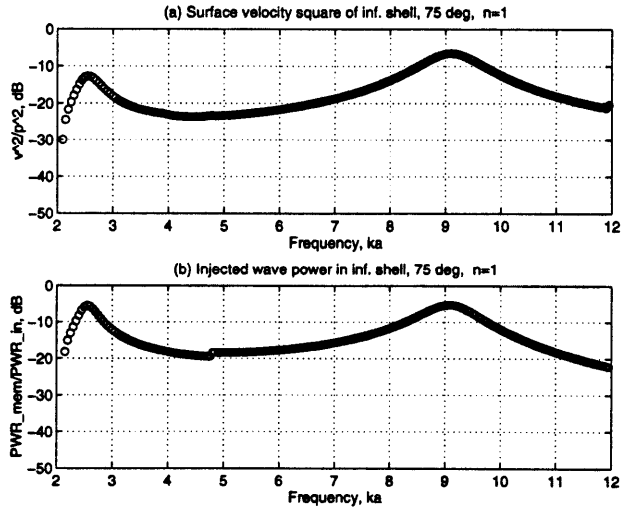

Figure 2-12: Shell velocity and wave power for n=1 mode. Sound incidence is at 75°. (a) Shell velocity scaled by incident sound pressure. (b) Injected wave power scaled by the incident sound power. The peak at $ka = 2.6$ and $ka = 9.1$ corresponds to the trace matching frequency of the n=1 shear wave and compressional wave respectively.

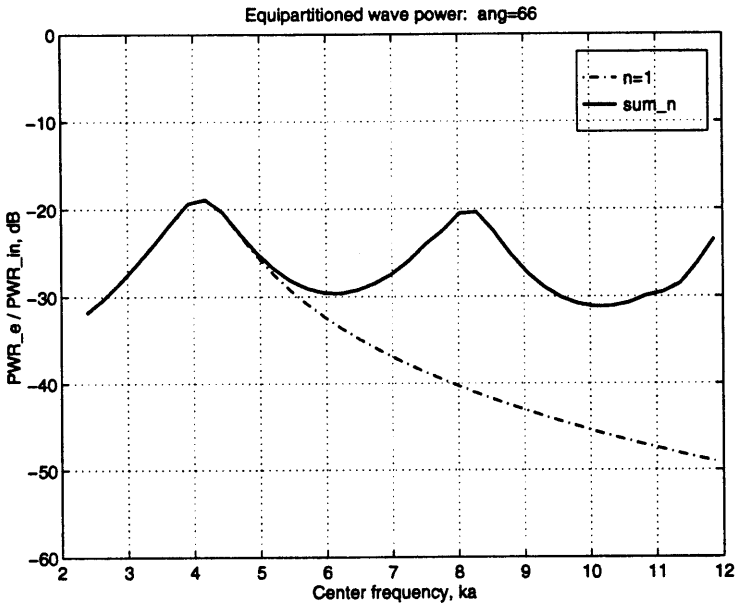

Figure 2-13: Equipartitioned elastic wave power in a finite shell under sound incidence at 66° (*solid* is summation over modes and *dash* is mode $n = 1$ only).

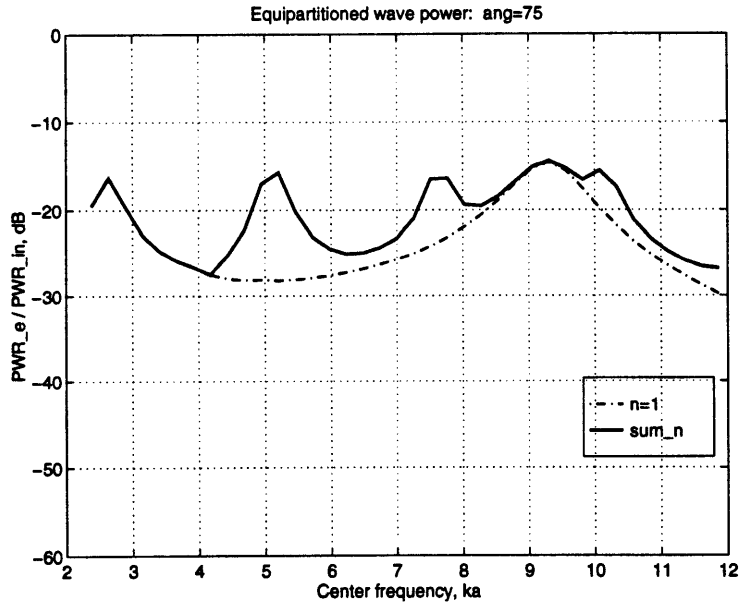

Figure 2-14: Equipartitioned elastic wave power in a finite shell under sound incidence at 75° (*solid* is summation over modes and *dash* is mode $n = 1$ only).

2.4 Summary

Under sound incidence close to beam aspect, the acoustic wave can trace match the supersonic compressional and shear waves. The energized membrane waves can couple to each other and to the subsonic flexural waves at the shell discontinuities. In the case of axially symmetric shell discontinuities such as rings and endcaps, the elastic wave coupling occurs within the same circumferential mode n. The converted waves can have different axial wave speed from the sound trace speed, causing a spread in the axial wavenumber and thus a complicated radiation directivity. In the $ka - k_x$ domain, one can conveniently check the interplay of excitation, elastic wave coupling and radiation using Fig. 2-9. In addition, I find that the trace matching occurs in a finite region rather than a point, an analog to the wide band excitation of a damped resonator.

Shear waves radiate above cutoff frequencies and become non-radiating below cutoff frequencies. Compressional waves have only *adhoc* cutoffs and radiate especially strongly near and below the *adhoc* cutoff frequencies. Since endcaps terminate the cylindrical shell by contracting its radius, thus forcing waves to cutoff, compressional waves are much more dissipative at endcaps than shear waves.

Based on the expectation of active wave coupling in finite complicated shells, equipartition of wave power, defined as wave energy density times axial group speed, is hypothesized. Wave power equipartition is shown to be similar to the concept of modal energy equipartition in traditional SEA. With use of the wave power equipartition hypothesis, the elastic wave power in finite shells can be expressed as the injected sound power scaled by wave group speed ratios. The power equipartition hypothesis is to be tested in Chap.3. In this chapter, the likelihood of power equipartition is speculated by comparing the wave coupling dissipation to wave dissipation. Wave coupling strength, shown as a product of wave interaction rate and conversion coefficient, must, for equipartition, be greater than the wave dissipation. According to a rough estimate of η_{coup}/η_{diss}, the ratio is likely to be much greater than 1, at least for the ringed shell and the internalled shell.

The sound power injected into finite shells is estimated using the analytical cal-

culation of the infinitely long shell. In this thesis, I restrict the sound incidence to within the membrane wave region $60° < \theta < 120°$, so that acoustic trace matching dominates other elastic wave excitation mechanisms in finite shells. Subsequently, the injected sound power can be derived from infinitely long shell results. The advantage of this infinitely long shell assumption is that the calculation of the injected sound power does not require detailed shell structural details. The power calculation indicates that the equipartitioned wave power is approximately 20 dB lower than the incident sound power.

The elastic wave power, if combined with a sound radiation model, can be used to predict scattering. A radiation model will be built in Chap.4.

Chapter 3

Test of the power equipartition hypothesis

This chapter studies the wave power in finite endcapped shells with and without rings, by means of numerical calculations based on the Finite Element Method (FEM) using SARA-2D code.

In this chapter, the SARA-2D calculation is first compared to the measured scattering data. The comparison shows that the target strength of the ringed shell using SARA-2D is slightly higher than the measurements, but by no more than 2-4 dB in most frequency bands and at most observation angles. The rest of the chapter evaluates elastic wave power equipartition, for both steady-state and transient cases. The analysis is intended to answer *if* and *when* the equipartition hypothesis is plausible. I find that the elastic wave power is equipartitioned for the ringed shell within 3 dB over most frequency bands, while the difference among the elastic waves is typically 5-10 dB for the empty shell. I take 3 dB difference as a criterion and conclude that power equipartition is plausible in the ringed shell. Furthermore, the hypothesis for the transient case is more appropriate during the second roundtrip period for the trace matched waves in the shells. Even for shells with only one or two rings, the wave power equipartition is still a good hypothesis, although equipartition needs a longer time to establish. I do not observe evidence of power equipartition for the empty shell, at least within the first 6 roundtrip periods of the trace matched wave

in the shell.

3.1 Comparison between SARA-2D and scattering measurements

The FEM SARA-2D code [31] is used to calculate the structural response of the empty shell and the ringed shell. The two shells are axially symmetric in structure, so that the three coordinates can be reduced to two: the axial and the radial coordinates, while the circumferential coordinate is compressed into mode n through Fourier transformation. I can decompose the sound field similarly, so that for fixed n, the shell scattering becomes a 2D problem. Correspondingly, the computation is significantly less intensive than the 3D case.

The internalled shell can not be calculated by SARA-2D because it is not axially symmetric and has to be modeled as a 3D structure. There may be other FEM codes to solve 3D elastic shell scattering problems at mid frequencies, including viscoelastic internals, but huge computation cost prevents calculation of the internalled shell in this study. In fact, it is the general difficulty of computing complicated shells that motivates the development of a statistical scattering prediction model in this thesis.

The FEM modeling details, post-processing efforts and initial evaluation of the wave decomposition are attached in App.C. SARA-2D can calculate harmonic surface velocities in axial, radial and circumferential directions as well as surface pressure. All surface responses are complex numbers and are expressed in circumferential mode n. In post-processing, the spatial distribution of the surface response can be Fourier transformed into the wavenumber domain so that wave components, in both forward and backward going directions, can be identified and evaluated. Restricted by the Fourier transform, only the surface response along the cylindrical part of the shell is evaluated. The shell length and the density of the elements provide sufficient wavenumber resolution in the frequency region $4 < ka < 12$. Because phase is retained in the complex harmonic response, transient response can be obtained by Fourier transform as well. The decomposed wave responses have been found to agree well with the infinite shell calculation.

To check SARA-2D modeling of the shells, a series of numerical monostatic and bistatic scattering 'measurements' of the ringed shell are carried out. The numerical calculation is tested against the MIT/NRL measured scattering data.

In the numerical calculations, the frequency range is $2 < ka < 12$ with a frequency increment of $ka = 0.05$, comparable to that in the MIT/NRL measurements. The sound incidence angle is 75°. The maximum mode number is chosen as 4. A point receiver is placed at $2\,m$ from the shell center, as in the MIT/NRL measurements.

The direct calculation from SARA-2D is steady-state while the MIT/NRL data are from time windowed transient scattering signals. To compare them, I first take the inverse Fourier transform of the calculated target strength from the frequency to the time domain and then use the same time window as in the MIT/NRL data. In addition, the same Gaussian frequency filter is applied as in the MIT/NRL measurement data.

I compare target strength with and without the geometric return, as shown in Fig. 3-1 and Fig. 3-2, for monostatic results of the ringed shell due to sound incidence at 75°. In each figure, a histogram is displayed for the decibel difference in target strength between the calculation and the data .

In spite of the differences at isolated frequencies, the calculated target strength agree with the MIT/NRL data well in both figures. In fact, if the target strengths averaged over frequency band are compared, the mean decibel difference is only approximately 1.4 dB, the calculated mean being larger than the data. (The source of the calculation bias is unknown to me, but it does not affect the main uses of the calculation).

Fig. 3-3 and Fig. 3-4 display the comparison of bistatic target strengths of the ringed shell due to sound incidence at 75°. The target strengths are averaged over three frequency bands: $2 < ka < 5$, $5 < ka < 8$ and $8 < ka < 11$.

I observe that the target strength from SARA-2D differs from the measurement data by no more than 3 dB for most observation angles, even including observations near the axial direction. Thus the accuracy of the SARA-2D modeling of the ringed shell is satisfactory.

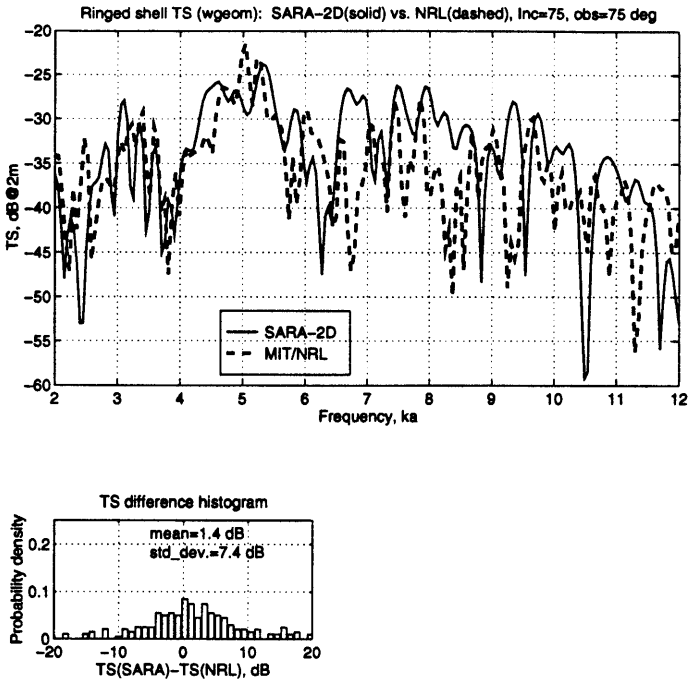

Figure 3-1: Total target strength for the ringed shell, obtained from the MIT/NRL data and from the SARA−2D calculation. Sound is incident at 75° and observed at 75°. Time window $-44\,\mu s < t < 1200\,\mu s$ is used.

Furthermore, the results in Fig. 3-3 and Fig. 3-4 show that elastic wave scattering dominates the geometric return in the two lowest frequency bands in the backward (monostatic) direction, but the geometric return dominates the elastic wave scattering for all frequencies in the forward (specular) direction. Thus an elastic wave model, such as proposed here, can not hope to give robust specular results. Fortunately, simple analytical models are available for bistatic geometric scattering [1], so that the elastic scattering component studied in this thesis can, in combination with such geometric models, provide estimates of the total bistatic scattering.

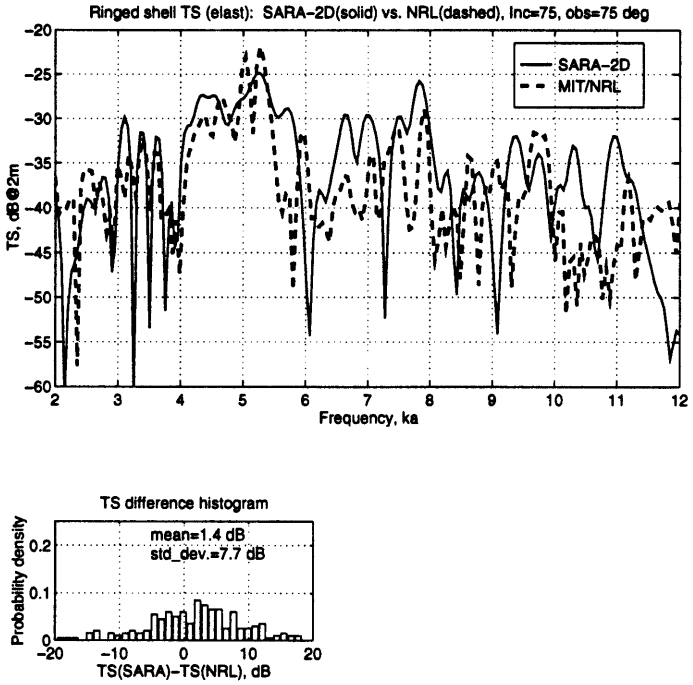

Figure 3-2: Target strength due to the *elastic* waves for the ringed shell, obtained from the MIT/NRL data and from the SARA−2D calculation. Sound is incident at 75° and observed at 75°. Time window $44\,\mu s < t < 1200\,\mu s$ is used.

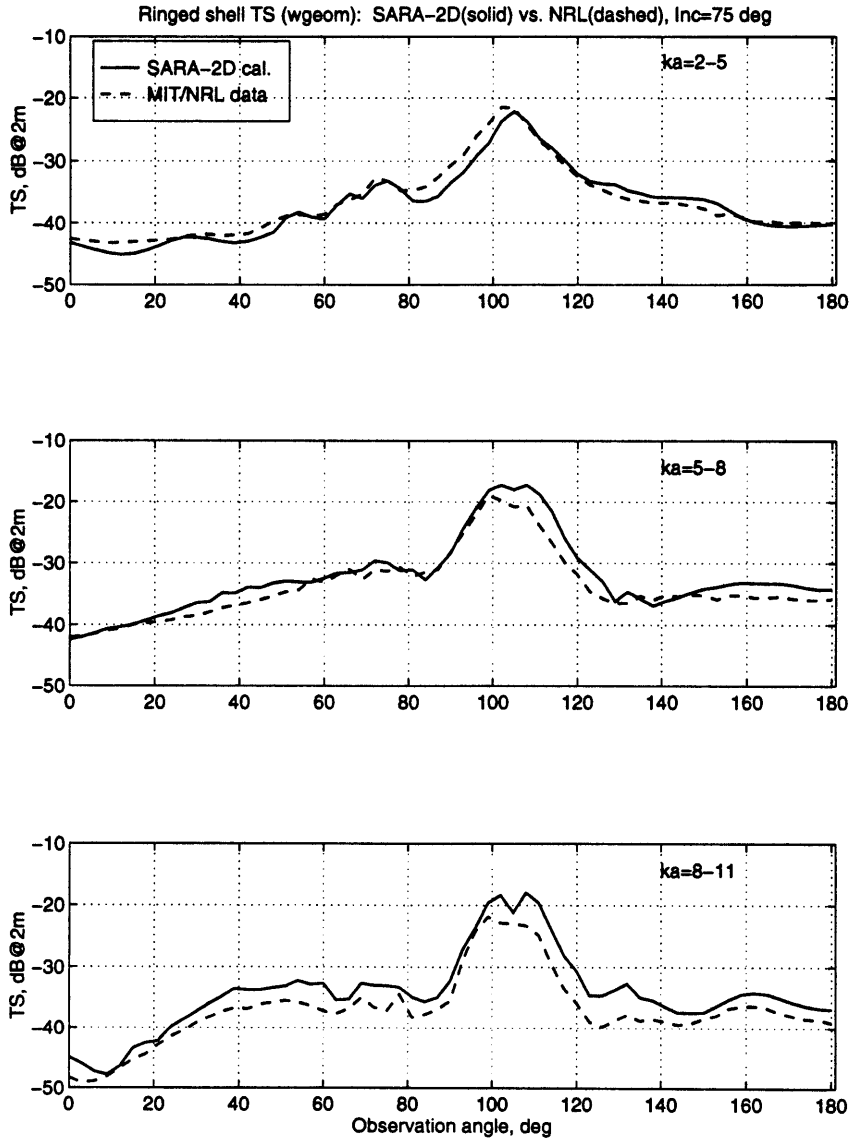

Figure 3-3: Bistatic target strength of the ringed shell, obtained from the MIT/NRL data and from the SARA−2D calculation. Sound is incident at 75°. The target strength contains **both** the elastic wave scattering and geometric return. Time window $-44\,\mu s < t < 1200\,\mu s$ is used.

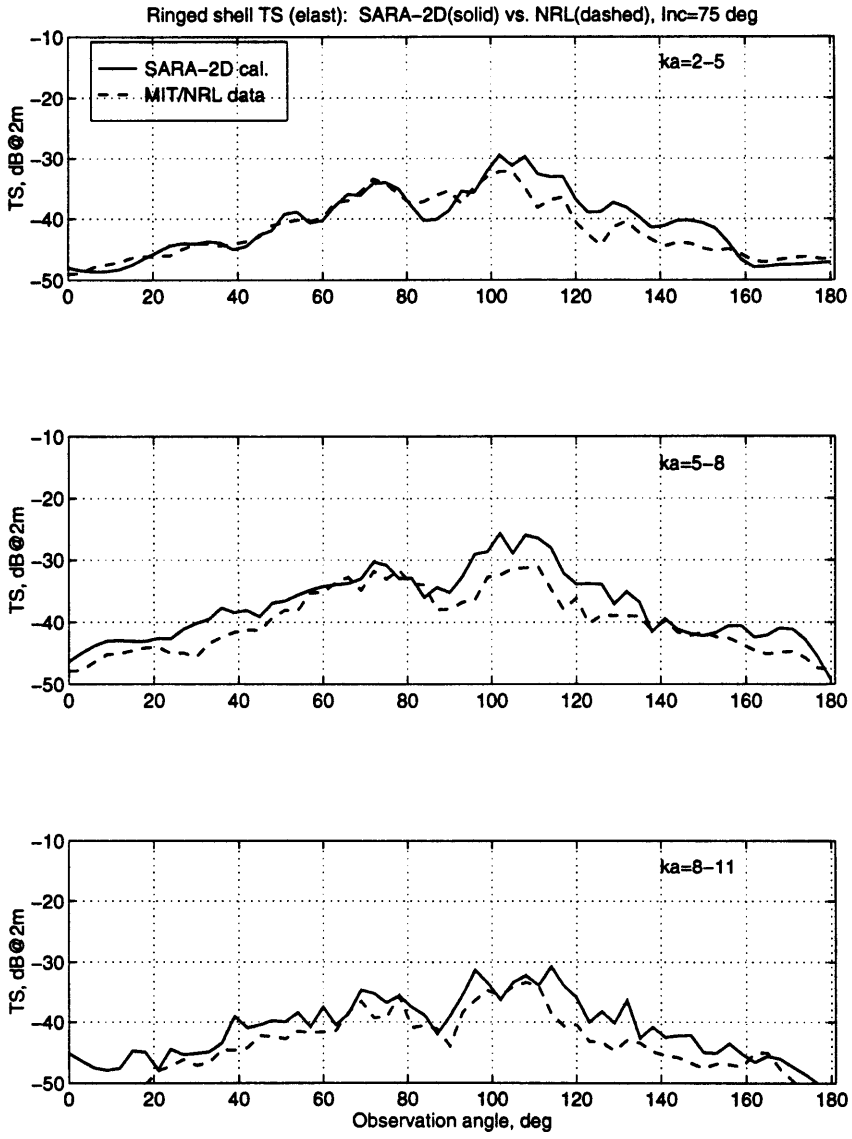

Figure 3-4: Bistatic target strength of the ringed shell, obtained from the MIT/NRL data and from the SARA−2D calculation. Sound is incident at 75°. The target strength contains the elastic wave scattering **only**. Time window $44\,\mu s < t < 1200\,\mu s$ is used.

3.2 Steady-state wave power analysis

The shell velocities from the direct SARA-2D calculation are steady-state values. The steady-state power analysis requires a small data set and relatively simple processing, making it easy to study wave power under various scenarios, such as for many sound incidence angles.

The wave power is extracted from the SARA-2D calculation of the shell surface responses, following steps illustrated in Fig 1-5. To decompose the surface velocities into elastic wave components, the responses on the shells are transformed into the wavenumber domain so that different wave components can be identified and evaluated separately. The details of wavenumber transform can be found in App.C. Once the shell velocities in the axial, radial and circumferential directions are obtained for each elastic wave type, the elastic wave power can be calculated using Eq. 2.13 and Eq. 2.14.

Since waves going forward and backward can be separated in the wavenumber domain, the power will be displayed for both forward waves and backward waves. In steady-state, the forward waves contain both forced waves (largely membrane waves due to trace matching) and free waves, while the backward waves are all free waves. The forced waves contribute to the initial geometric scattering, while the free waves contribute to the elastic scattering only. To study elastic wave power, the focus will be largely on the backward waves.

I consider wave power for each mode n as well as the summation over n. The summation is done incoherently, based on the reasoning that any shell response has a circumferential dependence of sines and cosines. The cross-products of the modal functions vanish after integration over $0 \leq \phi \leq 2\pi$. In other words, the functions are orthogonal within the azimuthal region.

In addition, the power is averaged over 10 non-overlapping frequency bands in $2 < ka < 12$, the width in each band being $\Delta ka = 1$. Furthermore, the power, pre-averaged over the frequency bands, is averaged further over two angular sound incidence regions: (I) $66° < \theta < 72°$ and (II) $74° < \theta < 80°$, with the angular resolution being $1°$. In region I, only the shear wave is trace matched, while in region

II both shear and the compressional waves are trace matched. Finally, the wave power is normalized by the incident sound power over a finite shell of a unit length using Eq. 2.23, and is expressed in dB.

Wave power for the empty shell

Fig. 3-5 and Fig. 3-6 display the mean and standard deviation of wave power in the angular regions I and II respectively, over a population of the wave power for each sound incidence angle, with the power first summed over mode n and then averaged over the frequency bands. In angular region I, the power difference among the backward elastic waves is more than 10 dB in most frequency bands; the power is not equipartitioned. In addition, I observe that the power in the shear wave dominates that of other wave types, consistent with the shear wave trace matching dominance in this angular region. Furthermore, the flexural wave power in the backward direction is considerably larger than in the forward direction, most likely due to interactions at the far endcap junctions. Although the compressional wave is not trace matched in angular region I, it has considerable power in the forward direction; I suspect that wave conversion at the insonified endcap plays a role. The reciprocity argument might provide yet another explanation. Namely, the compressional wave could be excited strongly at the insonified endcap because it radiates strongly at the endcaps (Sec.2.1.2). However, this second mechanism will be shown to be insignificant in Sec.4.1. That is, the compressional wave excitation at the endcap is a far weaker process in comparison with acoustic trace matching on the cylinder, as long as the sound incidence angle is above 60°.

In angular region II, the wave power difference among the elastic waves in the backward direction is significantly smaller than that in region I, due to trace matching of both shear and compressional waves in this region. Indeed, the forward compressional wave power is dominant. The wave power difference among the backward waves, however, is over 5 dB for most frequency bands, still too large to be regarded as equipartition. Other features remain the same as in angular region I.

To study the wave power variation over the sound incidence angle, Fig. 3-5 (c), (d) and Fig. 3-6 (c), (d) display the standard deviation of the wave power as a per-

centage of the arithmetic mean of the wave power over angular incidence regions I and II respectively. The wave power for each sound incidence angle has been summed over mode n and averaged over the frequency bands. Moreover, the standard deviation is averaged over the frequency region displayed; the average is labeled for each wave type. In region I, the standard deviation, if averaged over the frequency region displayed, is typically 30% for forward waves and slightly larger for the backward waves. The slight larger power fluctuation over the sound incidence angle in the backward direction is possibly due to wave conversion at the far endcap, indicating the angle selective nature of the the wave coupling process. In region II, wave power angular fluctuation is typically 40% for the forward waves and 50% for the backward waves. The angular fluctuation in region II is larger because compressional wave loci, as shown in Fig. 2-9, have larger gradient (with respect to k_x) than that of shear waves. Therefore, trace matching of compressional waves is in general more sensitive to incidence angle.

In order to see wave power in each mode n, Fig. 3-7 shows backward wave power for the empty shell for different circumferential modes, averaged over 6 incidence angles in region I. Fig. 3-7 indicates a clear frequency dependence of the wave power for each mode n. Namely, the wave power becomes important above the cutoff frequencies. For instance, the $n = 1$ shear wave cuts off at $ka = 2$ and dominates the whole frequency region $2 < ka < 12$ for the empty shell. The $n = 2$ and $n = 3$ shear waves in the empty shell become important above $ka = 5$ and $ka = 8$ respectively. This frequency dependence for the empty shell can be explained by acoustic trace matching within this angular region, which can be conveniently checked using Fig. 2-9.

The backward compressional wave power is mostly from the contribution of the $n = 1$ mode in $2 < ka < 9$ and of both the $n = 1$ and $n = 2$ modes above $ka = 9$. The contributions of the rest of the modes are insignificant.

The $n = 1$ flexural wave in the empty shell dominates $2 < ka < 5.5$ and remains important in the remaining frequency bands. The $n = 2$ and $n = 3$ flexural waves become important only above $ka = 5$ and $ka = 8$, respectively.

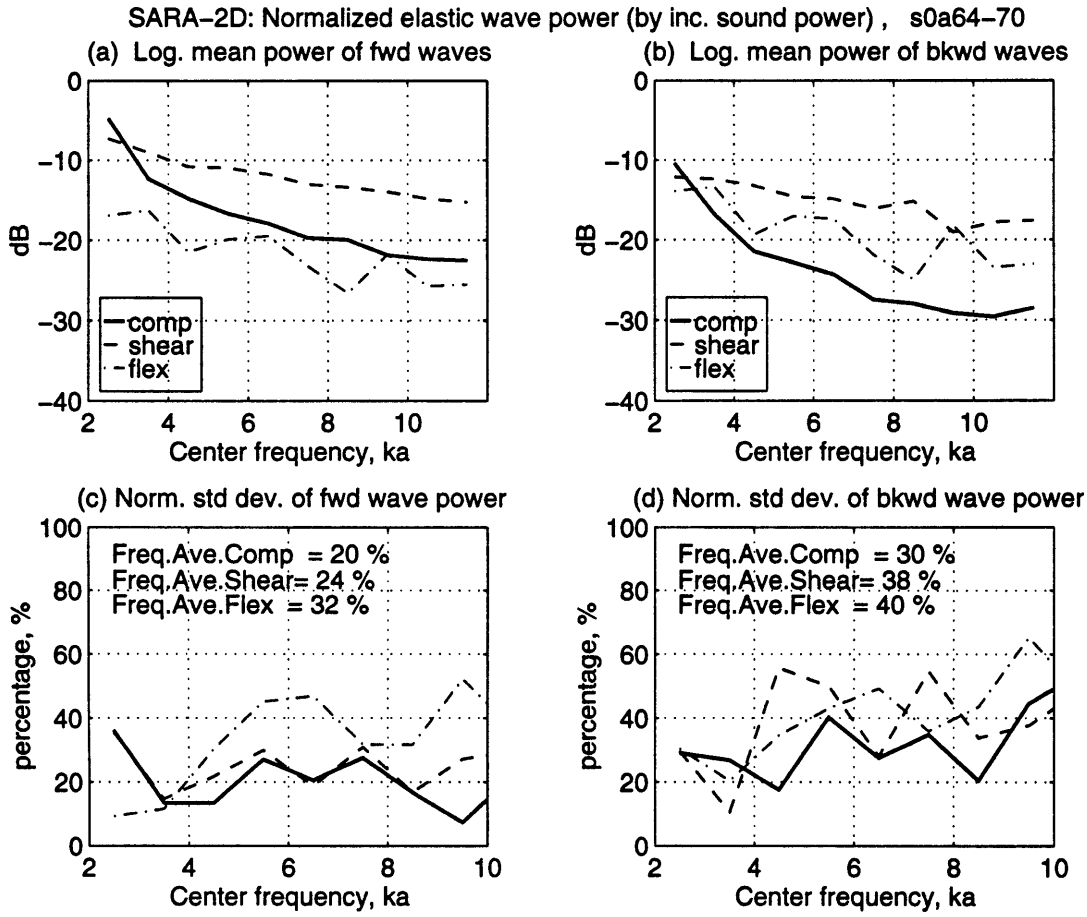

Figure 3-5: Summed power of (a) forward and (b) backward going elastic waves in the **empty** shell in region I, based on the SARA-2D calculation. The power, already summed over mode n and averaged over small frequency band $\Delta ka = 1$, is further averaged over the 6 incidence angles in region I. All points are plotted at the mid values of the 10 non-overlapping frequency bands in $2 < ka < 12$. (c) and (d) display standard deviation of the wave power over the 6 incidence angles in region I, for forward and backward waves respectively. The standard deviation is displayed as a percentage of the mean wave power evaluated over the angular region. Moreover, the standard deviation is averaged over the frequency region displayed; the average is labeled for each wave type.

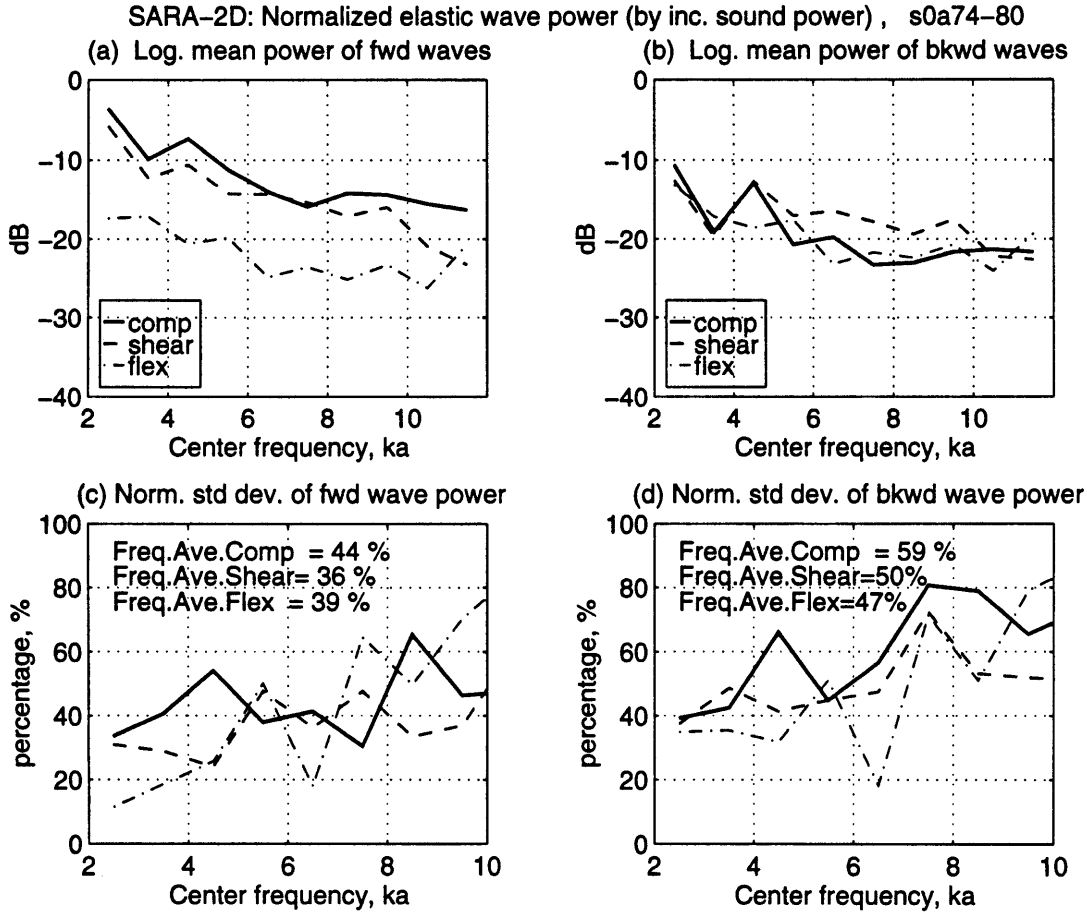

Figure 3-6: Summed power of (a) forward and (b) backward going elastic waves in the **empty** shell in region II, based on the SARA-2D calculation. The power, already summed over mode n and averaged over small frequency band $\Delta ka = 1$, is further averaged over the 6 incidence angles in region II. All points are plotted at the mid values of the 10 non-overlapping frequency bands in $2 < ka < 12$. (c) and (d) display standard deviation of the wave power over the 6 incidence angles in region II, for forward and backward waves respectively. The standard deviation is displayed as a percentage of the mean wave power evaluated over the angular region. Moreover, the standard deviation is averaged over the frequency region displayed; the average is labeled for each wave type.

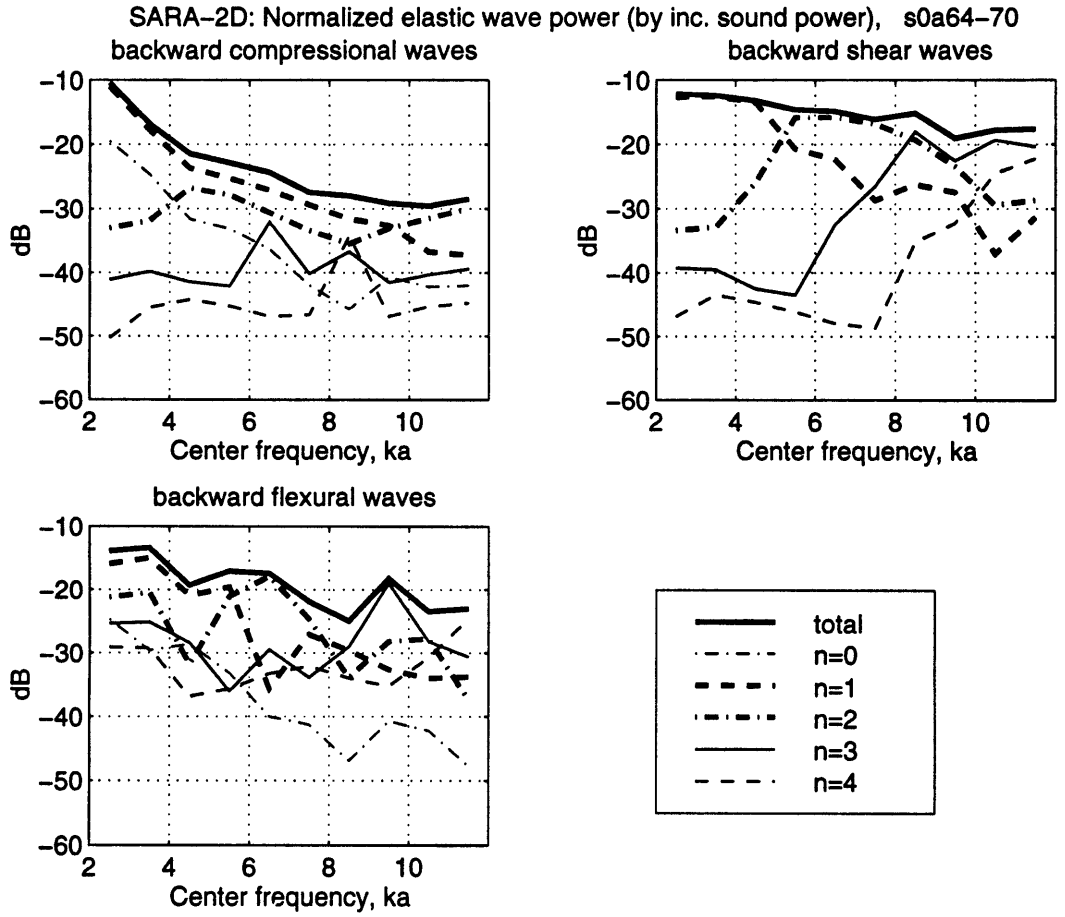

Figure 3-7: Wave power of the backward going elastic waves in the **empty** shell for different circumferential modes, based on SARA-2D calculation. The power is averaged over small frequency band $\Delta ka = 1$ and over 6 incidence angles in region I. All points are plotted at the mid values of the 10 non-overlapping frequency bands in $2 < ka < 12$.

Wave power for the ringed shell

Similar to the format in Fig. 3-5 and Fig. 3-6, the mean and standard deviation of the wave power for the ringed shell are plotted in Fig. 3-8 and Fig. 3-9 for regions I and II respectively. In angular region I, the power difference among the backward elastic wave types is considerably smaller in comparison with the empty shell case in Fig. 3-5. The power difference between the backward membrane waves is within 2 dB for most frequency bands. The flexural wave power is approximately 3-4 dB smaller than that of the membrane waves. Although the backward membrane wave power is equipartitioned, the power is not equally shared with the flexural wave. Total equipartition is strictly not achieved. In addition, I observe that the power difference among the forward waves is significantly smaller than for the empty shell case. In fact, the forward waves are almost as well equipartitioned as the backward waves. At least, they are much more so than for the empty shell. In the ringed shell, the forward forced waves are less important than the forward free waves; the latter are created more so due to strong scattering at the rings. Furthermore, I observe that in contrast to the empty shell case, the power difference among the elastic waves varies smoothly with frequency. This is again influenced by the rings, which can change the membrane wave speeds in the shell. The related discussion can be found in Sec.4.2.1. In addition, the wave power fluctuation over the sound incidence angles is shown in (c) and (d) of Fig. 3-8. The wave power fluctuates noticeably less over the incidence angle than for the empty shell case, especially for backward free waves. Strong wave coupling and associated creation of non-coincident axial wavenumber are believed to cause this insensitivity of wave power to the sound incidence angle for the ringed shell.

In angular region II, I observe basically the same power behavior as in region I. The backward elastic waves reach power equipartition only approximately. The angular fluctuation of the wave power of the backward free waves is significantly smaller than for the empty shell case.

Fig. 3-10 shows backward wave power in the ringed shell for different circumferential modes, averaged over incidence angles in region I. Both the $n = 1$ and $n = 2$ compressional waves are important over basically the whole frequency region

$2 < ka < 12$. The $n = 3$ compressional wave is significant only within some isolated frequency bands. It is hard to observe any cutoff influence on the compressional waves for the ringed shell, again apparently due to strong scattering.

To summarize the steady-state power analysis, I find that the elastic wave power is more equally distributed for the ringed shell than for the empty shell, but yet the total wave power equipartition is strictly not achieved for the ringed shell. The sound incidence angle and frequency have a strong influence on the wave power difference for the empty shell. The power difference among the elastic waves for the empty shell is significantly smaller if both shear and compressional waves are trace matched (region II). For the ringed shell, however, the wave power is considerably less sensitive to the incidence angle within both regions I and II. In addition, the power difference among the elastic waves is less sensitive to frequency, compared with the empty shell.

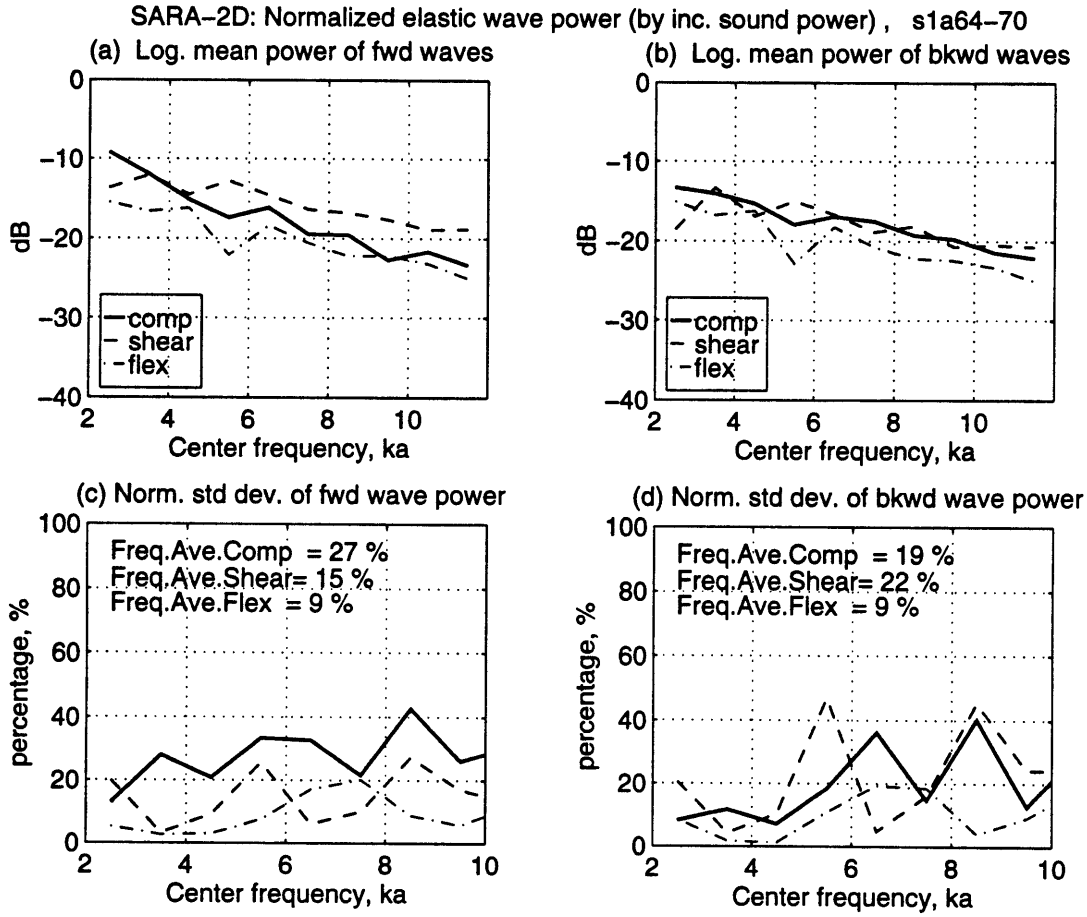

Figure 3-8: Summed power of (a) forward and (b) backward going elastic waves in the **ringed shell** in region I, based on the SARA-2D calculation. The power, already summed over mode n and averaged over small frequency band $\Delta ka = 1$, is further averaged over the 6 incidence angles in region I. All points are plotted at the mid values of the 10 non-overlapping frequency bands in $2 < ka < 12$. (c) and (d) display standard deviation of the wave power over the 6 incidence angles in region I, for forward and backward waves respectively. The standard deviation is displayed as a percentage of the mean wave power evaluated over the angular region. Moreover, the standard deviation is averaged over the frequency region displayed; the average is labeled for each wave type.

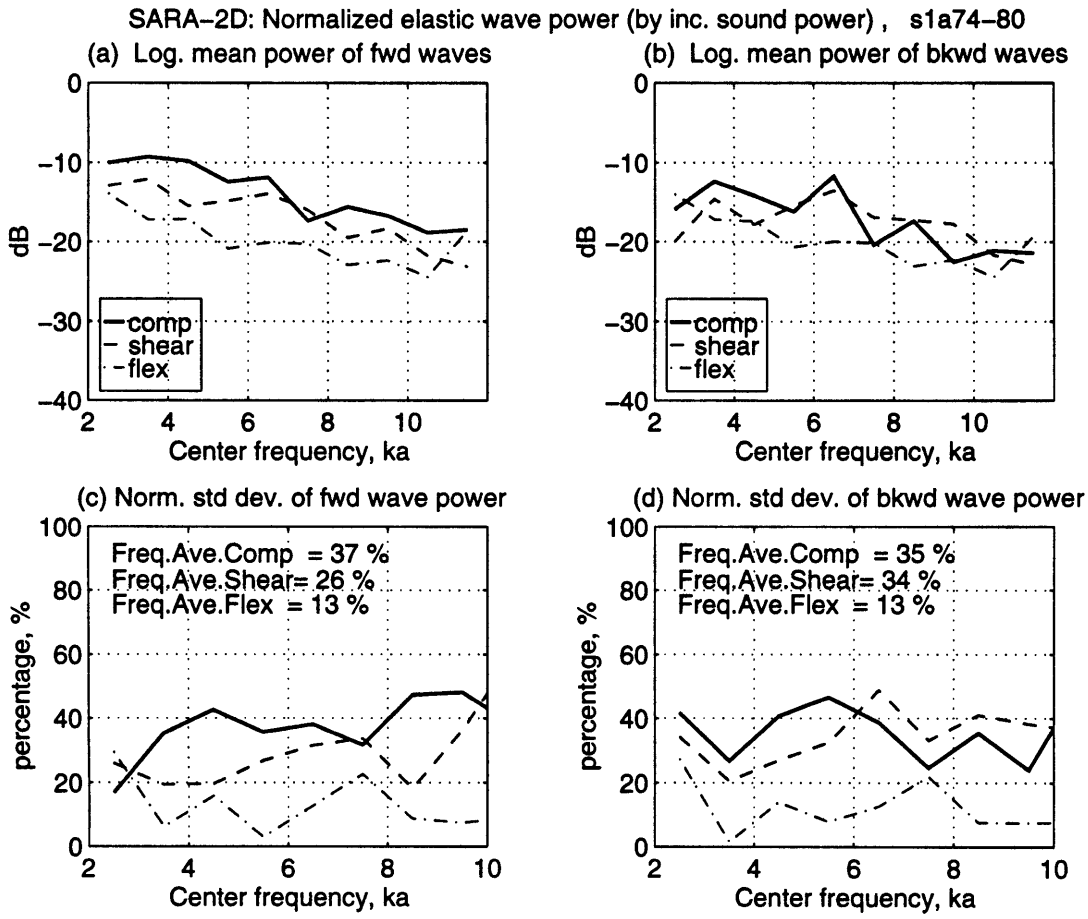

Figure 3-9: Summed power of (a) forward and (b) backward going elastic waves in the **ringed shell** in region II, based on the SARA-2D calculation. The power, already summed over mode n and averaged over small frequency band $\Delta ka = 1$, is further averaged over the 6 incidence angles in region II. All points are plotted at the mid values of the 10 non-overlapping frequency bands in $2 < ka < 12$. (c) and (d) display standard deviation of the wave power over the 6 incidence angles in region II, for forward and backward waves respectively. The standard deviation is displayed as a percentage of the mean wave power evaluated over the angular region. Moreover, the standard deviation is averaged over the frequency region displayed; the average is labeled for each wave type.

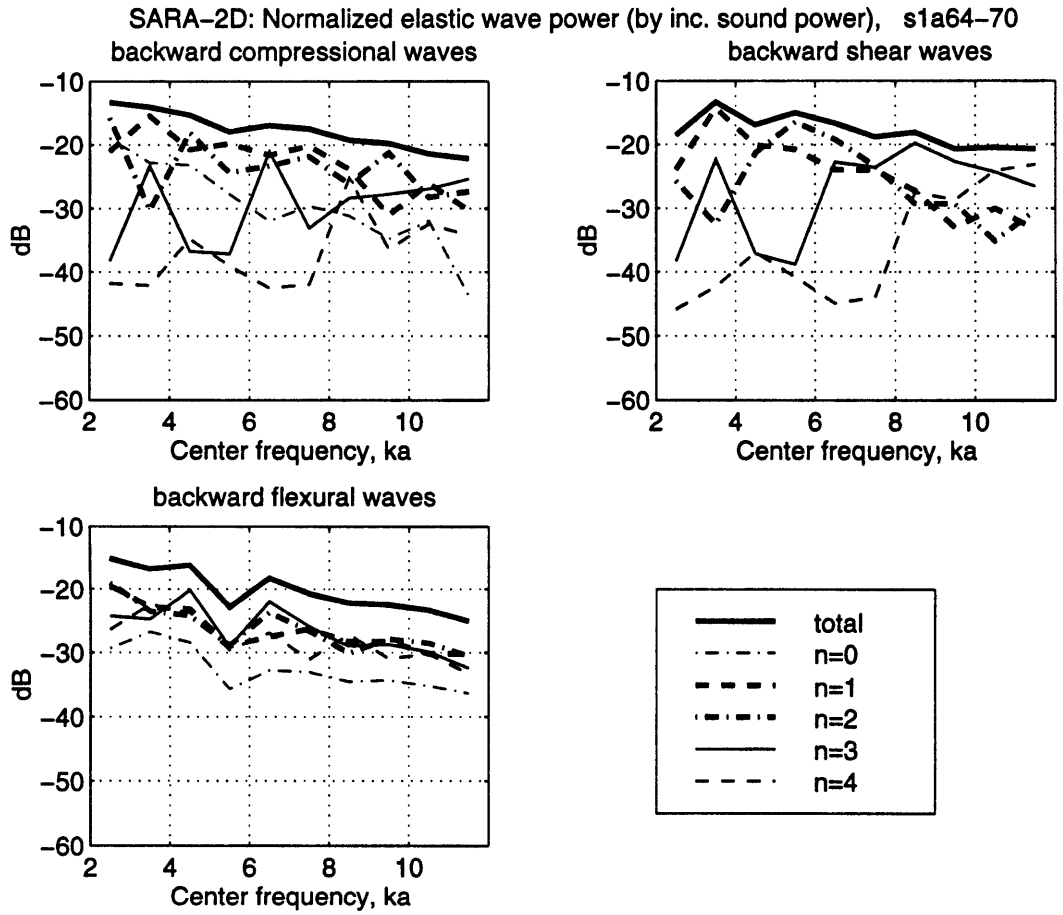

Figure 3-10: Power of the backward going elastic waves in the **ringed** shell for different circumferential modes, based on the SARA-2D calculation. The power is averaged over small frequency bands $\Delta ka = 1$ and over 6 incidence angles in region I. All points are plotted at the mid values of the 10 non-overlapping frequency bands in $2 < ka < 12$.

3.3 Transient wave power analysis

Many scattering processes of practical interest occur in the time domain. In this thesis, the transient nature of the scattering is especially remarkable for coupling among the elastic waves. Under sound insonification within $60° < \theta < 120°$ considered in this study, the supersonic membrane waves are immediately excited as the trace matched acoustic waves sweeps through the shell length. The subsonic flexural wave is, on the other hand, not immediately excited by trace matching, but energized when the trace matched membrane waves interact with a shell discontinuity. Since the flexural wave is far slower than the membrane waves, its influence usually can not be observed until very late in time, especially if shell discontinuities are sparsely distributed. The presence of the late flexural wave scattering in the ringed and the internalled shell has been observed by Machovjak [23] in analyzing the MIT/NRL measured data. This late influence of flexural wave scattering has been accounted for by Corrado [19] and Park [22] to explain the complicated decay behavior they observed in scattering. Although it is possible to determine decay behavior of each elastic wave, total scattering can decay at a rate different from any of the individual waves, because of wave conversion at the shell discontinuities. What is more, the total scattering decay rate can vary over time, as evident from the experiment analysis in [19] and [22]. Thus a transient scattering analysis in this study is not only beneficial to engineering practice, but also extremely informative about the physics of scattering. This section is intended to study wave power in successive time windows to determine *if* and *when* wave power equipartition occurs.

To extract the transient shell response from direct SARA-2D calculation, the steady-state shell surface velocities are first transformed from the frequency domain into the time domain. Then appropriate time windows are applied and the time windowed responses are inversely transformed back into the frequency domain. The rest of the steps of wave power calculation are similar to that in the steady-state analysis. Fig. 3-11 illustrates the flow chart of the process for the transient case.

The choice of the time windows is based on the temporal evolution of trace matched membrane waves in the shell. As shown in Fig. 3-12, similar to a diagram in Corrado's thesis [19], acoustic trace matching occurs during $0 \leq t \leq Lcos\theta/c$. The

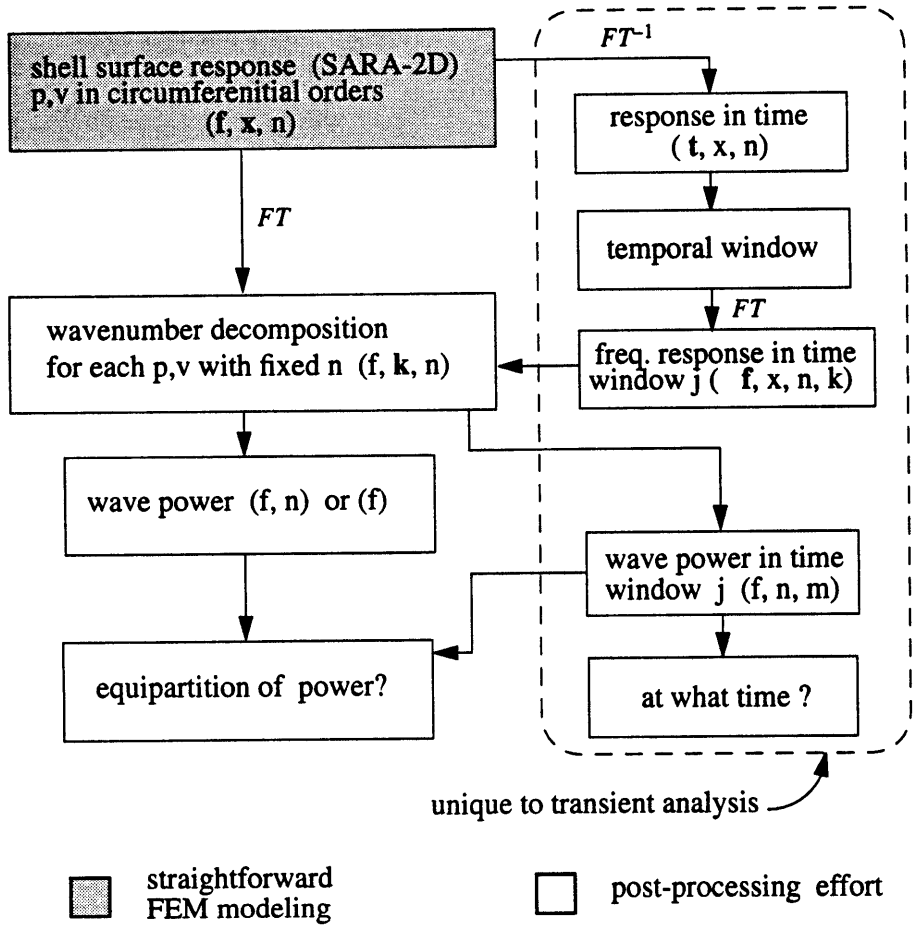

Figure 3-11: Flow chart of the transient wave power processing steps. The spatial wavenumber decomposition steps are listed on the left and they have been used in the steady-state power analysis as well. The big dotted box on the right represents steps that are unique to the transient analysis.

first backward membrane waves propagate to the insonified endcap within $Lcos\theta/c \leq t \leq 2Lcos\theta/c$ (assuming no elastic wave conversion at the far endcap). The free membrane waves would then reverse direction to finish a roundtrip along the shell within $2Lcos\theta/c$ period if the endcaps were instantaneous reflectors. I use this roundtrip period as a time scale in the study. Each time window is identical and is uniform (flat top) in the middle, but has cosine round-off taking 5% of the window length at the two ends.

I use the same time window for the ringed shell, although I realize that possible reflections at the rings can make the first backward going membrane waves observable earlier than for the empty shell.

Fig. 3-13 illustrates the time windows for both 66° incidence and 75° incidence. The consecutive time windows are labeled by (1), (2) and so on.

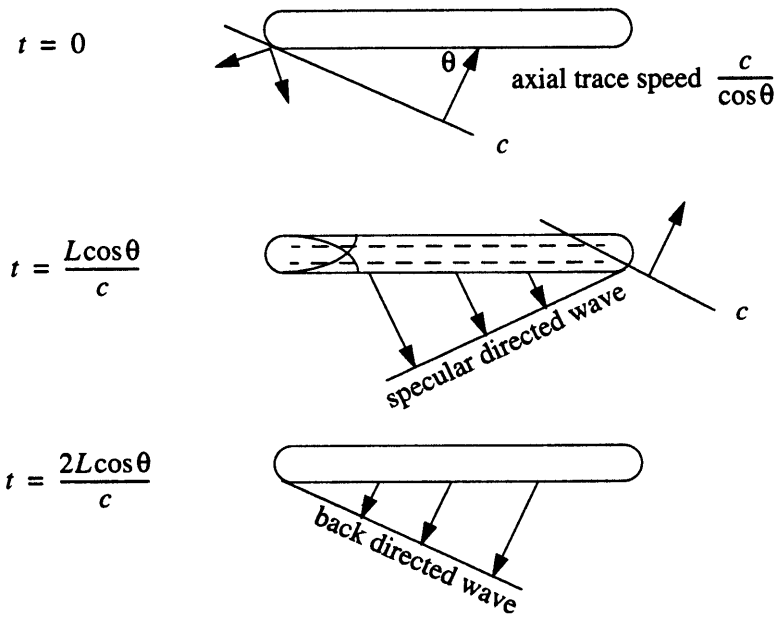

Figure 3-12: Illustration of the temporal evolution of helical waves in the shell due to plane acoustic wave incidence. Instantaneous reflection at the shell endcap is assumed in defining the time windows.

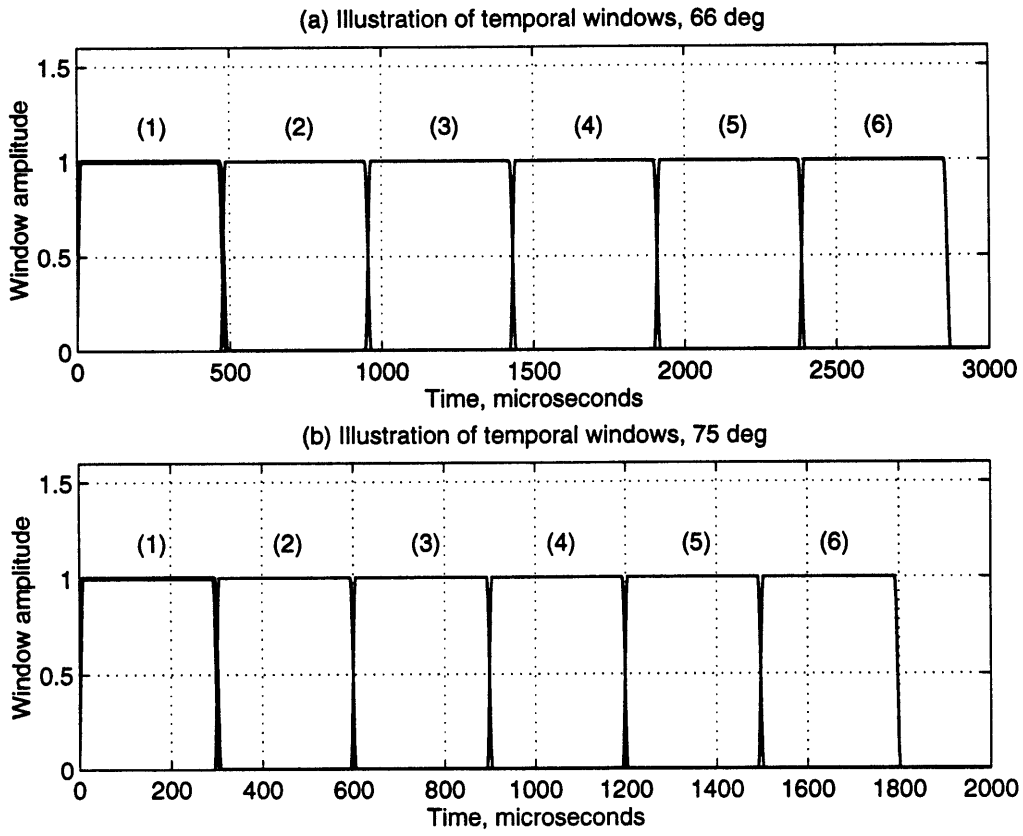

Figure 3-13: Illustration of the time windows for temporal wave power analysis. (a) Sound incidence at 66°; (b) Sound incidence at 75°.

The empty shell, 66° incidence

Fig. 3-14 displays wave power for time windows 1, 2 and 3 and Fig. 3-15 continues the display for time windows 4, 5 and 6. In each subplot, the normalized power is plotted against frequency. The forward wave power is shown in the left column while the backward wave power is shown in the right column. Note that the fixed vertical scale in windows 1, 2, 3 is modified in windows 4, 5, 6. The format will be used consistently in the next six figures. The forced waves are contained in the forward waves in window 1 only, while the rest of the windows depicting the power of the free elastic waves.

The emphasis of the analysis shown in the figures is on the power difference among the three elastic wave types and how the difference changes over time.

In window 1, the power difference among the forward elastic waves is as high as 25 dB. The forward shear wave carries most of the power, due to acoustic trace matching. The forward compressional wave, although not trace matched at 66°, carries considerable power which is only 10 dB lower than the shear wave. Acoustic excitation and wave conversion at the insonified endcap is believed to cause the energization. Furthermore, the flexural wave carries the least amount of power, although the backward going flexural wave increases significantly after the membrane waves interact with the far endcap.

In window 2, the wave power becomes more equalized. The forward shear wave power is still dominant, although already 12 dB down from window 1. The flexural wave dominates the wave power in the backward direction, after the trace matched membrane waves interact with the far end endcap in window 1. The reason for this backward flexural wave dominance in window 2 is that it is more captured, or exposed, in the wavenumber decomposition process, for window 2 (instead of in window 1), because of its slow wave speed. The reflection of this backward going flexural wave at the insonified endcap will be found in window 4 and later, as to be discussed in this subsection.

The elastic wave types continue to approach equilibrium in window 3. The shear wave power and the flexural wave power are rather close while the compressional wave

power is considerably lower.

In windows 4, 5 and 6, the forward flexural wave transfers energy to the membrane waves, especially to the compressional wave. It is interesting to note that the forward flexural wave power is highly energized in the high-frequency bands in window 4, and in mid-frequency bands in windows 5 and 6. The explanation is that the backward going flexural wave converted at the far endcap in window 1 finishes the one-way trip in the cylindrical shell to reach the insonified endcap, and then reverses the direction to travel forward. Since higher frequency flexural wave travels faster, the high frequency (near $ka = 11$) flexural wave is likely to arrive earlier in time, for instance in window 4, while the flexural wave in the mid-frequency bands (near $ka = 7$) can not be observed in window 5 or later.

To check this assertion, I estimate the one-way travel time of the flexural wave along the shell to be $1950\,\mu s$ and $1644\,\mu s$ at $ka = 7$ and 11 respectively, by using the shell length of 0.74 m and the corresponding axial flexural wave speeds of $380\,m/s$ and $450\,m/s$, obtained from Fig. 2-3. These two time estimates, according to Fig. 3-13, correspond to window 5 and window 4 respectively. Thus the assertion on the forward going flexural wave is plausible.

Since the reflected backward free membrane waves in window 1 are considerably weaker than the forward forced waves, I do not expect significant flexural wave power in the backward direction in late time windows, which is the case in Fig. 3-15 for windows 4, 5 and 6. I observe that the backward waves in windows 4 and 5 have power difference within 3 dB below $ka = 6$. However, power difference in other frequency bands and other windows are much larger. Overall, the elastic wave power **does not** reach equipartition for the empty shell at this angle of incidence, at least within the first 6 time windows.

The empty shell, 75° incidence

At this angular incidence, both shear and the compressional waves are trace matched. Fig. 3-16 and Fig. 3-17 display wave power for time windows 1, 2, 3 and 4, 5, 6 respectively. In window 1, the most distinguishing feature, in comparison with the 66° case in Fig. 3-16, is the considerably higher compressional wave power than in

66° incidence, due to trace matching of the compressional wave. In the next window, the elastic wave power difference continues to become smaller.

In windows 4, 5, the power difference among the elastic waves in both forward and backward directions is no more than 5 dB for most frequency bands. If I take 3 dB in power difference as a criterion for wave power equipartition, the elastic wave power in window 4 and 5 has not reached, although is close to, equipartition. In window 6, the forward flexural wave power becomes dominant, which can be explained by the reversal of the one-way travel of the backward flexural waves hitting the insonified endcap as discussed in the 66° case. Indeed, such one-way travel time has been shown to be $1644\,\mu s$ (at $ka = 11$), right in window 6 as shown in Fig. 3-13 for the 75° case. I can even predict that in later windows (no shown), one should observe dominant flexural wave power in the forward direction, particularly in the mid frequency bands near $ka = 7$.

Thus the flexural wave can carry a substantial amount of wave power converted from the trace matched membrane waves. This power is neither dissipated in the form of sound radiation nor converted back to the membrane waves unless a shell discontinuity is encountered. In the empty shell, the conversion can only happen at the endcaps and the one-way travel time of the flexural wave has been shown to be equivalent to several time windows, which in turn represents several roundtrip periods of the trace matched membrane waves in the shell. Since the membrane waves radiate strongly and attenuate fast, by the time the flexural wave is able to convert the power back to the membrane waves, the flexural wave carries higher wave power than the membrane wave do and thus behaves largely as a power source. One can speculate that if there were other shell discontinuities in the middle of the shell, this late flexural wave power surge would largely disappear. I will show in the next section that this is indeed the case for the ringed shell.

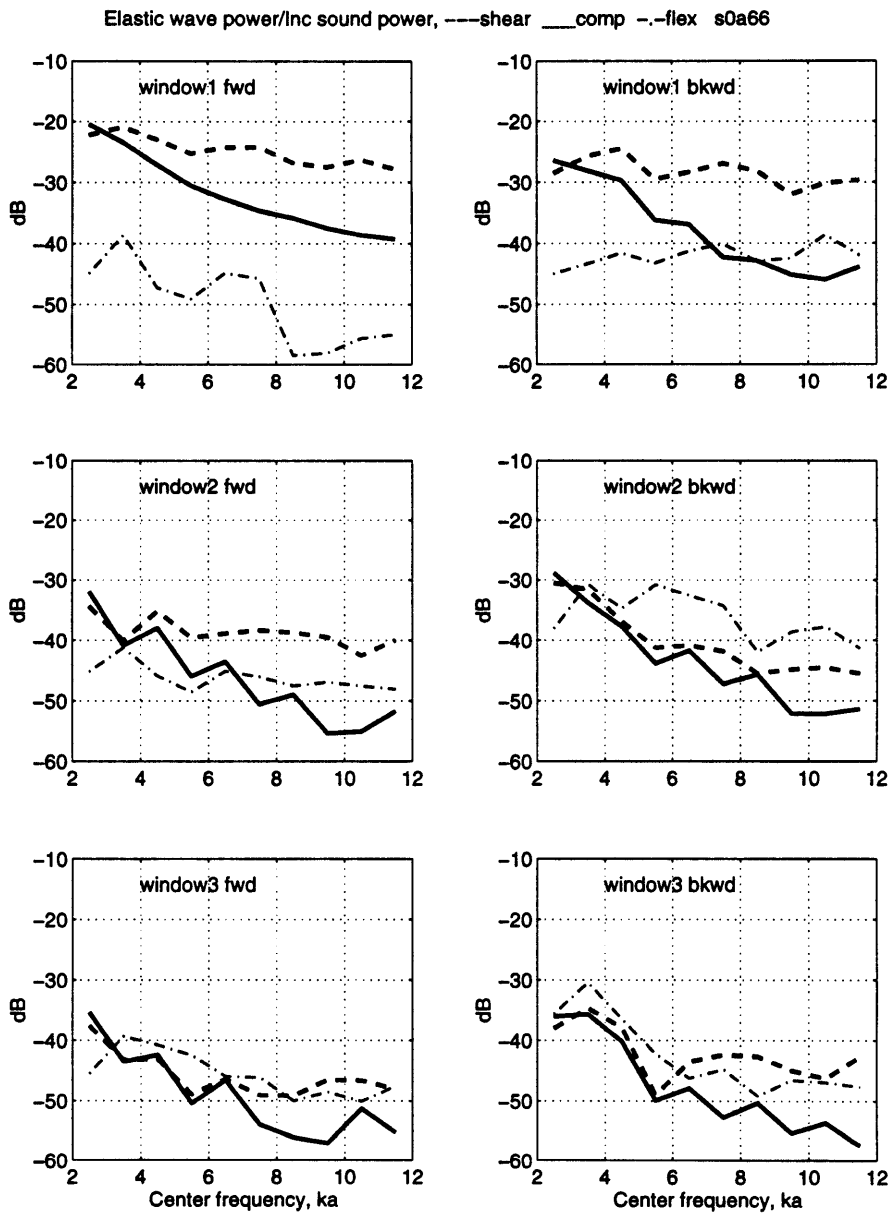

Figure 3-14: Wave power of the **empty** shell due to 66° sound incidence (SARA results). Time windows 1, 2 and 3 correspond to the first three roundtrip periods of the trace matched wave in the shell. The power shown is averaged over ten non-overlapping frequency bands in $2 < ka < 12$ with $\Delta ka = 1$. Wave power difference is the largest in window 1, especially for the forward going waves. The power difference decreases in window 2 and 3, but is still larger than approximately 10 dB. Membrane wave power below $ka = 4$ could be contaminated by poor resolution in the wavenumber decomposition. The same or similar legend and display format will be used in the following figures on transient wave power.

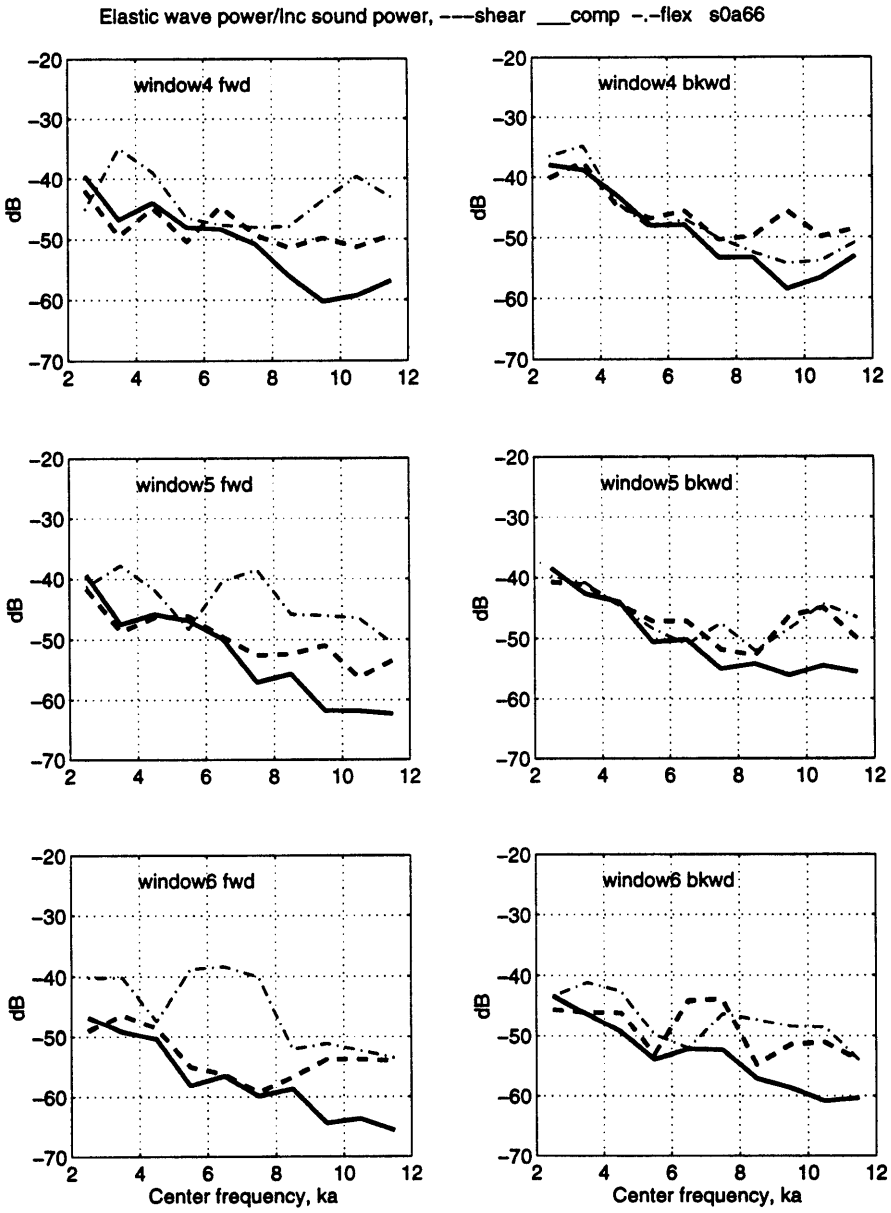

Figure 3-15: Wave power of the **empty** shell due to 66° sound incidence and in time window 4, 5 and 6 (SARA results). The legend and format are the same as in Fig. 3-14, except for the vertical scale.

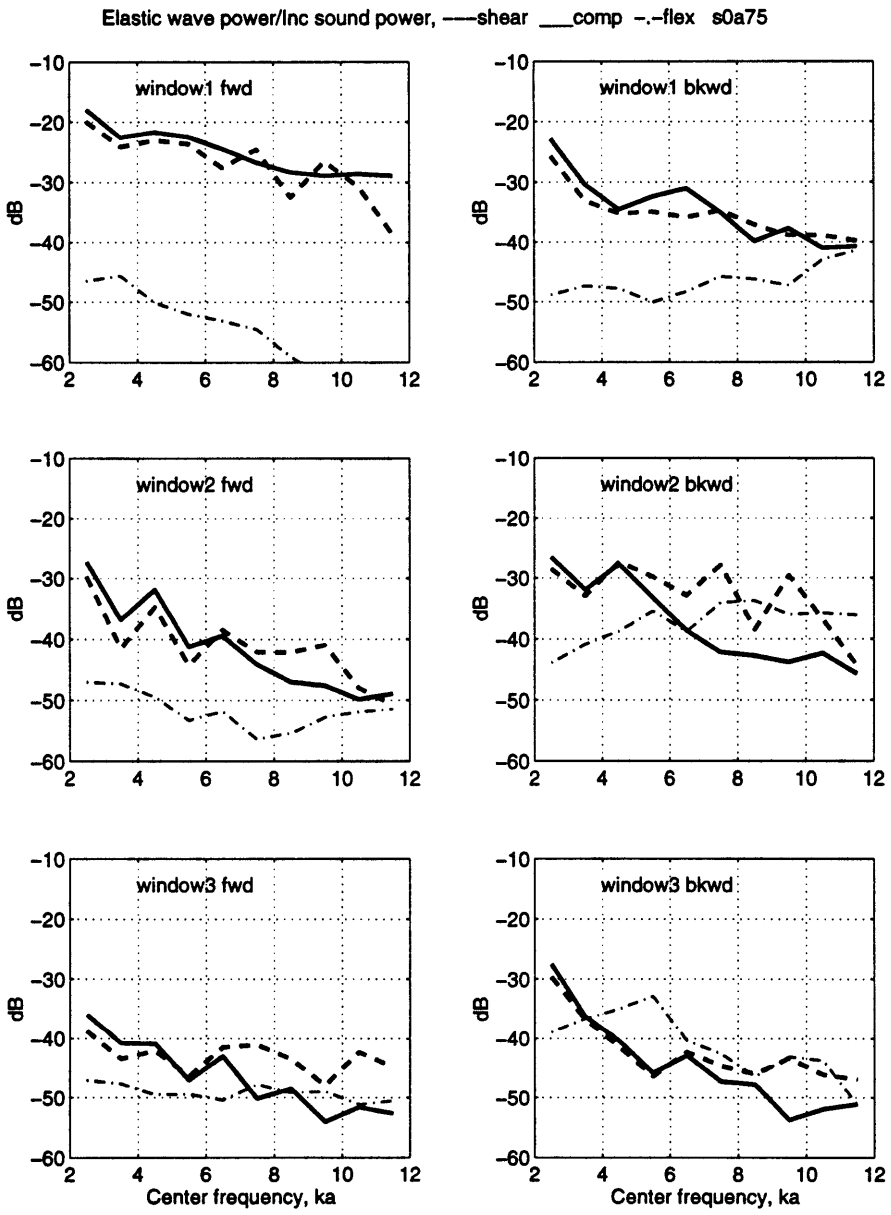

Figure 3-16: Wave power of the **empty** shell due to 75° sound incidence (SARA results). Time windows 1, 2 and 3 are used. The legend and format are the same as in Fig. 3-14.

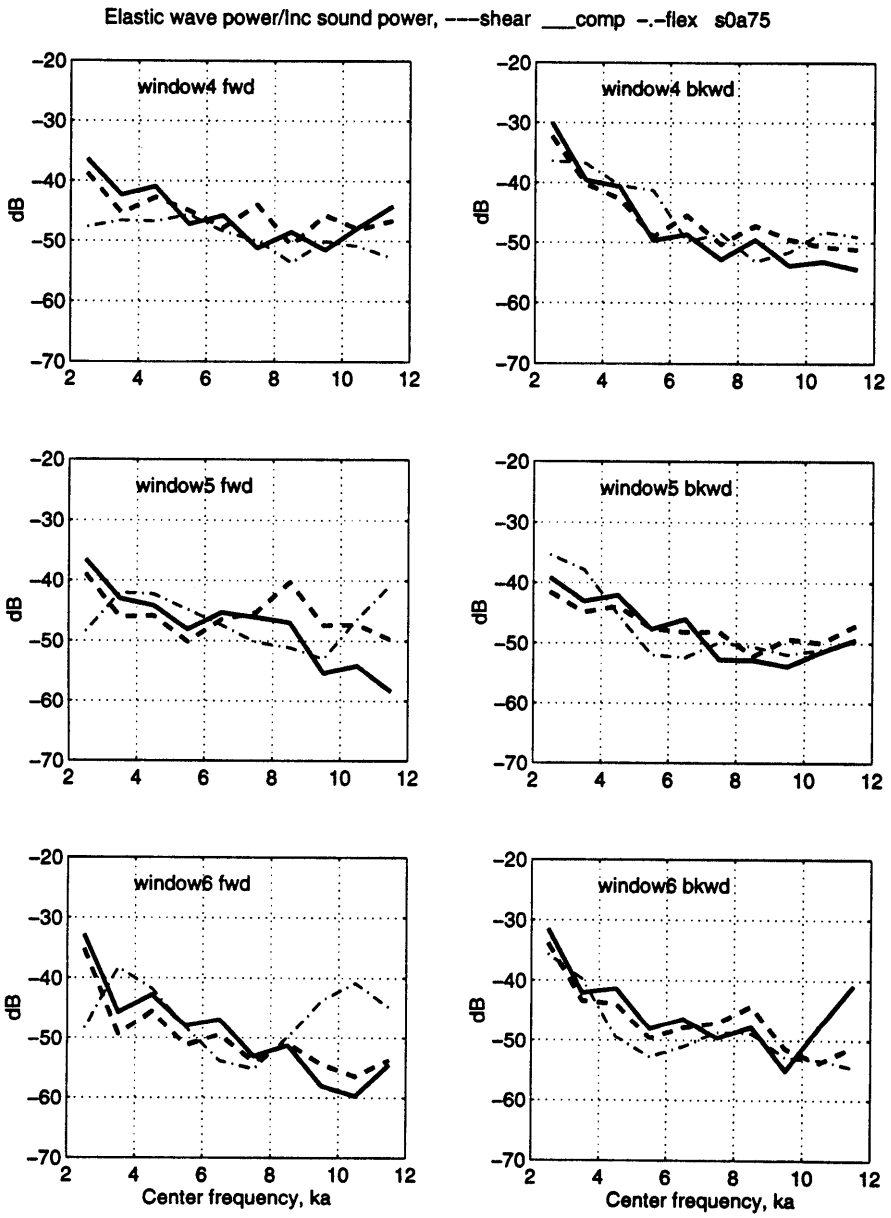

Figure 3-17: Wave power of the **empty** shell due to 75° sound incidence (SARA results). Time window 4, 5 and 6 are used. The legend and format are the same as in Fig. 3-14, except for the vertical scale.

The ringed shell, 66° incidence

Fig. 3-18 displays wave power for time windows 1, 2 and 3. Fig. 3-19 continues the display for time windows 4, 5, and 6. In window 1, the important distinction from the empty shell case in Fig. 3-14 is the drastic increase of forward flexural wave power, by approximately 10 dB. This earlier energization of the flexural waves is largely due to wave conversion at the rings from the trace matched shear wave. For a similar reason, the forward compressional wave power is smaller than the shear wave power, but by a difference significantly smaller than for the empty shell case. In the backward direction, the wave power difference among the elastic waves is further smaller, below 8 dB as opposed to above 12 dB for the empty shell result. In window 2, the elastic waves, in both forward and backward directions, share power almost equally, with the power difference within 2 dB for most frequency bands. Thus equipartition of wave power is achieved in window 2.

The equipartition of power observed in window 2 is impaired a little in window 3, and also in the rest of the windows. However, I note that the power difference among the elastic waves does not change over the time windows, as if the elastic wave power decays at a unified rate. This feature is critically different from the empty shell case, which has been shown in the previous subsection to be featured by the surge of the flexural wave power in late time windows. I believe this fundamental difference is caused by strong wave coupling and conversion at the rings. The wave coupling strength, discussed in Sec.2.1.5, can be strong enough to offset the dissipation of each elastic wave, creating not only equipartition of wave power, but also a unified decay rate. Based on this belief, a decay rate model is established later in Sec.5.1.

Further, I notice that the wave power in the forward direction is very close to that in the backward direction, at window 2 and the windows beyond. This indifference of the wave power to wave propagation direction justifies the assumption made in Sec.2.2 on $\mathcal{W}^+ = \mathcal{W}^-$.

To conclude, the power equipartition is reached in the ringed shell during the second round-trip time of the trace matched waves for this angle of incidence.

The ringed shell, 75° incidence

Fig. 3-20 displays wave power for time windows 1, 2 and 3 and Fig. 3-21 continues the display for time windows 4, 5, and 6. The overall elastic wave power for the ringed shell at 75° incidence is very similar to that at 66°. I observe that the power is more equally shared between the forward membrane waves in window 1, because of acoustic trace matching of both membrane waves at 75°. The flexural wave power is significantly higher than for the empty shell case in window 1, but still more than 6 dB lower than the membrane wave power. The power in this window is therefore not equally shared among all the three elastic waves.

In window 2, I observe that the wave power difference among the elastic waves reduces to below 3 dB for most frequency bands in $4 < ka < 12$. Thus the power is regarded as equipartitioned, according to the 3 dB criterion made in this study.

In the rest of the windows, the power equipartition is still valid except in some isolated frequency bands and time windows. Again, the relative power difference among the elastic waves are slowly varying over both frequency and time, the wave power decaying at a unified rate.

Summary of the results for the empty and the ringed shell

From numerical calculations I conclude that the elastic wave power is plausible for the ringed shell, but not for the empty shell, at least within the first 6 roundtrip periods of the trace matched wave in the shell. In the ringed shell, wave power reaches equipartition in the second time window.

The distinction between the ringed shell and the empty shell can be further highlighted graphically. In Fig. 3-22, I plot the wave power difference relative to the shear wave power for the case of sound incidence at 66°. The wave power is averaged over the frequency band $3 < ka < 5$, centered at the trace matching frequency of the $n = 1$ shear wave at $ka = 4$. The wave power is plotted against 6 successive time windows, where the point at each half window number represent forward waves and point at each integer window number represent backward waves.

From the comparison between (a) and (b) in Fig. 3-22, I observe that the trace

matched shear wave transfers power to both the compressional wave and the flexural wave for the ringed shell, at a significantly larger rate than for the empty shell. In the second time window, the power is already equalized among the elastic waves for the ringed shell while for the empty shell, the power difference among the elastic waves is large. The role of 'power source' for the flexural wave is clearly seen in late time windows. The flexural wave in the ringed shell in the late time windows also plays a role of power source since its power is consistently higher than both shear and compressional waves. The shear wave power itself, as observed from (c) of Fig. 3-22 in the first time window, is approximately 4 dB lower for the ringed shell than for the empty shell. This significant reduction of the shear wave power in window 1, caused by shear wave conversion to the compressional and flexural waves at the rings, is very important for practical reasons since the smaller shear wave power means lower scattering strength in the early process. In later time windows, the shear wave power for the ringed shell might exceed that for the empty shell and cause higher scattering strength. However, scattering very late in time is less interesting than early in time.

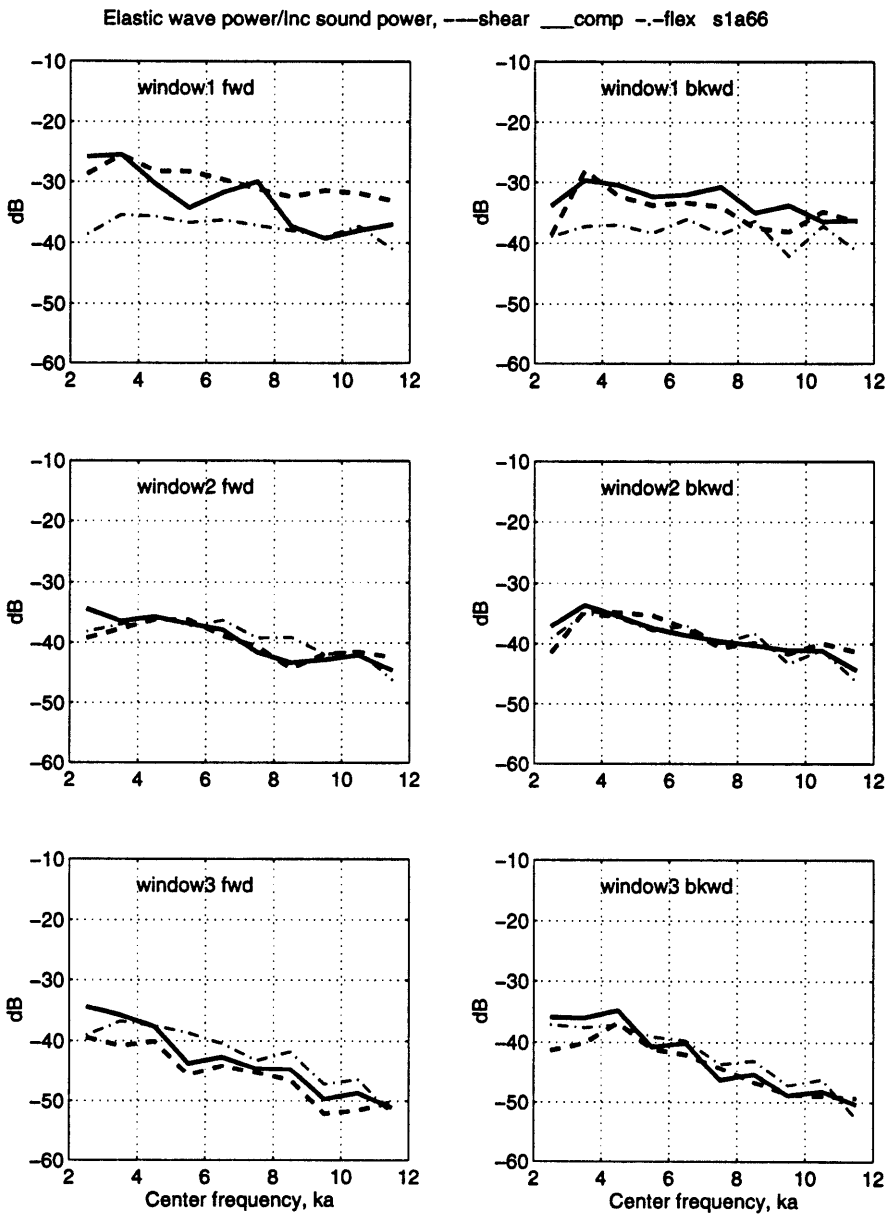

Figure 3-18: Wave power of the **ringed** shell due to 66° sound incidence (SARA results), in time windows 1, 2 and 3. Even in window 1, the forward wave power difference is significantly smaller than the empty shell case. In window 2, the power difference is below 3 dB in most frequency bands, indicating power equipartition. The figure has the same legend and format as in Fig. 3-14.

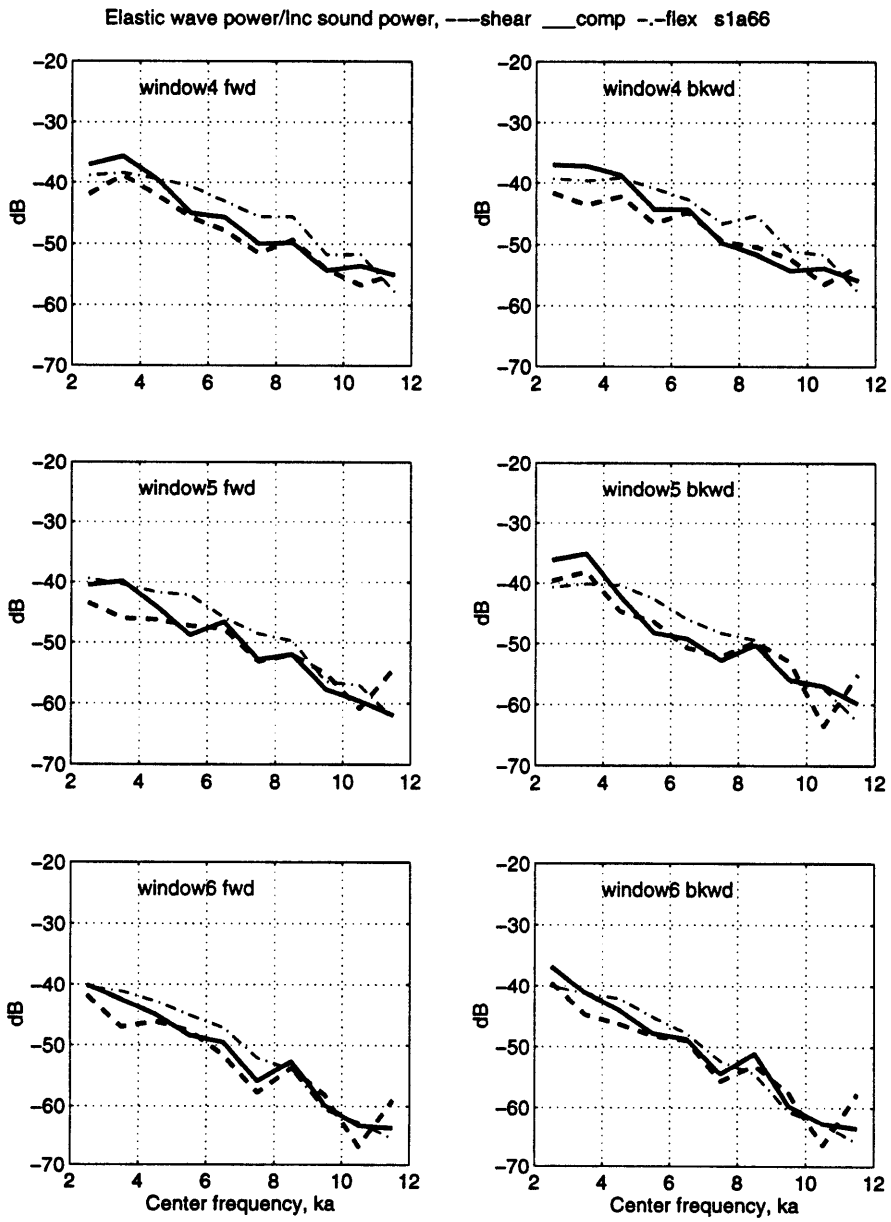

Figure 3-19: Wave power of the **ringed** shell due to 66° sound incidence (SARA results). Time window 4, 5 and 6 are The power shown is averaged over ten non-overlapping frequency bands in $2 < ka < 12$ with $\Delta ka = 1$. Even in window 1, the forward wave power difference is significantly smaller than the empty shell case. In window 2, the power difference is below 3 dB in most frequency bands, indicating power equipartition. The figure has the same legend and format as in Fig. 3-14, except for the vertical scale.

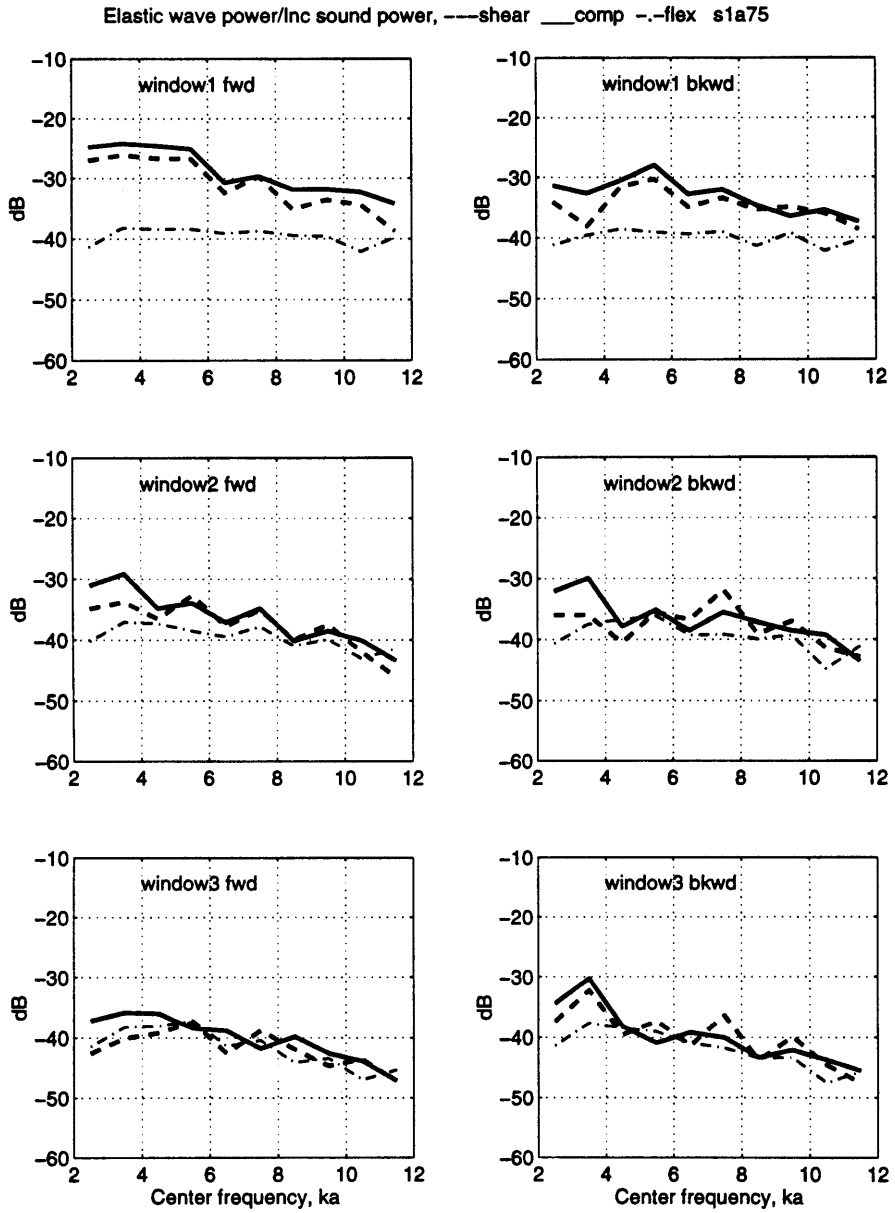

Figure 3-20: Wave power of the **ringed** shell due to 75° sound incidence(SARA results), in time windows 1, 2 and 3. The figure has the same legend and format as in Fig. 3-14.

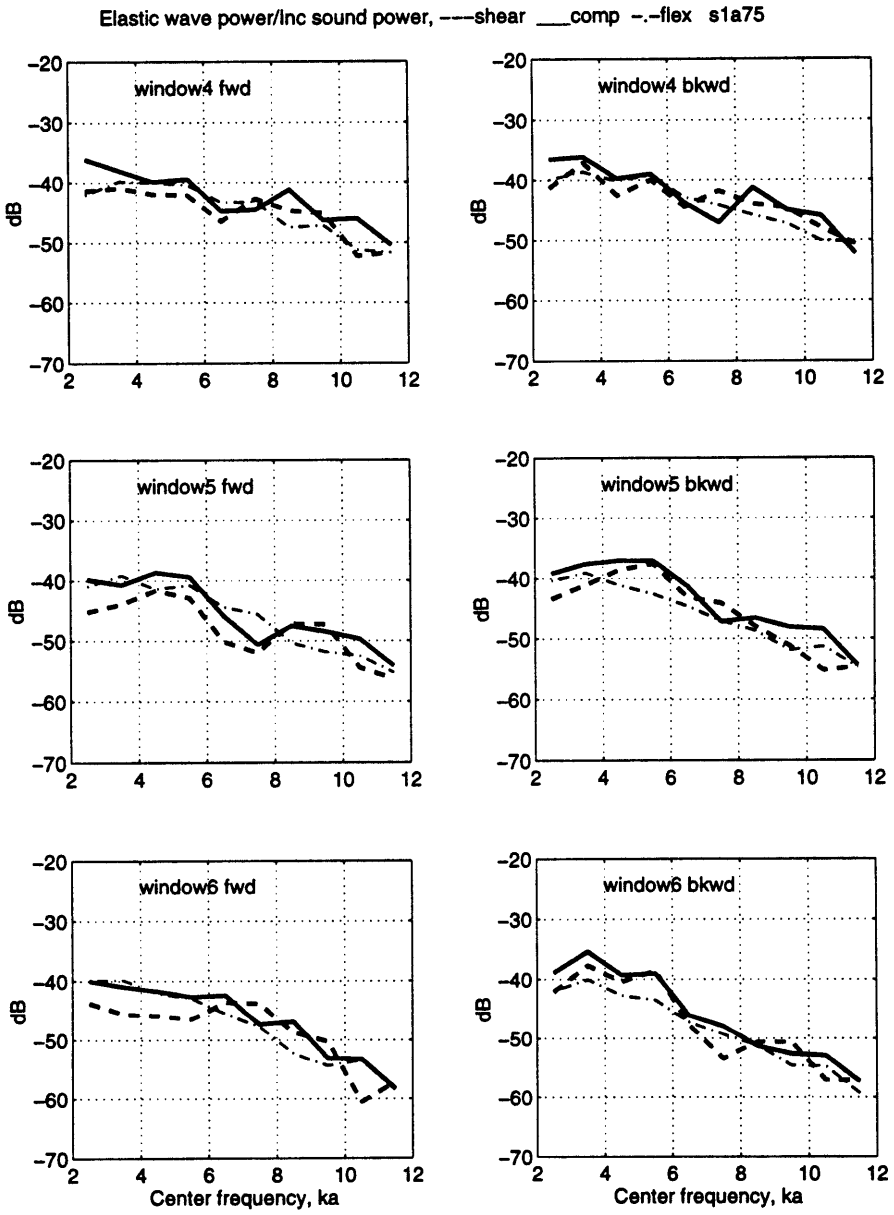

Figure 3-21: Wave power of the **ringed** shell due to 75° sound incidence(SARA results), in time windows 4, 5 and 6. The figure has the same legend and format as in Fig. 3-14, except for the vertical scale.

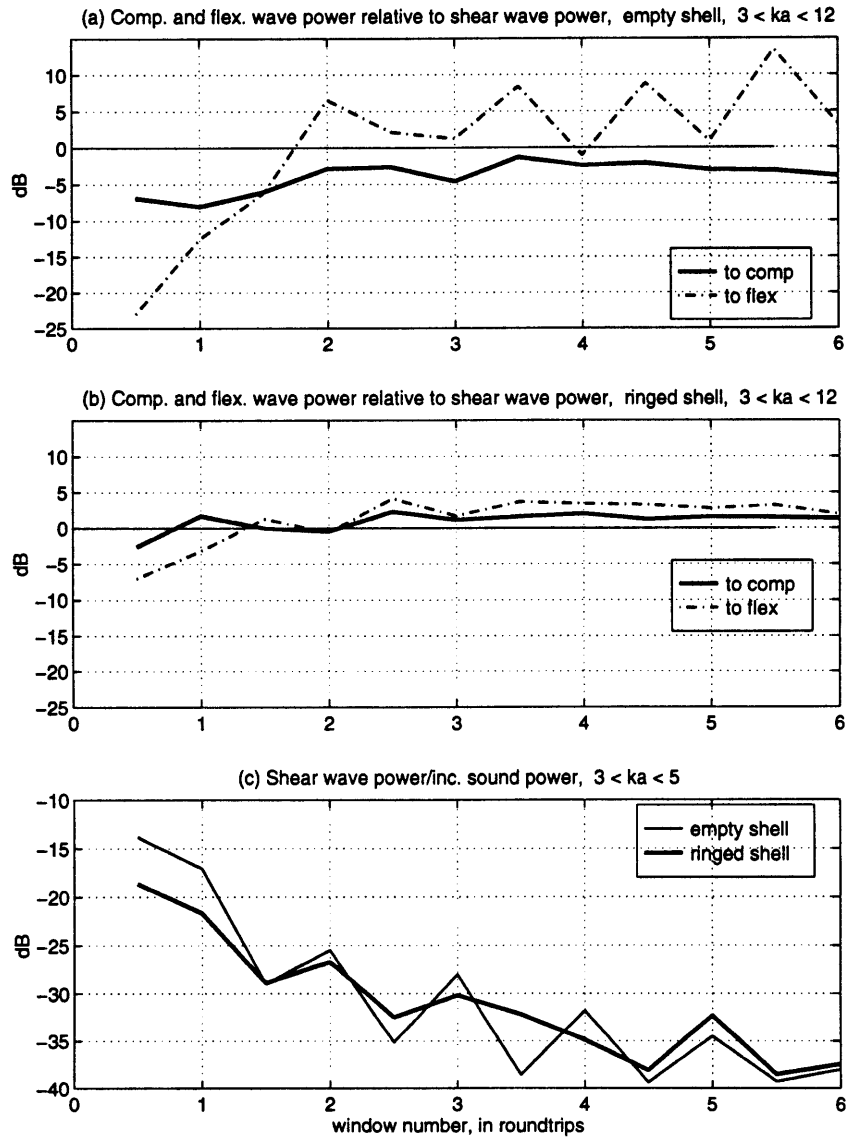

Figure 3-22: Wave power comparison between the empty shell and the ringed shell for sound incidence at 66° (SARA results). Subplots (a) and (b) display the compressional and flexural wave power relative to the shear wave power for the empty shell and the ringed shell respectively. The wave power is averaged over $3 < ka < 12$. (c) displays the shear wave power averaged over $3 < ka < 5$ for the two shells.

Shells with fewer rings, 75° incidence

The semi-quantitative analysis in Sec.2.1.5 has demonstrated that four rings can provide sufficient coupling loss because the rings drastically increase the wave interaction rates, by approximately $\sim (n_{ring}+1)^2$ times. One might conjecture that fewer rings might still create enough wave interactions for wave power equipartition. According to the formula, two rings should increase the wave interaction rate by 9 times in comparison with the empty shell case. As a result, wave equipartition could still be observed.

In the following I check if this conjecture is true, by performing a transient wave power calculation using SARA-2D with a reduced number of rings.

In the first case, I remove the two rings that are close to the endcap but keep the middle two rings. The transient wave power in Fig. 3-23 for windows 1, 2 and 3 and Fig. 3-24 for windows 4, 5 and 6 shows that the power difference among the elastic waves reduces to below 3 dB in window three(!), one roundtrip time later than for the ringed shell with four rings, shown in Fig. 3-20.

In another case, I keep one ring, the second ring from the bow endcap (see Fig. 1-1) and remove the rest. In this case, the wave coupling loss factors are expected to increase by four times. According to the semi-qualitative analysis in Sec.2.1.5, this increase of wave interaction rates might marginally increase wave coupling. The calculated transient wave power in Fig. 3-25 and Fig. 3-26 are very similar to the case of two rings in Fig. 3-23 and Fig. 3-24. The power difference reduces to below 3-4 dB in window 3.

I thus conclude that even one heavy deep ring can produce significantly different wave power behavior compared to the empty shell. At least one such ring is needed if wave power is expected to mix uniformly in the early scattering process.

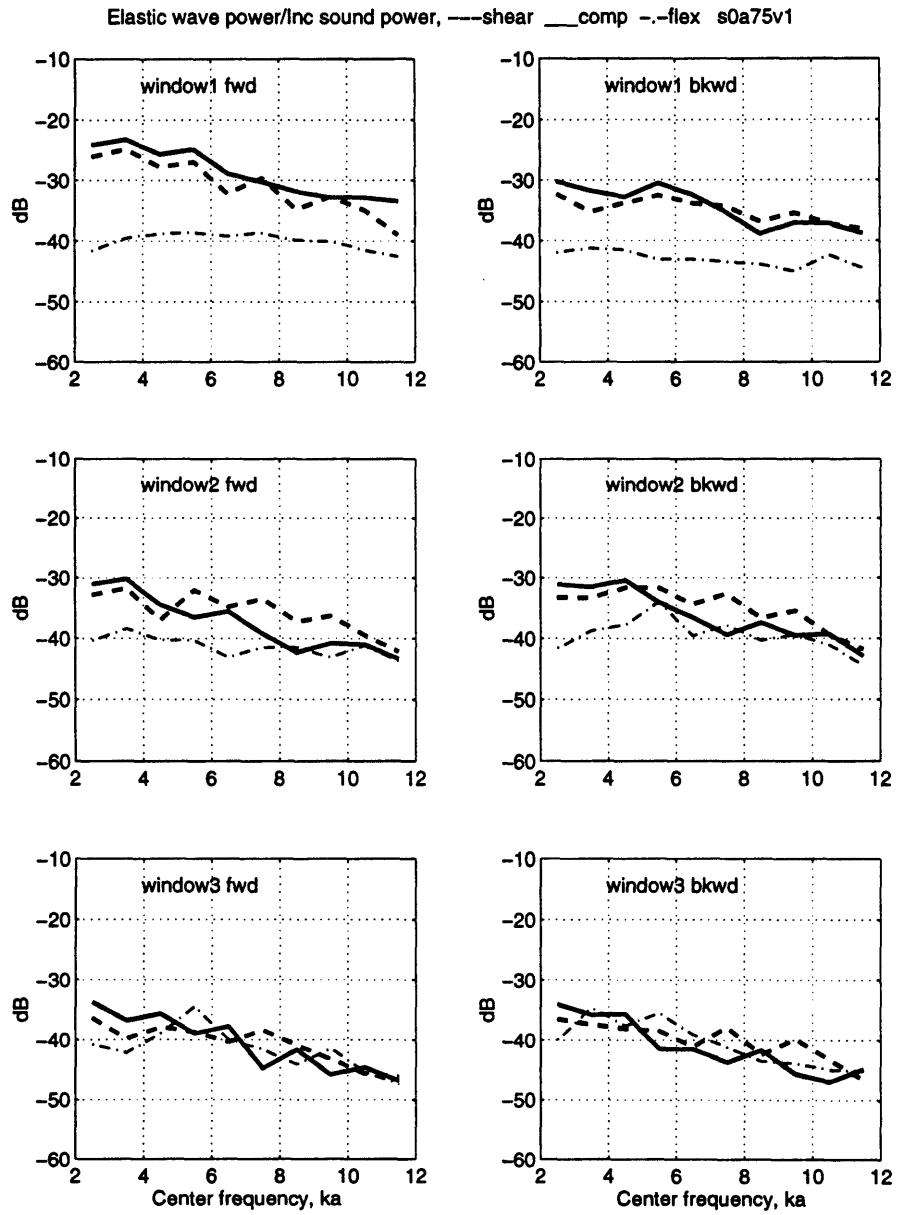

Figure 3-23: Wave power of the shell with the middle two rings only, due to 75° sound incidence(SARA results). Time windows 1, 2 and 3 are displayed. The power is averaged over ten frequency bands in $2 < ka < 12$. The same legend and format as in Fig. 3-14 is used.

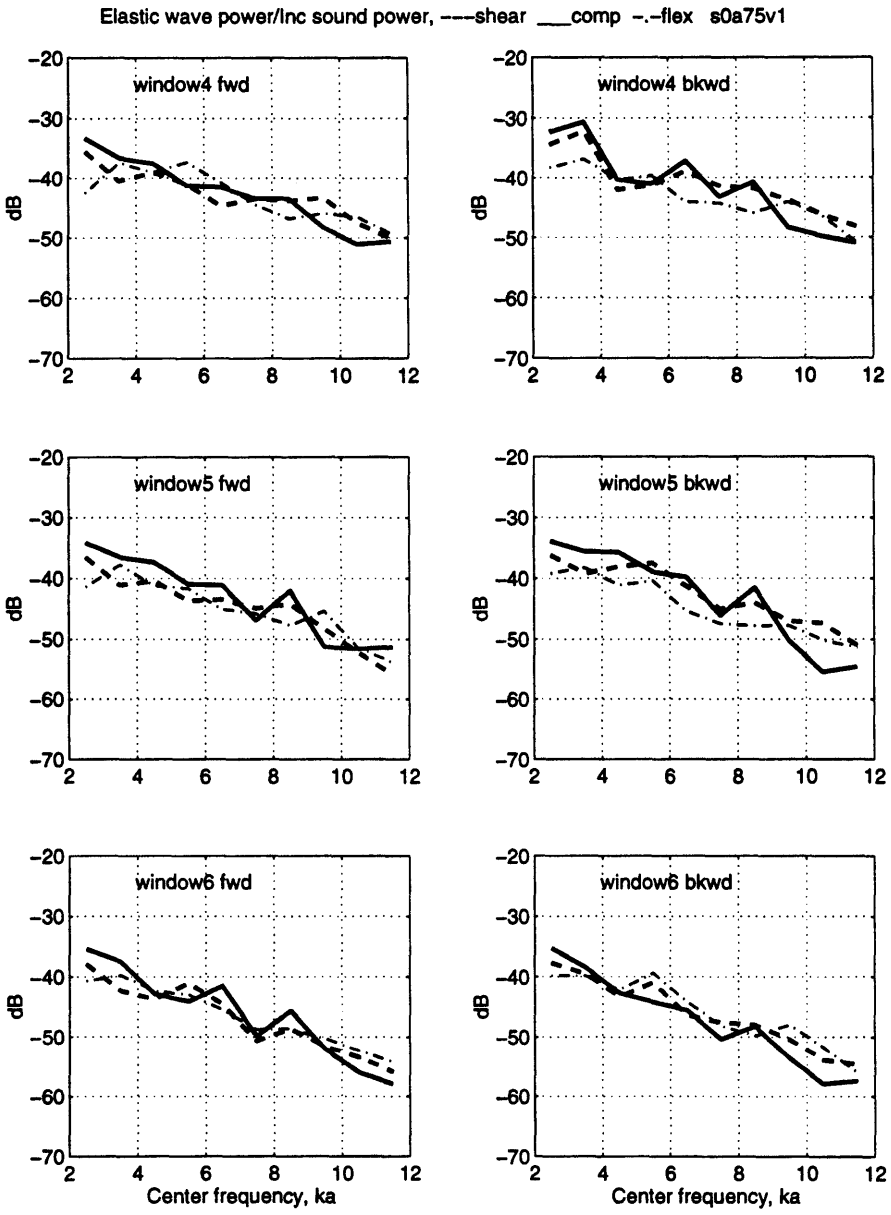

Figure 3-24: Wave power of the shell with the middle two rings only, due to 75° sound incidence(SARA results). Time windows 4, 5 and 6 are displayed. The power is averaged over ten frequency bands in $2 < ka < 12$. The same legend as in Fig. 3-14 is used.

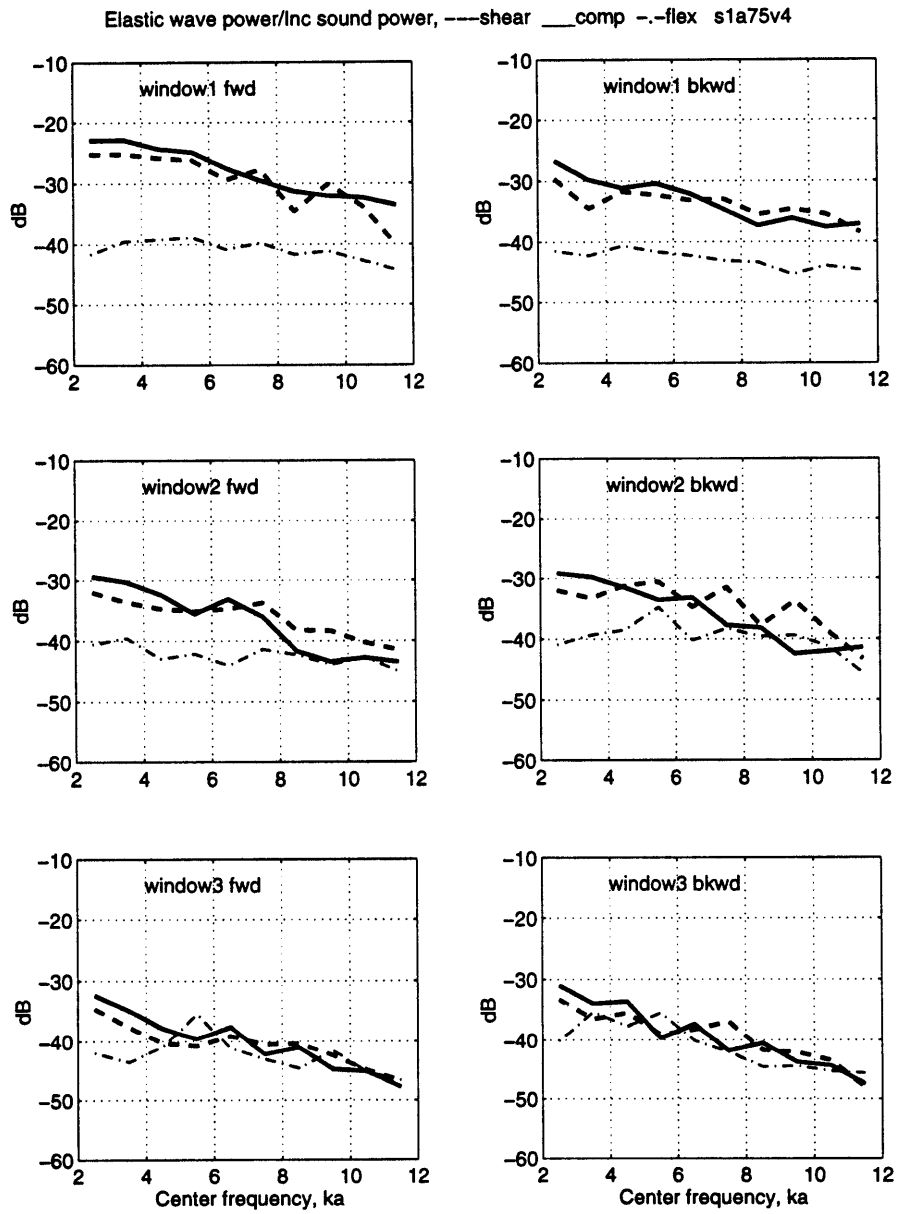

Figure 3-25: Wave power of the shell with the second ring only, due to 75° sound incidence(SARA results). Time windows 1, 2 and 3 are displayed. The power is averaged over ten frequency bands in $2 < ka < 12$. The same legend and format as in Fig. 3-14 is used.

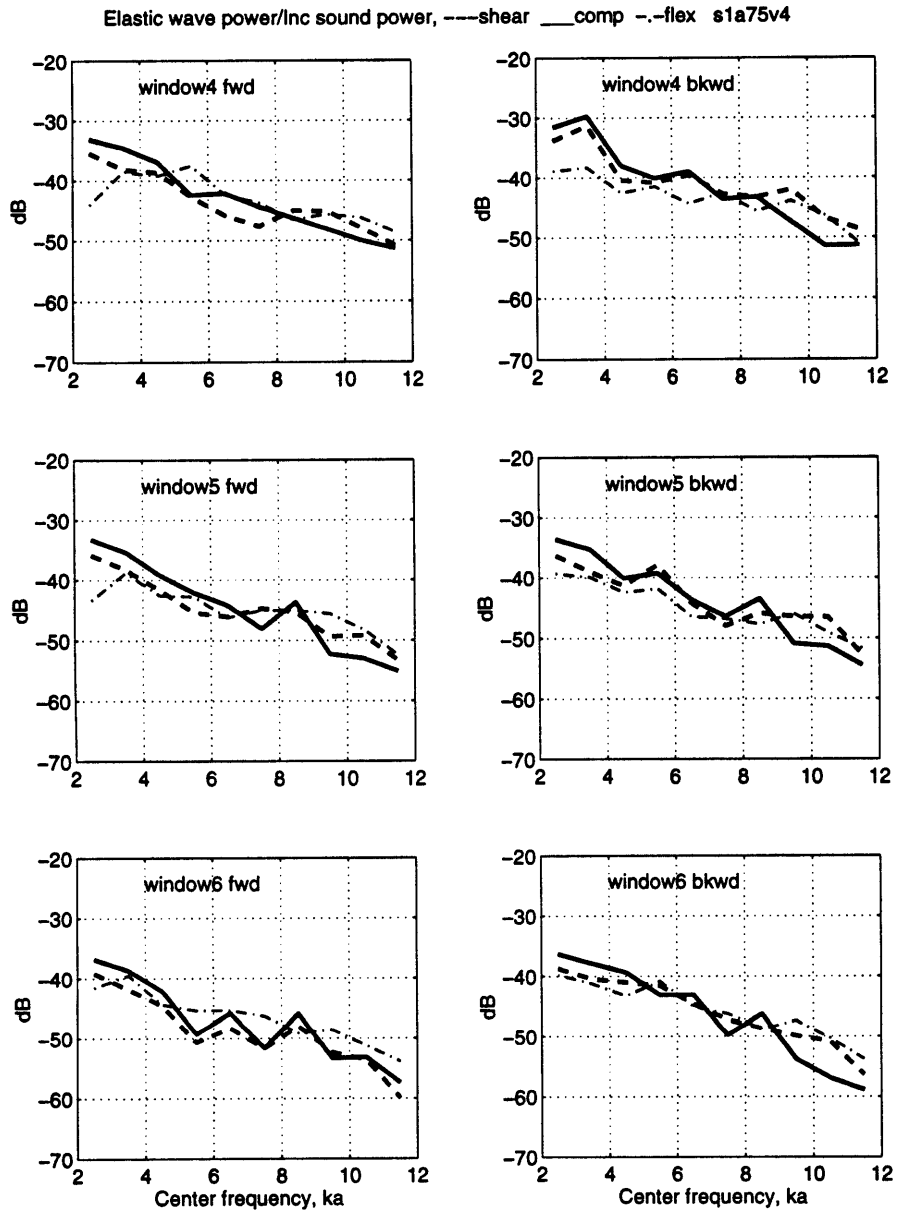

Figure 3-26: Wave power of the shell with the second ring only, due to 75° sound incidence(SARA results). Time windows 4, 5 and 6 are displayed. The power is averaged over ten frequency bands in $2 < ka < 12$. The same legend as in Fig. 3-14 is used.

3.4 Summary

According to the elastic wave power analysis based on the SARA-2D calculations, the elastic wave power of the various wave types in the ringed shell differs by less than 3 dB over most frequency bands, while the power difference for the empty shell is significantly larger. I take 3 dB difference as a criterion and conclude that power equipartition is plausible in the ringed shell. Moreover, the hypothesis is found to be appropriate in window 2 (the second roundtrip periods of the trace matched wave in the shell). Even in the case of only one or two rings attached, wave power equipartition is still a good hypothesis, although the equipartition needs a longer time to establish. It seems that the four ring stiffeners, working together with the endcaps, greatly increase the wave interaction rates for all three wave types and thus the strength of wave coupling. The steady-state wave power analysis suggests that the elastic power difference for the ringed shell is weakly dependent upon frequency, and slowly varying with the incidence angle in the membrane wave region.

I do not observe evidence of power equipartition in the empty shell, at least within the first 6 roundtrip periods of the trace matched wave in the shell. Low wave interaction rate and limited wave conversion efficiency at the endcaps are believed unable to provide sufficient wave coupling strength, to significantly offset the heavy radiation damping of the membrane waves.

The accuracy of the SARA-2D calculation is acceptable since a ringed shell target strength calculation using the SARA-2D code differs from the MIT/NRL ringed shell data by less than 2-4 dB for most frequency band and observation angles. I will continue to use the SARA-2D calculation for further investigations of the radiation model in Chap.4.

Chapter 4

Development of a radiation model

This chapter develops a radiation model that converts the elastic wave power in finite complicated shells into sound pressure in the fluid. Green's theorem is used for this purpose. In Sec.4.1, I investigate the possibility of ignoring the endcap radiation while considering sound radiation from the cylindrical shell section only. Through the SARA-2D calculation, I observe that the endcap radiation, if ignored, does not make the radiation significantly different from the direct SARA-2D scattering calculation, as long as the receivers are within the membrane wave region $60° < \theta < 120°$. In addition to the numerical approach, I probe experimental evidence of the unimportance of endcap radiation in the membrane wave region and confirm that it can be ignored.

Green's theorem requires a complex surface pressure and radial velocity in the shell as the input information. However, the calculation of elastic wave power, on the other hand, only produces the statement of the magnitude of total velocity. To fill the gap, I need to form the following three variables explicitly: (1) *the phase field*, (2) *the surface pressure* and (3) *the radial velocity*. In Sec.4.2.1, the phase field in the finite shells can be reconstructed from the axial phase wave speeds of the elastic waves. To the first order, the wave speeds from the infinitely long shell are used as an approximation which results in sound radiation only 1-2 dB smaller than the direct SARA-2D calculation. Still, the rings can change wave speeds. I observe from the measured scattering data, the SARA-2D calculation that the rings can modify the membrane wave speeds considerably but decrease the flexural wave speed only slightly.

The modified wave loci can be estimated using the simulation of a 1D bar system. The estimated wave loci will be used in Chap.5 for scattering prediction. In Sec.4.2.2, I estimate the surface pressure using the momentum equation. The test against the against the direct SARA-2D scattering results shows that the approximation is acceptable. Of course, the radial velocity itself has to be decomposed from the total velocity as well. In Sec.4.2.3, I estimate the wave motion polarization behavior for the ringed shell. The rings can increase the radial motion component of the membrane waves by $20 - 40\%$.

4.1 Radiation model: formulation and evaluation

Green's theorem is typically used to calculate radiation from general vibrating bodies [42]. It is used in this study to convert elastic wave motion in the shell to sound pressure in the fluid. Since Green's theorem generally requires detailed shell surface pressure and radial velocity field as input information, I compute in Sec.4.1.1 the spatial distribution of the elastic wave responses in the ringed shell using the SARA-2D calculation and the wavenumber decomposition. In Sec.4.1.2 Green's theorem is formulated for sound radiation from a finite cylindrical shell with zero-vibration at the endcaps. The endcap radiation is assumed to be insignificant when the receivers are in the membrane wave region. This assumption will be shown in Sec.4.1.3 to be reasonable based on both calculations using SARA-2D and an examination of the measured data.

4.1.1 Spatial wave response in the ringed shell

The complex spatial surface response of each wave type is needed as an input to the radiation model. Such information is difficult to obtain from the SARA-2D calculation (as implemented), because the requirements of good resolution in both the wavenumber domain (to identify and separate wave types) and in the spatial domain (to identify the locations of the four rings at least) are in conflict. This difficulty has the same nature as in identifying a narrow band event accurately in the time domain.

Particularly, I discussed in the previous chapters and in App.C that the elastic waves can be identified and separated in the wavenumber domain. To transform the elastic wave response back to the spatial domain (the shell axial location), however, the wavenumber windows have to be large enough to achieve a reasonable spatial resolution. Large wavenumber windows, however, make it difficult to separate the elastic waves in the wavenumber domain. This difficulty is especially true for the membrane waves, since the $ka - k_x$ curves of the shear and compressional waves are very close to each other in the wavenumber domain. Therefore, a compromise is needed in choosing a useful wavenumber window.

To achieve at least some resolution sufficient to the problem at hand, I choose a wavenumber window that covers both membrane waves as if they were a single wave. Fig 4-1 illustrates the typical windows for the membrane waves and the flexural wave. Even so, the spatial resolution of the membrane waves might be poor (the ring locations might not be well resolved) below $ka = 4.5$. The choice of the wavenumber window for the flexural wave is relatively easy because the flexural wave dispersion curve is well separated from that of the membrane waves. I choose the flexural wave window to extend close to the shear wave dispersion curve, as sketched in Fig 4-1.

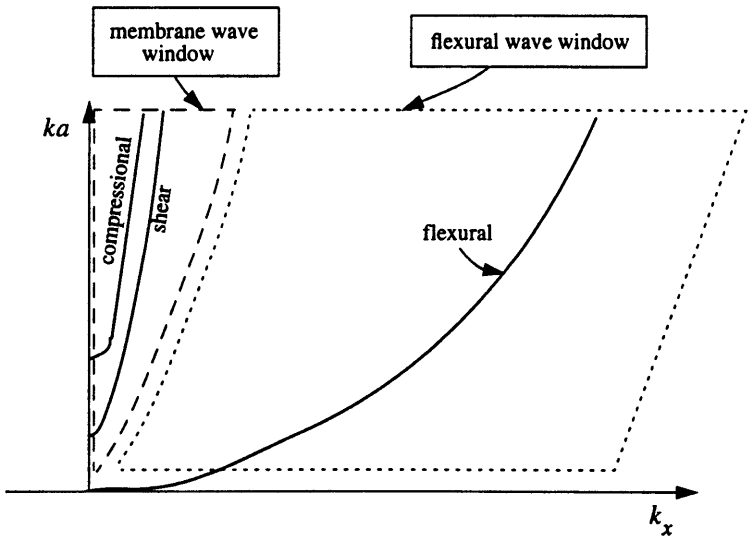

Figure 4-1: Illustration of windows used in the wavenumber domain, for the purpose of determining the surface response along the ringed shell.

I perform such a transformation for both radial velocity and surface pressure for each circumferential mode n. The transform is illustrated in the following in the

example of surface pressure

$$\hat{p}_n(\omega, k_x) = \frac{1}{2\pi} \int_{-\infty}^{\infty} p_n(\omega, x)\, T(x)\, e^{ik_x x}\, dx \ ,$$
$$p_n(\omega, x) = \int_{-\infty}^{-\infty} \hat{p}_n(\omega, k_x)\, T'[k_{x1}, k_{x2}]\ e^{-ik_x x}\, dk_x \ , \tag{4.1}$$

where $T(x)$ is a uniform spatial tapered function that has round-offs at the ends. The wavenumber window $T'[k_{x1}(\omega), k_{x2}(\omega)]$ is chosen according to Fig 4-1.

Fig. 4-2 shows the decomposed surface pressure(summed over mode n) of the ringed shell under 75° sound incidence. The locations of the rings are observed for both flexural waves and membrane waves. Note that the flexural wave has higher surface pressure. However, its subsonic wave speed prevents the surface pressure wave from propagating even a fraction of the wavelength into the fluid. On the other hand, the membrane wave surface pressure, although lower, contribute to the major sound radiation to the far field.

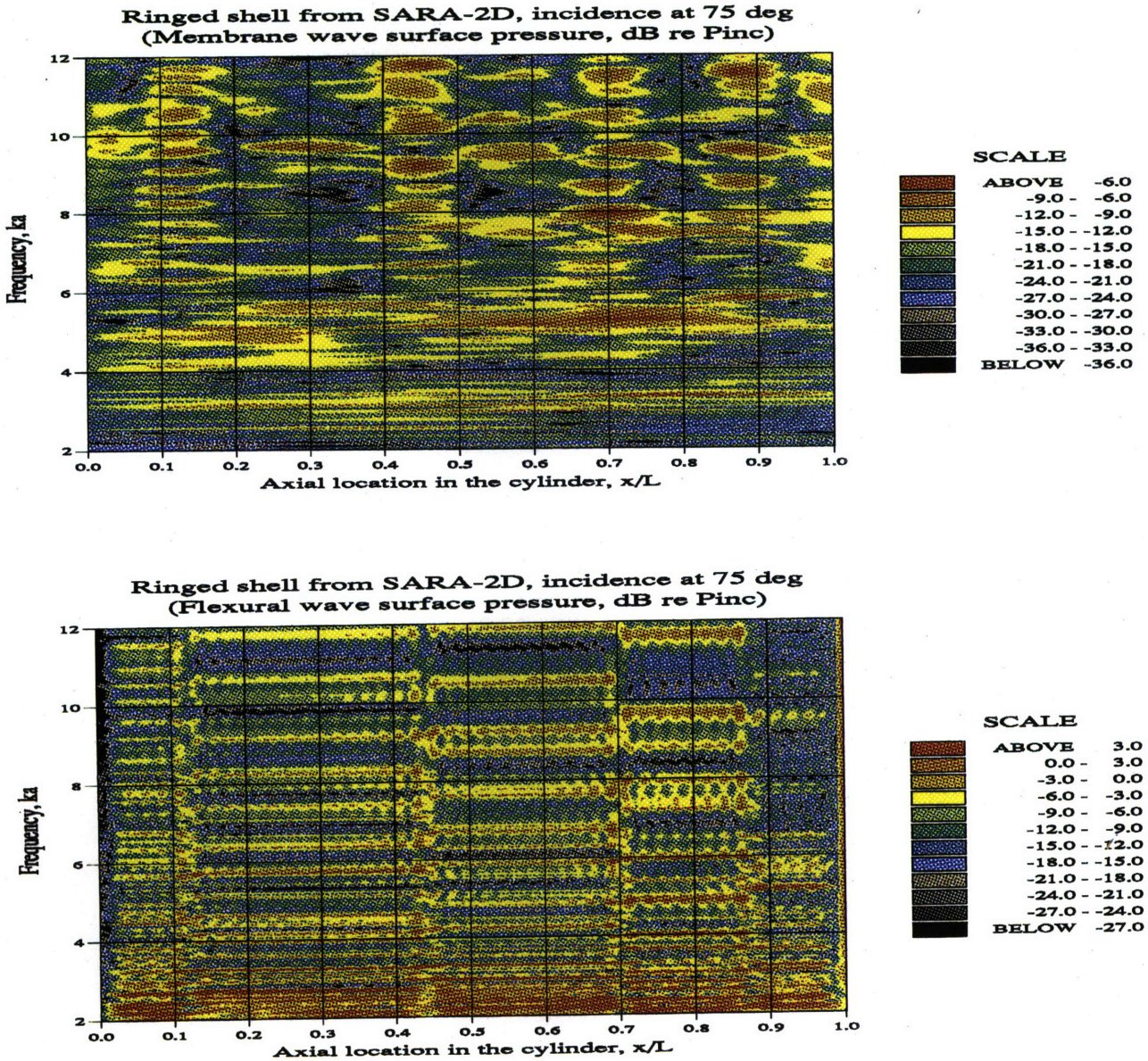

Figure 4-2: Decomposed surface pressure of the ringed shell under 75° sound incidence. The locations of the rings I, II, III and IV are at x/L = 0.13, 0.44, 0.70 and 0.87 respectively (see Fig. 1-1). The upper plot is for the membrane waves and the lower plot is for the flexural wave.

4.1.2 Green's theorem for sound radiation from shells

The cylindrical shell can be regarded as a waveguide that enables waves to propagate axially while it creates standing waves (modes) in the circumferential direction. If the shell radius is much smaller than the acoustic wavelength, the uniform expanding and contracting $n = 0$ mode can be thought of as a monopole radiator. Similarly, the $n = 1$ mode corresponds to the rigid shell oscillating back and forth, and has a dipole-like radiation. The $n = 2$ mode expands in one direction and contracts in the perpendicular direction, and has a quadrupole radiation pattern. In this small radius case, if one knew the shell motion of each mode and therefore the strength of those acoustic compact sources, the radiation could be summed over those compact sources. However, the shells studied in this thesis are not compact because the shell radius is larger than or comparable to the acoustic wavelength, $2 < ka < 12$. This explains why I have to model the shell radiation as a shell array instead of a line array. Note that the shell slenderness in the MIT shell models, $L/2a = 8$, plays no role in making such a decision.

Once the surface pressure and radial velocity (p_n, v_{rn}) are available for each wave type and each mode n, I can multiply the values by $cosn\phi$ to obtain the circumferential dependence, ϕ being the azimuthal angle. In doing so, the two waves of the opposite chiralities during the acoustic trace matching process are automatically considered. The concept can be better understood if one thinks of the duel relationship between mode and wave: $2\cos n\phi = e^{in\phi} + e^{-in\phi}$. The factor '2' does not appear in the multiplication for the circumferential dependence because it has already been included in the surface response for each wave type, and for each mode n.

The fundamental approach in solving sound radiation from a moving surface is to use Green's theorem, see Ref. [42],

$$p(\mathbf{r}) = \int_{s_0} ds_0 \left[G_w(\mathbf{r}, \mathbf{r}_0) \frac{\partial p(\mathbf{r}_0)}{\partial \mathbf{n}_0} - p(\mathbf{r}_0) \frac{\partial G_w(\mathbf{r}, \mathbf{r}_0)}{\partial \mathbf{n}_0} \right] , \tag{4.2}$$

where G_w is the Green's function. $\mathbf{n}_0$ represents the normal direction of the vibrating surface, s_0 the surface and $\mathbf{r}_0$ the point on the surface, see Fig. 4-3.

The relationship between the normal derivative of the pressure and normal velocity

is obtained from the momentum equation

$$\frac{\partial p}{\partial \mathbf{n}_0} = -i\rho\omega v_r \ . \tag{4.3}$$

The Green function can be chosen arbitrarily once both surface pressure and normal velocity are specified. If not, one can choose the Green's function so that either its value or its normal derivative vanishes at the surface (corresponding to a vacuum or to a rigid body respectively), to eliminate one of the two terms in the kernel of Eq. 4.2.

Since the SARA-2D calculation yields both surface pressure and normal velocity, I choose the Green's function as in the free space of the fluid

$$G_w(\mathbf{r}, \mathbf{r}_0) = \frac{e^{ik|\mathbf{r}-\mathbf{r}_0|}}{4\pi|\mathbf{r}-\mathbf{r}_0|} \ . \tag{4.4}$$

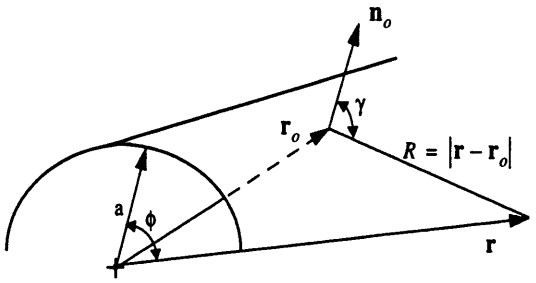

Figure 4-3: Sketch of sound radiation from the shell surface response using Green's theorem.

By considering the momentum equation in Eq. 4.3 and summation of sound pressure over circumferential mode n, the pressure integral in Eq. 4.2 over the cylindrical part of the ringed shell can be written as

$$p(\mathbf{r}) = \sum_n p_n \ , \tag{4.5}$$

and

$$p_n(\mathbf{r}) = \int_0^L \int_0^{2\pi} a d\phi dx \left[i\rho\omega \, v_{rn} + (ik - 1/R) \, p_n \, cos\gamma \right] cosn\phi \, \frac{e^{ikR}}{R} \ , \tag{4.6}$$

where angle γ is due to the difference between the surface normal and the observation direction, see Fig. 4-3.

4.1.3 Test of radiation model and evaluation of endcap and flexural wave radiation

The shell surface response can be decomposed into elastic wave component, and into each mode n. However, the concept of a finite 'array' for each wave needs yet another specification: the propagation direction.

The elastic waves in the shells propagating both forward and backward and both waves are important for the sound radiation. The two opposite going waves can be in general readily obtained by the wavenumber decomposition as discussed in App.C. In the steady-state case, however, the forward going waves are not free waves, but contain forced waves due to acoustic wave trace matching. Of course such forced waves can be eliminated in a time window if the steady-state responses are transformed into the time domain. Unfortunately, such an attempt is not successful because of numerical phase errors associated with the multiple Fourier transformations. I therefore make do with the steady-state results by estimating the forward free elastic waves as the complex conjugate of the backward waves. The approximation is reasonable because the power of the free waves going forward and backward have been shown to be very similar to each other in the transient wave power calculations, see Fig. 3-20 for windows 2 and 3.

Since each elastic wave can be regarded as a transmitting array uniquely tapered in both magnitude and phase, this approximation of using the backward waves to form the forward waves is not expected to affect sound radiation in the major part of the membrane wave region, except near beam aspect. For example, the backscatter at 75° is mainly due to contribution of the backward going waves; but near beam aspect, the radiation calculation might be in error because the phase of the forward waves is assumed to be opposite that of the backward waves. The canceling effect might be observed near beam aspect.

Based on the decomposed shell surface velocity and pressure, and the Green's

theorem formulation in Sec.4.1.2, the sound radiation from the cylinder of the ringed shell can be calculated, and tested against the direct SARA-2D scattering calculation, the latter being a complete solution of the ringed shell but with the geometric scattering extracted by time windowing.

Fig. 4-4 displays monostatic target strength at 2 m from the shell center against frequency ka for sound incidence at 75°. The radiation model result is obtained from Eq. 4.5 and Eq. 4.6, and is summed over circumferential mode n and elastic wave types. The results from the direct SARA-2D calculation are shown in the same plot. The decibel difference between the two results is analyzed and is displayed by the mean and standard deviation. I observe that the radiation model result is only 1.4 dB higher than the SARA-2D calculation, if averaged over the frequency band $3 < ka < 10$.

The small mean difference between the model and the SARA-2D calculation demonstrates that the endcap radiation, if neglected, does not make a significant difference, at least at this monostatic angle.

The flexural wave radiation is displayed in Fig. 4-4 by the dotted line. I observe that the flexural wave radiation does not significantly contribute to the total radiation. It is the membrane wave radiation that dominates.

A similar examination can be made for another monostatic angle: 66°. Fig. 4-5 displays the monostatic target strength of the ringed shell against frequency ka for sound incidence at 66°. Again, the role of the endcap radiation and flexural wave radiation is found to be insignificant.

To study radiation variation with bistatic angles, Fig. 4-6 shows the frequency-band averaged target strength of the ringed shell against observation angle. The sound incidence is at 75°. The decibel difference over the angular region $60° < \theta < 85°$ is analyzed and its mean and standard deviation are labeled in the figure. Within $60° < \theta < 85°$, the averaged radiation model result is found to be within 0.1 dB of the direct SARA-2D calculation. Below 60°, the radiation model result is significantly lower than the direct SARA-2D calculation, possibly due to the lack of endcap radiation in the model.

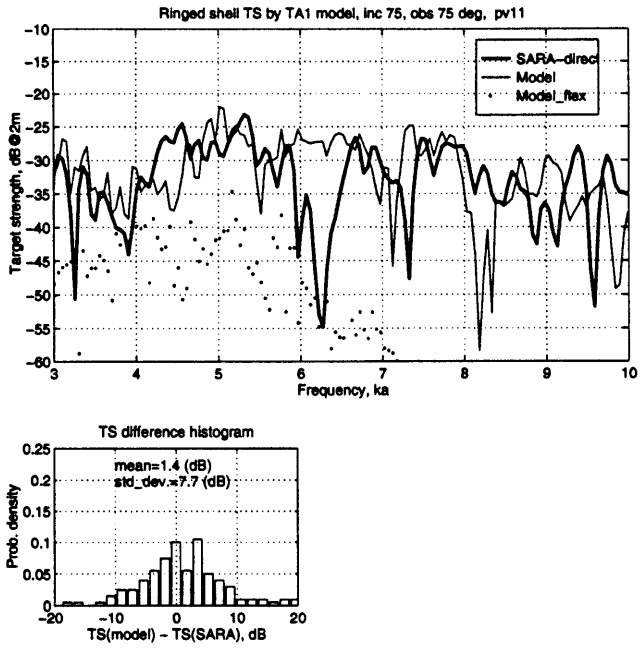

Figure 4-4: Monostatic target strength of the ringed shell from radiation model (thin line) and from SARA-2D (thick line). Sound incidence is at 75° and the receiver is at 2 m away from the shell center. Both pressure and velocity terms in Eq. 4.5 are considered.

In addition, the result from the radiation model is significantly lower near beam aspect. This is caused by the use of the backward going waves to represent the forward going waves in the model. Near beam aspect, both forward going and backward going waves contribute to the radiation actively. The approximation I used simply reverses the phase of the backward going waves and uses it as the forward going waves. Such an operation causes phase cancelation which reduces the target strength significantly. With random phase introduced into the radiation model later, this discrepancy will become less serious. Note that the purpose of this section is to test, numerically, the influence of the endcap radiation and that goal has been achieved.

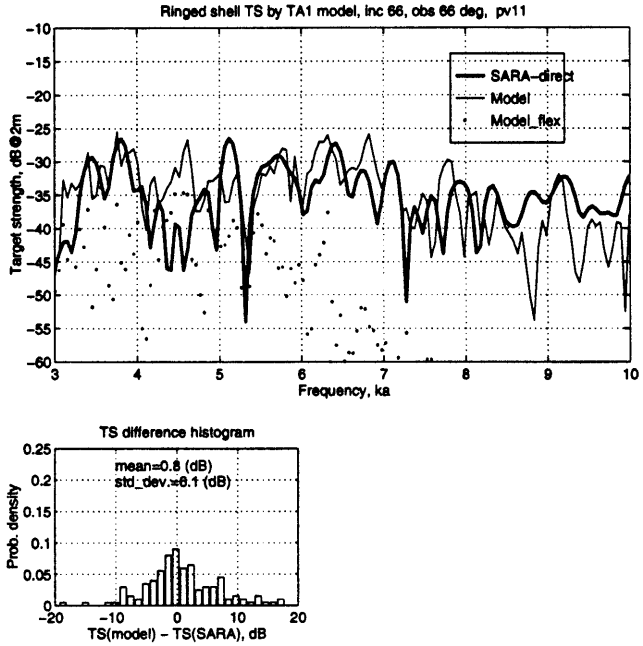

Figure 4-5: Monostatic target strength of the ringed shell from radiation model (thin line) and from SARA-2D (thick line). Sound incidence is at 66° and the receiver is at 2 m away from the shell center. Both pressure and velocity terms in Eq. 4.5 are considered.

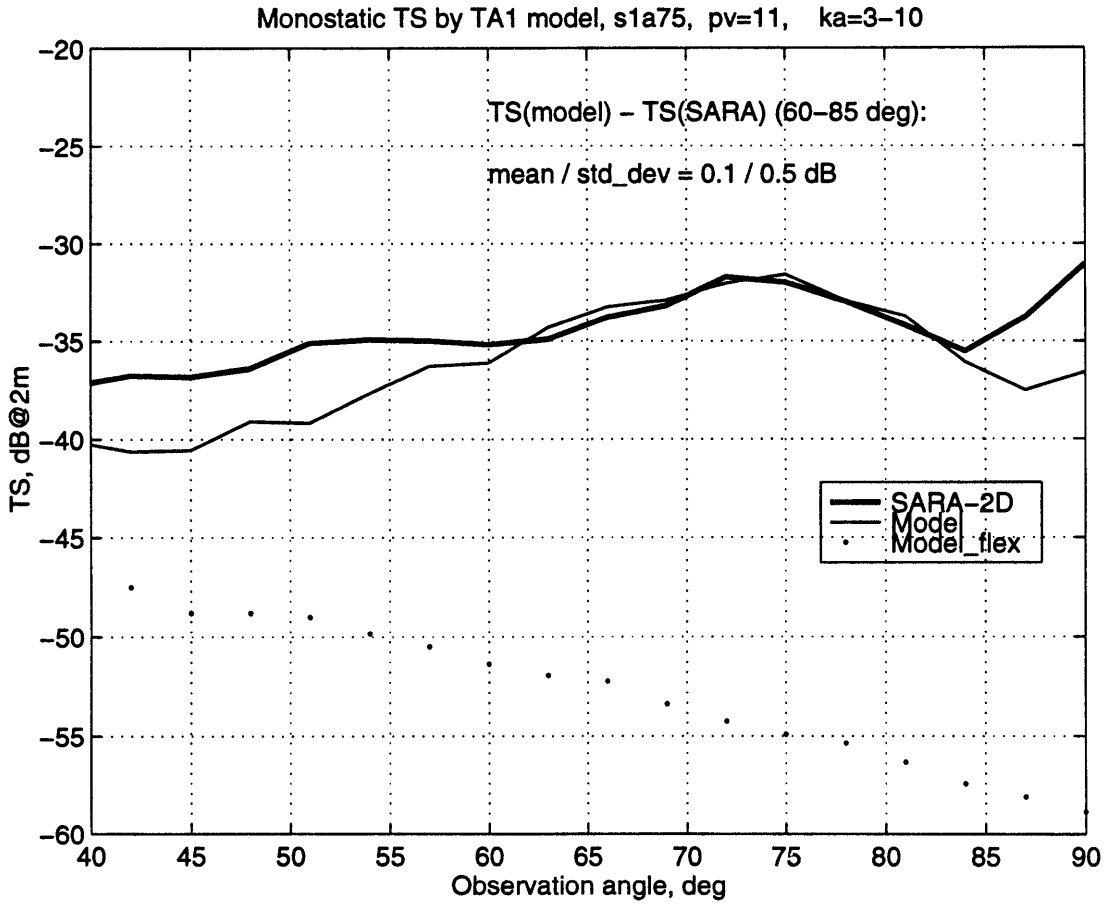

Figure 4-6: Bistatic target strength of the ringed shell from radiation model (thin line) and from SARA-2D (thick line). Sound incidence is at 75° and the receiver is at 2 m away from the shell center. Both pressure and velocity terms in Eq. 4.5 are considered.

4.1.4 Summary of the section and discussion

The comparison between the radiation model and the direct SARA-2D scattering calculation demonstrates that the endcap radiation is insignificant within $60° < \theta < 120°$. In addition, the flexural wave radiation is found to be at least 10 dB lower than the total radiation, especially at higher frequencies. The flexural wave radiation increases as the observation angle decreases, but is still approximately 10 dB lower than the total above 60°. This insignificant radiation from the endcaps and the flexural wave justifies the use of the infinitely long shell to estimate sound energy injection into elastic wave power, by a reciprocity argument.

The insignificant endcap radiation in this case is a little surprising if one notices Guo's theoretical analysis [26] showing extremely dissipative compressional waves at the endcap, see Fig. 2-5. This apparent contradiction, however, might be understood this way: the endcap radiation is not omni-directional. It is likely that the endcap radiation is directed more towards the axial direction than toward the beam direction because of the baffle effect of the cylindrical shell section.

The foregoing speculation on the endcap radiation is supported by the MIT/NRL data for bistatic scattering. In the bistatic measurement, sketched in 1-3, the response from an arc of bistatic receivers at 2 m from the shell can be phased and then summed, so that the local wet-surface pressure along the shell is obtained. Such acoustic focusing techniques have been used by Corrado [19] to study the influence of the rings on scattering. I use Fig.5.38 in his thesis, copied here as Fig. 4-7, to illustrate the endcap radiation. The figure shows the effective axial source distribution of the back- and specularly directed scatter of the internalled shell model for sound incidence at 75°. In the figure, 60 observation receivers within $60° < \theta < 120°$ are used, which cover the complete membrane wave region. The contour in Fig. 4-7 is plotted against the shell length and time, with the slanted red strip in the early process ($t < 140\mu s$) representing the trace matching wave in the shell. The ringed shell model is sketched on the right to provide a scale on the location of the rings and the endcaps. Along the trace matching strip, I observe that the source strength at both endcaps is at least one color level (3 dB) lower than on the cylindrical section of the shell. At the insonified endcap (x/L=1), the waves seem to propagate backward,

opposite to the trace matched waves. This can be explained by the forced wave at the endcap junction due to induced forcing excitation, which excites membrane waves that propagate to the apex of the insonified endcap. This suggests that the endcap is not trace matched, but energized by other forms of excitation such as induced forcing, and the energization is not as strong as the acoustic trace matching in the cylinder. The sound originating from the far endcap is also weaker than from the cylinder, indicating that the compressional wave transmitted to the endcap does not radiate strongly to the observation directions.

From the early elastic wave scattering process immediately after the the trace matching is completed, but no later than $400\,\mu s$ relative to the red strip, I observe that the source strength at the endcap is still smaller than at the cylinder portion. In one case, the radiation from the endcap is close to the radiation from the cylinder, which happens at the insonified endcap approximately $100\,\mu s$ after the acoustic wave excitation. My explanation is that the flexural wave, energized at the endcap junction, has completed one roundtrip in the insonified endcap and is converting to the radiating membrane waves at the junction. The $100\,\mu s$ time shift corresponds to the roundtrip time of the flexural wave in the endcap.

At later time, say, $400\,\mu s$ after the trace matching, the poor dynamic range prevents further analysis of the endcap strength.

A similar trend of weak endcap radiation observed within the membrane wave region can be found in Fig.5.2 and in Fig.5.42 of Ref. [19] for 90° and 66° sound incidence respectively. These two figures are not attached in this thesis.

This experimental evidence indicates, together with the numerical analysis, that the endcap radiation is not significant, as long as both the sound incidence angle and the observation angle are within $60° < \theta < 120°$. This does not mean that the compressional wave radiation at the endcaps plays no role in this study. In fact, its role as an important decay mechanism will be considered in Sec.5.1.2 in a decay rate model.

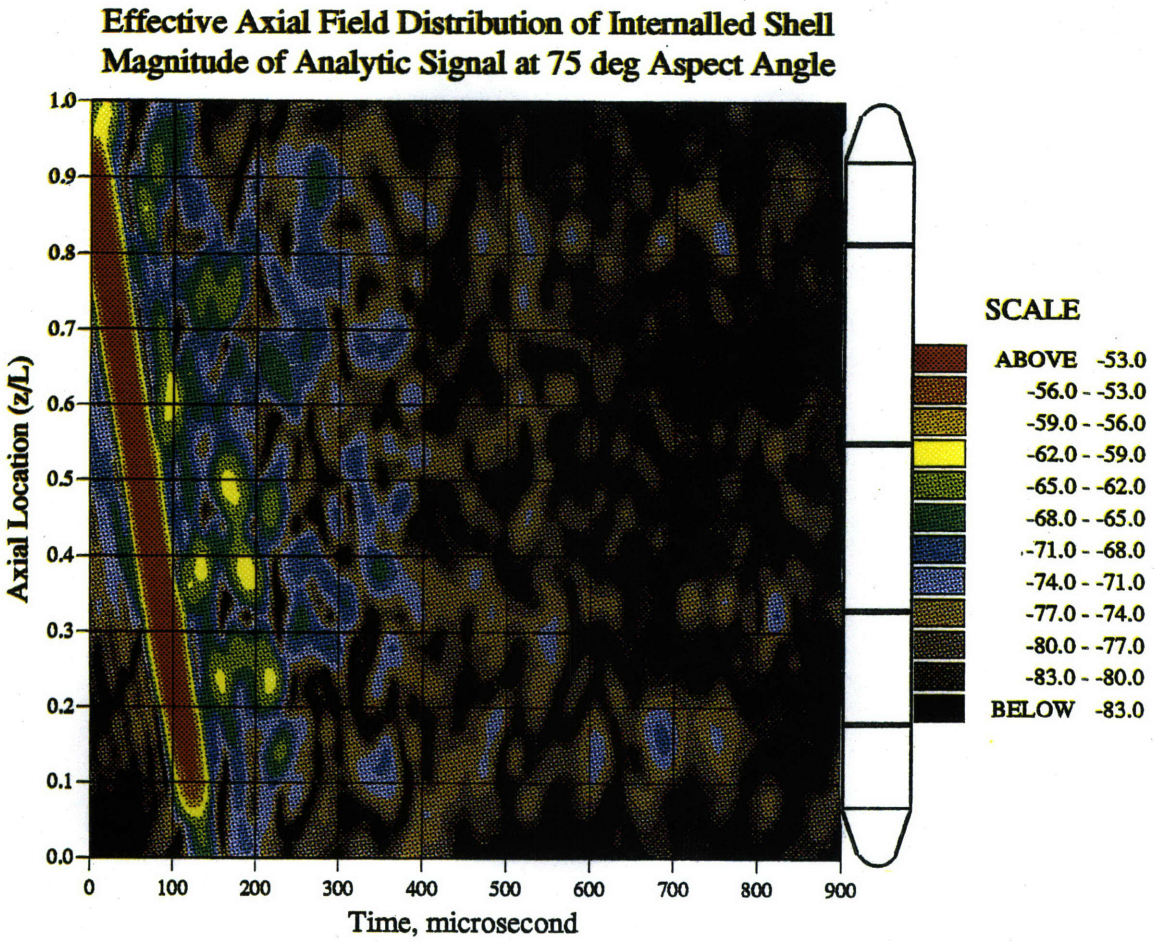

Figure 4-7: The internalled shell surface pressure reconstructed using acoustic focusing of the MIT/NRL bistatic scattering data, for frequency range of $2.75 < ka < 10.0$. Receivers within bistatic angle $60° < \theta < 120°$ are used. The sound incidence is at 75° and the surface pressure is normalized by the incident sound pressure. Copied from Fig. 5.38 of Corrado's thesis [19].

4.2 Radiation model: estimate of parameters not provided by the wave power hypothesis

The previous section converted elastic wave motion to sound pressure in the fluid using Green's theorem. In the calculation, the detailed shell surface pressure and radial velocity were obtained from the SARA-2D calculation. However, the detailed complex surface pressure and velocity are not readily provided by the wave power equipartition hypothesis. The wave power calculation in Sec.2.3 gives only the power, or the magnitude of the *total* velocity for each wave type. Thus, there is a gap between the output of the wave power calculation and the input required by the radiation model. To fill the gap, I need to obtain the following variables explicitly:

- the phase field
- the surface pressure
- the radial velocity

Sec.4.2.1 estimates the phase field by using axial phase speeds from the calculation of the infinitely long shell. The influence of the heavy deep rings on the axial speeds of the membrane and flexural waves is tested, through SARA-2D calculation and through the MIT/NRL measured data analysis. I find that the membrane wave speeds can be either increased or decreased by the rings, by about 10% or even more. The flexural wave speed, on the other hand, is decreased only slightly by the rings. The membrane wave region for the ringed shell still remains approximately as $60° < \theta < 120°$. The sound radiation using the estimated wave speed is tested against the direct SARA-2D calculation, and the difference in target strength is less than 2 dB. Although the membrane wave speed changes do not significantly affect the membrane wave region and radiation, they can modify the trace matching and therefore the scattering strength, in terms of frequency and observation angle. This latter issue will be discussed in Sec.5.2.4.

Sec.4.2.2 estimates the surface pressure by using the momentum equation. The shell radial velocity is obtained from the decomposed wave magnitude from the SARA-

2D calculation. Again, the radiation is compared with the direct SARA-2D calculation and the two agree well, with the results of the radiation model being smaller, by less than 2 dB.

Sec.4.2.3 estimates the ratio of the radial velocity to the total velocity for the ringed shell, by the analytical results from the infinitely long shell. The estimate is tested numerically using SARA-2D, and is found to predict the ratio for the flexural wave very accurately, but to underestimate the ratio for the membrane waves by $20 - 40\%$.

4.2.1 Estimate of the phase field

The estimate of propagating phase for each elastic wave is based on the notion that each wave, either forward going or backward going, can be regarded as a finite array. The phase of the 'array' is closely related to the axial wave speed by the following expression, in the example of surface pressure of mode n:

$$\hat{p}_{rn}^{+} = |\hat{p}_{rn}|\, e^{ik_{xn}x} \quad , \quad \hat{p}_{rn}^{-} = |\hat{p}_{rn}|\, e^{-ik_{xn}x} \quad , \tag{4.7}$$

where '+' indicates forward going waves and '−' indicates backward going waves. $k_{xn} = \omega/c_n$ is obtained from the infinitely long shell calculation.

Thus, the estimate of the phase field is equivalent to the estimate of the axial wave speed. The latter can be influenced by the rings, which are tightly coupled to the shell.

Analysis of aspect angle shift from the measured scattering data

The MIT/NRL monostatic scattering data for the three shell models are analyzed. I expect to observe changes in the membrane wave speeds from shifting of aspect angle of the backscatter peaks, because the axial wave speeds of the supersonic membrane waves is related to the sound speed in the fluid by the cosine of the aspect angle, with faster wave corresponding to larger aspect angle. At beam aspect ($\theta = 90°$), the axial wave speed is infinite.

Fig. 4-8, Fig. 4-9 and Fig. 4-10 display the monostatic Gaussian bandlimited im-

pulse response for the empty, the ringed and the internalled shell models respectively. Four Gaussian frequency bands, $2.75 < ka < 10$, $2.5 < ka < 5$, $5 < ka < 7.5$ and $7.5 < ka < 10$, are used. For the empty shell, the periodic backscatter, clearly observed in (a) of Fig. 4-8 later than the the predicted arrival of the direct scatter from the far endcap junction (indicated by the black line), is largely due to the backward helical shear wave circumnavigating the shell, discussed in detail by Corrado [19]. The important feature for the empty shell data is that the elastic target strength cuts off at below 60°, indicating that the membrane wave speeds for the empty shell are essentially the same as for the infinitely long shell. The membrane wave region, defined as $60° < \theta < 120°$ in Sec.2.1.3, can describe the empty shell well.

For the ringed shell, the backscatter within $60° < \theta < 90°$ comes much earlier in time and has no obvious periodic pattern, unlike the the empty shell case. The four red lines indicate the predicted arrivals of the direct backscatter from the four rings and the black line has the same indication as for the empty shell. Overall, the elastic scattering after $44\,\mu s$ in (a) of Fig. 4-9 is largely concentrated within the angular region $60° < \theta < 90°$. Different from the empty shell case, however, there exists considerable elastic scattering below 60°. The scattering coinciding with the 2nd, 3rd and 4th ring lines indicates that induced forcing at the rings plays a role. The scatter near the 1st ring line, which extends from 75° to 50°, is surprising. I suspect that it is caused by the resonance between the insonified endcap and the 1st ring, because it is more significant for one (mid) frequency band, $5.0 < ka < 7.5$ than for the whole frequency region, $2.75 < ka < 10$.

The scattering feature for the internalled shell in Fig. 4-10 is similar to that for the ringed shell, except that scattering below 60° seems to be even more notable than for the ringed shell.

Next, I take the mean target strength of the three shell models evaluated in the time window $44\,\mu s < t < 800\,\mu s$ and the frequency bands $2.5 < ka < 5$, $5 < ka < 7.5$ and $7.5 < ka < 10$. Fig. 4-11, Fig. 4-12 and Fig. 4-13 display the mean target strength against aspect angle for the three frequency bands. I expect to resolve from the figures scattering for different mode n and different membrane waves. The correspondence between trace matching angle and wave speed follows a cosine relationship,

as discussed in Sec.2.1. In order to identify the modes and waves easily in Fig. 4-11, Fig. 4-12 and Fig. 4-13, I use horizontal bars to denote the angular bands corresponding to the frequency bands for the compressional and shear waves in the infinitely long cylindrical shell. The frequency-angle $(ka - \theta)$ correspondence can be derived from Fig. 2-9, or more directly from Fig. 4-14, a modified version of Fig. 2-9 with the horizontal axis changed from k_x to θ.

In the frequency band $2.5 < ka < 5$, the scattering is dominated by the $n = 1$ shear wave, according to Fig. 4-14. The peak at 66° for the empty shell in Fig. 4-11 must be the $n = 1$ shear wave. The two peaks above 75° for the empty shell are not resolved because both the $n = 2$ shear and the $n = 1$ compressional waves are possible in the angular region. For the ringed shell, there is a significant peak near 75°, which I believe is related to the $n = 1$ shear wave. That is to say, the phase speed of the $n = 1$ shear wave is increased, by almost 60%. The scattering behavior of the internalled shell is similar to that of the ringed shell.

In the frequency band $7.5 < ka < 10.0$, I expect to resolve the $n = 1$, 2 and 3 shear waves and $n = 1$, 2 compressional waves, as indicated by the horizontal bars in Fig. 4-13 which are not overlapping along the aspect angle. The corresponding scattering peaks are observed for the three shell models. For example, I believe that the $n = 1$ shear wave scattering occurs at 61° for the empty shell, 59° for the ringed shell and 58° for the internalled shell. Table. 4.1 lists the 5 'modal angles' for the three shells, as well as the corresponding wave speed change relative to the empty shell. I observe that the wave speeds are decreased considerably in this frequency region. Furthermore, the internals seem to play a role in changing the wave speeds, although the role is small.

In the frequency band $5 < ka < 7.5$, it is hard to make a convincing guess about the 'modal angles' for the shell models, because the peaks for the ringed shell and the internalled shell are not obvious below 75°, and can not be resolved at all above 75°.

Table 4.1: The angle change and relative velocity change for the shell models, for the frequency band $7.5 < ka < 10$. The corresponding wave speed change relative to the empty shell are displayed by Λ in percentage. 'Sn' and 'Cn' denote the shear and compressional waves of different mode n. λ_x/b denotes the ratio of the axial wavelength to the average separation of the rings.

wave/mode	S1	S2	S3	C1	C2
θ_{empty}, deg	61	66	71.5	76	79
θ_{ringed}, deg	59	63.5	67	72.5	78
$\theta_{int.}$, deg	58	62.5	67	71.5	77
Λ_{empty}, %	0	0	0	0	0
Λ_{ringed}, %	-6	-9	-19	-20	-9
$\Lambda_{int.}$, %	-9	-12	-19	-24	-16
$[\lambda_x/b]$	0.5	0.5	0.8	1.0	1.6

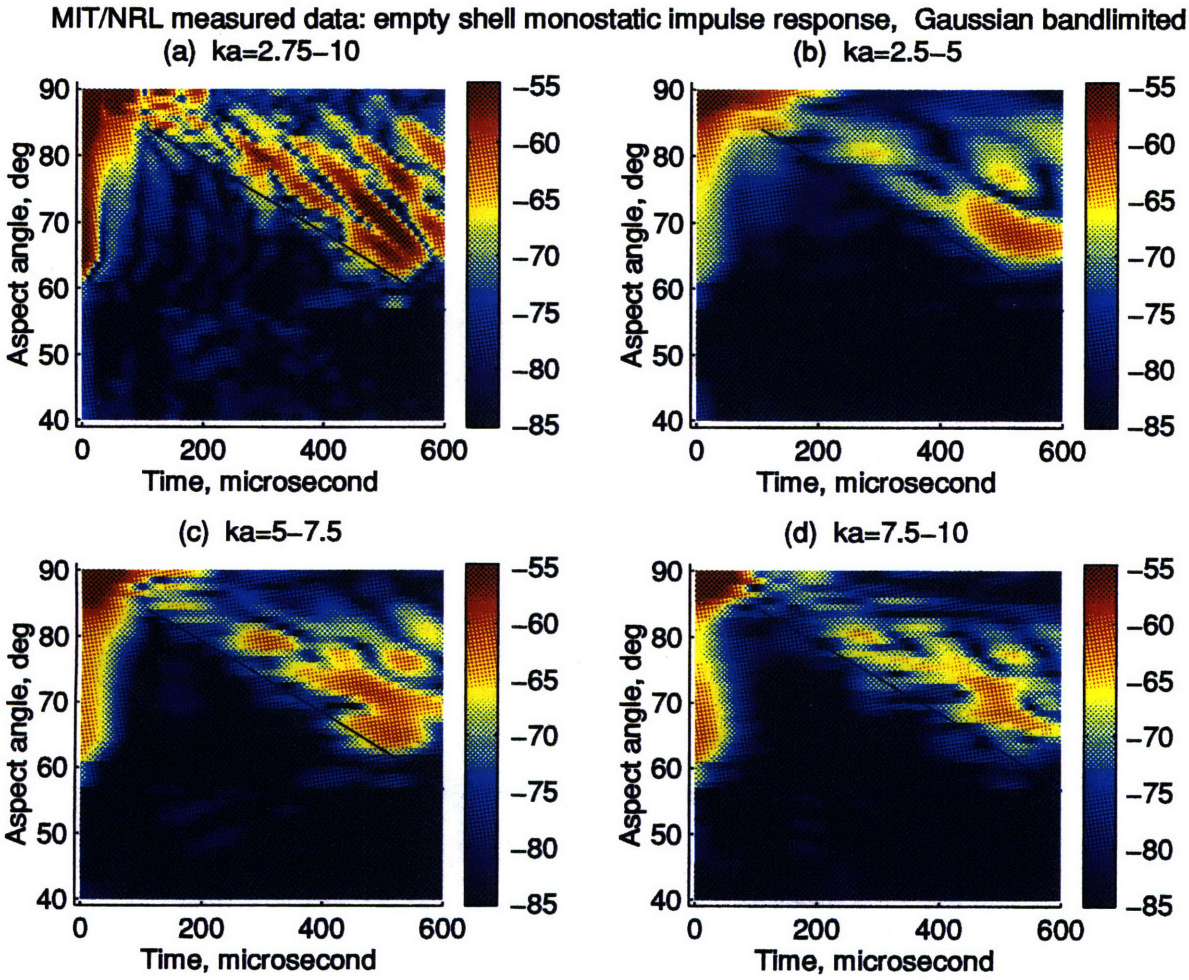

Figure 4-8: The MIT/NRL measured monostatic impulse response for the **empty** shell, Gaussian bandlimited in (a) $2.75 < ka < 10$; (b) $2.5 < ka < 5$; (c)$5 < ka < 7.5$ and (d) $7.5 < ka < 10$. The black line indicates the predicted arrival of the direct scatter from the far endcap junction.

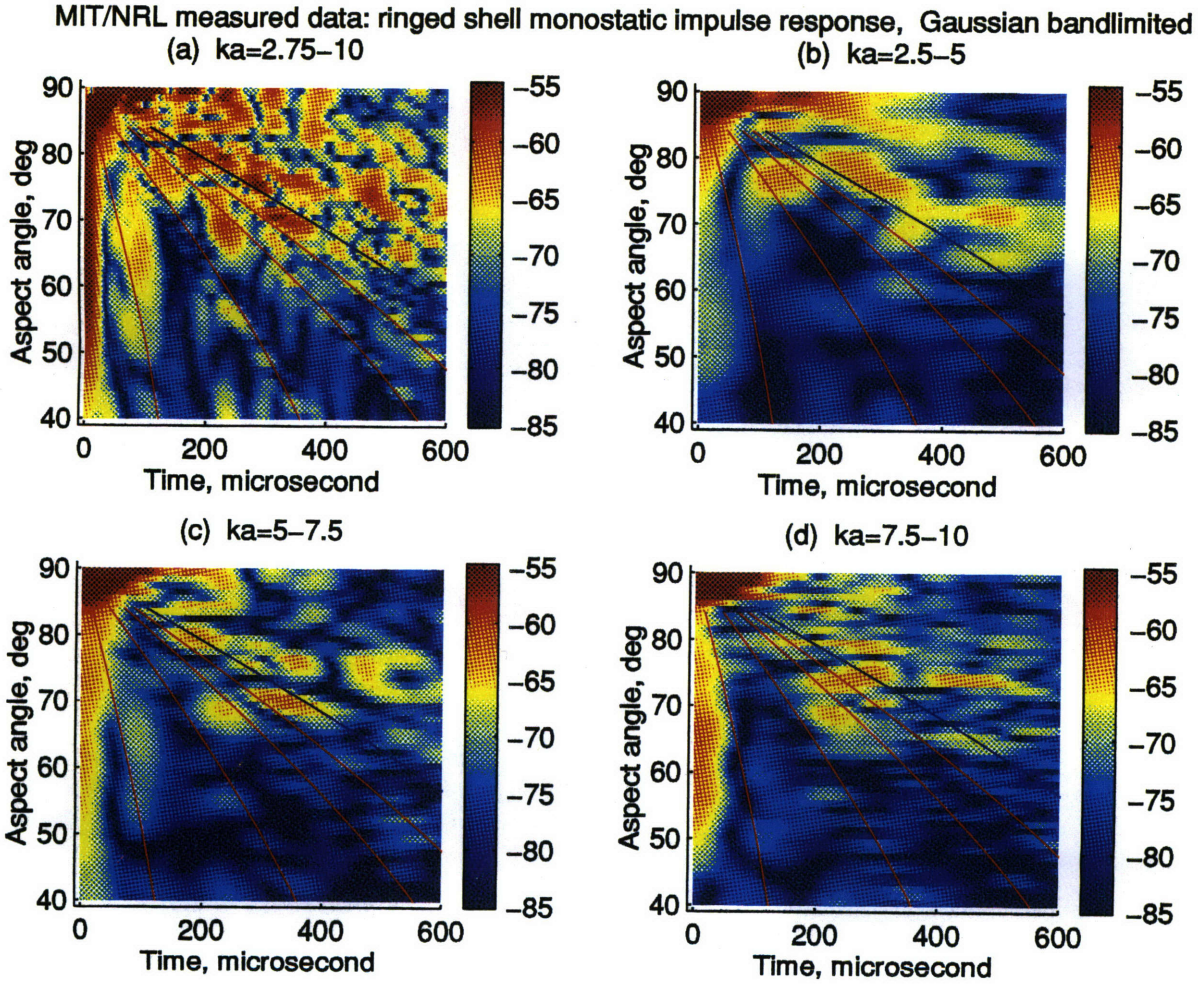

Figure 4-9: The MIT/NRL measured monostatic impulse response for the **ringed** shell, Gaussian bandlimited in (a) $2.75 < ka < 10$; (b) $2.5 < ka < 5$; (c)$5 < ka < 7.5$ and (d) $7.5 < ka < 10$. The black line indicates the predicted arrival of the direct scatter from the far endcap junction. The red lines indicate the predicted arrivals of the direct scatter from the four rings.

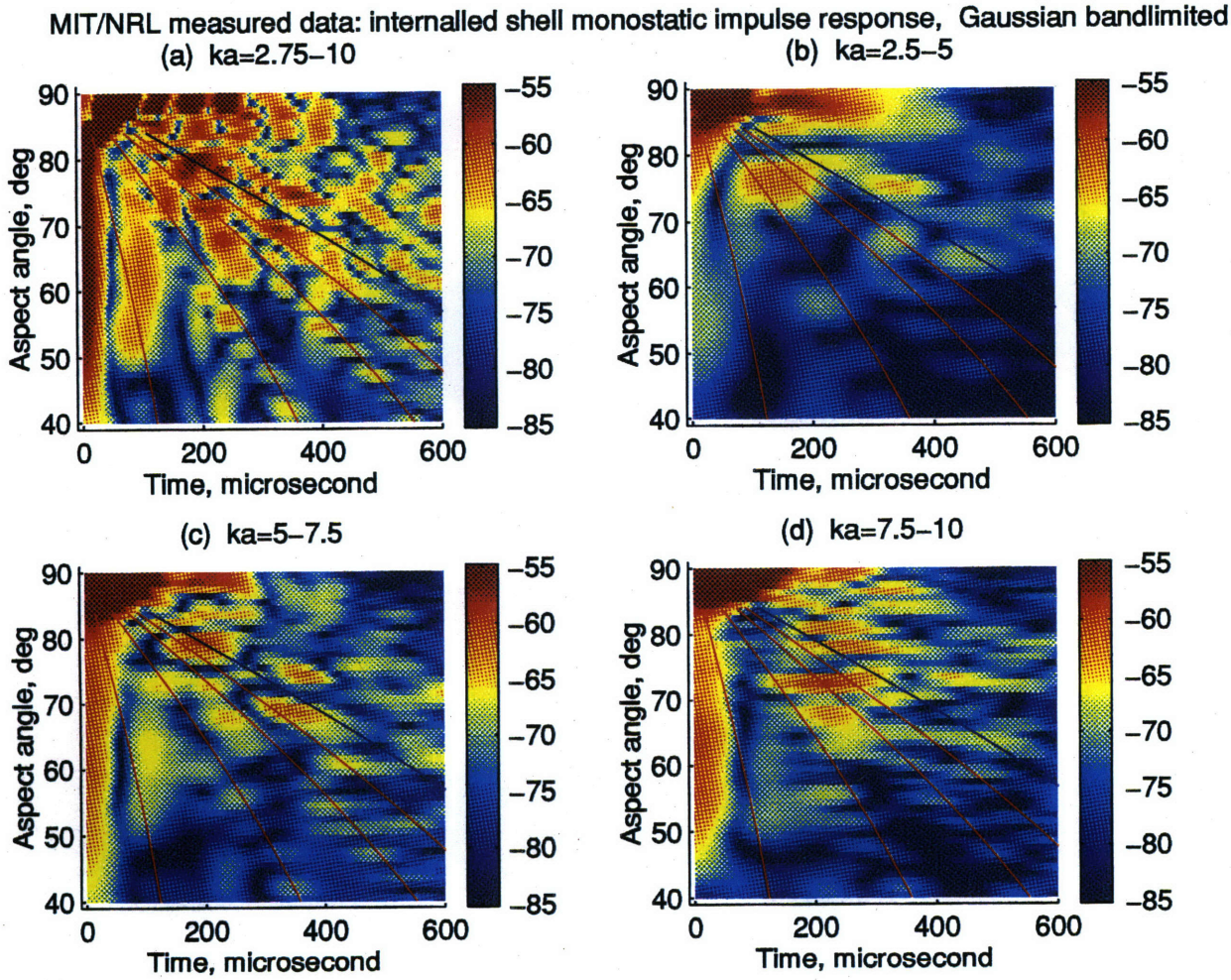

Figure 4-10: The MIT/NRL measured monostatic impulse response for the **internalled** shell, Gaussian bandlimited in (a) $2.75 < ka < 10$; (b) $2.5 < ka < 5$; (c)$5 < ka < 7.5$ and (d) $7.5 < ka < 10$. The black line indicates the predicted arrival of the direct scatter from the far endcap junction. The red lines indicate the predicted arrivals of the direct scatter from the four rings.

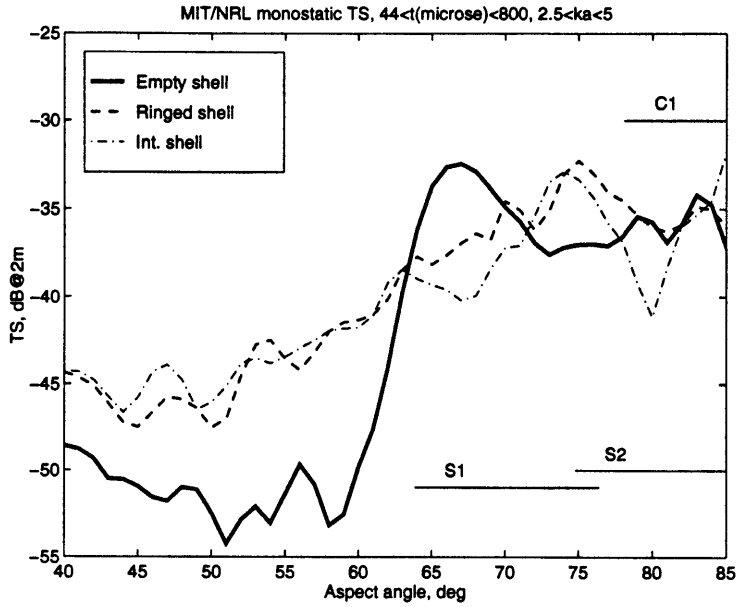

Figure 4-11: The MIT/NRL measured monostatic target strength for $44\,\mu s < t < 800\,\mu s$ and $2.5 < ka < 5$. The horizontal bars represent angular bands for the shear and compressional waves of different mode n, denoted by 'Sn' and 'Cn' respectively.

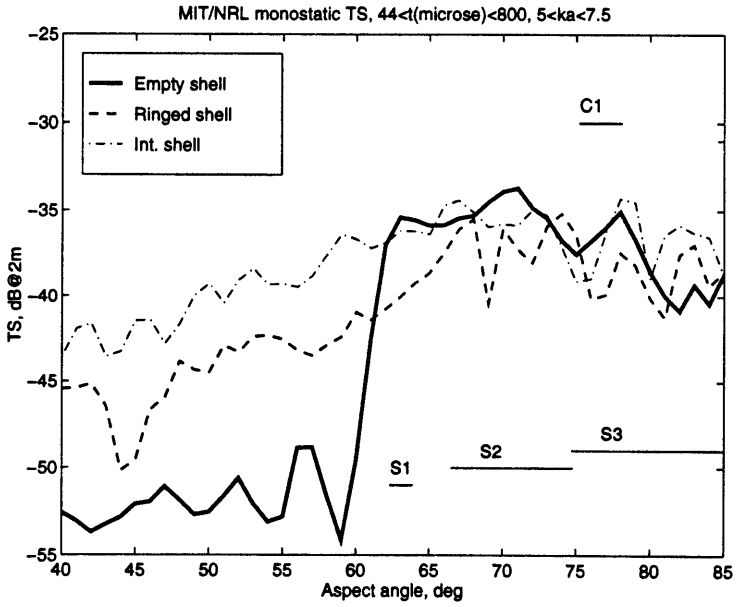

Figure 4-12: The MIT/NRL measured monostatic target strength for $44\,\mu s < t < 800\,\mu s$ and $5 < ka < 7.5$. The horizontal bars represent angular bands for the shear and compressional waves of different mode n, denoted by 'Sn' and 'Cn' respectively.

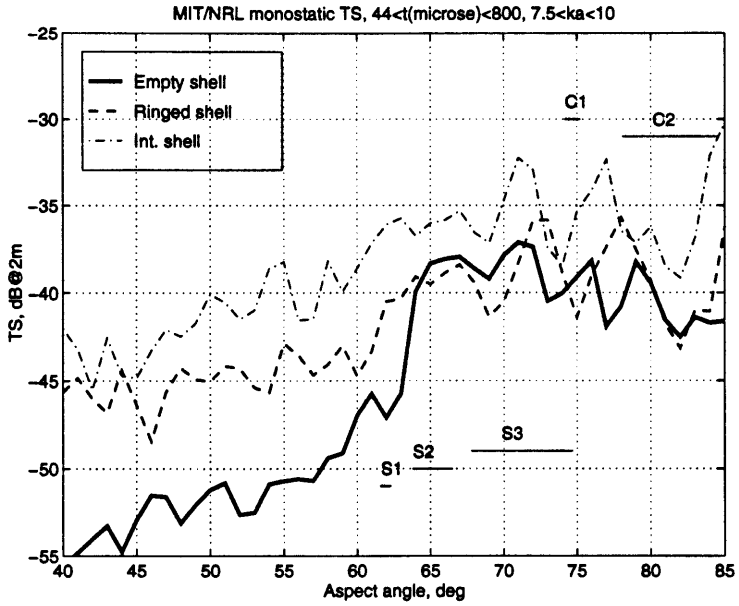

Figure 4-13: The MIT/NRL measured monostatic target strength for $44\,\mu s < t < 800\,\mu s$ and $7.5 < ka < 10$. The horizontal bars represent angular bands for the shear and compressional waves of different mode n, denoted by 'Sn' and 'Cn' respectively.

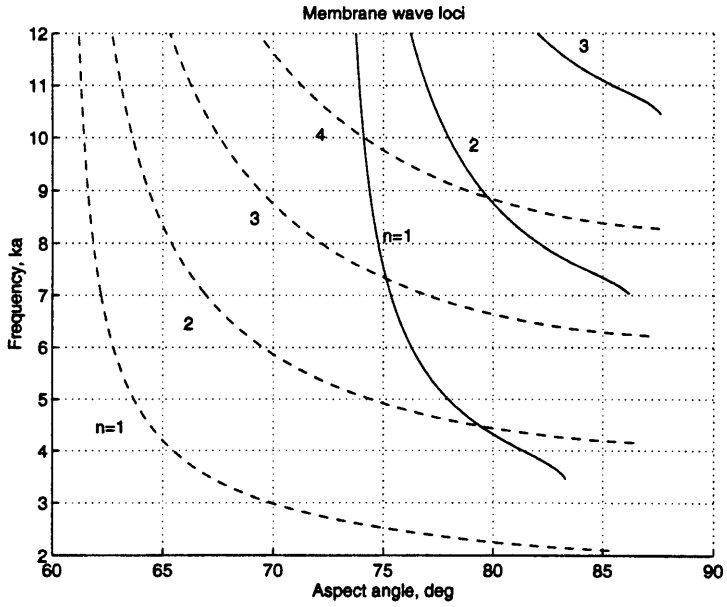

Figure 4-14: Trace matched shear (dash) and compressional (solid) wave loci for different mode n. From the theoretical calculation on the infinitely long cylindrical shell.

Examination of wave loci from the SARA-2D calculation

The SARA-2D calculation of the empty and the ringed shells provides shell velocities for each mode n. In the wavenumber domain, the membrane waves can be identified by their characteristic wave loci. By comparing the wave loci for the ringed shell with that for the empty shell and with that for the infinitely long shell from the theoretical calculation, I expect to see how the membrane wave speeds are changed by the rings, noting that the wavenumber is inversely proportional to the wave speed.

Fig. 4-15 displays the in-plane velocity in the $ka - k_x$ domain, for the empty shell and the ringed shell, under 75° sound incidence. The shear and compressional waves of modes $n = 1$ and $n = 2$ are clearly identified for the empty shell because the wave loci (more exactly, the finite strips due to spatial sampling over the finite shell) coincide with the loci from the infinitely long shell calculation, indicated by the red lines. The shear and compressional waves in the ringed shell can be similarly identified. For $ka > 5$, I observe that the center of the shear and compressional wave strips for the ringed shell is shifted towards larger axial wavenumber; for $ka < 5$, the wave loci are shifted towards smaller axial wavenumber. The increase of the axial wavenumber for $ka > 5$ indicates a decrease of the wave speed. For $ka < 5$, the decrease of the axial wavenumber is dramatic, indicating a dramatic increase of the wave speed. These trends agree with the measured data observed in the previous subsection. The understanding of this observation will be discussed shortly through a simulation study of a 1D bar system.

Further, I use the SARA-2D calculation to verify that the flexural wave speed is essentially unchanged for the ringed shell. I derive the flexural wave speed from the derivative of the unwrapped phase with respect to the axial distance, see Eq. 4.8. The flexural wave response along the ringed shell is obtained from the SARA-2D calculation using the wavenumber decomposition discussed in Sec.4.1.

$$c_x = \frac{\omega}{\partial \Phi / \partial x} \quad . \tag{4.8}$$

Fig. 4-16 displays the axial wave speed of the $n = 1$ flexural wave at 75° sound incidence for the ringed shell. The flexural wave speed for the ringed shell is less than

2% smaller than the infinitely long shell calculation.

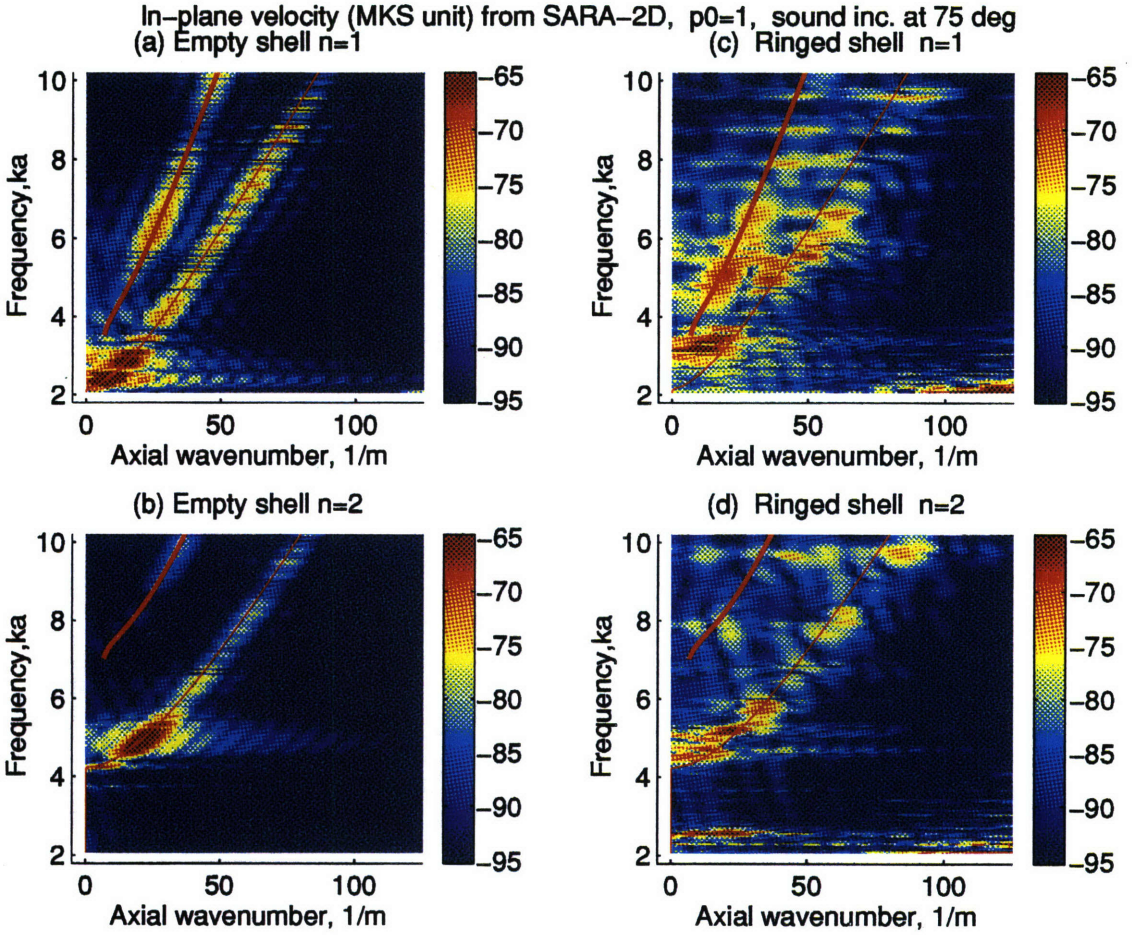

Figure 4-15: In-plane velocity in the $ka - k_x$ domain, from the SARA-2D calculation and the wave number decomposition. (a) empty shell, $n = 1$; (b) empty shell, $n = 2$; (c) ringed shell, $n = 1$ and (d) ringed shell, $n = 2$. The red lines are from the theoretical calculation of membrane wave loci on the infinitely long shell; thick line: compressional waves; thin line: shear waves.

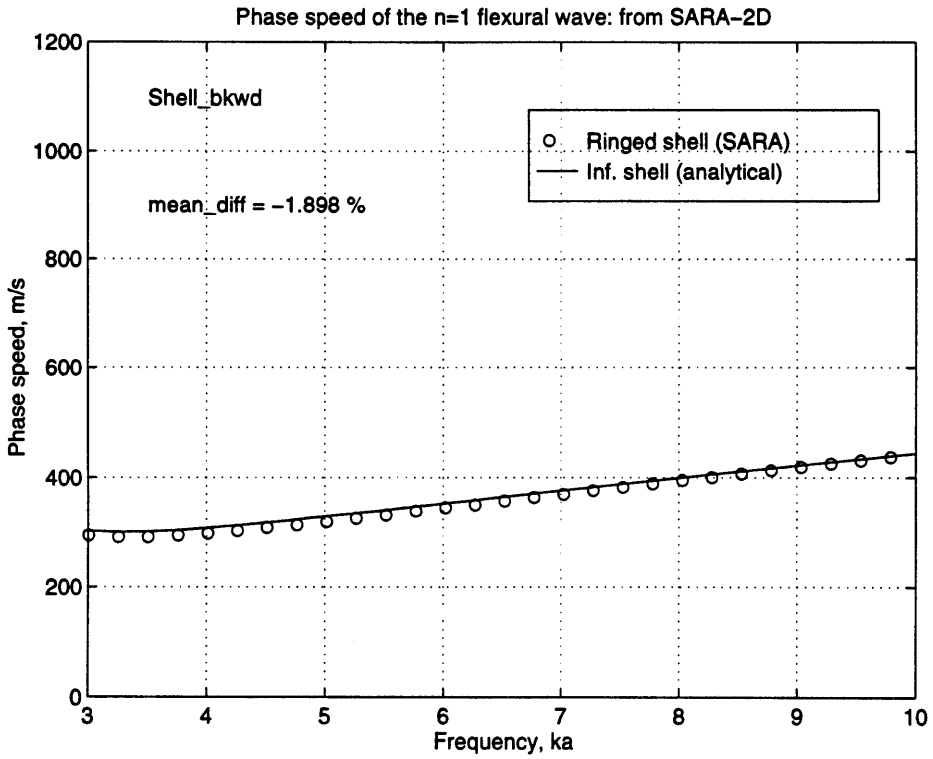

Figure 4-16: Axial phase speed of the $n = 1$ flexural wave. The circles represent the SARA-2D calculation on the ringed shell, where backward going flexural wave field is evaluated over the whole shell length. The solid line represents the analytical results of the infinitely long shell(without rings).

Understanding of the wave speed change

According to the observation of the measured data and the numerical results, the rings have a clear influence on the membrane wave speeds and the influence is frequency dependent. In order to understand the observation, I consider an elastic bar attached by four, randomly distributed, identical mass-spring systems, as shown in Fig. 4-17. Using the transfer matrix formulation (see App. E), I calculate the phase speed by measuring the slope of the propagation phase in the bar for many random realizations (20 used in this study) of the ring locations. Fig. 4-18 illustrates a phase slope from one of the realizations.

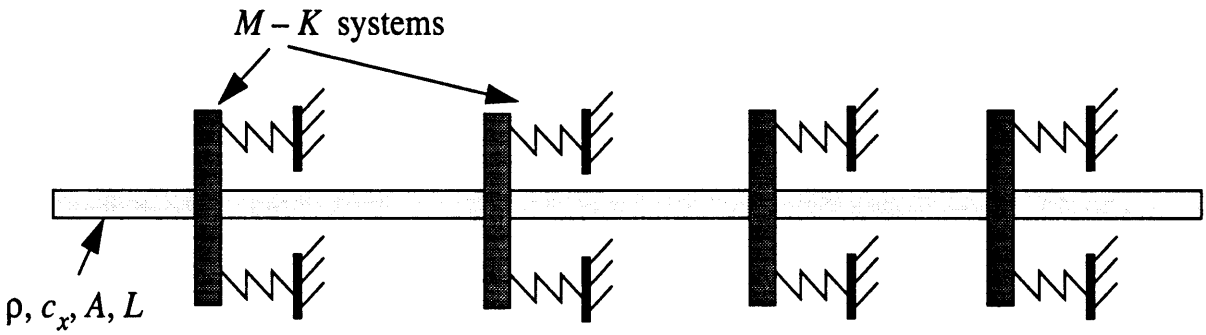

Figure 4-17: An elastic bar with 4 random distributed mass-spring subsystems.

In the simulation, the mass M is fixed such that the total mass of the $M - K$ subsystems equals the mass of the bar, $4M = \rho AL$, consistent with the ringed shell model configuration. Furthermore, the operating frequency is fixed so that the corresponding ratio of the axial wavelength (λ_x) to the average spacing (b) of the discontinuities in the bar is also fixed. The natural frequency of the $M - K$ systems, f_0, however, is allowed to vary. Fig. 4-19 plots the change of phase speed, relative to the wave speed in the bar, against the normalized frequency, f/f_0, for $\lambda_x/b = 0.65$. The rings can decrease the bar phase speed by approximately 10% above the resonance and increase the bar phase speed by approximately 15% below the resonance. In addition, this change in wave speed fluctuates with the standard deviation being 5-10 percentage points.

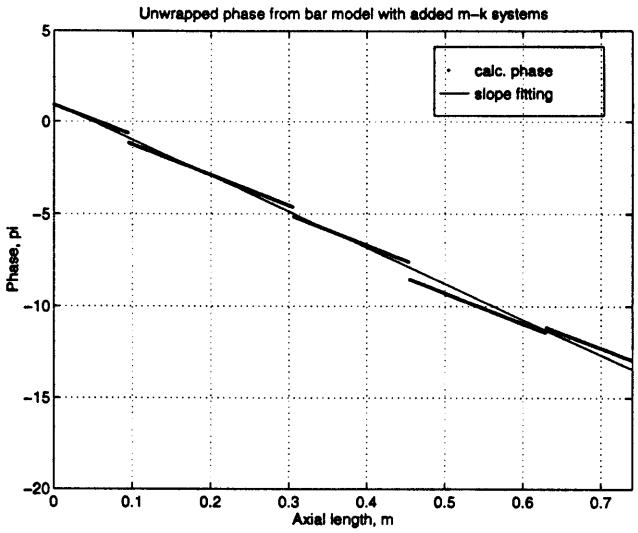

Figure 4-18: The modified wave speed is obtained by measuring the slope of the propagation phase.

Fig. 4-20 shows the relative wave speed change for $\lambda_x/b = 1.6$. Again, the rings can decrease the bar phase speed above the resonance and increase the bar phase speed below the resonance. In this case, both the mean and the standard deviation of the wave speed change are significantly larger than for the case of $\lambda_x/b = 0.65$ as shown in Fig. 4-19.

Fig. 4-21 shows the relative wave speed change for $\lambda_x/b = 0.16$. The same trend of the ring influence on wave speed is observed. For this small λ_x case, the mean and the standard deviation of the wave speed change are only a few percent (except near the natural frequency), significantly smaller than for the case of $\lambda_x/b = 0.65$ as shown in Fig. 4-19.

Thus, the wave speed change due to the attachment of the $M - K$ subsystems depends on: (1) the resonance of the $M - K$ systems; (2) the ratio of the axial wavelength to the average spacing of the subsystems. Above the resonance, the $M-K$ subsystems behave as masses and decrease the wave speed. Below the resonance, the $M - K$ subsystems behave as stiffeners and increase the wave speed. The wave speed change is significant for $O(\lambda_x/b) \sim 1$ or $O(\lambda_x/b) < 1$, but not significant for $O(\lambda_x/b) \ll 1$.

Based on the simulation and the analysis, the ring effect on the the membrane

wave speeds can be understood in the following way. The increase of the $n = 1$ shear wave speed above $ka = 5$ and the decrease of the wave speed below $ka = 5$ are caused by the resonance of the rings, which is near $ka = 5$. Taking $ka = 5$ as the resonance frequency for the $n = 1$ shear wave in the bar-mass simulation model, I can make an estimate of the modified dispersion locus for the $n = 1$ shear wave. Similarly, I can obtain the modified loci for shear waves of other mode n and for compressional waves as well. Fig. 4-23 plots the modified wave loci for the $n = 1$ and $n = 2$ membrane waves on the background of Fig. 4-15. Again, I use 20 realizations of the ring locations for each frequency. In Fig. 4-23, the mean wave loci, smoothed by curvefitting, are indicated by the black solid thick lines. The two thin black lines indicate the standard deviation of the axial wavenumber relative to the mean. The modified wave loci and their associated 'bandwidth' seem to match the numerical calculation well.

The absolute value of the standard deviation of the mean wave loci in Fig. 4-23 does not seem to change significantly. Relative to the mean, however, it can change from approximately 10% at the higher frequency band to approximately 50% near the cutoffs. In other words, the standard deviation is small for large axial wavenumber, but large for small axial wavenumber. This trend is consistent with the observation of Fig. 4-19, Fig. 4-20 and Fig. 4-21 by noting that the axial wavenumber is inversely proportional to the axial wavelength, or to the normalized wavelength λ_x/b.

The approximated ratio λ_x/b for the ringed shell is shown in Fig. 4-22 for mode $n = 1$, 2 and 3, where λ_x is obtained from the calculation on the infinitely long cylindrical shell and b is the averaged bay spacing for the ringed shell model. The ratio for the flexural waves is typically 0.1 or smaller, comparable to the case in Fig. 4-21. The ratio for the membrane waves is on the order of 1 for most frequencies, comparable to the case shown in Fig. 4-20 and in Fig. 4-21.

To summarize, the rings have considerable effect on the membrane wave speeds, but not on the flexural wave speed. This effect can be understood in a simple way. That is, the rings modify both the amplitude and the phase of the waves in the shell. If the phase shift is positive, the wave speed is increased, and vice versa. The larger the ring spacing (or the smaller the wavelength), the less significant the modification in wave speed. In this study, the ring spacing is large for the flexural wave, the speed

of which is almost unaffected by the rings; the bay spacing is small for the membrane waves, the speeds of which are modified considerably.

The change of the wave speeds might lead to the change of the trace matching region. However, the cutoff angle for the $n = 1$ shear wave turns out to be insignificantly lower than without the rings. The angle is shifted from 61.3° for the infinitely long shell to 59.7° for the ringed shell and to 58.7° for the internalled shell, using the $n = 1$ shear wave result in Table 4.1 for the last two shells. Thus, I continue to use $60° < \theta < 120°$ as the definition of the membrane wave region in this thesis.

The change of the wave speeds have other effects on the prediction model in this thesis. First, the change of the membrane wave loci can directly change the frequencies at which the trace matching occurs. Second, the wave speed change can affect sound excitation of the shell as well. As a result, the infinitely long shell excitation model discussed in Sec.2.3. should be modified through the consideration of a 'magic' infinitely long shell with its wave speed varying with frequency and mode n. For $ka > 5$, both shear and compressional wave speeds decrease, which effectively increases the shell bulk modulus. For $ka < 5$, the $n = 1$ shear wave dominates the scattering, and its wave speed is increased. The magic shell therefore has larger bulk modulus. The scattering prediction using the modified wave speeds will be shown in Sec.5.1.4 and Sec.5.2.2.

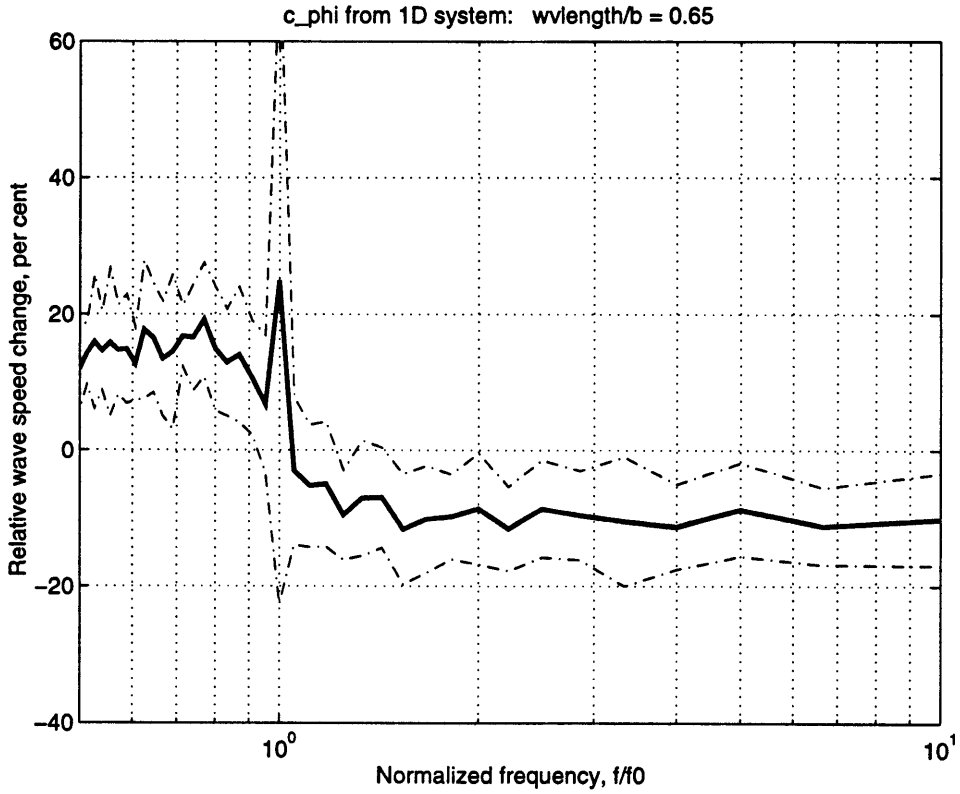

Figure 4-19: Wave speed change (relative to the uniform bar) for the 1D bar system with M-K subsystems. The operating frequency is fixed, so that the ratio of the axial wavelength to the average bay spacing remains to be a constant, 0.65. The natural frequency of the $M-K$ systems is allowed to vary. At each frequency, 20 random realizations are used for the locations of the $M-K$ subsystems. The solid line represents the mean wave speed change; the dashed lines represent the standard variation of the mean.

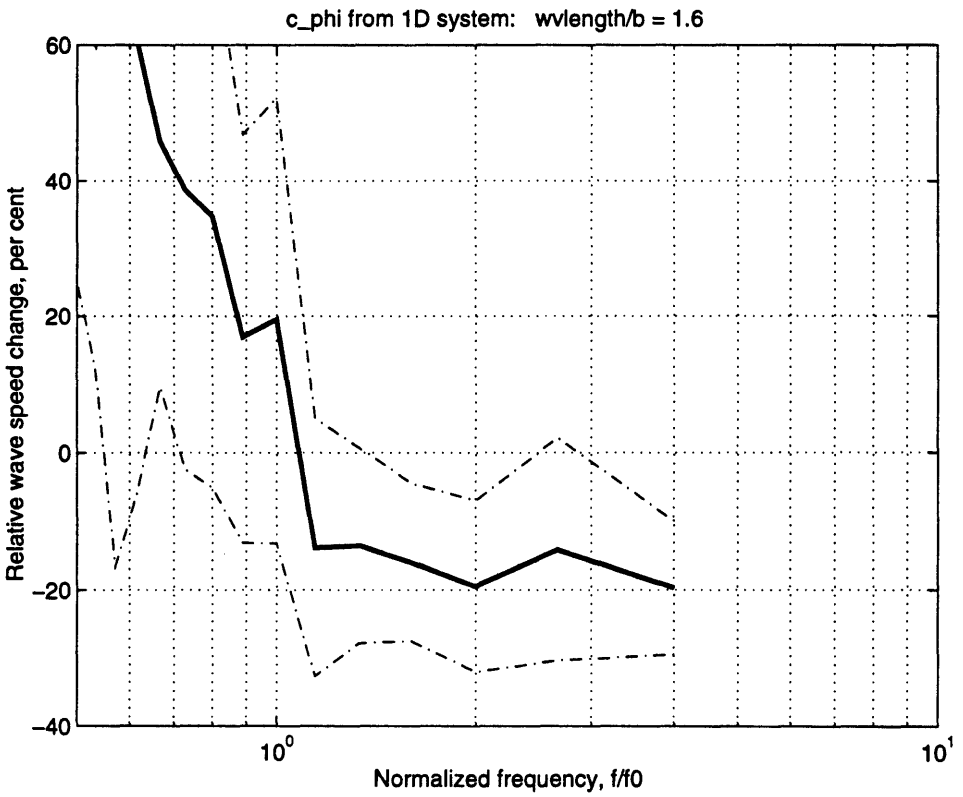

Figure 4-20: Wave speed change (relative to the uniform bar) for the 1D bar system with $M - K$ subsystems. The operating frequency is fixed, so that the ratio of the axial wavelength to the average bay spacing remains to be a constant, 1.63. The natural frequency of the $M - K$ systems is allowed to vary. At each frequency, 20 random realizations are used for the locations of the $M - K$ subsystems. The solid line represents the mean wave speed change; the dashed lines represent the standard variation of the mean.

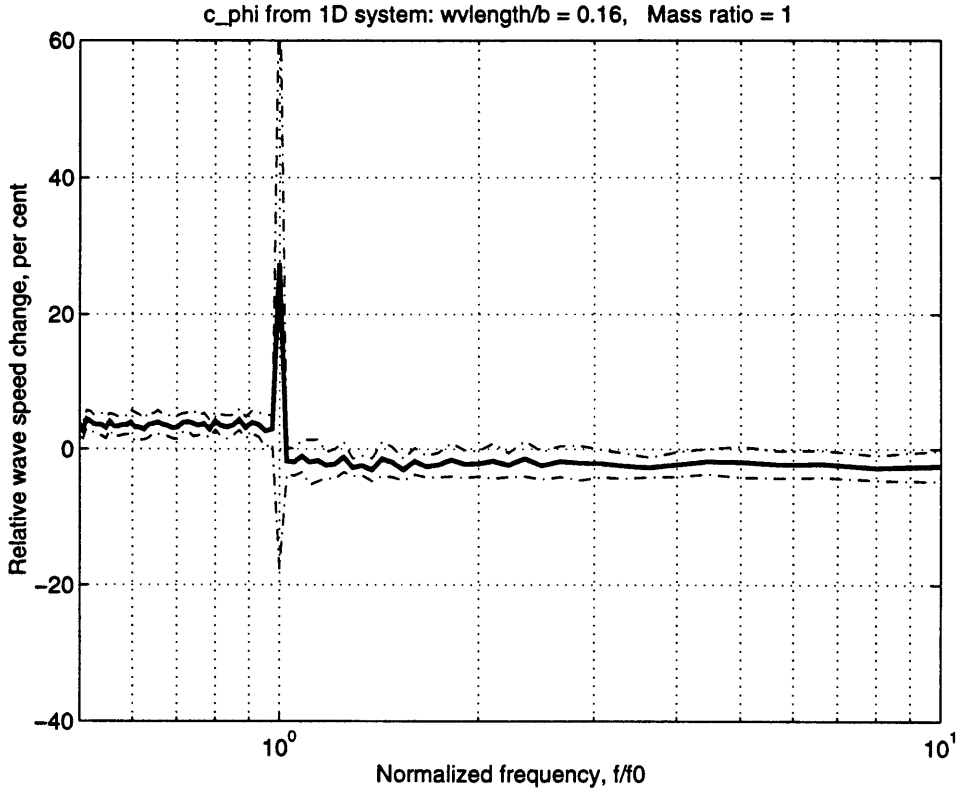

Figure 4-21: Wave speed change (relative to the uniform bar) for the 1D bar system with $M-K$ subsystems. The operating frequency is fixed, so that the ratio of the axial wavelength to the average bay spacing remains to be a constant, 0.16. The natural frequency of the $M-K$ systems is allowed to vary. At each frequency, 20 random realizations are used for the locations of the $M-K$ subsystems. The solid line represents the mean wave speed change; the dashed lines represent the standard variation of the mean.

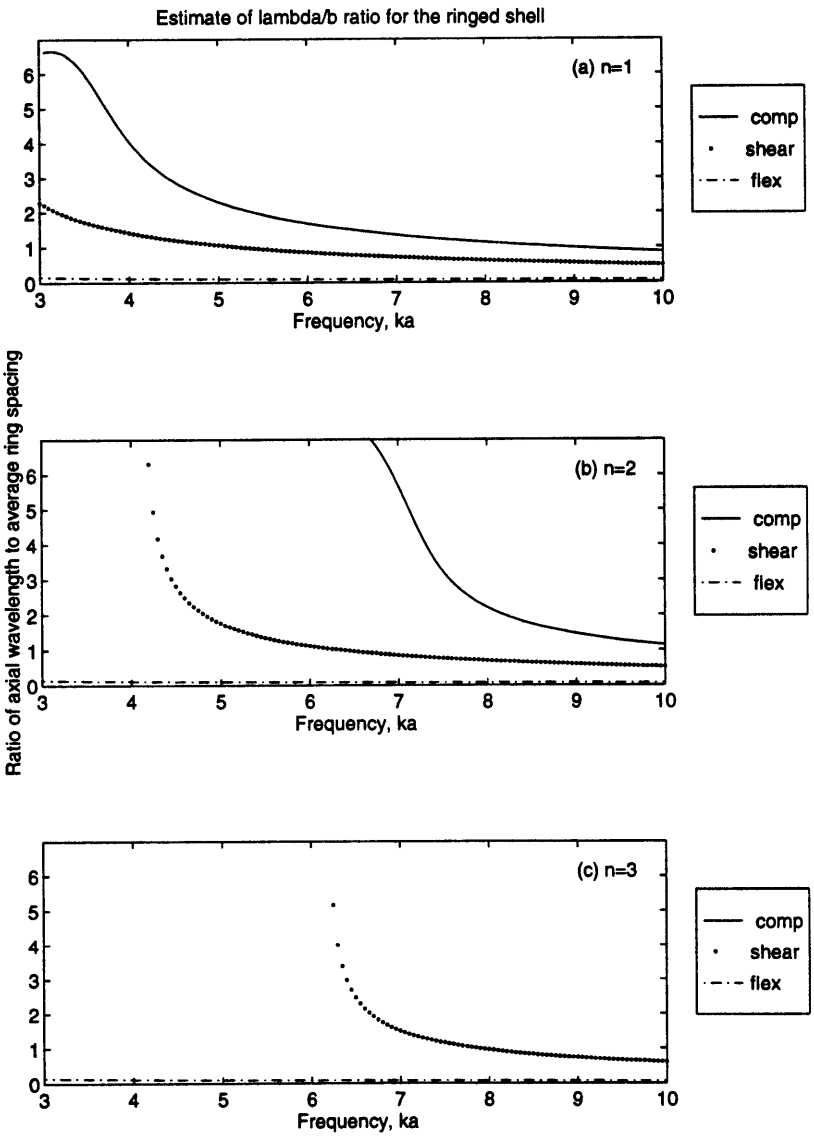

Figure 4-22: The axial wavelength for the infinitely long cylindrical shell, normalized by the average bay spacing for the ringed shell.

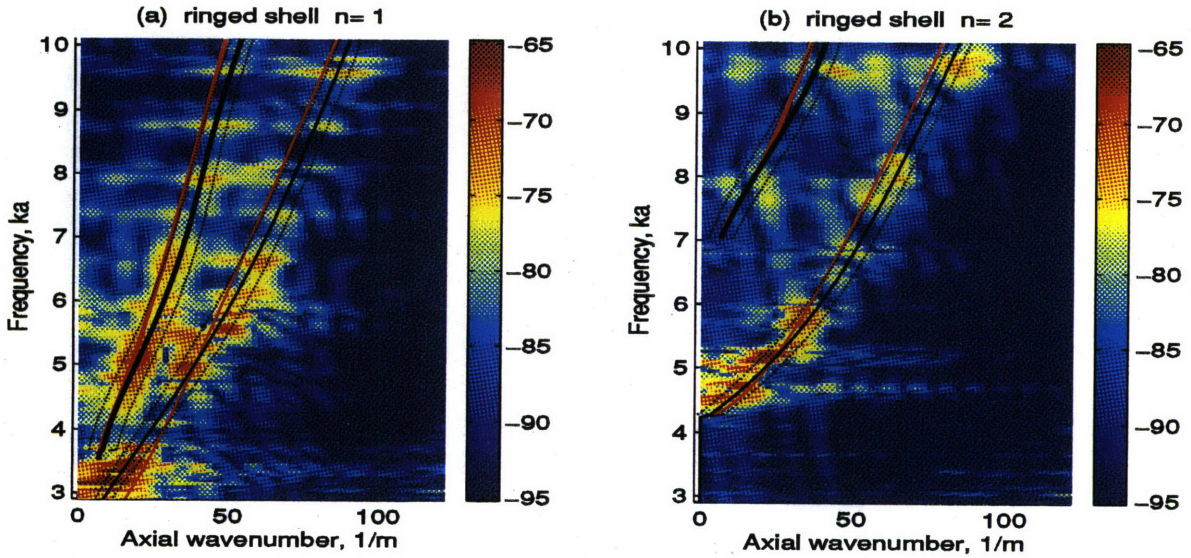

Figure 4-23: Modified wave loci (black lines) from the simulation on the 1D bar system. The thick black lines represent the mean of the modified wave loci and the thin black lines represent the standard deviation of the mean. (a) $n = 1$; (b) $n = 2$. The background and the red lines are identical to (c) and (d) of Fig. 4-15.

Initial test of phase field reconstruction

To see how the radiation model works with the wave speed approximation using the infinitely long shell results, I reconstruct the complex wave response in the shell by using Eq. 4.7. The radiation from the elastic waves is then summed, using Eq. 4.5 and Eq. 4.6, over the three wave types including both forward and backward going waves, as well as over circumferential mode n. All the summation is done incoherently by assigning random phase to each component, such as in Eq. 4.7. The reason for incoherent addition is multiple scattering and wave conversion in the ringed shell. It is true that the initial trace matching might create some coherence among waves of different type and mode n, but this coherence quickly diminishes because the sound power injected into each mode n is scattered and exchanged among all the elastic waves due to coupling at the shell discontinuities. Along with redistribution of the power among the elastic waves, the phase of the waves are likely to become unknown and is taken to be random.

Fig. 4-24 displays monostatic target strength of the ringed shell at 75° incidence against frequency ka, using infinitely long shell wave speeds without the modification by the rings. The result is compared with the direct SARA-2D scattering calculation. The mean decibel difference between the two results is labeled in the figure. The radiation model result is 1.6 dB smaller than the direct SARA-2D calculation.

Similarly, I use the wave phase speeds modified by the influence of the rings to calculate sound radiation. I find that the radiation is approximately 1.3 dB smaller than the direct SARA-2D results, where I use the mean modified axial membrane wavenumber shown in Fig. 4-23.

Fig. 4-25 displays bistatic target strength of the ringed shell at 75° incidence against observation angle, using infinitely long shell wave speeds without modification by the rings. The result is also compared with the direct SARA-2D scattering calculation. The mean decibel difference between the two results is labeled in the figure. The target strength from the radiation model, averaged over angular region $60° < \theta < 85°$, is 1.2 dB smaller than the direct SARA-2D calculation.

Therefore, I conclude that the radiation model is quite acceptable even if only the magnitude of the surface pressure and radial velocity is given. Moreover, the infinitely

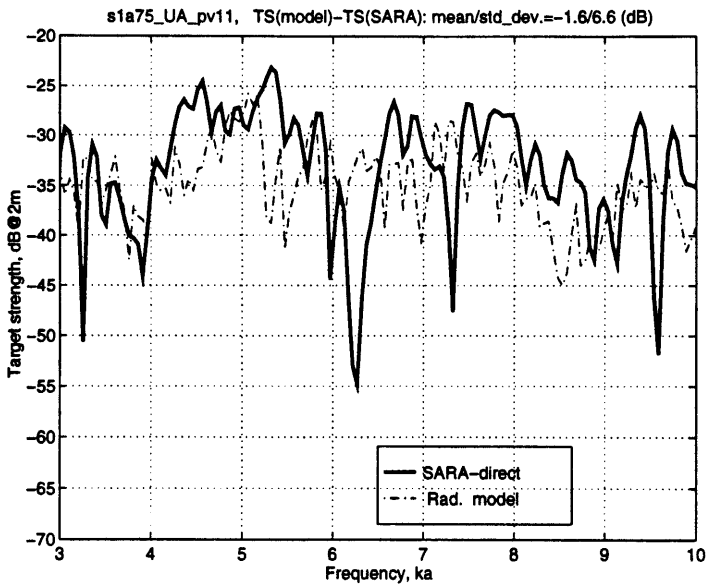

Figure 4-24: Monostatic target strength of the ringed shell from radiation model (thin line) and from SARA-2D (thick line). Sound incidence is at 75° and the receiver is at 2 m away from the shell center. Both pressure and velocity terms in Eq. 4.5 are considered.

long shell wave speed approximation is good enough to reconstruct the phase field.

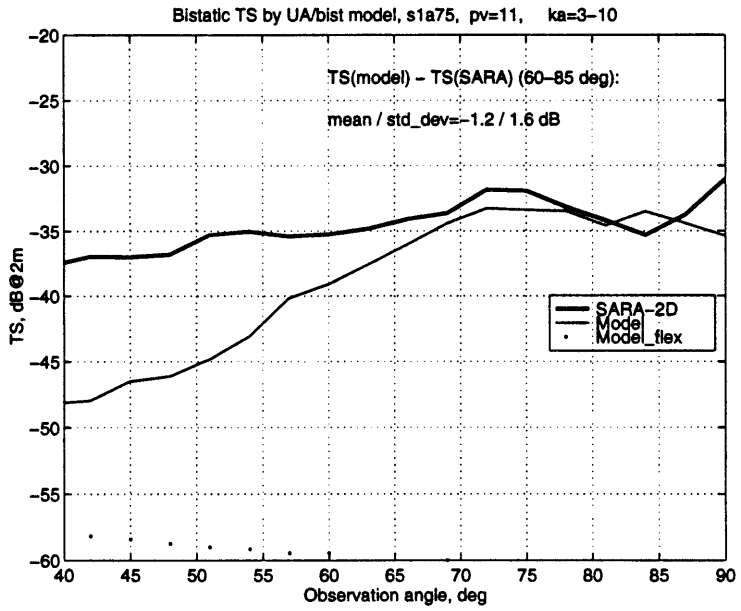

Figure 4-25: Bistatic target strength of the ringed shell from radiation model (thin line) and from SARA-2D (thick line). Sound incidence is at 75° and the receiver is at 2 m away from the shell center. Both pressure and velocity terms in Eq. 4.5 are considered.

4.2.2 Estimate of the surface pressure

The kernel of Eq. 4.5 includes both the pressure term and the radial velocity term. The wave power calculation in Sec.2.3, however, gives only the wave velocity, without the surface pressure. In this subsection, I will first check if the pressure term for the ringed shell radiation can be ignored at all. If not, I will find an approximation for the surface pressure based on shell radial velocity.

First, I keep only the surface velocity term and calculate the ringed shell radiation for 75° incidence, shown in Fig. 4-26. Second, I keep only the pressure term, and display the radiation in Fig. 4-27.

Compared with the results at the same incidence angle using both terms, shown in Fig. 4-24, the absence of the surface pressure causes the sound radiation level to decrease by 2.3 dB. On the other hand, if only the surface pressure term is kept, the sound radiation is decreased by 4.5 dB. Thus the surface pressure can not be ignored and has to be estimated.

For given radial velocity, the surface pressure can be derived from the momentum equation which states that the acceleration of the fluid on structure surface times the fluid mass density equals the pressure gradient, see Eq. 4.3. In the wavenumber domain, the spatial derivative of the pressure is a product of the radial wavenumber k_r and the pressure, which is a function of k_r. The momentum equation can then be rewritten as

$$k_r \hat{p}(k_r) = \rho\omega\hat{v}_r \ , \tag{4.9}$$

or further rewritten in the form of impedance

$$Z = \frac{\hat{p}}{\hat{v}_r} = \frac{\rho\omega}{k_r} \ . \tag{4.10}$$

The radial wavenumber k_r can be expressed in Cartesian coordinates as

$$k_r = \sqrt{k^2 - k_x^2} \ , \tag{4.11}$$

where $k = \omega/c$ is the sound wavenumber in the fluid and k_x is the axial wavenumber. k_x is generally a function of frequency, mode n and wave type, and has to be solved from the dispersion equation of the coupled fluid-shell system. However, the property of such a coupled system depends on k_r, which in turn depends on k_x. Thus, k_x can not be expressed explicitly and has to be solved numerically. As an approximation, however, I use k_x from the infinitely long shell calculation. k_r is then given by Eq. 4.11 directly. Under such an approximation, Eq. 4.10 can be rewritten in the form of normalized impedance, in Eq. 4.12, where I express the dependence on mode and wave type by subnote n and e respectively, and use the characteristic acoustic impedance ρc in the fluid as the normalization factor.

$$\begin{aligned} \frac{Z_{ne}}{\rho c} &\approx \frac{1}{\sqrt{1 - {k_{x_{ne}}}^2/k^2}} = \frac{1}{\sqrt{1 - {c_{x_{ne}}}^2/c^2}} , \qquad k_x < k , \\ &\approx \frac{1}{i\sqrt{{k_{x_{ne}}}^2/k^2 - 1}} , \qquad k_x > k . \end{aligned} \tag{4.12}$$

For membrane waves, the axial wavenumber is always smaller than the sound wavenumber in fluid, $k_x < k$. For the flexural waves within the frequency range of this study, however, the axial wavenumber is larger than the sound wavenumber in the fluid, $k_x > k$.

To check whether the above approximation is good enough, I calculate the normalized impedance using the decomposed surface pressure and radial velocity from the SARA-2D results for the ringed shell, and then compare it with the result from Eq 4.12. Fig. 4-28 shows the comparison for the three wave types of mode $n = 1$. The two sets of impedance ratios differ by only a few percent for membrane waves; for flexural waves, the two results are almost identical. The pressure approximation is thus acceptable.

The radiation result based on the estimated pressure also shows good agreement with the direct SARA-2D calculation. I estimate the surface pressure using the given shell radial velocity from the SARA-2D results, and then compute the sound radiation using Eq. 4.5 and Eq. 4.6. The radiation result is less than 1 dB lower than the direct

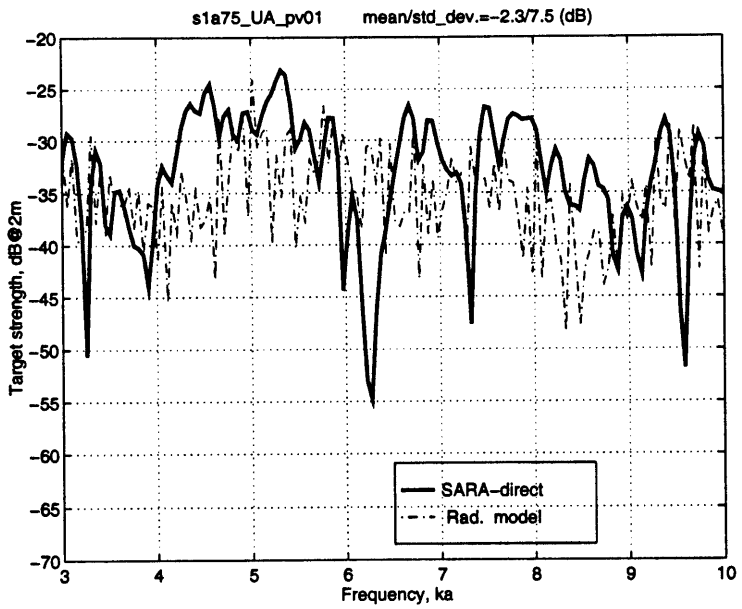

Figure 4-26: Monostatic target strength of the ringed shell from radiation model (thin line) and from SARA-2D (thick line). Sound incidence is at 75° and the receiver is at 2 m away from the shell center. Only the velocity term in Eq. 4.5 is considered.

SARA-2D calculation, as shown in Fig. 4-29.

In conclusion, the missing surface pressure can be retrieved approximately by using the impedance relation in Eq. 4.12. The radiation model can thus still be applied even if only the shell radial velocity is available, a useful conclusion since this thesis aims to test elastic wave equipartition from which only velocity is obtained.

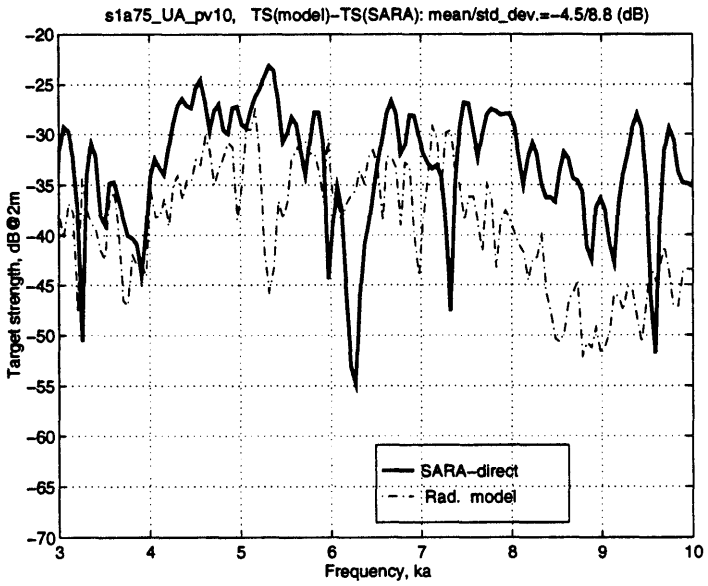

Figure 4-27: Monostatic target strength of the ringed shell from radiation model (thin line) and from SARA-2D (thick line). Sound incidence is at 75° and the receiver is at 2 m away from the shell center. Only the pressure term in Eq. 4.5 is considered.

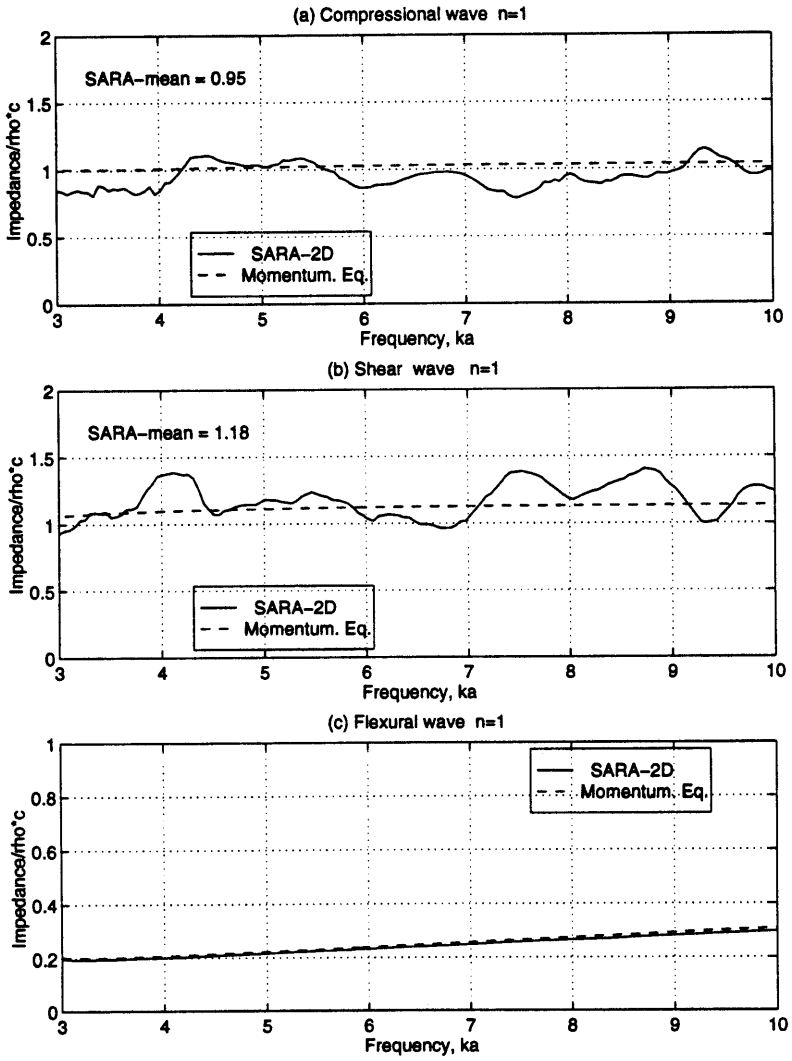

Figure 4-28: The ratio of ringed shell surface pressure to radial velocity for the n=1 mode. (a) compressional waves; (b) shear waves; (c) flexural waves. Solid line is from SARA-2D calculation and dashed line is from momentum equation formulation in Eq 4.12 for (a) and (b) and Eq 4.12 for (c).

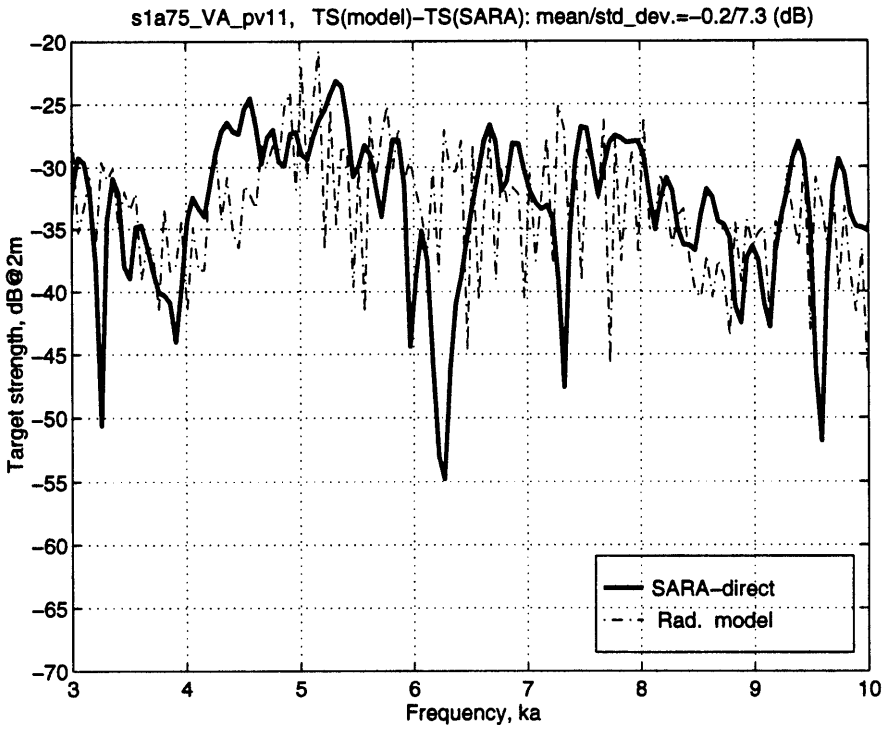

Figure 4-29: Monostatic target strength of the ringed shell from radiation model (thin solid-dot line) and from SARA-2D (thick solid line). Sound incidence is at 75° and the receiver is 2 m away from the shell center. The pressure term is estimated through Eq. 4.12 while decomposed radial velocity is extracted from the SARA-2D calculation.

4.2.3 Estimate of the radial velocity

The wave power calculation in Sec.2.3. is capable of computing the total velocity, but not the radial velocity directly. Because the radiation model requires radial velocity as input, the radial velocity component must be estimated. The ratio of radial velocity to total velocity can be derived conveniently for infinitely long shells, using the formulation in App. A. This subsection studies the ratio for the ringed shell using the SARA-2D calculation.

In particular, the total velocity magnitude of each wave type can be derived from elastic wave power,

$$\hat{v}_{ne} = \sqrt{\frac{\mathcal{W}_n}{2\pi a h \rho \, c_{g_{ne}}}} \ , \tag{4.13}$$

where subnote e represents elastic wave type. The axial wave group velocity $c_{g_{ne}}$ is estimated from the infinite shell calculation. This velocity formulation has considered waves of opposite helical angles in the shell.

I denote the ratio of radial velocity to total velocity by β, so that

$$\hat{v}_{rne} = \hat{v}_{ne}\beta_{ne} \ , \tag{4.14}$$

where $\hat{v}_{ne}$ is the total velocity summed over axial, circumferential and radial directions, as used in Eq. 4.13. The ratio, β_{ne}, is generally a function of mode n, elastic wave type 'e' and frequency. For the infinitely long shell, it can be theoretically calculated using the formulation in App. A. Fig. 4-30 displays the ratio for different circumferential modes and wave types. The ratio is essentially 1 for flexural waves while much smaller than 1 for membrane waves, particularly so above the ring frequency $ka = 3.5$ where the shell behaves more like a flat plate. This result is consistent with the in-plane nature of membrane waves and the out-of-plane nature of flexural waves.

For finite complex shells, the ratio β is generally difficult to analyze rigorously. The shell discontinuities such as the endcap truncations or the ring stiffeners might

modify β in a rather complicated way. One can, however, study the influence of shell discontinuities on β through numerical methods. To investigate the influence of the rings, the shell velocities from the SARA-2D calculation in axial, circumferential and radial directions are decomposed into each elastic wave type and each mode n. The results are compared with those for the infinitely long shell, in Fig. 4-31 for mode $n = 1$ and in Fig. 4-32 for $n = 2$. For membrane waves, the rings increase the radial motion in most frequency bands. When averaged over all frequencies, the increase is below 20% for compressional waves, and approximately $15 - 40\%$ for shear waves. Similar calculations are performed for the empty shell, shown in Fig. 4-33. For the empty shell, the ratio for the shear wave is almost the same as that for the infinite shell. This result is not surprising since the endcaps should not modify elastic wave behavior seriously in the middle portions of the empty shell.

Unlike the membrane waves case, the velocity ratio for the flexural wave is not modified by the rings. Fig. 4-34 compares the ratios for the finite ringed shell with the calculation of the infinitely long shell. The two ratio curves are identical. The flexural wave motion is predominantly radial, as seen from the figure. The slight in-plane motion of the flexural wave is not evident in this figure.

Based on the above analysis, I conclude that the infinitely long shell results can be used as an approximation. For accurate scattering prediction, however, the corrections should be made. In the case of four rings, the ratio β should be adjusted to be approximately 20% higher for the shear wave and 40% higher for the compressional waves. I will use the corrections for the scattering prediction in Chap.5.

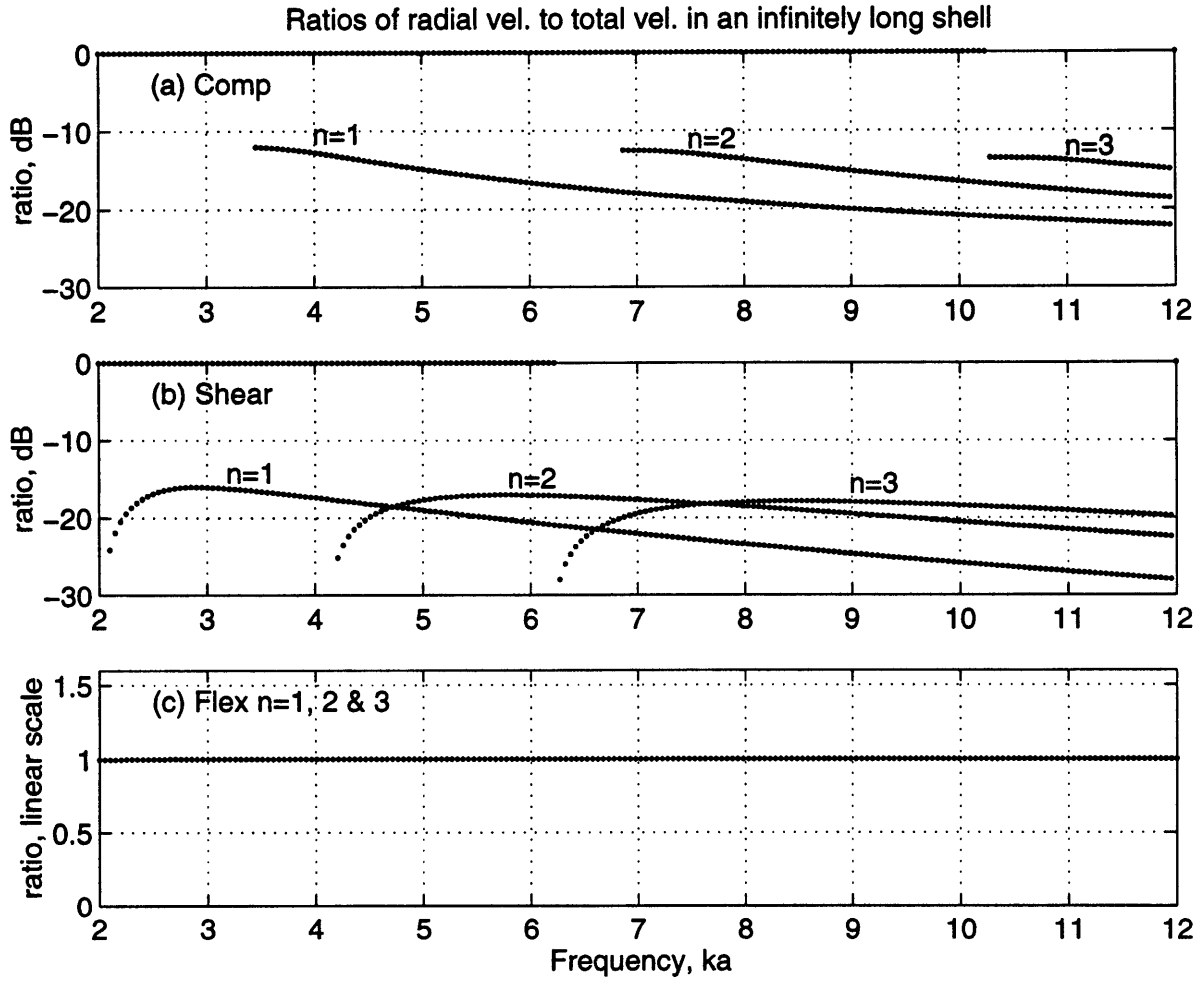

Figure 4-30: The ratios of radial velocity to total velocity in an uniform infinitely long cylindrical shell with fluid loading. (a) compressional waves. (b) shear waves. (c) flexural waves.

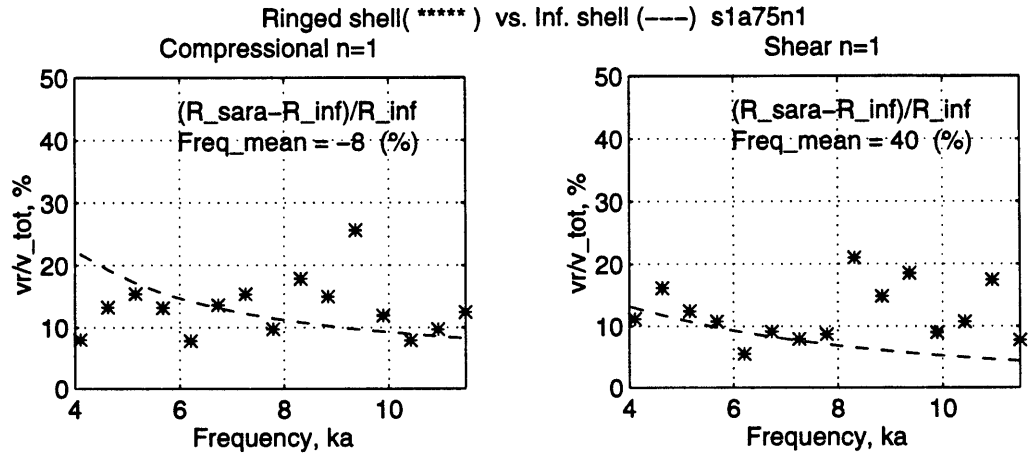

Figure 4-31: The ratios of radial velocity to total velocity, $n = 1$, for the ringed shell under sound incidence at 75°. 'Freq-mean' represents the relative difference of the ratio averaged over the frequency band, in percentage. Negative means the infinitely long shell ratio is larger.

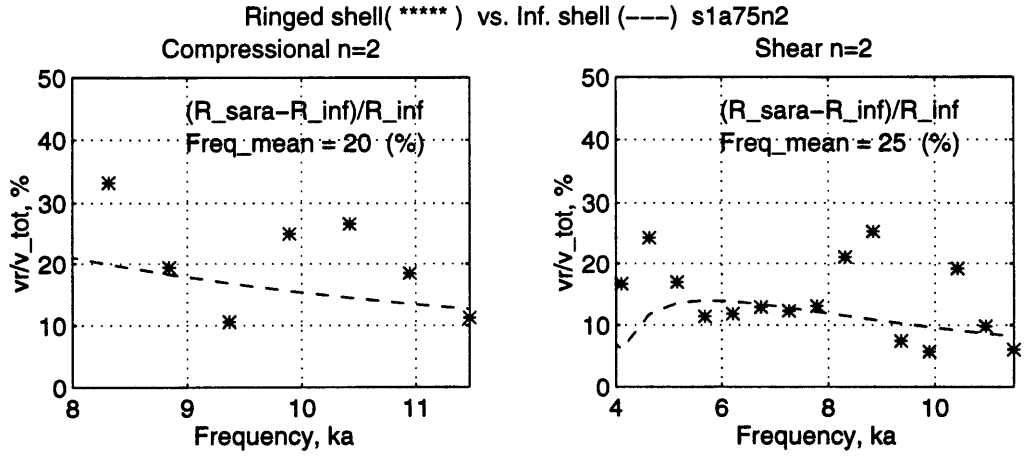

Figure 4-32: The ratios of radial velocity to total velocity, $n = 2$, for the ringed shell under sound incidence at 75°. 'Freq-mean' represents the relative difference of the ratio averaged over the frequency band, in percentage. Negative means the infinitely long shell ratio is larger.

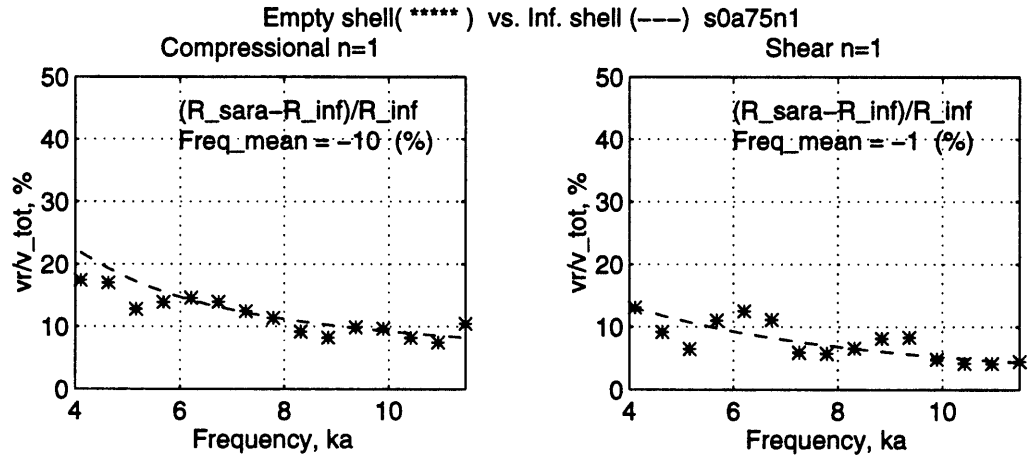

Figure 4-33: The ratios of radial velocity to total velocity, $n = 1$, for the empty shell under sound incidence at 75° 'Freq-mean' represents the relative difference of the ratio averaged over the frequency band, in percentage. Negative means the infinitely long shell ratio is larger.

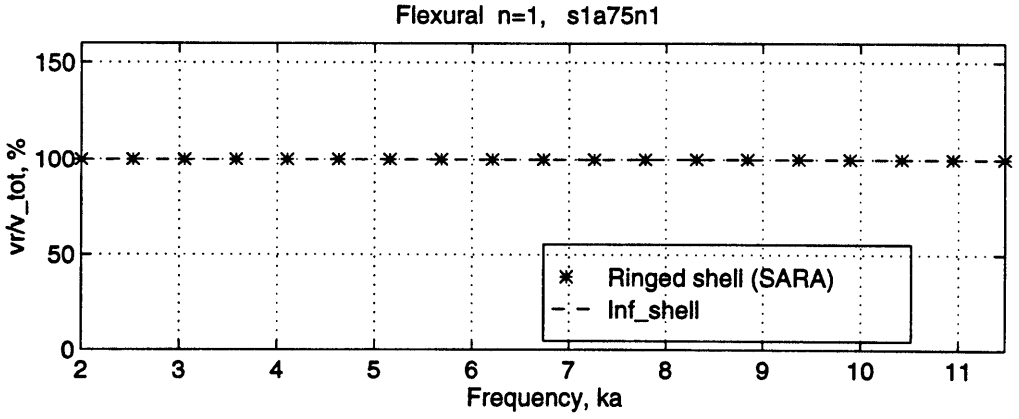

Figure 4-34: The ratios of the radial velocity to the total velocity of the flexural waves, $n = 1$, or ringed shell under sound incidence at 75°.

4.3 Summary

In this chapter, I formulate and test a radiation model from a finite cylindrical shell without endcaps, by using Green's theorem. The radiation model seems to work well as long as the observation point is in the membrane wave region $60° < \theta < 120°$. Within the region, the radiation model result differs from the direct SARA-2D calculation by less than 2 dB. In addition, the flexural wave radiation is shown to be at least 10 dB lower than the total radiation. Below 60°, the radiation model performs poorly, possibly due to increasing endcap radiation and flexural wave radiation. The weak endcap radiation within the membrane wave region is further supported by examining the MIT/NRL ringed shell measured data, and it is not in conflict with the analytical result from Guo [26] about strong compressional wave radiation at the endcap. I speculate that such radiation is largely directed towards the axial direction. This wave dissipation effect at the endcaps will be considered in the decay rate modeling in Sec.5.1.2.

As a byproduct, the evidence of insignificant endcap and flexural wave radiation within the membrane wave region justifies the use of the infinitely long shell to estimate sound energy injection into a finite shell.

Green's theorem requires complex pressure and radial velocity field in a finite shell to compute radiation. However, the elastic wave power equipartition hypothesis produces the magnitude of total velocity (combination of both in-plane and out-of-plane velocities, see Eq. 2.14). To bridge the gap between the output of the wave power calculation and the input of Green's theorem, the following approximations have been made, examined and tested.

- Form phase field through estimated wave speeds with and without the influence of the rings

  The propagating phase field along the shell can be formed if the wave speed is known. The wave speed calculation of the infinitely long uniform shell can be used as an approximation, which results in sound radiation only 1-2 dB smaller than the direct SARA-2D calculation, not significantly different from the results if the influence of the rings is considered. The influence of the rings on wave

speed is first observed from the measured scattering data and from the analysis of the SARA-2D calculation. The rings can increase the membrane wave speeds considerably, but decrease the flexural wave speed only slightly. Moreover, the modification is frequency dependent. Above $ka = 5$, the rings can decrease the membrane wave speeds by somewhat 10%. Below $ka = 5$, the rings can decrease the $n = 1$ shear phase speed by as much as 50%. In spite of this wave speed change, the membrane wave region is only $2° - 3°$ smaller. Further, the observed wave speed change is understood and characterized by a simulation of a 1D bar system with mass-spring subsystems attached. I find that the resonance of the rings determines the frequency region of decreased and increased wave speed, corresponding to mass and stiffness effect respectively. In addition, the ratio of the axial wavelength to the average ring spacing, λ_x/b, plays an important role. The wave speed change is especially significant if λ_x/b on the order of 1. The modified wave loci shown in Fig. 4-23 will be used to predict scattering in Chap.5, and will be shown to yield better agreement with the measured data.

- Estimate surface pressure from known radial velocity

  The estimated impedance for the ringed shell is tested against the SARA-2D calculation. The difference is insignificant. Further, I use the estimated surface pressure with the radial velocity from the SARA-2D calculation, and predict sound radiation within 1-2 dB in comparison with the direct SARA-2D scattering results.

- Estimate radial velocity by considering the influence of the rings

  The rings can mildly modify the ratio of radial motion to total motion for the membrane waves. According to the SARA-2D calculations, the rings can increase the compressional wave radial velocity ratio to total velocity by as much as 20% and the corresponding radial velocity ratio of the shear wave by as much as 40% over $4 < ka < 12$. Thus, the ring effect should be considered if accurate radiation prediction is required.

Chapter 5

Prediction of transient scattering and comparison with measured data

Following the calculation of elastic wave power in Sec.2.3 and the development of a radiation model in Chap.4, scattering prediction seems to be straightforward. However, the prediction model so far only predicts the magnitude of sound scattering, because no phase information is retained in the wave power calculation, which is steady-state. Since the scattering processes of concern in this study are transient, the prediction model has to be extended to the time domain. I do not attempt to predict the detailed transient scattering signatures since they are highly dependent on shell details. Instead, I seek to depict the decay trend of the transient scattering by using the hypothesis of wave power equipartition. Random phase realizations are first introduced. A wave energy decay model is then developed based on wave power equipartition. Various decay mechanisms are considered including radiation from the shell cylinder, coupling loss to the endcaps and the internals, and also material damping. Finally, the prediction is compared to the measured bistatic target strength of both the ringed and the internalled shells. The prediction differs from the measurements by no more than 2.5 dB, for time windows 2, 3 and also for a time-integrated case. Explanations for the discrepancies are given and the strength and limitations of the prediction model are also discussed in this chapter. Random wavenumber real-

izations are considered. Inclusion of a random wavenumber realization in the model, however, does not yield a better agreement with the measured data.

5.1 Prediction of transient scattering

5.1.1 Random phase realizations

Without phase, it is impossible to transform sound pressure from the steady-state into the time domain. The phase is generally related to the multiple wave reflections and transmissions at the shell discontinuities, and is therefore highly dependent on shell details.

Since shell details are often unknown or at best vaguely known, I assume random phase realizations in this study. As illustrated by a flow-chart in Fig. 5-1, the predicted scattering, appended with random phase, can be inversely Fourier transformed into the time domain. Time windows are then applied so that the target strength in each time window can be Fourier transformed back to the frequency domain. Again, the time windows correspond to roundtrip periods of the trace matched wave in the shells, as shown in Fig. 3-13.

In each realization, the phase, $\Phi_{ne}(\omega)$, is an arbitrary value chosen with equal likelihood from 0 to 2π. The sound pressure, with the phase appended to the sound pressure magnitude from the steady-state calculation, $|p_{ne}|$, then becomes a complex number.

$$p_{ne} = |p_{ne}| e^{i\Phi_{ne}(\omega)} \quad . \tag{5.1}$$

The total pressure field is a coherent summation of the wave types and mode components, shown in the following:

$$p_{tot}(\omega, \theta) = \sum_{e} \sum_{n} p_{ne}\ (\omega, \theta) \ . \tag{5.2}$$

In Eq. 5.1 and Eq. 5.2, the sound pressed magnitude, for each wave type e and

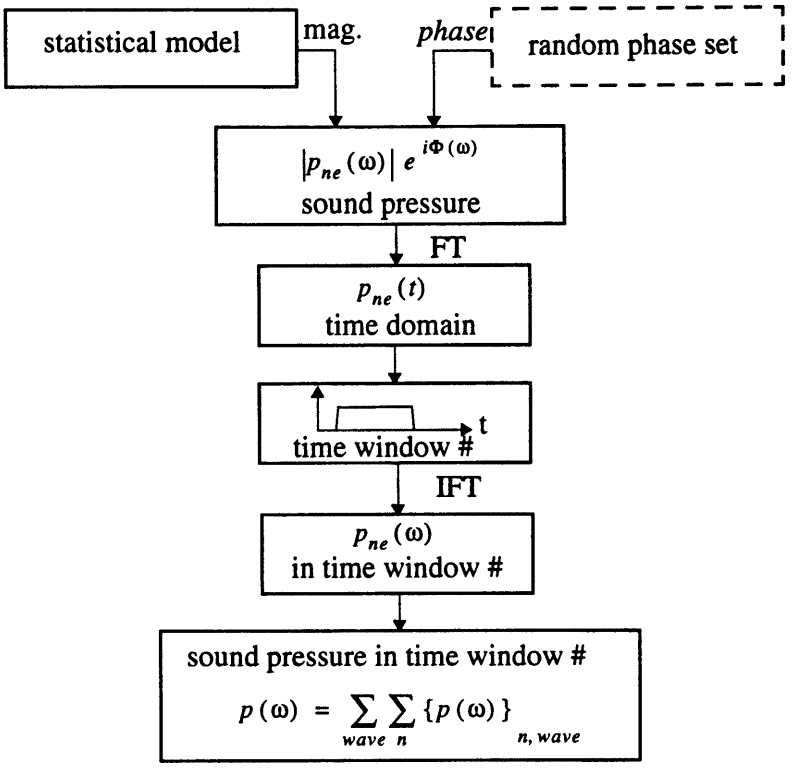

Figure 5-1: Idea of random phase realization for temporal response.

mode n, is appended by a random phase set for each wave type e and mode n. This is equivalent to randomizing the relative phase among the wave types and the circumferential modes.

It is true that the predicted scattering fluctuates because of the random phase realizations. With many such realizations, however, I expect the mean to predict a typical experiment. That is to say, I can obtain a scattering level that captures the average shell behavior.

Random phase realizations alone are not enough for predicting transient scattering, because they do not provide temporal decay behavior. In fact, a random phase realization gives a flat scattering amplitude (at least statistically) in the time domain. Thus, the next step of the transient scattering prediction is to introduce a proper decay behavior.

5.1.2 Measurement and formulation of decay rate

For a multi-degree-of-freedom system, the decay rate of the impulse response is generally not a constant, but varies with time. One reason is that different modes might have different loss factors that create time varying decay behavior of the total system response. In the presence of weak coupling, the system response is affected by both modal loss factor and coupling loss factor (among modes), and even by the initial energy conditions of each mode. In such a case, the decay rate can be determined when detailed information about the system is known. To be consistent with the wave power equipartition hypothesis, I consider strong modal coupling case, where the coupling loss factors are not specified, but are sufficiently strong to offset the modal loss factors. As a result, the system response does not decay at a rate of any particular mode, but at a unified rate and should be time invariant.

Before a decay rate model is developed, it is necessary to examine the MIT/NRL measurement data of the shell models, in order to derive experimental understanding of the decay behavior in the MIT shell models. In particular, I examine the MIT/NRL monostatic data within the membrane wave region.

Fig. 5-2, Fig. 5-3 and Fig. 5-4 display the frequency bandlimited impulse response envelope for the ringed shell, the internalled shell and the empty shell, respectively, for aspect angle at 66°. Four frequency bands, $2.75 < ka < 10$, $2.5 < ka < 5.0$, $5.0 < ka < 7.5$ and $7.5 < ka < 10.0$ are used for the analysis. In Fig. 5-3, Fig. 5-2, and Fig. 5-4, the peak at $t = 0$ corresponds to the geometric return. In monostatic scattering, the elastic wave backscatter is largely observed when the trace matched wave is reflected at the rings and the endcaps.

The significant peak near $230\,\mu s$ in Fig. 5-2 and Fig. 5-3 is due to such reflections at the rings. After $230\,\mu s$, the backscatter signal contains multiple events that are hardly resolvable in time. The impulse response envelope from $230\,\mu s$ to $1300\,\mu s$ for the ringed and internalled shells can be fitted by a straight line. The associated decay rate, measured from the slope of the line, is labeled in each subplot in dB/ms. For the ringed shell, the decay rate is 12 dB/ms in the broad band $2.75 < ka < 10$, and is essentially the same in the three narrow bands as well. For the internalled shell, the decay rate increases considerably in the broad band as well as in the mid-band

$5 < ka < 7.5$, due to the presence of the internal structures. For the empty shell, the back directed elastic wave scattering is observed later in time, at approximately $480\,\mu s$, due to the absence of the rings. The peaks within $480\,\mu s < t < 850\,\mu s$ are due to circumferential navigation of the shear waves. The associated decay rate measures 53.3 dB/ms in band $2.75 < ka < 10.0$, significantly larger than for the ringed and the internalled shells.

The above analysis is performed for each monostatic angle in $64° < \theta < 80°$, with 1° increment. Fig. 5-5 displays the decay rate for the three shells for the frequency band $2.75 < ka < 10$. I observe that the decay rates fluctuate moderately for the ringed and the internalled shells, but drastically for the empty shell. I evaluate the mean decay rate for the ringed and the internalled shells over three angular bands: $64° < \theta < 80°$, $64° < \theta < 70°$ and $74° < \theta < 80°$ and then display the results beside the plots in Fig. 5-5. Within $64° < \theta < 70°$, only shear waves are excited while within $74° < \theta < 80°$ both shear and compressional waves are trace matched. I observe that the decay rate for the ringed shell does not differ significantly for either the frequency bands or the angular bands. I observe a similar trend for the internalled shell as well. Further, I notice that the decay rate for the internalled shell is approximately 30% higher than for the ringed shell. This observation is the same as obtained by Corrado [19], who analyzed sound incidence at 75° and 66° and for the frequency range $2.75 < ka < 10$.

The foregoing experimental analysis is helpful to reach the following conclusions about the scattering decay behavior in the shells.

- There exists a unified decay rate for the ringed shell and the internalled shell, but not for the empty shell. In addition, the decay rate for the ringed and the internalled shells is in general far smaller than for the empty shell. This observation is directly related to the strong elastic wave coupling due to the rings, which is in turn responsible for the elastic wave power equipartition observed previously in Chap.3.

- The unified decay rate for the internalled shell is approximately 30% larger than for the ringed shell.

- The unified decay rate for the ringed shell and the internalled shell is rather insensitive to either the aspect angle bands, or the frequency bands.

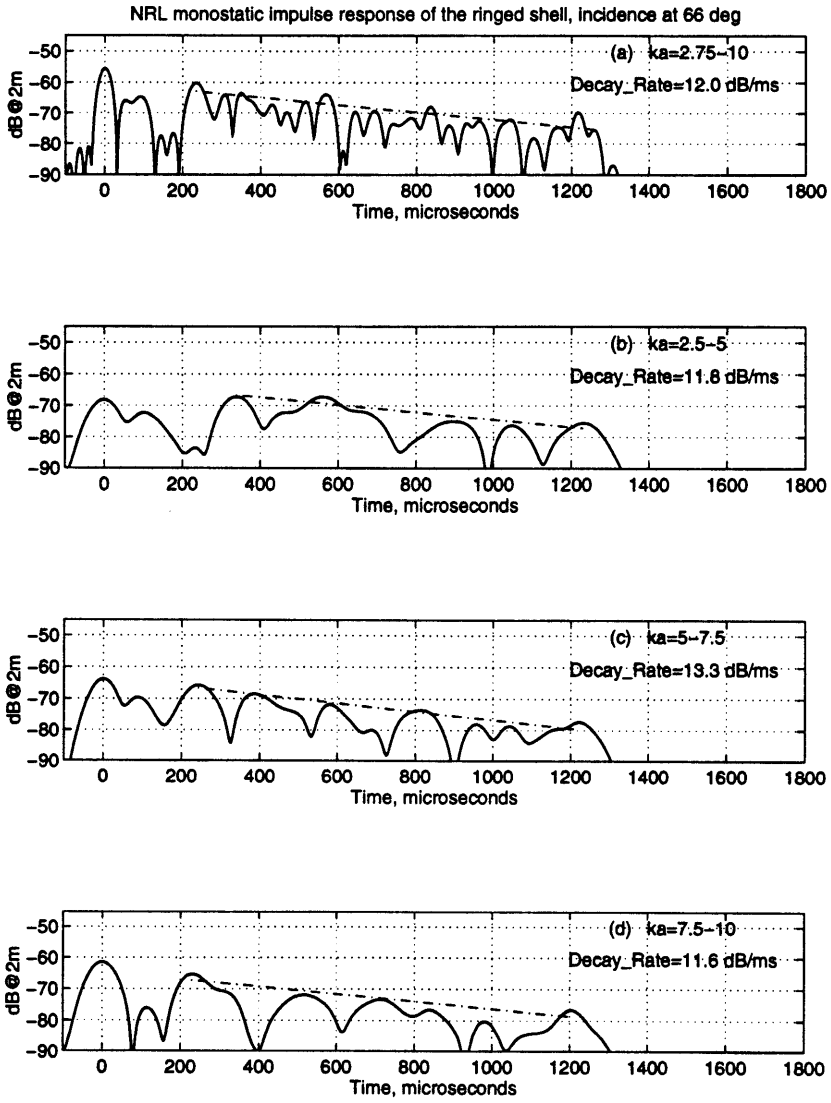

Figure 5-2: Measured monostatic bandlimited impulse response of the **ringed** shell and decay rate measurements. The aspect angle is 66°. Four different frequency (ka) bands are used. The $t = 0$ peak corresponds to the geometric return.

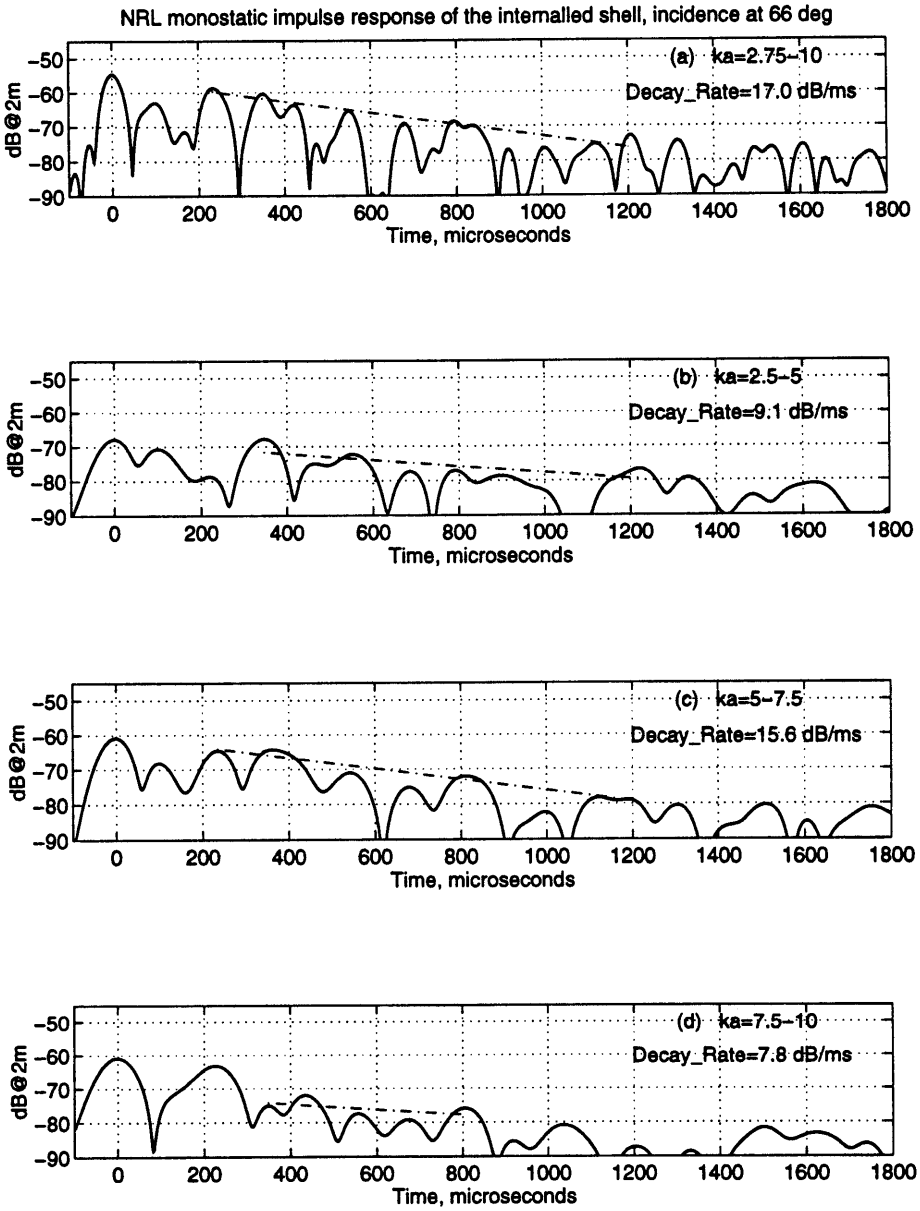

Figure 5-3: Measured monostatic bandlimited impulse response of the **internalled** shell and decay rate measurements. The aspect angle is 66°. Four different frequency (ka) bands are used. The $t = 0$ peak corresponds to the geometric return.

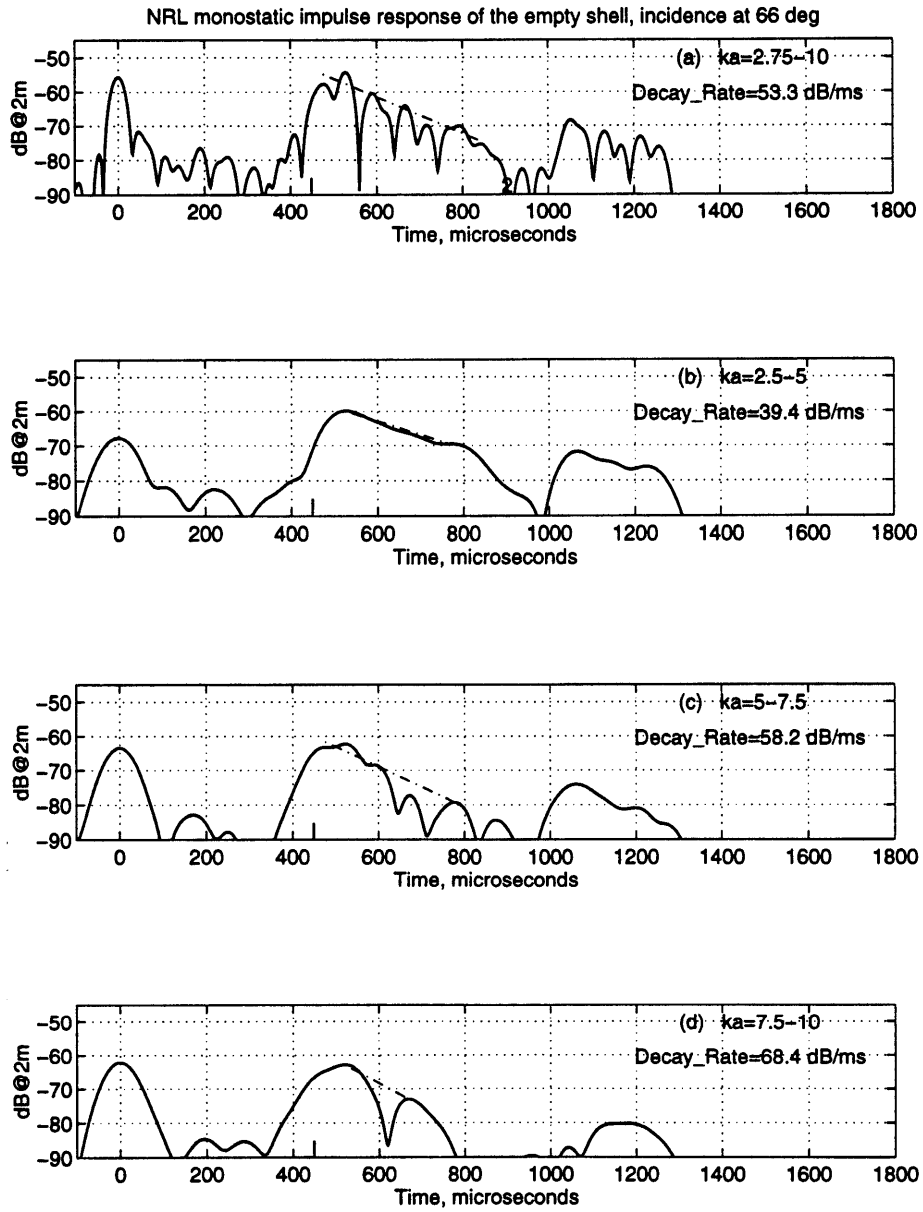

Figure 5-4: Measured monostatic bandlimited impulse response of the **empty** shell and decay rate measurements. The aspect angle is 66°. Four different frequency (ka) bands are used. The $t = 0$ peak corresponds to the geometric return.

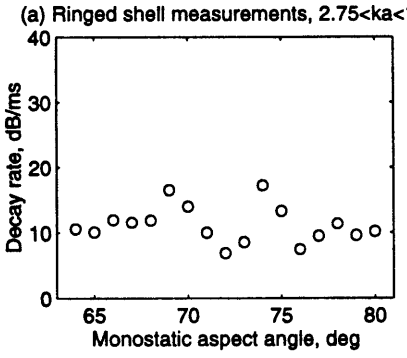

Mean/Std-Dev. of decay rate in (ka–angle) bands, dB/ms

	64<ang<80	64<ang<70	74<ang<80
2.75<ka<10	11.2/2.8	12.4/2.2	11.2/3.2
2.5<ka<5	10.7/3.4	13.1/1.8	10.1/2.3
5<ka<7.5	11.4/4.7	14.6/4.7	10.1/3.3
7.5<ka<10	12.5/3.4	11.5/2	11.4/3.3

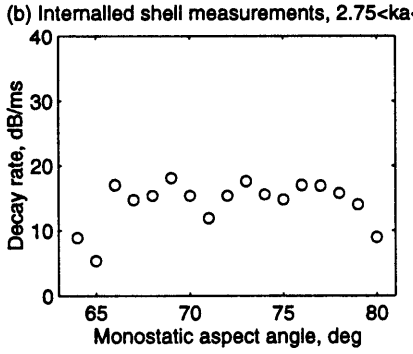

Mean/Std-Dev. of decay rate in (ka–angle) bands, dB/ms

	64<ang<80	64<ang<70	74<ang<80
2.75<ka<10	14.3/3.5	13.6/4.6	14.7/2.7
2.5<ka<5	11.6/4.6	9.4 /1.1	14.4/5.9
5<ka<7.5	13.9/3.6	13.8/3.8	14.2/4.4
7.5<ka<10	14.9/4.5	14.8/4.8	14.5/4.5

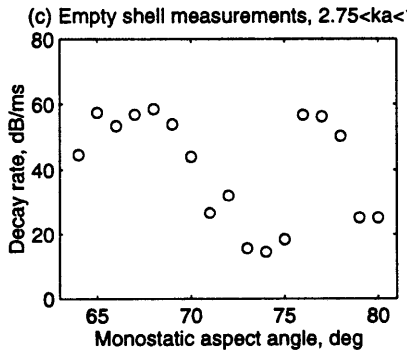

Figure 5-5: Decay rate measurement for different aspect angles and different frequency bands and the three shell models. From the MIT/NRL measured data. (a) the ringed shell; (b) the internalled shell and (c) the empty shell. The tables on the right list the means and standard deviation of the decay rate measurements for frequency and angular bands.

In the following I will focus on the prediction of the unified decay by using the hypothesis of elastic wave power equipartition.

At an arbitrary time t, the total elastic wave energy E_{tot} decays to a new level $E_{tot}\, e^{-\alpha \Delta t}$ during an infinitesimal time interval Δt at t,

$$E_{tot}\ e^{-\alpha \Delta t} = E_c\, e^{-\alpha_c \Delta t} + E_s\, e^{-\alpha_s \Delta t} + E_f\, e^{-\alpha_f \Delta t} \tag{5.3}$$

where subnotes **c**, **s** and **f** denote compressional, shear and flexural waves, respectively.

Decay rate α is defined by the following relation, also discussed previously in Eq. 2.9.

$$\alpha = \omega \eta = \nu \tau \tag{5.4}$$

The decay rate in Eq. 5.4 has the unit of $neper/s$. In oder to read it in dB/s, it has to be multiplied by a constant 4.34.

The decay rate should, in principle, include material damping, radiation damping from the shell and coupling damping to dissipative substructures such as the endcaps and the internal structures. The coupling among the elastic waves in the shell do not appear in Eq. 5.3 because the coupling effect will be canceled.

Eq. 5.3 states that the total energy is the sum of the energy in the elastic wave types. However, the relative energy distribution among the elastic waves is dictated by equipartition of wave power, which is defined as the product of wave energy and axial elastic wave group speed, as shown in Eq. 2.13.

$$E_c\, c_{gc} = E_s\, c_{gs} = E_f\, c_{gf}\ . \tag{5.5}$$

The unified energy decay within the small time interval Δt is derived by expanding the exponentials in Eq. 5.3 and keeping only the first two terms,

$$\alpha = \frac{\frac{c_{gf}}{c_{gc}}\,\alpha_c + \frac{c_{gf}}{c_{gs}}\,\alpha_s + \alpha_f}{1 + \frac{c_{gf}}{c_{gc}} + \frac{c_{gf}}{c_{gs}}} \quad . \tag{5.6}$$

The unified decay rate turns out to be a weighted summation of the individual decay rate of each elastic wave type, with the weighting determined by the axial group speed ratios. Since the flexural group speed in this study is much smaller than membrane wave group speeds, the decay rate of the flexural wave is crucial in determining the unified decay rate. The weight of the membrane wave decay rates, on the other hand, is relatively small. The group speeds of the elastic waves can be conveniently obtained from the infinitely long shell calculation, discussed in Sec.2.1. Since the group speeds are usually dependent on circumferential mode n, so is the decay rate for each wave type, the unified decay rate is necessarily evaluated for each mode n as well. The formulation in this subsection should be understood as pertinent to each mode n component, although the subnote n is not always shown. In the following, I focus on estimating the decay rate of each elastic wave type and for each mode n.

5.1.3 Estimate of decay of each elastic wave type

For each elastic wave, the decay rate is estimated by considering radiation damping, net coupling damping to other dissipative structures, and material damping.

Decay due to radiation damping

The membrane radiation decay in the cylindrical shell section can be calculated from the loss factor of the infinitely long shell shown in Fig. 2-4, and from Eq. 5.4.

The subsonic flexural waves do not radiate except at shell discontinuities such as the rings and the endcap junctions. Flexural wave radiation from shells is complicated at or below the ring frequency. Above the ring frequency, however, the shell curvature effect fades and flexural wave radiation from a flat plate can be used as an approximation. In this study, the ring frequency is at $ka = 3.5$, so the flat plate approximation can be used for the frequency range $4 < ka < 10$. With the use of Eq. 2.11 for the radiation coefficient and Eq. 2.12 for the corresponding loss factor, the flexural decay rate due the subsonic radiation from the rings can be estimated from Eq. 5.4. The decay rate is in general dependent on frequency. At the mid point of the frequency range, $ka = 7$, the decay rate is approximately 3.6 dB/ms, close to Corrado's estimate of 3.8 dB/ms [19] based on an analytical calculation of the elastic wave interaction in the ringed shell model.

The decay rate estimates due to the radiation damping at the cylinder are displayed in Fig. 5-7 by the solid line.

Decay due to coupling loss at endcaps

Dissipative substructures attached to the cylindrical shell provide additional means of wave energy attenuation. Endcaps are important in this regard, so are the internal structures. This subsection estimates the dissipation at the endcaps. The subsequent subsection estimates the dissipation into the internal structures.

The dissipation at the endcaps is caused by the heavy compressional wave radiation when the local endcap radius forces the compressional waves to the *ad hoc*

cutoffs. According to the discussion in Sec. 2.1 based on Guo's results [25], the compressional wave amplitude is reduced significantly during a roundtrip in the endcap. This strong compressional dissipation at the endcap is also experimentally evident by the lack of compressional wave backscattering from the empty shell [19].

Again, the decay has to be estimated for each mode n since the compressional wave attenuation is highly dependent on mode n.

The general expression for the compressional wave decay rate at the endcaps is

$$\alpha_n = 2\tau_{ccn}\delta_n c_{cn}/L \,, \tag{5.7}$$

where $2c_{cn}/L$ represents the interaction rate with the endcaps, c_{cn} being the axial phase speed of the compressional wave at mode n and L being the shell length; δ_n represents the compressional wave energy attenuation during one roundtrip at the endcap, given by Fig. 2-5; τ_{cc} is the compressional wave transmissibility at the shell-endcap junction, which will be evaluated briefly in this section together with the wave transmissibilities for the shear wave, τ_{scn}, and for the flexural wave, τ_{fcn}.

Similarly, the shear wave can scatter to the compressional wave at the endcap junctions due to the slope discontinuity. The resultant decay can be estimated according to Eq. 5.8:

$$\alpha_n = 2\tau_{scn}\delta_n c_{sn}/L \,. \tag{5.8}$$

Finally, the flexural wave can also scatter to the compressional wave at the endcap junctions due to the slope discontinuity. The resultant decay can be estimated according to

$$\alpha_n = 2\tau_{fcn}\delta_n c_{fn}/L \,. \tag{5.9}$$

Wave transmissibilities in Eq. 5.7, 5.8 and 5.9 are generally dependent on shell junction details. Instead of pursuing extensive computation of the exact wave conversion at the shell-endcap junctions, I estimate the wave conversion by modeling the

discontinuity as two flat plates in vacuo, joined with the same slope discontinuity as in the shells. The requirement of continuous forces and displacements across the junction yields 8 boundary conditions, so that the amplitude of the reflected and transmitted elastic waves can be solved. The incident angles are measured from the normal to the junction line include 0°, 17°, 35° and 60°, corresponding to the helical angle ψ for the compressional waves of mode $n = 0$, 1, 2 and 3 respectively. The wave conversion coefficients are listed in Table 5.1.

As seen from Table 5.1, the compressional-to-compressional transmissibility is approximately 1/3, for $n = 0$, 1 and 2. The flexural-to-compressional transmissibility decreases as n increases, from 28% at $n = 0$, to 15% at $n = 2$. On the other hand, the shear-to-compressional transmissibility increases as n increases, from 0% at $n = 0$, to 10% at $n = 2$ and 30% at $n = 3$.

Table 5.1: The percentage of reflected and transmitted wave power of the the incoming compressional wave to a plate joint. Discrete incidence angles (ψ) correspond to helical angles of compressional waves of circumferential mode n. τ' denotes reflection and τ denotes transmission. Analytical details are attached in App. D.

mode	ψ	τ'_{cc}	τ'_{sc}	τ'_{fc}	τ_{cc}	τ_{sc}	τ_{fc}
0	0°	19.2	0	20.0	33.7	0	27.6
1	17°	20.4	1.5	17.8	34.3	1.5	25.1
2	35°	25.0	9.1	10.0	33.4	9.0	15.2
3	60°	25.5	31.4	0.4	13.1	30.3	0.1

The decay rate estimates due to dissipation at the endcaps are displayed in Fig. 5-7 by the dash-dot line.

Decay due to coupling loss to internal structures

The internal structures are resiliently mounted on the rings and have many degrees-of-freedom. Because of many joints, isolations and high-loss-factor materials used, the internal structures are likely to have very large damping. What is more, it takes time for the transmitted waves to convert back to the shell in case they are not completely attenuated. As long as the observation time is limited to the first few time windows, such as I am studying, the elastic waves transmitted from the shell into the internal

structures can be assumed to decay fast before they are possibly projected back to the shell. In other words, the internal structures are treated as a energy sink - a black hole assumption.

Thus any amount of energy transmitted from the outer shell to the rings can be regarded as dissipation. Conti [21] has shown that the rings for $n = 0$ compressional and flexural waves are typically mass-like, because their two fundamental vibration modes, hooping and rolling, are all below $ka = 3$ and the next order resonance is far above $ka = 12$. In Sec.4.2.1, I observe that the rings above $ka = 5$ are mass-like for n=1, 2, 3 and 4, because the membrane wave speeds are generally lower above $ka = 5$. Thus, I treat the rings as limp masses, not only for the $n = 0$ case, but also for $n \geq 1$ cases.

The energy of 'massive rings' can be calculated as heavy 'accelerometers' picking up vibration of a structure (shell). Since the rings are heavy, the mass loading effect must be considered. Without losing generality, I consider one 'average' shell bay with one ring at the end, sketched in Fig. 5-6 as a rectangular flat-plate with a finite beam attached. The mass of the ring m_r is approximately the same as the mass of the shell bay. The ratio of the ring square velocity to the spatially averaged mean square velocity of the ring is determined by an impedance ratio, which can be easily deduced from the analysis in Ref. [41].

$$\frac{< v_r^2 >}{< v_s^2 >} = \frac{2Z_s^2}{2Z_s^2 + (\omega m_r)^2} \quad , \tag{5.10}$$

where the wave impedance of the shell bay is $Z_s = 2\pi a h_s \rho \, c_{nx}$, a, h_s and ρ being the shell radius, thickness and density, respectively, and c_{nx} being the axial wave speed for mode n. In comparison with the mass impedance of the ring, ωm, the wave impedance Z_s in the shell is much smaller, only 1/50 of ωm_r for the $n = 0$ compressional wave at $ka = 4$. Therefore, the denominator of the right-hand-side of Eq. 5.10 can be approximated by $\omega^2 m_r^2$ alone.

In the following formulation, the membrane waves are treated as in-plane and the flexural wave is treated as out-of-plane. In addition, the rotational coupling of the ring is neglected.

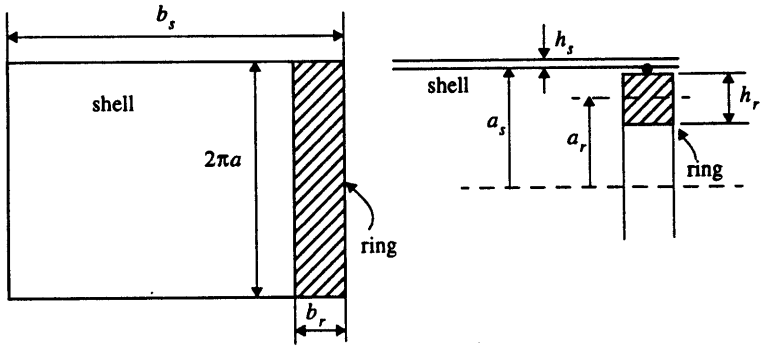

Figure 5-6: Sketch of shell-ring coupling, to estimate energy loss into internal structures, which are (not shown) resiliently mounted to the massive ring(s) and are assumed to be energy sink in this study.

The energy loss factor due to the energy transported to the ring can be expressed as

$$\eta = \frac{E_{ring}}{E_{shell}} = \frac{\rho\, 2\pi a_r\, b_r h_r\, v_r^2}{\rho\, 2\pi a_r\, b_s h_s\, < v_s^2 >} \quad , \tag{5.11}$$

or

$$\eta \approx \frac{b_r h_r}{b_s h_s} \frac{4 Z_s^2}{\omega^2 m_r^2} \quad , \tag{5.12}$$

where the shell and the ring have the same mass density ρ and approximately the same radius ($a_r = a_s$), but different width b and thickness h. Subnote s and r represent the shell and the ring respectively.

The decay rate (dB/s) is then written as

$$\alpha = 4.34\omega\eta = \frac{17.36 c_{nx}^2 h_s}{\omega b_r h_r b_s} \quad . \tag{5.13}$$

Eq. 5.13 estimates the decay rate due to the energy transmission into the internal structures, for both membrane waves and the flexural wave. The axial wave speed c_{nx} can be obtained from the analytical results in Fig. 2-1, Fig. 2-2 and Fig. 2-3 for the compressional, shear and flexural waves respectively.

Following the foregoing formulation, I make an estimate of such a decay rate, for a shell with lossy but detail-unknown internal structures which are mounted to

four heavy deep rings identical to the rings in the MIT ringed shell. The decay rate estimates due to dissipation into the internal structures are displayed in Fig. 5-7 by the dotted line.

Decay due to other attenuation mechanisms

The shell structural damping might play a role as well. However, if no extra damping treatment such as the constrained layer damping is applied, the material loss factor of steel is normally less than 0.002 [41], which yields a decay rate of 1.65 dB/ms at $ka = 7$. This damping is insignificant in comparison with the membrane wave attenuation but might be important for the flexural wave dissipation.

Decay rate comparison for different mechanisms

Fig. 5-7 summarizes the decay rate estimates due to three major dissipation mechanisms in finite complicated shells: radiation from cylinder, radiation from the endcaps and vibrational energy loss into the internal structures. For both compressional and shear waves, the radiation damping from the cylinder is the most important attenuation mechanism, followed by the coupling loss into the internal structures. Radiation from the endcaps are not as important as the other two, possibly due to the limited rate for the membrane waves to reach the endcaps.

For the flexural waves, the most important dissipation mechanism is the subsonic radiation from the shell discontinuities such as rings and endcap junctions. The coupling loss to the heavily radiating compressional waves at the endcaps plays a role as well. The energy loss into the internal structures, however, is unimportant. The explanation is that the heavy deep rings are effectively rigid to the slow flexural waves, so that the flexural wave incident on a ring will be reflected almost completely. In other words, the flexural wave is too 'soft' to drive the 'hard' rings to move. This confinement of the flexural wave within the ring bay can be visualized in Fig. 4-2. In comparison with the membrane waves, the flexural wave radiation is generally by far smaller. Although small, the flexural wave radiation is very important because the slow flexural wave has a larger weight in the calculation of the unified decay rate, see

Eq. 5.6.

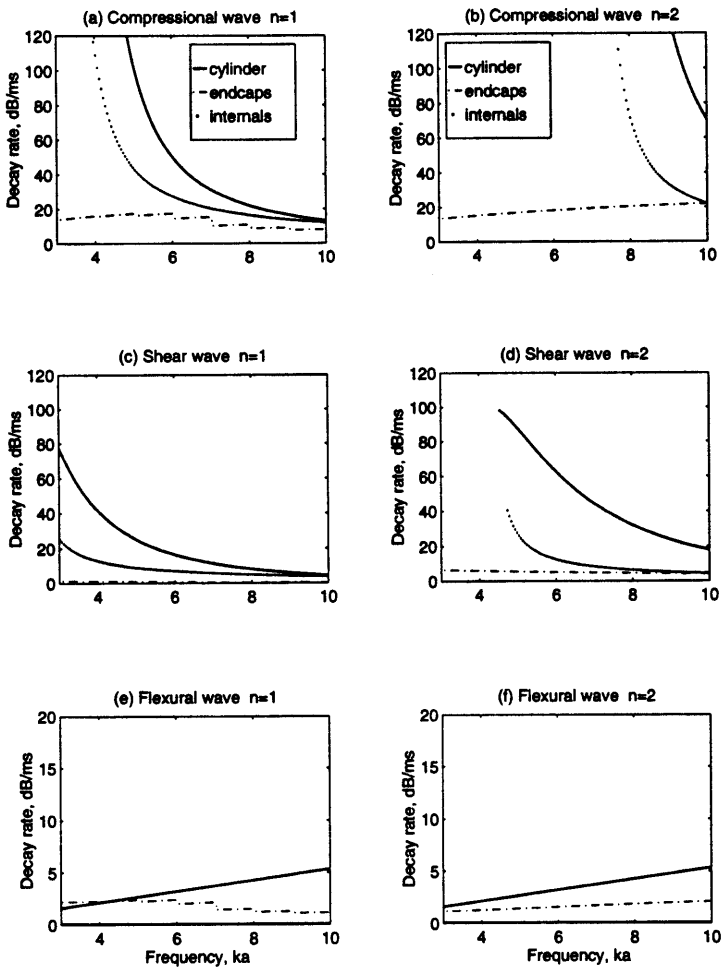

Figure 5-7: Decay rates for radiation decay at cylindrical shell and coupling decay due to coupling to the compressional waves at endcap. (a,b): Compressional wave n=1 and 2. (c,d): Shear wave n=1 and 2. (e,f): Flexural wave n=1 and 2. Solid line: radiation damping at cylinder. Dash-dot line: coupling loss at endcaps. Dotted line: coupling loss to internal structures.

The total decay rate is then computed based on Eq. 5.6 and is shown in Fig. 5-8 for each mode n. The total decay rate is normally zero below the shear wave cutoff. The drastic increase just above the cutoff is caused by the sharp increase of the shear wave radiation. As frequency increases further, the decay rates begin to taper down except near the *ad hoc* cutoff of the compressional waves. The spike in the $n = 2$ decay rate curve corresponds the drastic increase of the compressional wave radiation near the *ad hoc* cutoff at $ka = 7$.

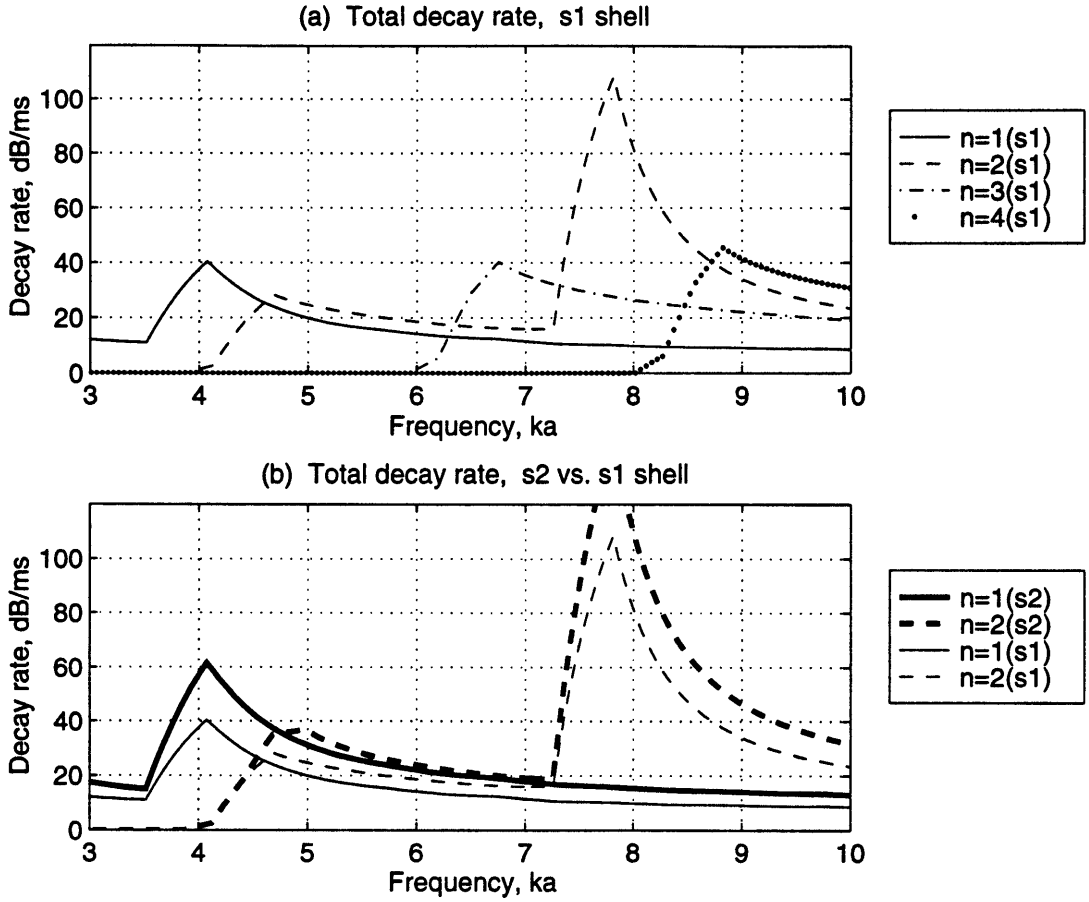

Figure 5-8: Total decay rates from Eq. 5.6. (a) prediction for the ringed shell (s1) and (b) prediction for the internalled shell shell (s2).

Comparison between the decay rate estimate with the measurements

It is possible to check the calculated decay rate by comparing it with the measurements. I observe from the measured scattering signal in this section that a typical unified decay rate within the membrane wave region is 11.2 dB/ms for the ringed shell, and 14.3 for the internalled shell, for frequency band $2.75 < ka < 10$ and angular band $64° < \theta < 80°$.

However, the decay rate comparison is not straightforward because the calculated decay rates are for each mode n while the measured decay rates are for total scattering response. To make the comparison meaningful, I make an assumption of energy equipartition among the circumferential mode n. This assumption is certainly not reasonable for any particular frequency or any particular incidence angle. However,

if the decay rate is averaged over a frequency band and angular band, for instance $3 < ka < 10$ and $60° < \theta < 80°$, I would expect the assumption to be reasonable. Assuming such equal distribution of energy among circumferential modes, I estimate that the decay rate, obtained in the similar way as in Eq. 5.6, is 13.2 dB/ms for the ringed shell and 15.2 dB/ms for the internalled shell. The values are respectively 14% and 8% higher than the measured decay rates in Sec.5.1.2.

In addition, the estimate of the decay rate for the internaled shell is approximately 25% higher than for the ringed shell, consistent with the measured data discussed in Sec.5.1.2.

5.1.4 Scattering prediction of finite ringed and internalled shells

In the following, I will predict the target strength of a finite ringed shell and a finite internalled shell. The shells are the same as the MIT shell models in terms of the following parameters: the shell length, radius, thickness, and material properties; the ring width, thickness, density as well as the number of the rings. In addition, the shells are assumed to have many discontinuities for sufficient conversion among the elastic waves, so that the power of the elastic waves in the shell can reach equipartition. Scattering from the shells is observed at 2 m from the shell center, the same as in the MIT/NRL measured data. I consider two sound incidence angles: 75° and 66°. At 75° both compressional and shear waves can be trace matched while at 66° only the shear wave is trace matched in the cylindrical section of the shell.

The prediction of the transient scattering includes the following general steps:

1. Specify input information about shell, fluid, sound incidence and receiver location.

2. Compute the elastic wave total velocity for each wave type, mode n and frequency using the infinitely long shell model and the wave power equipartition hypothesis.

3. Compute the shell radial velocity, estimate the surface pressure using the formulation in Sec.4.2, and form the phase field with the estimated axial wave phase speeds.

4. Compute shell radiation (steady-state) using Green's theorem in Sec.4.1.

5. Append the steady-state scattered pressure magnitude with random phase realizations and compute target strength for a time window that corresponds to one roundtrip time of the trace matched wave in the shell. The target strength is a function of frequency, observation angle and mode n.

6. Adjust the target strength with different decay for different windows, by using the decay rate estimates in Sec.5.1.2.

7. Display the target strength in the $ka - \theta$ plane, or, frequency *vs.* bistatic observation angle.

In the above steps, the phase speeds and group speeds of the elastic waves are estimated either from calculation of the infinitely long shell with no rings, or from simulation that considers the effect of the rings (Sec.4.2.1). In the latter case, I need to calculate an infinitely long shell in Step 2, with its membrane wave speeds modified by the influence of the rings. Above $ka = 5$, the membrane phase speed is increased while below $ka = 5$, the $n = 1$ shear wave is dominant and its phase speed is decreased. The finite width of the modified wave loci shown in Fig. 4-23 in fact enables random realization of the axial wavenumber, in addition to random realization of phase. Random realization of the axial wavenumber will be discussed shortly.

Fig. 5-9 displays the bistatic target strength for 75° incidence for time window 1, with no modification of the wave speeds. The upper two figures are from two random phase realizations and the lower figure is the average over 6 random realizations. Since the first half of window 1 involves sound excitation (trace matching) of the elastic waves in the shell, I apply no decay to window 1.

Fig. 5-9 demonstrates the following features:

- The scattered field is spread over angular region $60° < \theta < 120°$, although the incident sound is a plane wave at a single angle. This is caused by the wave conversion at the shell discontinuities that spreads the single trace matched axial wavenumbers into many axial wavenumbers.

- The scattering below 60° or above 120° decreases sharply, because membrane wave trace matching is assumed to dominate both excitation and radiation within $60° < \theta < 120°$. Acoustic coupling to the endcaps is not considered in the prediction model.

- The predicted target strength is symmetrical around beam aspect (90°), due to the assumption used in the prediction (Eq. 2.20), which ignores the magnitude difference between the waves going forward and backward.

- The predicted target strength has 'hot spots' close to the trace matching frequencies for different mode n. In the example of 75° sound incidence, the trace matching to the $n = 2$ and $n = 3$ shear waves occurs at $ka = 5.0$ and $ka = 7.2$ respectively. The trace matching to the $n = 1$ compressional wave happens at approximately $ka = 9$. Such clear 'modal' behavior is consistent with the peaks of the equipartitioned elastic wave power displayed in Fig. 2-14.

Furthermore, I find that different phase realizations create fluctuations in both magnitude and pattern of the predicted target strength, as indicated by the comparison between (a) and (b) in in Fig. 5-9. Denoting $\bar{TS}$ as the logarithmic mean of the target strength over $3 < ka < 10$ and $60° < \theta < 120°$, I find that the average of $\bar{TS}$ over random phase realizations does converge. In this study, averaging over 6 phase realizations is sufficient. The value of $\bar{TS}$ has been labeled in each plot in Fig. 5-9, and all subsequent target strength contours. For example, $\bar{TS}$ is -36.1 dB for one realization in (a) of Fig. 5-9 and -35.5 dB for another realization in (b) of Fig. 5-9.

I also find that the standard deviation of $\bar{TS}$ is approximately 0.7 dB for the 6 random phase realizations shown in Fig. 5-9.

Fig. 5-10 displays the bistatic target strength for 66° incidence for the internalled shell. Again, the wave speeds are from the infinitely long shell calculation without the ring influence. The left figure is from one phase realization and the right figure is the average over 6 random phase realizations, with the standard deviation of $\bar{TS}$ being 1.2 dB. At this angle of incidence, only the shear wave is trace matched. The hot spots are concentrated on two frequency bands near $ka = 4$ and $ka = 8$, corresponding to the trace matching frequencies of the $n = 1$ and $n = 2$ shear waves. This strong frequency dependence, however, is not observed in the measured data, as will be shown later in Sec.5.2. Thus, it might be helpful to consider the ring effect on wave speeds for this angle of incidence.

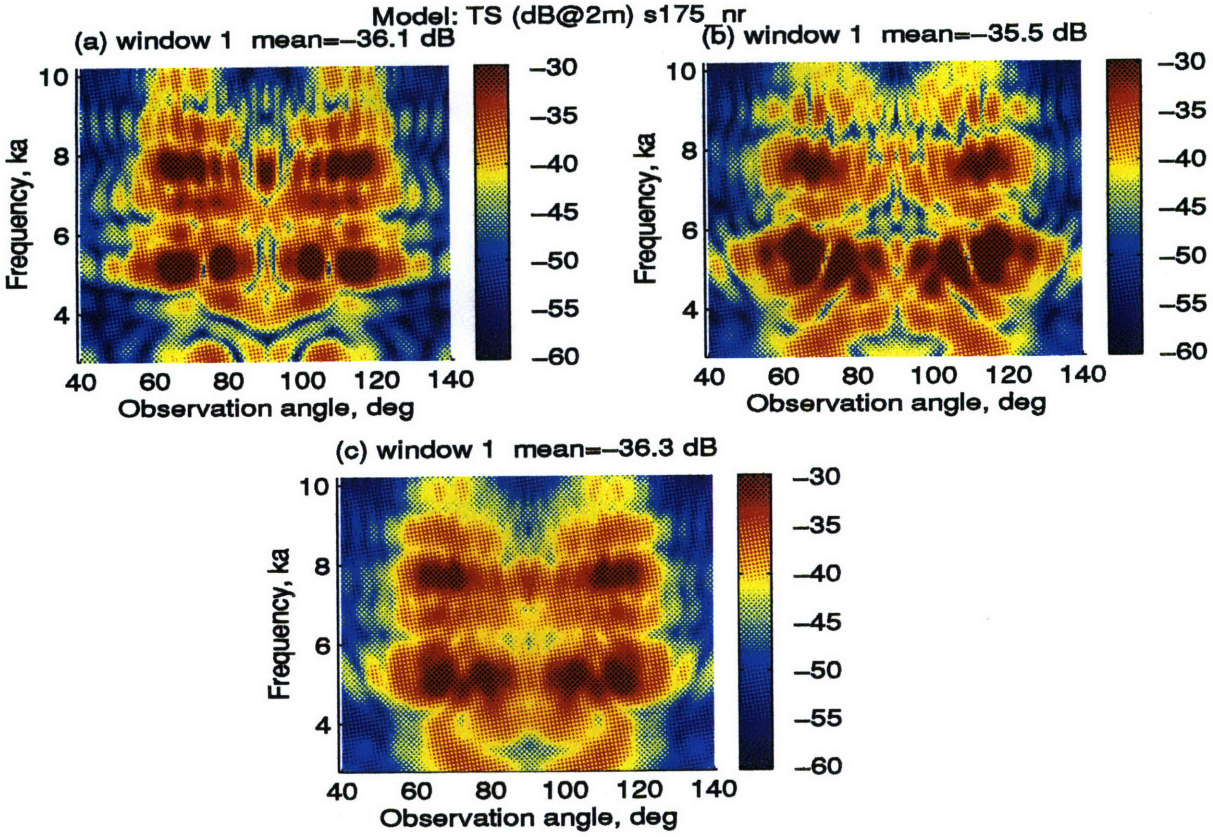

Figure 5-9: Predicted **ringed** shell bistatic target strength in dB re 2m in window 1 for sound incidence at 75°. Modified wave speeds are not used. (a), (b) correspond to results from two random phase realizations and (c) is the average over 6 random phase realizations. The logarithmic mean target strength over $60° < \theta < 120°$ and $3 < ka < 10$, $\bar{TS}$, is labeled in each contour.

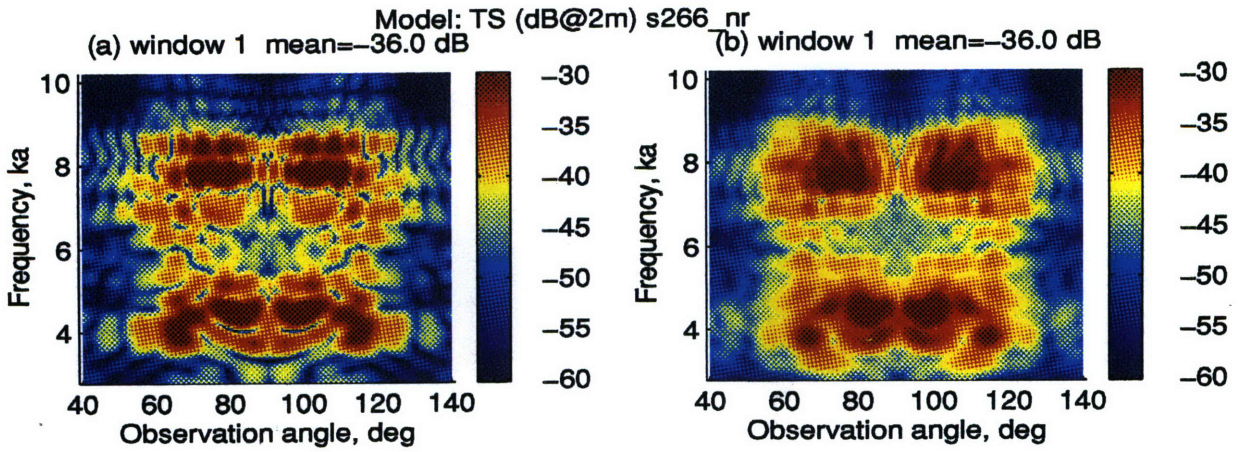

Figure 5-10: Predicted **Internalled** shell bistatic target strength in dB re 2m in window 1 for sound incidence at 66°. Modified wave speeds are not used. (a) is from one phase realization and (b) is the average over 6 random phase realizations. $\bar{TS}$ is labeled in each contour.

Prediction using modified wave speeds

The influence of the rings on wave speeds is studied in Sec.4.2.1. The modified wave loci are estimated from the simulation of the 1D bar system and the results are shown in Fig. 4-23. Note that the modified wave loci are in fact narrow strips, the center of which is determined by the mean and the width of which is determined by the standard deviation of the simulation results of 1D bar with 20 random location realizations of 4 identical M-K systems. The center and width curves of the modified wave loci in Fig. 4-23 are already smoothed by curvefitting in the $ka - k_x$ plane, making it possible to estimate modified group speeds by measuring the derivative of the curves.

To predict scattering, I use random wavenumber (or wave speed) realizations. For a fixed frequency, the modified wave locus becomes a rectangular window. In Fig. 5-11, the wave speed (wavenumber) is nonzero and equally likely within the wavenumber window, but vanishes outside the window. I choose one wavenumber that has equal likelihood within the wavenumber window and use it for the scattering prediction. This operation is then repeated for all the 140 frequencies within $3 < ka < 10$. Thus, a random wavenumber realization means that the wavenumber is randomly chosen within the finite wave strip.

The group speeds are obtained from the derivatives of the mean wave loci, which is fairly representative of the slope of the modified wave loci (strips). Thus, I only randomize phase speeds (wavenumber), but not the group speeds.

Adding random wavenumber realizations to random phase realizations, Fig. 5-12 displays the bistatic target strength for 66° incidence for time window 1. The left figure is from one phase realization and one wavenumber realization, while the right figure is the average over 6 random wavenumber realizations. In comparison with (a) of Fig. 5-10, the target strength in (a) of Fig. 5-12 is much more spread in the frequency region displayed. The prediction in Fig. 5-12 will be used in Sec.5.2.2 to compare with the measured data.

The average over 6 random phase realizations, shown in (b) of Fig. 5-12, yields the standard deviation of $\bar{TS}$, 0.5 dB. The averaging process significantly smears the pattern of the target strength. Moreover, the predicted target strength is essentially

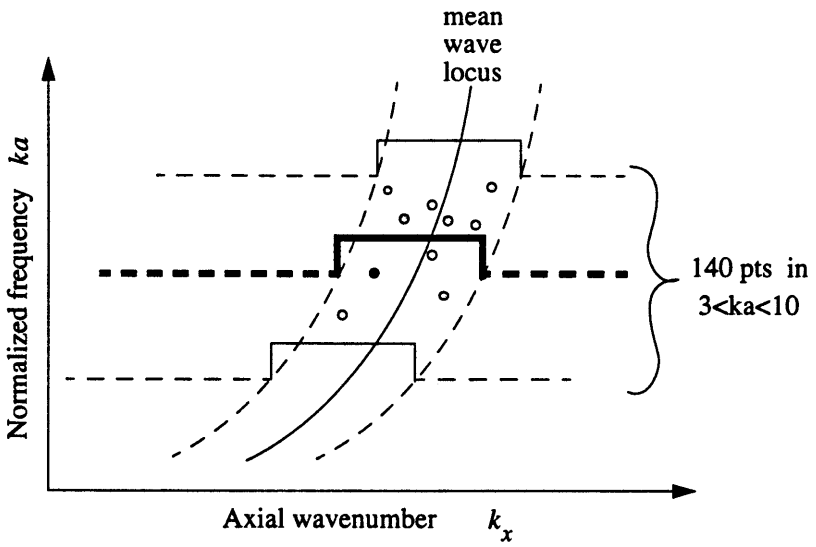

Figure 5-11: Illustration of random wavenumber realization.

the same even if a different wavenumber realization is used, possibly due to many frequency pins within $3 < ka < 10$. Therefore, one wavenumber realization is sufficient. Averaging over many wavenumber realizations is not necessary.

The mean target strength, $\bar{TS}$, in (b) of Fig. 5-12 is 1.7 dB smaller than in (b) of Fig. 5-10. I suspect that the smaller mean target strength is caused by weaker coherence introduced by random wavenumber realizations.

To demonstrate prediction in later time windows, Fig. 5-13 shows the target strength in windows 2 and 3 for 75° incidence. Both random phase and random wavenumber realizations are used. The decay for window 2 is the product of the estimated decay rate shown in Fig. 5-8 multiplied by $300\,\mu s$, the interval between windows 1 and 2. The decay for window 3 is the product of the estimated decay rate multiplied by $600\,\mu s$, the interval between windows 1 and 3. These time intervals for 75° and 66° incidence are defined in Fig. 3-13.

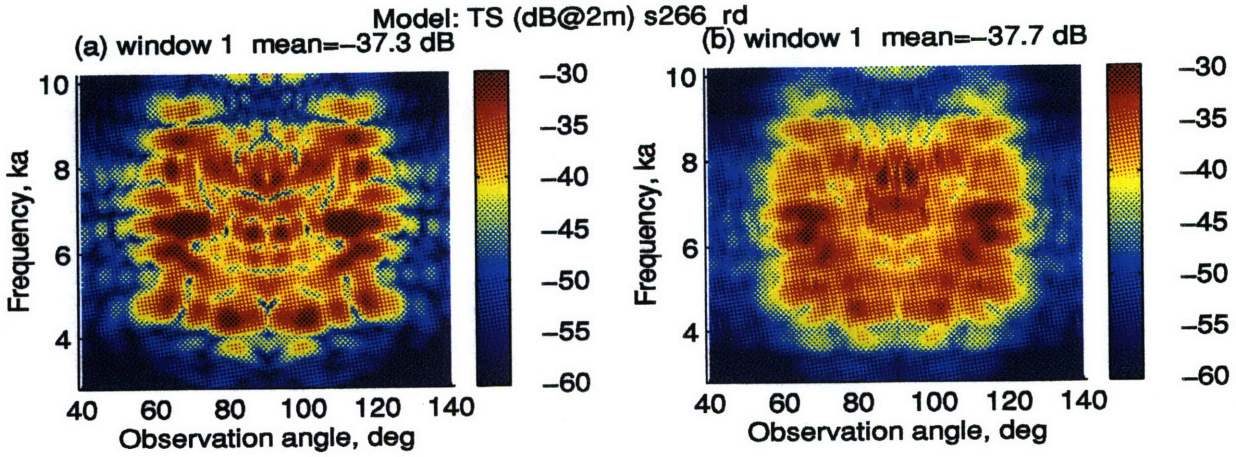

Figure 5-12: Predicted **internalled** shell bistatic target strength in dB re 2m in window 1 for sound incidence at 66°. Modified wave speeds are used. (a) is from one phase realization and one wave phase speed realization. (b) is the average over 6 random phase realizations. $\bar{TS}$ is labeled in each contour.

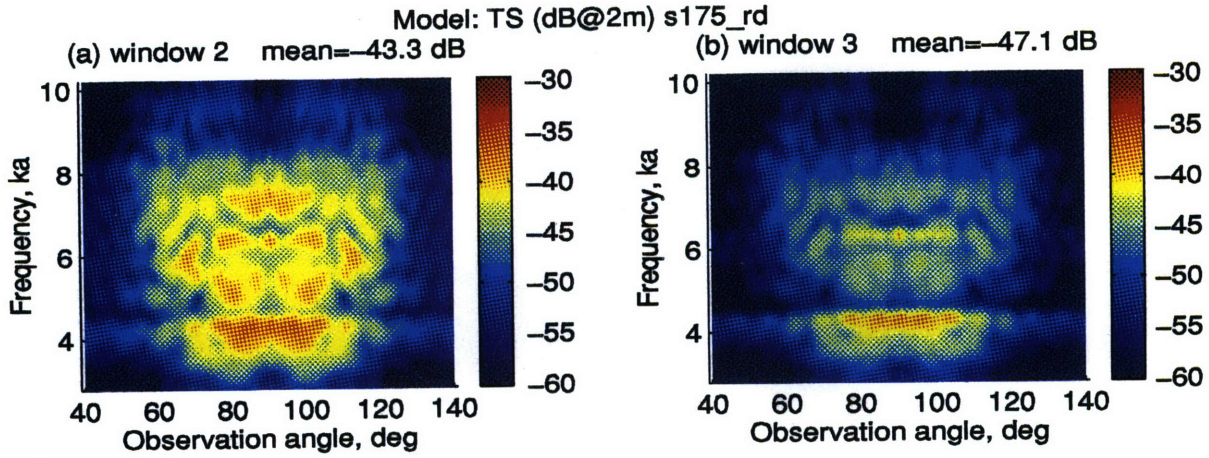

Figure 5-13: Predicted **ringed** shell bistatic target strength in dB re 2m in windows 2 and 3 for sound incidence at 75°. (a) is for window 2 and (b) is for window 3. Both random phase and wavenumber realizations are used. $\bar{TS}$ is labeled in each contour.

5.2 Measurement data and comparison with prediction

5.2.1 Measurement data

The MIT/NRL bistatic scattering measurement setup has been shown in Fig. 1-3. I will use the bistatic data at two sound incidence angles within the membrane wave region: 75° for the empty, ringed and internalled shells, and 66° for the internalled shell only.

The transient scattering signal at each receiver position is time windowed in the same way as shown in Fig. 3-13, except that the first time window is delayed by $44\,\mu s$ from the peak of the initial scattering signal. Such an operation is intended to remove the geometric scattering component from the total scattering and retain only the elastic scattering.

The target strength of the measured data is displayed for windows 1, 2 and 3. Fig. 5-14 displays the bistatic target strength of the ringed shell and the internalled shell at sound incidence of 75°. Fig. 5-15 shows the empty shell target strength at 75° incidence on the left and the internalled shell data at 66° incidence on the right.

For the empty shell model, the target strengths of the forward scatter and the backward scatter are not symmetric in windows 1, 2 and 3. For the ringed and the internalled shell, however, an approximate symmetry is observed in windows 1, 2 and 3.

The observed asymmetry in target strength for the empty shell in windows 2 and 3 is caused by two factors: strong backward shear wave radiation and weak forward wave radiation. First, the strong backward directed waves are due to the trace matched membrane wave interaction with the far endcap. The endcap not only makes the trace matched membrane waves convert to each other and to the subsonic flexural wave, but also greatly attenuates the compressional wave through sound radiation from the endcap, as discussed in Sec.2.1.2. The shear wave attenuation at the endcap is, however, very small. As a result, the shear wave is largely reflected at the endcap and contributes to the target strength in the backward direction. Second, the backward

shear wave attenuates greatly by the time it reaches the insonified endcap so that the forward going waves are weak and radiate much less sound than the backward waves do. The slower flexural wave is converted from the trace matched membrane waves at the far endcap. It then travels along the length of the shell to the insonified endcap. From there, the energy is converted back to the radiating compressional and shear waves. According to the transient wave power analysis in Sec. 3.3, this forward wave radiation does not become significant until after window 3.

The approach to symmetry in window 3 in the ringed and internalled shell data is caused by multiple wave scattering at the rings. Extensive wave interactions are completed by the time window 3 is reached, which leads to almost symmetric target strength for the ringed and the internalled shells. The logarithmic mean of target strength is evaluated over the same region ($3 < ka < 10$ and $60° < \theta < 120°$) as in the prediction, and is labeled in Fig. 5-14 and Fig. 5-15.

I also observe that the target strength of the ringed shell differs from that of the internalled shell. The internal structures seem to decrease the target strength, approximately, by 1 dB in window 1, 3 dB in window 2, and 3.5 dB in window 3. Therefore, the scattering of the internalled shell decays slightly faster than that of the ringed shell, and energy must be transferred to the internal structures. This observation is consistent with the decay rate measurement discussed in Sec.5.1, where I find the internalled shell tends to have a decay rate 30% larger than the ringed shell.

The scattering of the empty shell is largely limited to the membrane wave trace matching region. However, the target strength of the ringed shell, and especially the internalled shell, is still quite high outside the membrane wave region. A similar observation has been discussed in Sec.4.2.1. Apparently, the rings can considerably alter the wave speeds, which might affect the scattering.

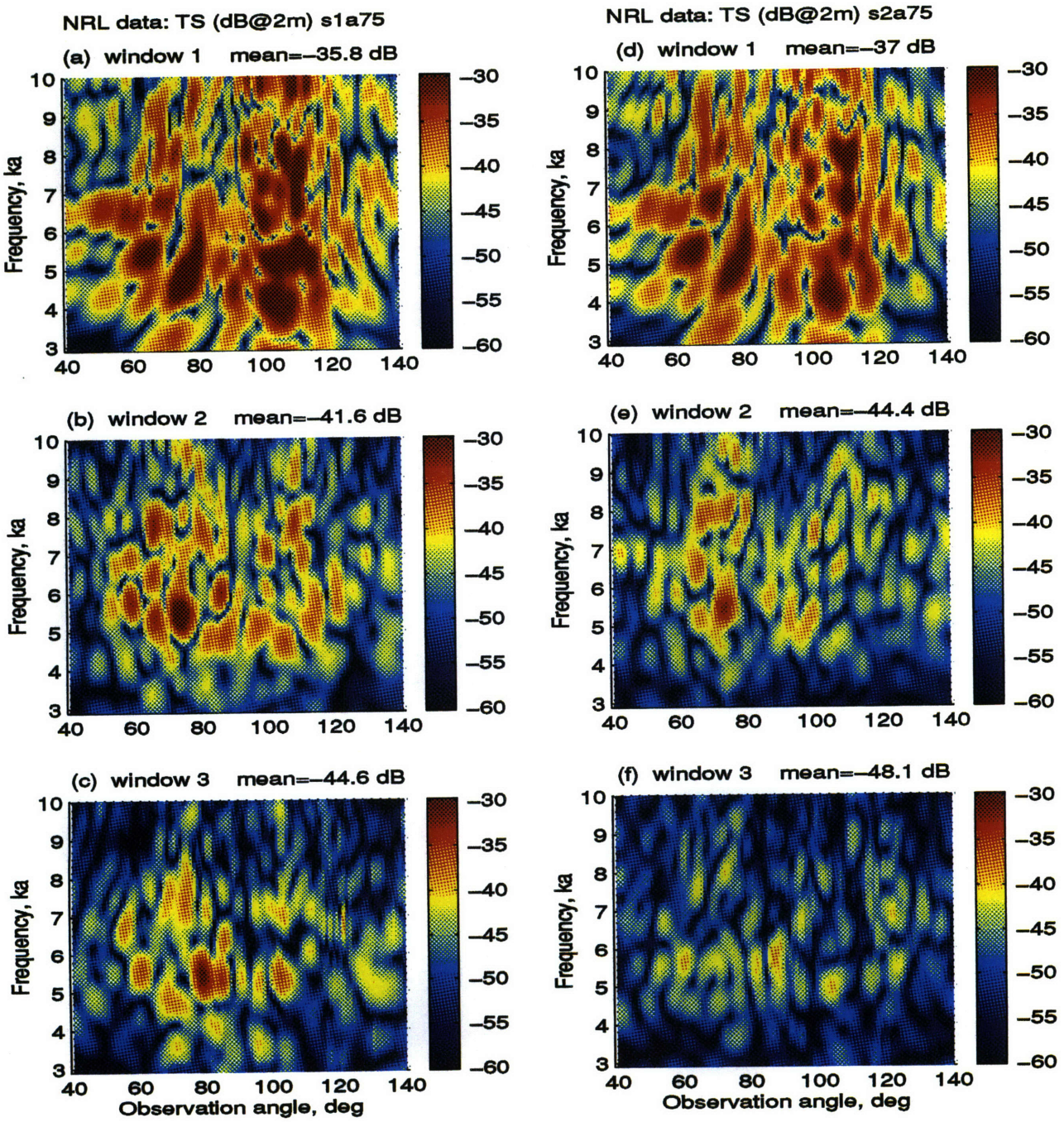

Figure 5-14: Measured bistatic target strength in dB re 2m in time windows 1, 2 and 3, corresponding to (a), (b), and (c) respectively for the **ringed** shell and (d), (e), and (f) for the **internalled** shell at 75° sound incidence. The logarithmic mean of the target strength over $60° < \theta < 120°$ and $3 < ka < 10$ is labeled in each plot.

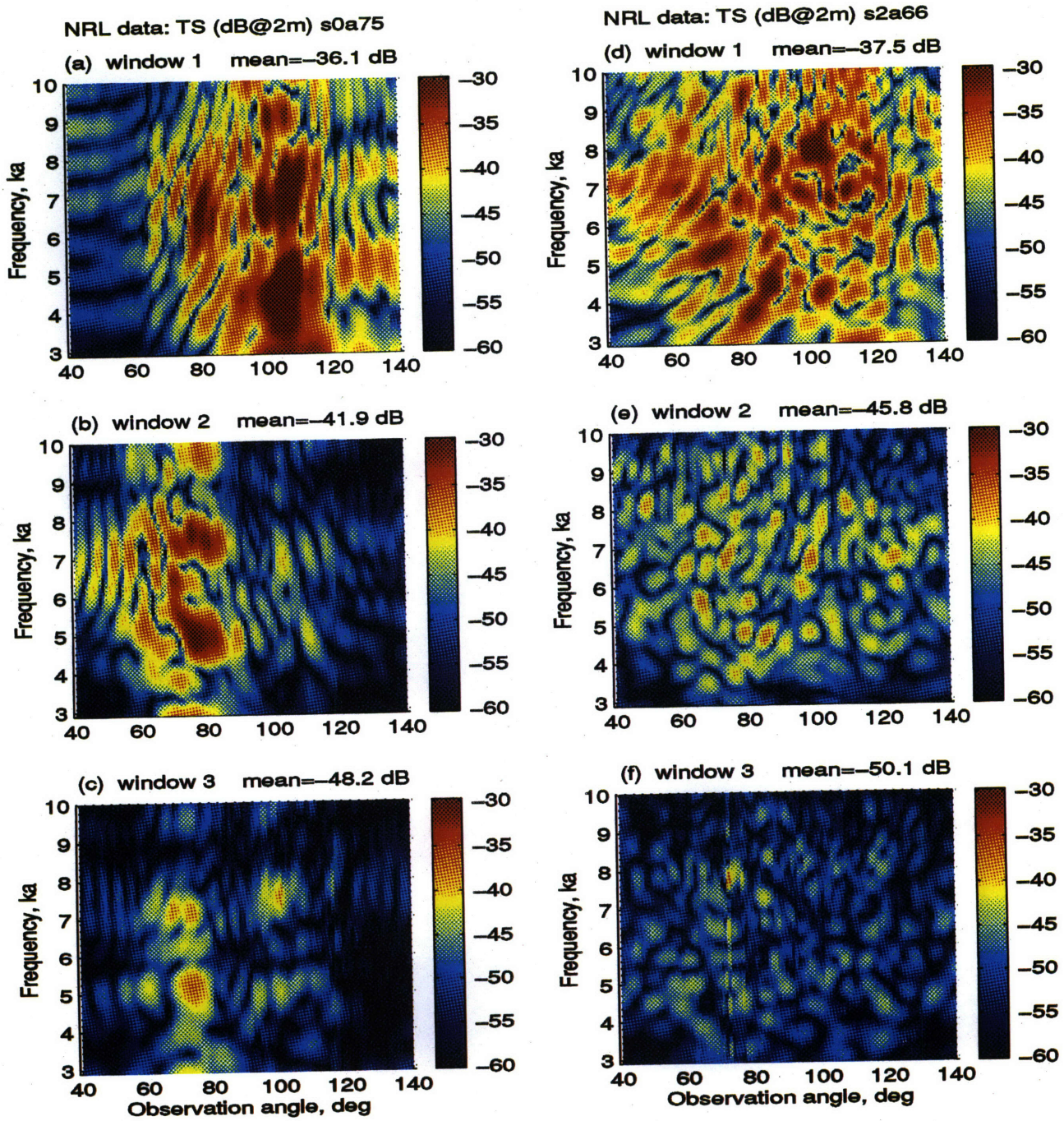

Figure 5-15: Measured bistatic target strength in dB re 2m in time windows 1, 2 and 3, corresponding to (a), (b), and (c) respectively for the **empty shell** shell at 75° sound incidence. Plots (d), (e), and (f) are for the **internalled** shell at 66° sound incidence. The logarithmic mean of the target strength over $60° < \theta < 120°$ and $3 < ka < 10$ is labeled in each plot.

5.2.2 Comparison with prediction

Note from Fig. 5-9 that the predicted target strength from two random phase realizations is not the same for a particular frequency or angle, but is similar if averaged over the $ka - \theta$ domain, for instance, in terms of $\bar{TS}$. Therefore, the comparison between the prediction and the measured data will not focus on the detailed scattering pattern, but on the global pattern and on average over the $ka - \theta$ domain. To do so, the prediction should be averaged over random phase realizations.

In the measurements, the shells are deterministic in structure. If there were no measurement uncertainties, the scattering from the shells is a deterministic process. However, measurement uncertainties, such as fluid pressure disturbances after each new setup is made, and the corresponding unwanted motion of the shell model and the transmitting and receiving hydrophones, might introduce random phase to the scattering process and make it less deterministic. At each incidence and observation angle, the measured data are averaged over 100 runs in order to reduce the influence of the measurement uncertainties and noise. By and large, the measured data can hardly be taken from an average over a fully random phase process. Thus, the comparison between prediction and measurement should again focus on the average in the $ka - \theta$ plane, than on the value at a particular frequency or angle.

To make the comparison easier, I place the measurement-prediction pairs on the same page, as shown in Fig. 5-16 for the ringed shell at 75° incidence, in Fig. 5-17 for the internalled shell at 75° incidence, and in Fig. 5-18 for the internalled shell at 66° incidence. The prediction consists of results from two different realization approaches: (c) and (d) are from using only random phase realizations, while (e) and (f) are from using both random phase realizations and a random wavenumber realization, as shown in Fig. 5-16, Fig. 5-17 and Fig. 5-18. The observation angle range is $60° < \theta < 120°$, instead of $40° < \theta < 140°$ used in the previous sections, because the prediction model is expected to work well in the membrane wave region. A prediction will be regarded as good if its averaged target strength over the region $3 < ka < 10$ and $60° < \theta < 120°$, or $\bar{TS}$, is within 2.5 dB of the measured data - one color step in the contour plots. The modified wave speeds are not used for the 75° cases, but are used for the 66° case. In the prediction, 6 random phase realizations

are used.

The direct model-data comparison is shown for windows 2 and 3 only. The direct comparison for window 1 is not reasonable and is not shown in the three figures. The reason is that several assumptions, which the prediction model is based on, such as wave power equipartition, might not be valid for window 1. Despite its disappearance in the direct visual comparison, the target strength in window 1 is listed by its mean, $\bar{TS}$, in Table 5.2, together with $\bar{TS}$ for windows 2 and 3, for the sake of completeness.

75° sound incidence (see Fig. 5-16 and Fig. 5-17)

In both windows 2 and 3, the predicted target strength using random phase realizations, in (c) and (d), is spread in the $ka-\theta$ plane, similar to the measured data in (a) and (b). The predicted target strength for the ringed shell, $\bar{TS}$, is 0.5 dB lower than that of the measured data. The predicted internalled shell target strength is 1.2 dB higher than the measured data. In window 3, the predicted $\bar{TS}$ for the ringed shell is 1.5 dB lower than the measured data. However, the predicted $\bar{TS}$ for the internalled shell is 0.7 dB higher than the measured data.

The predicted target strength using both random phase and random wavenumber realizations, in (e) and (f), also exhibits a similar global pattern to the measured data in (a) and (b), particularly below $ka = 8$. Above $ka = 8$, the prediction seems to be at least one color level smaller than the measured data. The lower target strength in the prediction might be caused by the lower trace matching frequency of the $n = 1$ compressional wave because of the reduced wave speed. Without the rings, the $n = 1$ compressional wave can be trace matched at approximately $ka = 9$, which explains why (c) and (d) have relatively stronger target strength above $ka = 8$. With the rings, the modified wave loci in the random wavenumber realization can easily shift the trace match frequency to below $ka = 8$, thus reduce the target strength above $ka = 8$ because no other modes are important in $8 < ka < 10$ except for the $n = 4$ shear wave.

In terms of $\bar{TS}$, the random wavenumber realization seems to make the prediction more close to the measured internalled shell data, although it is not so for the ringed shell. Table 5.2 lists the dB difference of $\bar{TS}$ for 75° incidence.

Table 5.2: Decibel difference between the predicted and measured mean target strength, $\bar{TS}$, evaluated over $3 < ka < 10$ and $60° < \theta < 120°$ for window 1 through 3. Positive value means the prediction is larger. 's1' and 's2' represent the ringed shell and the internalled shell respectively. 'a75' indicates sound incidence at 75°. Two different approaches are used in the prediction: one uses random phase realizations; the other uses a random wavenumber realization, in addition to random phase realizations, as shown in brackets.

Incidence angle	s1a75	s2a75
TS difference in window 1	-0.5 [-2.6]	+0.7 [-1.4]
TS difference in window 2	-0.7 [-1.7]	+1.2 [+0.1]
TS difference in window 3	-1.4 [-2.5]	+0.7 [-0.4]

Although wave power equipartition in window 1 is not evident from the numerical calculation of the ringed shell, I observe that the predicted ringed and the internalled shell target strengths differ from the measured data only slightly.

66° sound incidence (see Fig. 5-18)

In terms of the mean target strength, $\bar{TS}$, the prediction is close to the measured data. In window 2, the prediction using only random phase realizations in (c) is approximately 0.9 dB higher than the measured data. In window 3, the prediction in (d) is -1.5 dB smaller than the measured data. The prediction using both random phase realizations and random wavenumber realizations does not yield better agreement with the data. In fact, the prediction in (f) is -3.5 dB lower than the measured data, a difference larger than using random phase realizations alone in (d).

In terms of scattering pattern, the measured data display a rather uniform target strength distribution in the whole $ka - \theta$ plane, while the predicted target strength using random phase realizations, in (c) and (d), concentrates on two trace matching frequencies near $ka = 4$ and $ka = 8$. The predicted target strength using both random phase and wavenumber realizations, in (e) and (f), seems to reduce the frequency concentration to a certain degree. The sharp decrease of the predicted target strength for $ka > 8$ is due to the drastic increase of the estimated decay rate for the $n = 2$ mode as seen in Fig. 5-8. The drastic increase in decay rate is mainly caused by the drastic increase of the $n = 2$ compressional wave radiation damping near the *ad hoc* cutoff frequency. That is to say, the decay rate model for $n = 2$ near $ka = 8$ might be inaccurate because of the cutoff. Other explanations might be available, since the predicted target strength can still be fairly significant if the target strength in modes other than $n = 2$ is significant near or above $ka = 8$. This is possible for the measured data, because the axial asymmetry of the internalled shell might transfer wave energy across mode n. However, such a possibility is excluded in the prediction model.

Time integrated target strength

So far the comparison has been done in separate time windows. In the following, I will compare time integrated target strength in order to provide a different view of the scattering process.

The measured time integrated target strength caused by the elastic wave scattering is obtained by time windowing the impulse response in the time domain and then

transforming it back to the frequency domain. The time window starts $44\,\mu s$ after the geometric return and spans the whole effective data length in the MIT/NRL scattering measurements.

The predicted time integrated target strength is obtained in a different way. The wave power calculation and the direct radiation calculation are in steady-state, rather than in the time domain. Although a decay rate model is developed in Sec.5.1.3, it does not estimate the decay rate of the total scattering, but only for its fixed frequency component and mode n. As a result, it is impossible to use the same approach as in the measured data case. I take each frequency component of the steady-state target strength (harmonic response) and let it decay at $t = 0$ at a rate predicted by the decay rate model. I then apply the same time window as in the scattering measurements and transform the attenuated single frequency temporal response back into the frequency domain. In this way, the new target strength approximates the time integration, and is used to compare with the measurements. Fig. 5-19 displays the comparison for the ringed shell at 75° and the internalled shell at 75° and 66° respectively. Again, the logarithmic mean over $3 < ka < 10$ and $60° < \theta < 120°$ is labeled in each contour plot. I observe that the measured target strength has approximately the same magnitude in the forward and backward direction. The mean of the measured internalled shell target strength is 1.8 dB smaller than the measured ringed shell, for 75° incidence. The reduction is due to energy loss into the internal structures. In the prediction, only random phase realizations are used. The modified wave speeds are not considered.

In terms of the mean target strength evaluated over the $ka - \theta$ region, the prediction of the ringed shell is 1.6 dB lower than the measured data at 75°. The prediction of the internalled shell is different from the measured data by only a fraction of dB at 75° and 66°, respectively.

Summary of the comparison

The statistical model can predict the target strength of the ringed shell and the internalled shell target strength within ±2.5 dB, in window 2 and window 3. Table 5.3 displays the decibel difference of the logarithmic mean of the target strength, already

labeled in each contour plot. In general, the model works well within the membrane wave region, but not outside the membrane wave region. In terms of the mean target strength, $\bar{TS}$, a random wavenumber realization generally does not yield a better agreement with the measured data. Therefore, if one is interested in estimating an averaged target strength only (average at least along the frequency), random wavenumber realization is not necessary.

Table 5.3: Decibel difference between the predicted and measured mean target strength, evaluated over $3 < ka < 10$ and $60° < \theta < 120°$ for window 1 through 3. Positive value means the prediction is larger. 's1' and 's2' represent the ringed shell and the internalled shell respectively. 'a75' and 'a66' represent sound incidence at 75° and 66° respectively. Two different approaches are used in the prediction: one uses random phase realizations; the other uses a random wavenumber realization, in addition to random phase realizations, as shown in brackets.

Incidence angle	s1a75	s2a75	s2a66
TS difference in window 1	-0.5 [-2.6]	+0.7 [-1.4]	+1.5 [-0.2]
TS difference in window 2	-0.7 [-1.7]	+1.2 [+0.1]	+0.9 [-0.9]
TS difference in window 3	-1.4 [-2.5]	+0.7 [-0.4]	-1.5 [-3.5]
TS Difference, time integrated	-1.6	-0.1	+0.2

Discussion

In the above comparison between the prediction and the measured data, the mean target strength over the whole $ka-\theta$ plane, $\bar{TS}$, is used. This does not mean the model can only predict $\bar{TS}$. The comparison using $\bar{TS}$ is rather coarse. In the following, I discuss another way of comparing the prediction with the data, that is, to average over the frequency.

Fig. 5-20 and Fig. 5-21 show the frequency averaged target strength for the ringed and the internalled shells, respectively, at 75° incidence. Fig. 5-22 shows the frequency averaged target strength for the internalled shell at 66° incidence. The average is conducted over $3 < ka < 10$ using the real value of target strength rather than its decibel values.

The predicted target strength is no more than a few decibels above or below the measured data for most of the observation angles within $60° < \theta < 120°$. The mean evaluated over the angular region is similar to $\bar{TS}$ shown in Table 5.3. They are,

however, not identical because the former is the mean of decibel levels (along the angle) while the latter is the logarithmic mean.

The spike near 72° of the measured internalled shell target strength in window 3 (shown in Fig. 5-22) might be caused by noise contamination in the data. This abnormality is also observed in Fig. 5-15, plot (f).

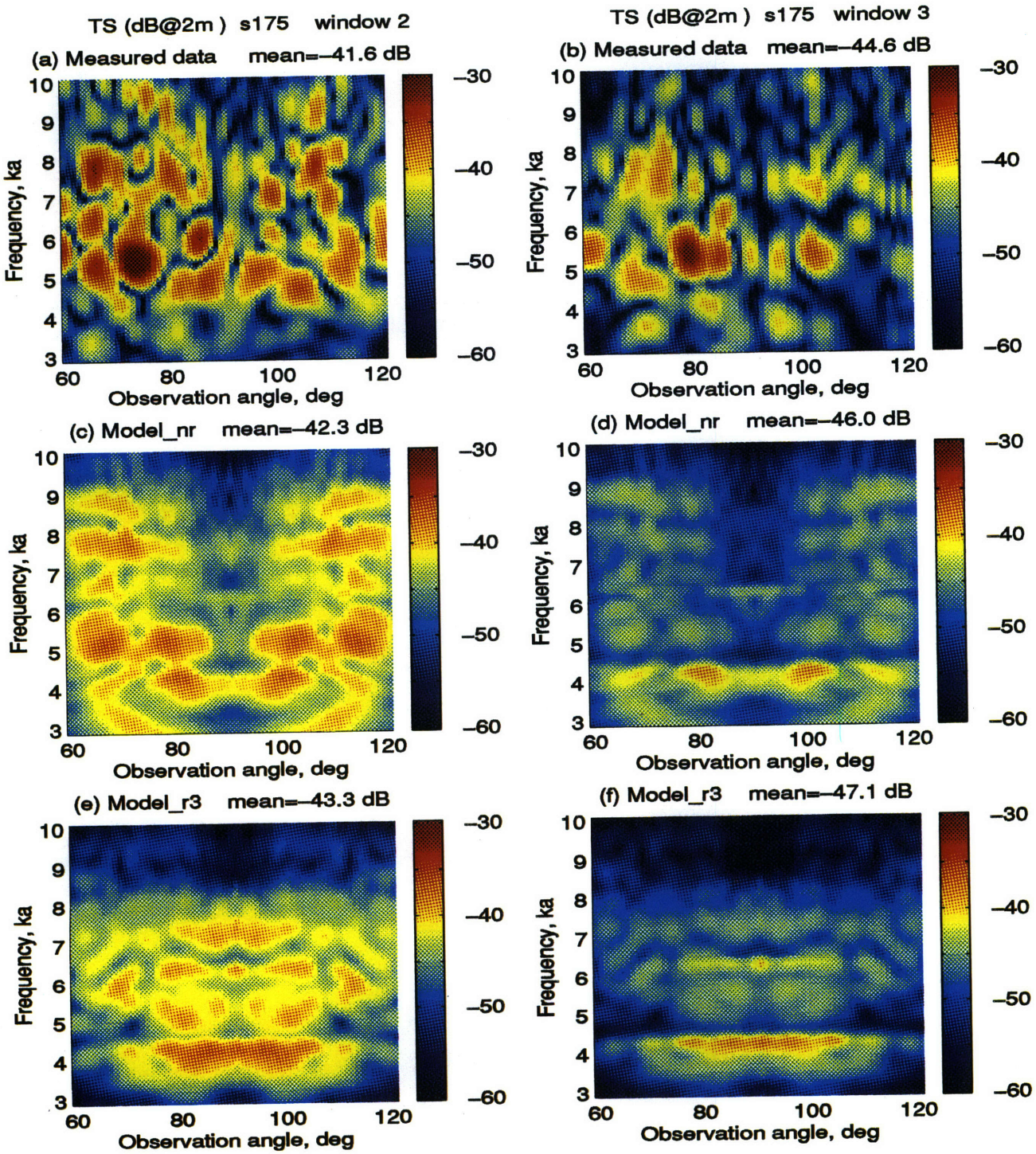

Figure 5-16: **Ringed** shell bistatic target strength in dB re 2m in window 2 and 3 for sound incidence at 75°. (a) and (b) are measured data; (c) and (d) are predictions using random phase realizations only; (e) and (f) are predictions using both random phase realizations and random wavenumber realizations. The logarithmic mean target strength over $60° < \theta < 120°$ and $3 < ka < 10$, $\bar{TS}$, is labeled in each contour.

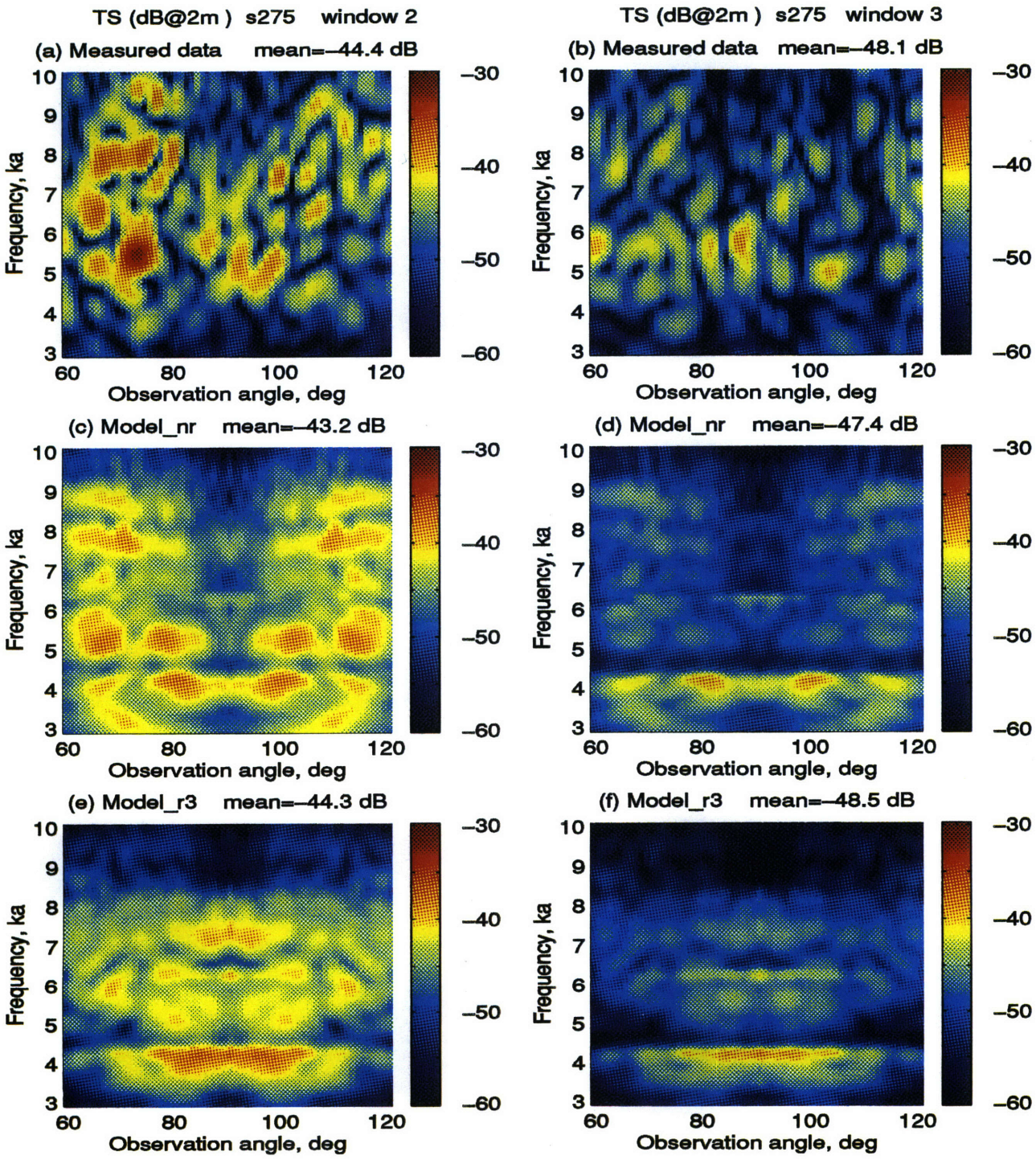

Figure 5-17: **Internalled** shell bistatic target strength in dB re 2m in window 2 and 3 for sound incidence at 75°. (a) and (b) are measured data; (c) and (d) are predictions using random phase realizations only; (e) and (f) are predictions using both random phase realizations and random wavenumber realizations. The logarithmic mean target strength over $60° < \theta < 120°$ and $3 < ka < 10$, $\bar{TS}$, is labeled in each contour.

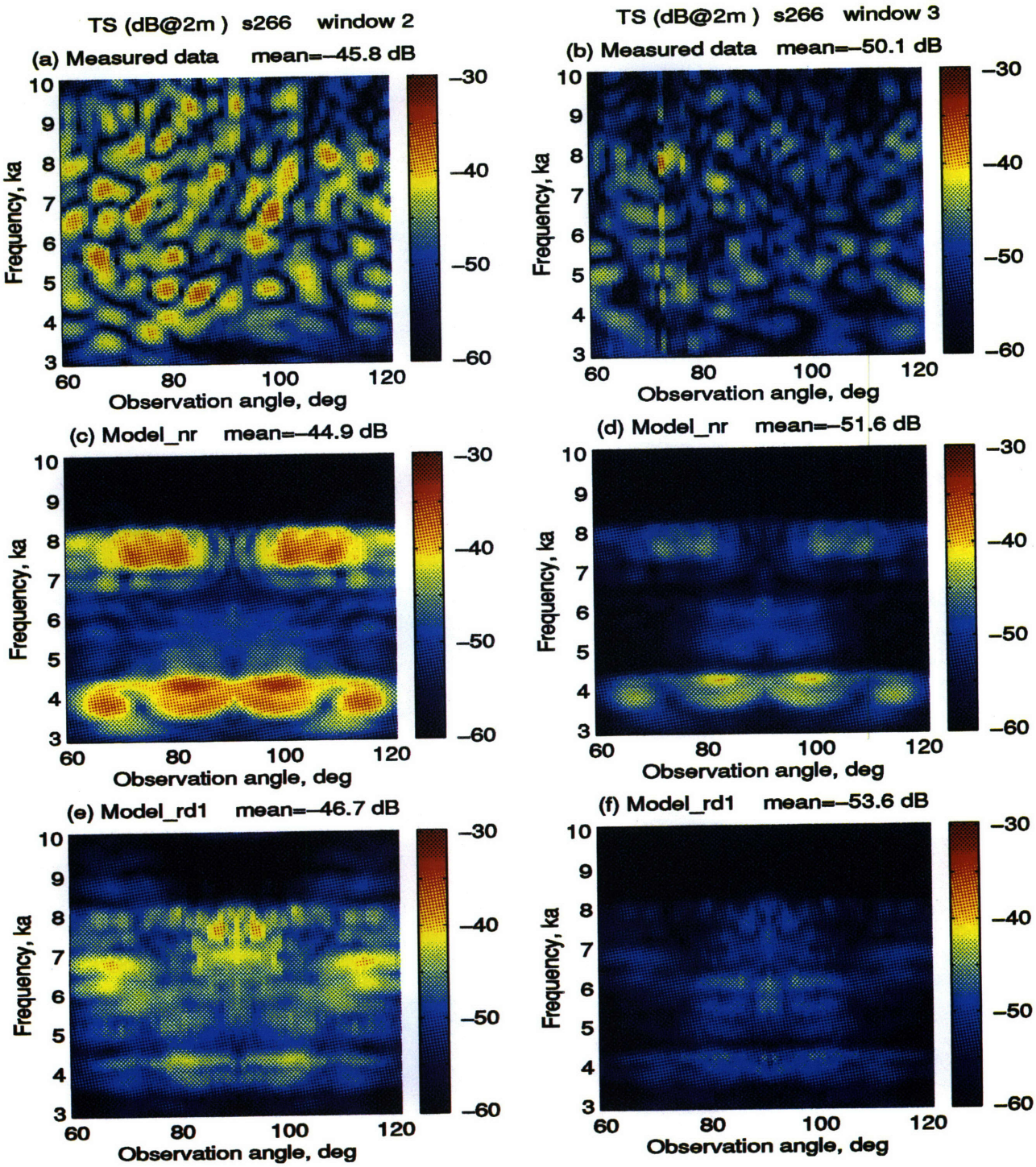

Figure 5-18: **Internalled** shell bistatic target strength in dB re 2m in window 2 and 3 for sound incidence at 66°. (a) and (b) are measured data; (c) and (d) are predictions using random phase realizations only; (e) and (f) are predictions using both random phase realizations and random wavenumber realizations. The logarithmic mean target strength over $60° < \theta < 120°$ and $3 < ka < 10$, $\bar{TS}$, is labeled in each contour.

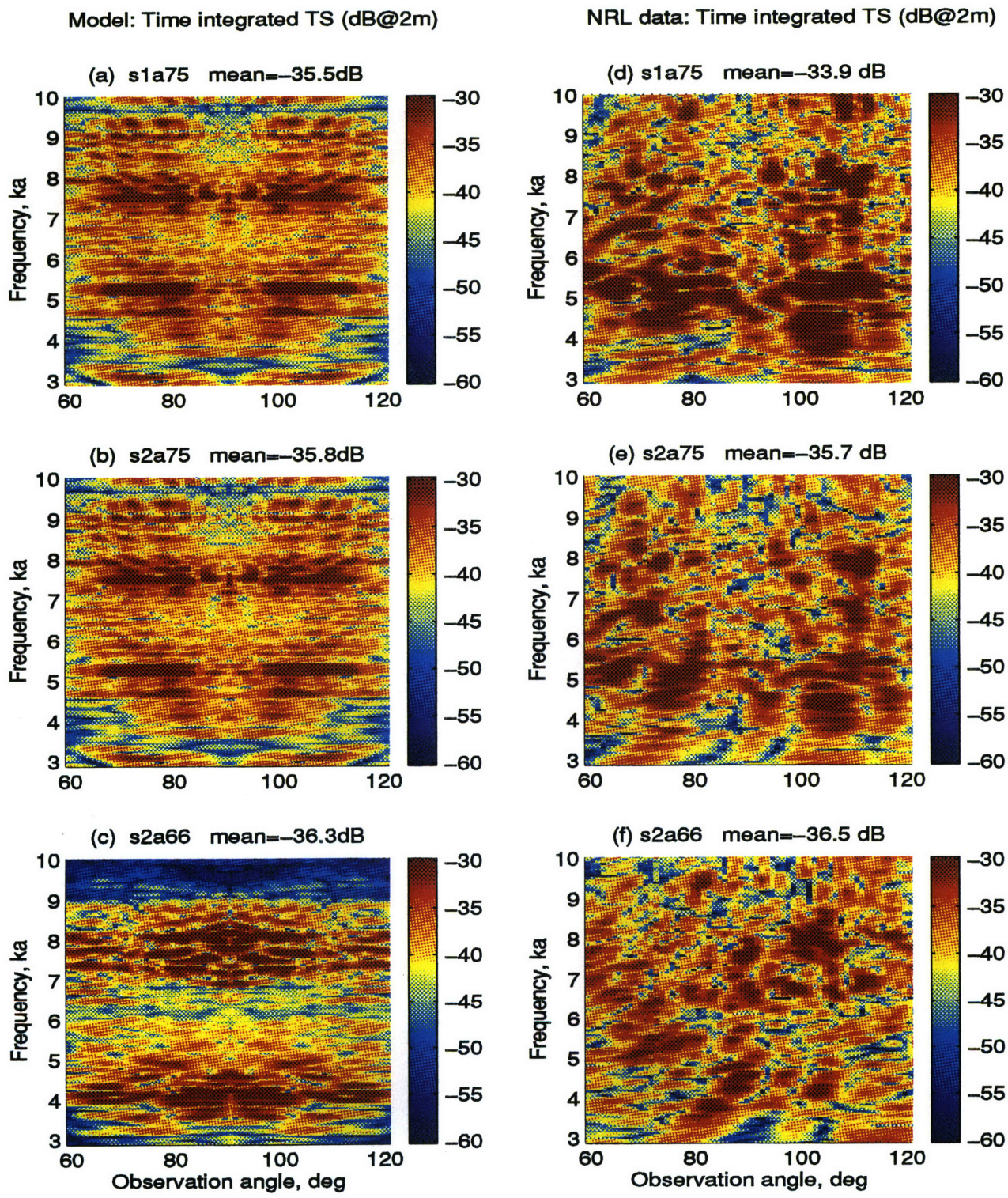

Figure 5-19: Time integrated bistatic target strength in dB re 2m. Contour (a-c) are predictions and (d-f) are the MIT/NRL measured data. (a, d) are the ringed shell for incidence at 75°. (b, e) are the internalled shell for incidence at 75°. (c, f) are the internalled shell too, but for incidence at 66°. In the prediction, only random phase realizations are used. The logarithmic mean target strength over $60° < \theta < 120°$ and $3 < ka < 10$ is labeled in each contour.

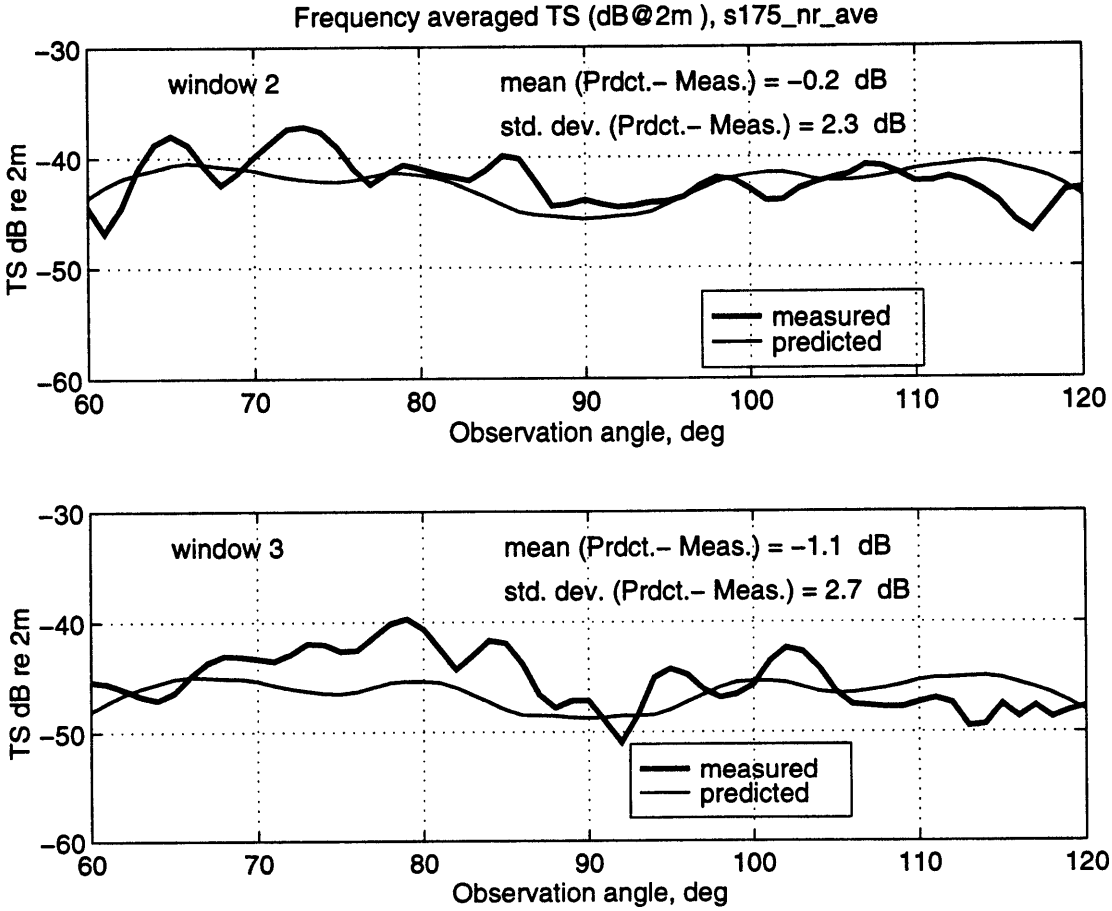

Figure 5-20: **Ringed** shell bistatic target strength in dB re 2m in window 2 and 3 for sound incidence at 75°. The prediction is averaged over 6 random phase realizations. The target strength is averaged over the frequency band $3 < ka < 10$. The mean and standard deviation of the decibel difference (prediction minus measurement) are labeled in dB.

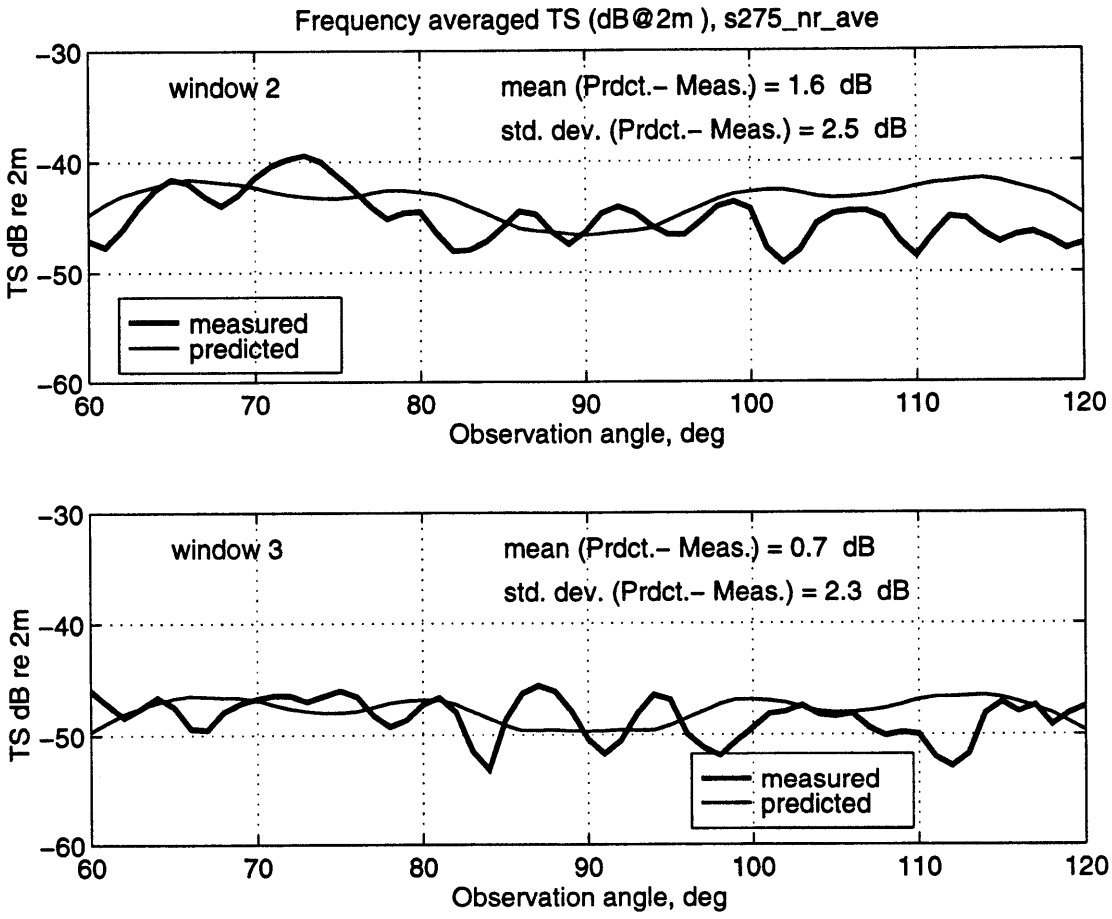

Figure 5-21: **Internalled** shell bistatic target strength in dB re 2m in window 2 and 3 for sound incidence at 75°. The prediction is averaged over 6 random phase realizations. The target strength is averaged over the frequency band $3 < ka < 10$. The mean and standard deviation of the decibel difference (prediction minus measurement) are labeled in dB.

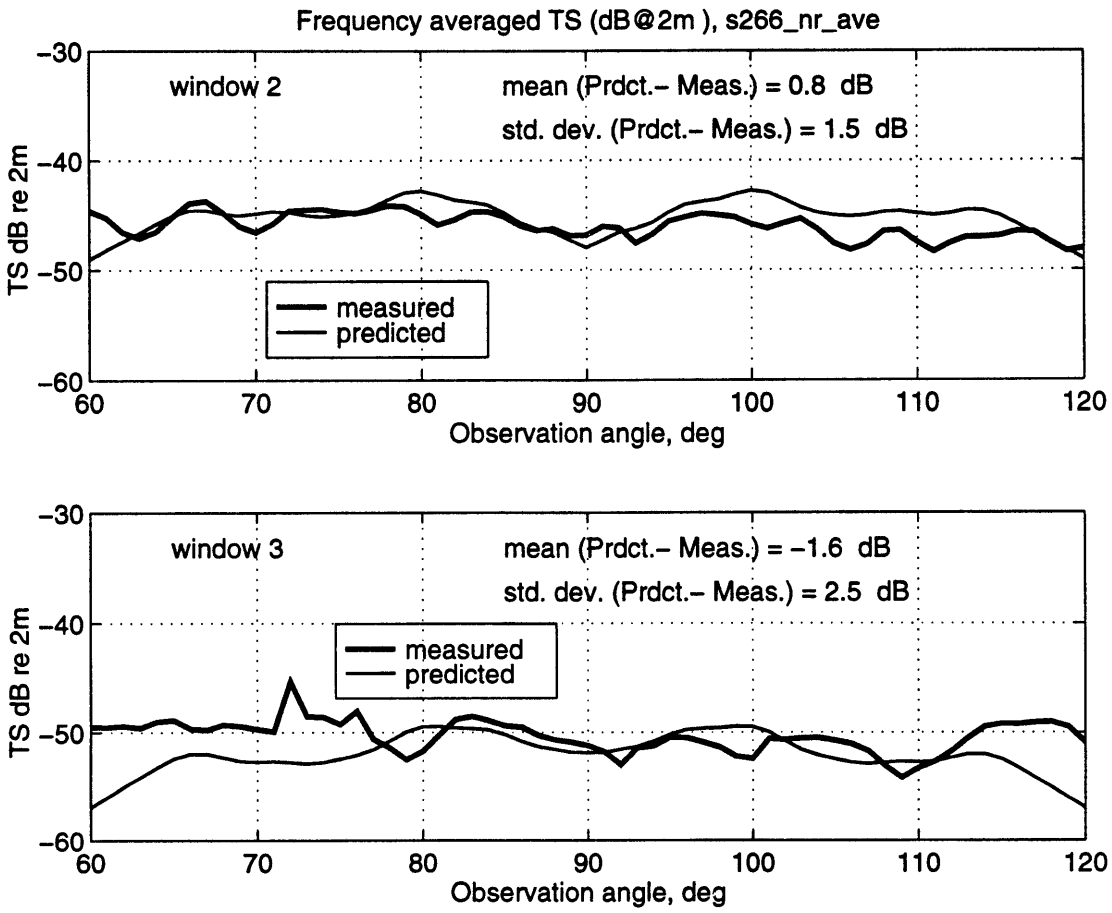

Figure 5-22: **Internalled** shell bistatic target strength in dB re 2m in window 2 and 3 for sound incidence at 66°. The prediction is averaged over 6 random phase realizations. The target strength is averaged over the frequency band $3 < ka < 10$. The mean and standard deviation of the decibel difference (prediction minus measurement) are labeled in dB.

5.3 Applicability of the prediction model

To provide a general description of the strength and limitations of the statistical model, this section examines the assumptions and approximations used in its development.

- The statistical model is designed to predict the general trend of elastic wave scattering behavior of finite complicated shells. Thus, the model is not intended to predict detailed target strength along the frequency, time or aspect angle coordinates. In addition, no geometric scattering is considered in the model. Thus, the model must be supplemented with a geometric response model (Ref. [1]) in order to predict total scattering.

- The key assumption of the model is elastic wave power equipartition. The numerical calculations in this study indicate at least approximate wave power equipartition for the ringed shell. Stronger wave coupling at the rings and the endcaps, relative to wave dissipation, accounts for the equipartition. Most finite complicated shells in the real world have several heavy ring-like bulkheads and possibly heavy keels (stringers), all of which create strong elastic wave coupling. I therefore expect elastic wave power equipartition to be valid in most shells of practical concern. In addition, sound trace matching serves as distributed forcing that can inject sound energy into the shell globally and possibly into multi-wave types simultaneously. Such forcing can accelerate wave coupling and energy mixing and thus can help to achieve the equipartition of elastic wave power earlier in time.

- Sound incidence in the statistical model is limited to the region $60° < \theta < 120°$, because I assume that a finite shell is acoustically excited by trace matching in the cylindrical shell section only. Within $60° < \theta < 120°$, shear and compressional waves can be trace matched strongly, so that other mechanisms are relatively less important. Outside this region, other forms of forcing must be considered, but the possibility of elastic wave power equipartition is still likely to be met, at least under some conditions in the frequency, time and aspect angle domains.

- The observation region is also limited to $60° < \theta < 120°$. Inside this region, the membrane waves, either trace matched or not, dominate the radiation. But outside the region, other processes such as the endcap radiation, neglected in the model, might become important.

5.4 Summary

This chapter extends the prediction model to the time domain. I estimate the scattering decay trend, predict the scattering and compare it with the measured data. I conclude that the statistical model provides a satisfactory prediction of the elastic wave scattering from both the ringed and the internalled shells. The predicted target strength, averaged over the membrane wave region $60° < \theta < 120°$ and frequency band $3 < ka < 10$, differs from the MIT/NRL measured data by no more than ± 2.5 dB, in windows 2, 3 (2nd and 3rd roundtrip time of the trace matched wave in the shells), as well as in the time integrated case. The consideration of the modified wave speeds in the prediction model does not yield better agreement with the measured data. The unmodified wave speeds (from the infinitely long uniform shell) alone can provide acceptable prediction results.

The prediction model does not work outside the membrane wave trace matching region. Outside the membrane wave region, trace matching is impossible. Other sound excitation mechanisms such as endcap radiation and subsonic flexural wave radiation must play important roles and must be included.

The decay rate model developed in this section provides an understanding of the elastic wave decay trend in finite complicated shells. I show that the shell decay rate does not equal the decay rate of any particular elastic wave, but is a weighted average of the decay rates of all the elastic waves. The weight is determined, in the case of wave power equipartition, only by the elastic wave group speed ratios. The estimate of the decay rate for each wave type includes the effect of radiation damping from the shell section, the coupling loss at the endcaps, the coupling loss into the internal structures, as well as the shell material damping. This decay rate model proves acceptable, and its estimate of the decay rate of the ringed shell and the internalled shell is less than

14% higher than the MIT/NRL measured data. Finally, the internal structures are found to increase the total scattering decay rate by approximately $25-30\%$, obtained from both the prediction and the measurement.

Chapter 6

Summary of the thesis

6.1 Summary of the results

This thesis formulates and tests the concept of elastic wave power equipartition and uses it as a hypothesis to predict bistatic sound scattering from finite elastic shells in water. The statistical model provides a simple, quick and inexpensive way of estimating elastic scattering from finite complicated shells, and does not suffer from the numerical difficulties that plague conventional numerical approaches. The conventional approaches, however, give both the geometric and elastic wave scattering components, while the present statistical model only gives the elastic wave part. Of the two, the elastic wave component is by far the most complicated. By adding the statistical model developed here to a simple geometric model, such as those already in the literature [1], a total estimate of scattering can be readily made.

The basic idea of the statistical prediction model is to treat compressional, shear and flexural waves as coupled systems and to investigate a simple statistical description of the power and energy ratios among the elastic wave types. Each wave type has a different wave speed and can radiate sound uniquely like an array with a finite aperture. Once the strength and phase speed of each wave type is known, the sound radiation is then the sum of contributions from each wave.

In the case of shell scattering, the incident sound can inject energy into the elastic waves in the shells. Within about 30° of beam aspect, the supersonic elastic membrane

waves are apt to be excited by acoustic trace matching. Once excited, the elastic waves are coupled and converted at shell discontinuities such as bulkheads and endcaps. The energy of each wave is thus redistributed among the wave types. With many shell discontinuities functioning as strong elastic wave scatterers, it is then reasonable to hypothesize that the strong wave coupling can offset wave dissipation and cause the wave power (energy flux in shell cross section) to be equipartitioned among the elastic waves. The concept of wave power equipartition is similar to the commonly known concept of modal energy equipartition in traditional SEA. In fact, I show that the definition of wave power, energy density times wave axial group speed, is proportional to the modal energy in SEA.

To test the wave power equipartition hypothesis, the MIT empty and ringed shells are modeled by a finite element approach, using SARA-2D. According to the numerical analysis, the elastic wave power is at least approximately equipartitioned for the ringed shell with four heavy deep rings. Thus, the wave power equipartition hypothesis is plausible for the ringed shell. For the empty shell, no wave power equipartition is found in the early scattering process. Sec.6.1.3 summarizes related results in detail.

Elastic wave power equipartition is a powerful tool because it allows one to derive any elastic wave strength once the total injected power is known, by means of energy conservation. Mathematically, the equipartitioned wave power is expressed as the injected wave power divided by the elastic wave group speed ratios. This greatly simplifies the relationship among the elastic waves which is otherwise extremely difficult to determine for finite complicated shells. The usefulness of this tool is demonstrated in this study by predicting elastic wave scattering from finite complicated shells in water for the mid-frequency range $3 < ka < 10$.

In order to predict elastic wave scattering based on elastic wave power equipartition, three major steps are taken. The first is to compute the sound power injection into finite shells. The second is to build a radiation model to project the wave motion into sound pressure in the fluid. The third is to convert the steady-state scattering from the first two steps into the time domain and to compare the predicted target strength with the measured transient scattering data. The first two steps will be summarized in Sec.6.1.1 and the third will be summarized in Sec.6.1.2.

6.1.1 Sound injection and radiation modeling

The sound power injection into finite shells is obtained not directly, but indirectly through calculation on a infinitely long shell. I restrict sound incidence to the membrane wave region, $60° < \theta < 120°$, so that acoustic trace matching to the membrane waves dominates the excitation. Other excitation mechanisms in finite shells, such as acoustic induction at endcaps and the rings, are of secondary importance. As a result, the injected sound power per unit length is the same, whether it be an infinitely long shell or a finite shell. For the infinitely long shell, this injected sound power is readily calculated by means of Donnell's thin shell theory. Once the injected sound power is obtained, the power in each elastic wave becomes the injected sound power scaled by a factor that is related to the elastic wave group speed ratios only.

In the sound radiation modeling, I consider sound radiation from the cylindrical section of the shell while I ignore the endcap radiation. According to the numerical analysis, the endcap radiation is insignificant if the receivers are within the membrane wave region, $60° < \theta < 120°$. This observation is further supported by experimental evidence. What is more, this observation of small endcap radiation also justifies the neglect of acoustic excitation at the endcap for sound incidence in $60° < \theta < 120°$, as well as the use of the infinitely long shell excitation model, since acoustic excitation and radiation are in principle reciprocal processes.

The sound radiation model is based on Green's theorem. However, the input of Green's theorem requires detailed complex surface pressure and radial velocity, while the wave power calculation only outputs the magnitude of the total velocity. To fill the gap, I estimate the following variables and test the estimates numerically using SARA-2D:

1. the axial wave phase speed
2. the surface pressure
3. the radial velocity

I find it possible to estimate the axial wave speed and radial velocity for the ringed shell through a calculation on the infinitely long cylindrical shell. Once the radial

velocity is known, the surface pressure are approximated by the momentum equation. The comparison with the direct SARA-2D calculation shows that the approximations are satisfactory, with an error less than 2 dB.

Furthermore, the experimental observation and numerical calculations show that the rings hardly affect the flexural axial wave speed, but decrease the axial membrane wave speeds considerably (from several to tens of per cent) for $ka > 5$. The reason is that the ring spacing in this study is smaller than, or comparable to, the membrane wavelength, the phase shift caused by the rings has notable effect on the membrane wave speeds. The ring spacing, on the other hand, is much large for the flexural wave, so its speed is much less affected. The membrane wave speed change is further estimated using a simple statistical model of a 1D bar system with several resonators. In spite of the wave speed change, I find the membrane wave region is only slightly modified (by $2° - 3°$), because the $n = 1$ shear wave phase speed is decreased by approximately 6% near $ka = 9$.

6.1.2 Transient scattering prediction

No phase is retained in the steady-state wave power calculation. The measured scattering is, on the other hand, transient. I need to extend the steady-state scattering into the time domain, not only because I need to compare the prediction to the measurements, but also because the elastic wave scattering can be conveniently identified, examined and separated in the time domain.

Two steps are taken to predict the transient scattering. First, random phase realizations transform the steady-state sound pressure into the time domain. Second, a model is built to predict the decay rate of the elastic wave scattering by using the hypothesis of elastic wave power equipartition. The decay rate model shows that the elastic wave response, as a whole, decays at a rate not dictated by any particular wave type, but rather by weighted contributions from all the elastic wave types. The weight is determined by the group speed ratios only. The decay rate of each wave type is estimated with the following mechanisms considered: (1) radiation from the cylindrical shell; (2) coupling loss at the endcaps (3) coupling loss into the internal structures and (4) material damping. The coupling loss at the endcaps is due to wave

Table 6.1: Summary of input information needed and not needed by the prediction model.

Information needed
shell length
shell radius
shell thickness
shell material
number of rings
ring thickness
ring width
ring density
Information not needed
detailed ring location
detailed ring-shell joint
all internal properties

conversion to compressional waves which radiate sound heavily there. The estimated decay rate is close to the MIT/NRL measurement analysis of the ringed shell and the internalled shell, with overpredictions no more than 14%. Further, the decay rate model estimates that the internal structures increase the total scattering decay rate by approximately 25%. The similar trend is observed in the measured data as well.

Finally, I predict the transient elastic scattering from two finite complicated shells, a ringed shell and an internalled shell. Each shell has the same shell length, radius, thickness and material property as the MIT empty shell model. To estimate the wave decay rate into the internalled shell, the dimensions, material as well as the number of the rings are needed. The ring information is obtained from the MIT/NRL ringed and internalled shell models. Table 6.1 summarizes the input information needed and not needed by the prediction model.

For sound incidence at 75° and 66°, both measured data and the predicted target strength contour in the $ka - \theta$ domain is displayed in separate time windows, corresponding to the integer number of the roundtrip periods of the trace matched wave in the shells. In addition, I compare the time integrated target strength for the prediction and the data. I find that the predicted target strength averaged over the angular

region $60° < \theta < 120°$ and frequency $3 < ka < 10$ is quite acceptable for sound incidence at the two angles. Table 5.3 summarizes the comparison for sound incidence at 66° and 75°. In general, the prediction is within 2.5 dB of the measurement data.

Moreover, consideration of the modified wave speeds in the prediction model does not seem to yield a better agreement with the measured data.

The discrepancies observed between the prediction and the measured data might be caused by the exclusion of other sound excitation mechanisms such as acoustics induction at the endcaps and the rings, especially near 60° and 120° and outside the region $60° < \theta < 120°$.

6.1.3 More on elastic wave power equipartition

The numerical analysis of the wave power in the time domain demonstrates that the elastic wave power takes time to reach wave power equipartition in the ringed shell (with 4 rings). In window 1, defined as the 1st roundtrip time of the trace matched wave in the shells, the flexural wave power is 8-10 dB less than the membrane wave power, i.e. wave power is not equipartitioned. However, the flexural wave power increases considerably in window 2 and the power difference among the elastic waves is less than 3 dB for most frequency bands. That is, wave power is approximately equipartitioned in window 2. In the later time windows, the wave power difference remains small and the power of different elastic wave attenuates at almost the same rate. The numerical calculation also indicates that even with two rings or one rings attached, the wave power equipartition is still approximately true, although it occurs one window later in time. Finally, the steady-state wave power analysis shows that the relative wave power difference are weakly dependent upon frequency, and slowly varying over the incidence angle for the ringed shell. In comparison, the numerical wave power analysis shows that the power difference among the elastic waves for the empty shell is typically 5-10 dB. No elastic wave power is equipartitioned for the empty shell, at least for the first 6 time windows observed.

Thus, the heavy elastic rings play a crucial role in the equipartitioning of the elastic wave power. The rings not only create significantly more wave interaction rate

($\sim (n_{ring}+1)^2$), but also function as strong elastic wave scatterers themselves. This latter point can be demonstrated by the fact that even one ring can make a drastic difference in wave power behavior, compared to that of the empty shell.

Although the wave power equipartition concept is tested in this study for the case of the ringed shell, and for sound incidence near beam aspect, I expect that it holds true for other finite complicated shells, and under other forms of excitation as well. Any shell discontinuity, even a single point, can convert wave energy from one type to others. Since most finite shells of practical concern have numerous stiffeners and other forms of discontinuities, I expect wave power equipartition to be true in many cases.

6.2 Suggestions for future work

This thesis considers elastic wave scattering which normally dominates backscattering. In forward or specular directions, however, the geometric scattering plays an important role. By adding a simple but separate model for the geometric scattering to the current elastic wave scattering model, one can predict the complete bistatic scattering process.

I am convinced that trace matching is able to capture the major elastic scattering process via energy injection into and emission from finite shells within the angular region considered. However, the comparison between the prediction and measurements indicates that other mechanisms can play some role as well, and a very important role outside the trace matching region. Therefore, another topic for future work is to expand the applicability of the prediction model for elastic wave scattering to sound incidence outside the trace matching region.

Apart from considering more excitation and radiation mechanisms, the cross-mode energy sharing among the elastic waves is another important topic. In the current shell model, the ring and endcap discontinuities are axisymmetric so that the elastic wave of mode n couples only to another wave of the same mode n. Once axial symmetry is destroyed, such as by having a stringer in the shell, cross-mode coupling can become important. The current statistical model should be modified to account

for such an effect, and is expected to describe the physical systems better in doing so.

Further, the wave power equipartition concept can be used to solve sound radiation problems in air. Generally, flexural waves dominate sound radiation in air while membrane waves have poor coupling to the air, contrary to the case in water. Traditionally, membrane waves are often ignored in dealing with sound radiation in air. However, ignoring the membrane waves can cause serious errors in some cases. One such case is transient sound radiation. In this study, the flexural wave plays a very important role in scattering, even if it does not radiate strongly. Similarly, membrane waves should be considered in air even if they might radiate poorly. Even in steady-state, membrane waves which are energized by conversion from the flexural waves at structural discontinuities may not convert the energy back to the flexural waves because they can attenuate by other means than sound radiation to air, such as coupling loss to other elastic or fluid media which are outside the systems considered. In such a case, the membrane wave should not be ignored. Moreover, the associated sound radiation prediction scheme has basically no restriction on frequency, and therefore is a very promising possibility for tackling the mid-frequency noise problems, commonly of interest in the aerospace and automobile industries.

Appendix A

Donnell thin cylindrical shell equations

Donnell's thin shell theory [2] is one of the many shell theories developed to describe dynamic motions of shells. It is justified to use Donnell's thin shell theory in this thesis because the shell models considered satisfy two conditions:

- The wavelengths of the elastic waves in the shells are large compared with the shell thickness ($\lambda_s > 20h$). In these cases the transverse shear and rotatory inertia may be neglected.
- The radii of curvature are large compared with the shell thickness.

In the formulation, an assumed harmonic time dependence $e^{-i\omega t}$ is suppressed. The free motion of the shell is described by

$$\frac{\partial^2 u}{\partial x^2} + \frac{\sigma_m}{a^2}\frac{\partial^2 u}{\partial \phi^2} + \frac{\sigma_p}{a}\frac{\partial^2 \vartheta}{\partial x \partial \phi} + \frac{\sigma}{a}\frac{\partial w}{\partial x} - \frac{1}{c_p^2}\frac{\partial^2 u}{\partial t^2} = 0, \tag{A.1}$$

$$\frac{\sigma_p}{a}\frac{\partial^2 u}{\partial x \partial \phi} + \sigma_m \frac{\partial^2 \vartheta}{\partial x^2} + \frac{1}{a^2}\frac{\partial^2 \vartheta}{\partial \phi^2} + \frac{1}{a^2}\frac{\partial w}{\partial \phi} - \frac{1}{c_p^2}\frac{\partial^2 \vartheta}{\partial t^2} = 0, \tag{A.2}$$

$$\frac{\sigma}{a}\frac{\partial u}{\partial x} + \frac{1}{a^2}\frac{\partial \vartheta}{\partial \phi} + \frac{w}{a^2} + \beta_b\Big[a^2\frac{\partial^4 w}{\partial x^4} + 2\frac{\partial^4 w}{\partial x^2 \partial \phi^2} + \frac{1}{a^2}\frac{\partial^4 w}{\partial \phi^4}\Big] + \frac{1}{c_p^2}\frac{\partial^2 w}{\partial t^2} = -\frac{(1-\sigma^2)p}{E_Y h}. \tag{A.3}$$

In the equation, σ is Poisson ratio and

$$\sigma_p = \frac{1-\sigma}{2} \quad , \quad \sigma_m = \frac{1+\sigma}{2} \tag{A.4}$$

β_b represents the influence of bending stresses

$$\beta_b = \frac{h^2}{12a^2} \ . \tag{A.5}$$

The displacements in an infinitely long cylindrical shell can be generally expressed by double wavenumber integrals, one in the axial direction and one in the circumferential direction. Due to the periodic nature in an uniform shell in the circumferential direction, the corresponding integral can be replaced by a modal summation, that is

$$\begin{aligned} u(x,\phi) &= \int_{\infty}^{\infty} \sum_{-\infty}^{\infty} \hat{u}_n \, e^{in\phi} \, e^{-ik_x x} dx \\ \vartheta(x,\phi) &= \int_{\infty}^{\infty} \sum_{-\infty}^{\infty} \hat{\vartheta}_n \, e^{in\phi} \, e^{-ik_x x} dx \\ w(x,\phi) &= \int_{\infty}^{\infty} \sum_{-\infty}^{\infty} \hat{w}_n \, e^{in\phi} \, e^{-ik_x x} dx \ . \end{aligned} \tag{A.6}$$

Similarly, we can express the incident sound pressure p_i and the scattered pressure field p_s in the form

$$\begin{aligned} p_i &= p_0 \int_{\infty}^{\infty} e^{ik_x x} \sum_{n=-\infty}^{+\infty} (-i)^n J_n(k_r r) \, e^{in\phi} \, dx \\ p_s &= \int_{\infty}^{\infty} e^{ik_x x} \sum_{n=-\infty}^{+\infty} C_n H_n^{(1)}(k_r r) \, e^{in\phi} \, dx \ . \end{aligned}$$

where J_n and H_n are the nth order Bessel and Hankel functions respectively of the first kind. k_r is given by

$$k_r = (k^2 - {k_x}^2)^{1/2} \quad . \tag{A.7}$$

The sound field and the shell motion is related by the momentum equation

$$-\omega^2 \rho w = -\frac{\partial\,(p_i + p_s)}{\partial r} \quad @\ r = a$$

The resulting linear algebraic equations are

$$\begin{aligned}
[\bar{\alpha}^2 + \sigma_m n^2 - \Omega^2]\ \hat{u}_n + n\sigma_p \bar{\alpha}\ \hat{\vartheta}_n - i\sigma\bar{\alpha}\ \hat{w}_n &= 0\ , \\
n\sigma_p \bar{\alpha}\ \hat{u}_n + [\sigma_m \bar{\alpha}^2 + n^2 - \Omega^2]\ \hat{\vartheta}_n + -in\ \hat{w}_n &= 0\ , \\
\sigma\bar{\alpha}\ \hat{u}_n + n\ \hat{\vartheta}_n - i[1 + \beta_b^2 \bar{\alpha}^4 - \Omega^2]\ \hat{w}_n & \\
+i\frac{a^2 p_0 (-1)^{n+1} H_n(k_r a)}{c_p^2 h \rho_s}\ C_n &= \frac{ia^2 p_0 (-1)^{n+1} J_n(k_r a)}{c_p^2 h \rho_s}\ , \\
\omega^2 \rho\ \hat{w}_n + k_r H_n'(k_r a)\ C_n &= -k_r p_0 (-1)^n J_n'(k_r a)\ .
\end{aligned} \tag{A.8}$$

where $\bar{\alpha} = k_x a$ and $\Omega = \omega a / c_p$.

Such linear equations are in the form of $\mathbf{LU} = \mathbf{F}$. The displacement coefficients $[\hat{u}_n\ \hat{\vartheta}_n\ \hat{w}_n]$ and the pressure coefficient C_n can be solved if the forcing matrix $\mathbf{F}$ is known.

The dispersion relation is obtained from the determinant of the operator matrix $\mathbf{L}$ from Eq. A.8.

$$\begin{aligned}
D_n = (1 + \beta_b^2 \bar{\alpha}^4 - \Omega^2 + F_u\, E_f\, k^2 a^2)(\Omega^2 - \bar{\alpha}^2)(\Omega^2 - \sigma\bar{\alpha}^2) - \Omega^4 & \\
-\sigma^2[\Omega^2 n^2 + (2\sigma + 3)\Omega^2 \bar{\alpha}^2 - (1 - \sigma^2)\bar{\alpha}^4] = 0 &
\end{aligned} \tag{A.9}$$

where

$$F_u = \frac{H_n(k_r a)}{k_r a H_n'(k_r a)} \quad , \quad E_f = \frac{c^2 \rho a}{c_p^2 \rho_s h} \quad , \tag{A.10}$$

The complex axial wavenumber roots, $k_{xr} + k_{xi}$, which satisfy the transcendental dispersion equation can be found numerically using a root finder.

Appendix B

Parameters of the MIT shells

Shell Parameters		
General Properties		
Overall shell length	86	cm
Cylinder length, L	74	cm
Cylinder radius, a	5.54	cm
Shell thickness, h	0.053	cm
Thickness to radius, h/a	0.96	%
Shell Properties		
Shell material	Ni-200	
Compressional plate wave speed	5270	m/s
Transverse shear wave speed	3100	m/s
Young's modulus, E_s	$2.2\text{x}10^{11}$	N/m^2
Density, ρ_s	8900	kg/m^3
Poisson's ratio, σ	0.31	
Ring Properties		
Ring material	Ni-200	
Mass ratio (rings:shell)	1:1	
Symmetry	Axisymmetric	
Internals Properties		
Resilient material	EAR c1002 rubber	
Wave bearing rods	General purpose Delrin	
Delrin rod compressional wave speed	1625	m/s
Mass Ratio (internals+rings:shell)	3:1	
Symmetry	Quadrant symmetric	

Table B.1: Shell Parameters

Appendix C

SARA shell modeling and wave decomposition

This section introduces SARA-2D [31] modeling of the empty shell and the ringed shell, discusses post-processing issues, and evaluates the initial wave decomposition results.

C.0.1 FEM modeling of the shells

The finite element code SARA-2D solves the steady-state problem of a structure submerged in an infinite fluid subjected to incident traveling waves or vibrational loads within the structure. Finite elements are used to model both the structure and the fluid field. Conventional displacement elements are used for the structure, and pressure type acoustic elements are used for the external nearfield. The unbounded external fluid is modeled with infinite elements that include in their formulation the outward traveling and decaying waves. The coupled fluid-structure model results in a complex, symmetric, banded set of equations which can be efficiently solved by Gaussian elimination for displacements and pressures throughout the model. Selecting normal velocities and pressures at the fluid-structure interface permits the field response to be obtained from the Helmholtz integral equation.

The SARA-2D software enables all loadings and response quantities to be repre-

sented in a cosine and sine Fourier series for circumferential coordinate in axisymmetric analyses. In other words, the circumferential coordinate is compressed, so that '**2D**' refers to dimensions in radial and axial directions of the cylindrical shell models. The equations for the Fourier circumferential modes are uncoupled and each is solved separately for coefficients of the response quantities. These coefficients must be multiplied by the appropriate sine or cosine variation to obtain the actual response. By superposition of modes, arbitrary loadings and responses can be obtained.

Of the three shell models, only the axisymmetric empty shell and the ringed shell are calculated. The shell element is conventional isotropic quadratic element that has three nodes. The basic surface responses include velocities in the radial, axial and circumferential directions and surface pressure, represented by v_r, v_a, v_c and p respectively. Their formulations can be explained in the example of the surface pressure. The surface pressure is represented by $p_n(\omega, x)$ for circumferential mode n, frequency ω, and node point position in axial coordinate x. For arbitrary azimuthal angle ϕ, the total surface pressure is then

$$p(\omega, x, \phi) = \sum_{n=0}^{n_{max}} p_n(\omega, x) \cos n\phi \ . \tag{C.1}$$

In the special case of $\phi = 0$, summing up the pressure components leads to the total pressure along the meridian of the shell

$$p(\omega, x, \phi = 0) \ = \sum_{n=0}^{n_{max}} p_n(\omega, x) \ . \tag{C.2}$$

The mean squared pressure on a cylindrical shells is then proportional to the squared value of the total pressure on the meridian, by a factor of $1/2$.

$$< p^2(\omega, x) >_{0<\phi<2\pi} = \sum_{n=0}^{n_{max}} < p_n p_n^* > = \frac{1}{2} \sum_{n=0}^{n_{max}} < p_n p_n^* >_{\phi=0} \ , \tag{C.3}$$

where $*$ denotes the complex conjugates.

The MIT shell models have been calculated before by Dr. Liu and Dr. Vasudevan [32] for separate studies. The basic version of the SARA-2D input file in this

study is kindly provided by them. Fig. C-1 illustrates the grid point of the empty shell in the calculation. Only the upper half of the shell surface is modeled because of symmetry. 206 quadratic shell elements are used to model the outline of the shell. The number of nodes (grids) is 413 and the number of Gaussian integration point is 618. The FEM results in this thesis are sampled at the Gaussian integration points. The sampling wavenumber is $k_{sampling} = 4233\ 1/m$. Within frequency range $2 < ka < 12$, the maximum wavenumber of the elastic waves (flexural) is 650 $1/m$, smaller than $k_{sampling}/2$, so that spatial aliasing is avoided.

Fig. C-2 and Fig. C-3 display the detailed grids for the endcap and the rings respectively. The elastic properties of the rings are included and rings are attached to the shell middle plane by a portion of the ring width.

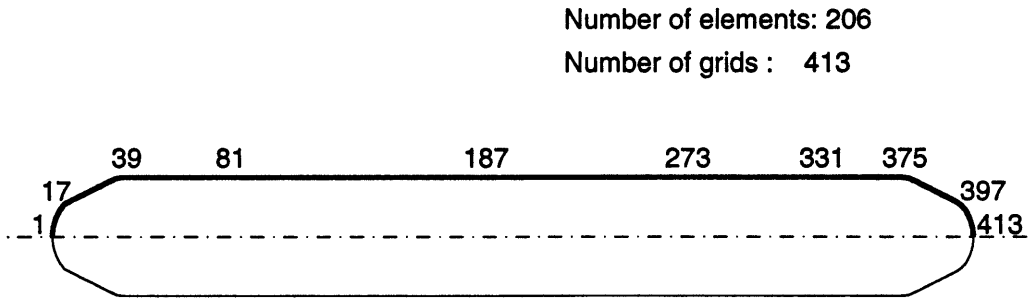

Figure C-1: Illustration of the empty shell for FEM calculation. Only half shell, shown by the thick line, is modeled due to symmetry. The grid point numbers at the shell discontinuities are displayed. In the ringed shell case, grid number 81, 187, 273 and 331 indicate the locations of the ring stiffeners.

Another parameter to choose is the maximum mode number n_{max}. Within frequency range $2 < ka < 12$, the highest compressional mode is $n = 3$ near $ka = 11$, and the highest shear mode is $n = 5$ near $ka = 10.5$. The highest flexural mode is $n = 36$ near $ka = 12$. Since the flexural wave is subsonic and is mainly generated due to elastic wave coupling at the shell discontinuities, the circumferential mode number of the actual flexural waves on the shells is no greater than that of the membrane waves. I chose $n_{max} = 4$ in the calculation.

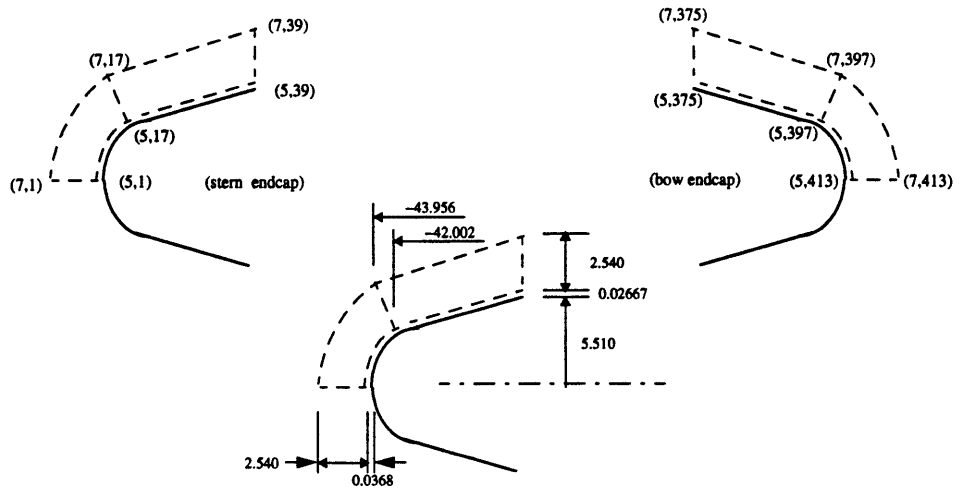

Figure C-2: Detailed FEM grid display of the endcaps. Dimensions are in *cm* and are roughly in scale.

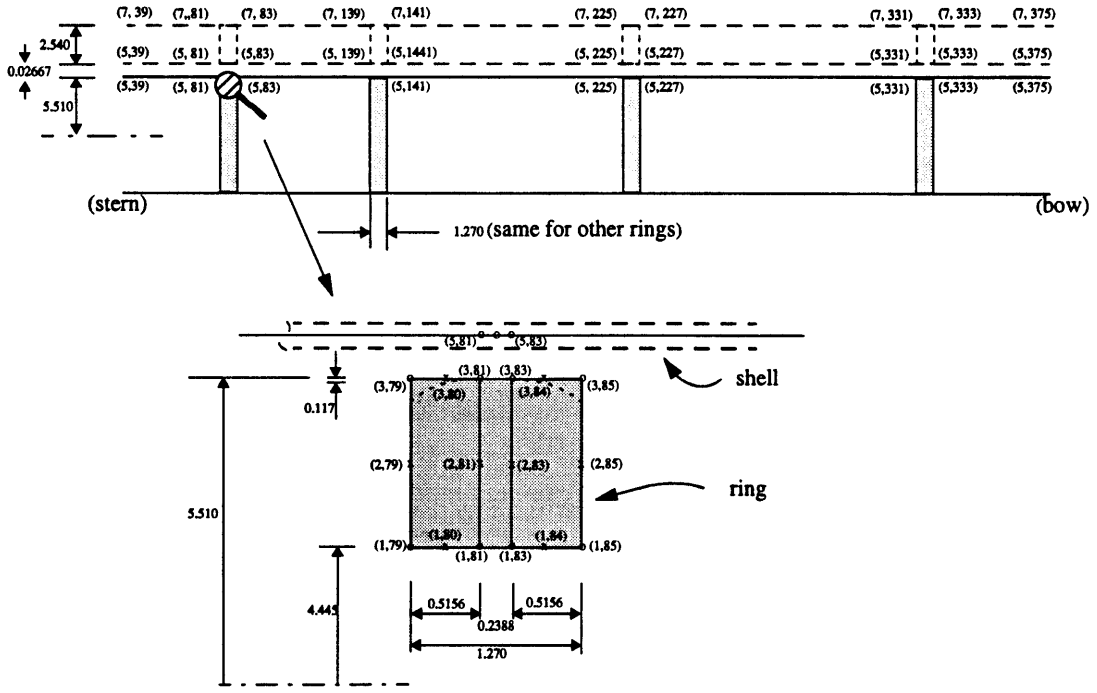

Figure C-3: Detailed FEM grid display of the rings. Dimensions are in *cm* and are roughly in scale.

C.0.2 Wavenumber decomposition

On the basis of the SARA-2D generated shell surface response, I perform the wavenumber transformation, according to the following equations (again, I take surface pressure as an example),

$$\hat{p}_n(\omega, k_x) = \frac{1}{2\pi} \int_{-\infty}^{\infty} p_n(\omega, x)\, e^{ik_x x}\, dx\ , \quad p_n(\omega, x) = \int_{-\infty}^{\infty} \hat{p}_n(\omega, k_x)\, e^{-ik_x x}\, dk_x\ . \quad \text{(C.4)}$$

Since the shells are of finite length, $p_n(\omega, x)$ is zero outside the region of the shell length. To reduce artifacts due to abrupt truncation, a tapered rectangular spatial window is used on the cylindrical part of the shell only, as shown in Fig. C-4. Each tapered part of the window is a half Hanning window and takes 5% of the total window length.

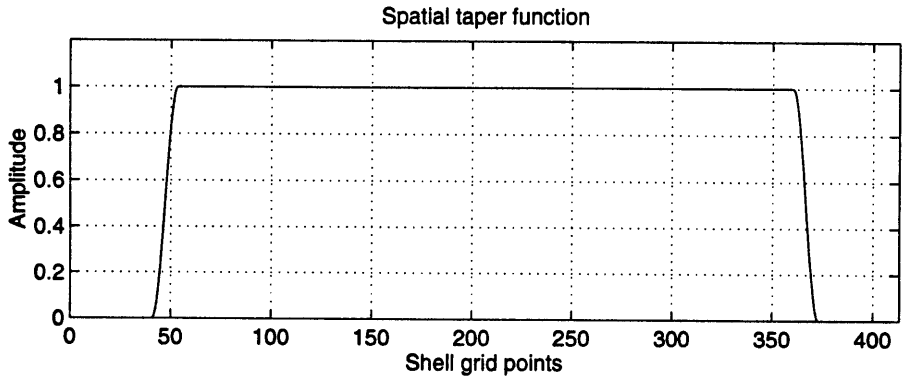

Figure C-4: Spatial taper function for sampling shell surface responses. Only the cylindrical shell section is sampled with each tail about 5 % of the shell length.

Fig. C-6 shows a typical surface pressure of the empty shell in $ka - k_x$ domain. Positive wavenumber represents forward going waves and negative wavenumber represents the backward going waves. Since the axial wave speed is proportional to ka/k_x, the fast wave has smaller $|k_x|$ if the frequency is fixed. In the backward direction, the fast compressional and shear wave can be clearly identified close to $|k_x| = 0$ while the flexural wave is far into the negative k_x domain. In the forward direction, the surface response is dominated by the acoustic wave, and also by the flexural wave. At 66° sound incidence, the acoustics wave trace matches the shear wave near $ka = 3$.

The acoustic wave and the elastic wave loci have a width. It has a different nature from radiation damping discussed in Chap.2, and caused by data sampling over finite length. If the pressure had been sampled from a much longer shell, the width associated would have been much smaller. The half power bandwidth for a rectangular window of length L is about $0.88\pi/L$. Fig. C-5 shows the wavenumber response of the spatial window. Since the shell length is the only factor here, the width is the same for all wave loci, independent of wave types.

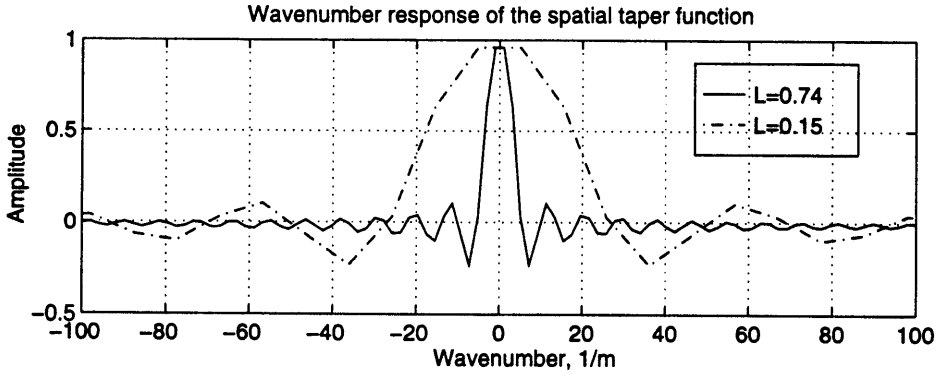

Figure C-5: Wavenumber response of the spatial tapering window in Fig. C-4. The solid line uses the full shell length $L = 0.74\ m$ while the dash-dot line uses the average shell bay length(0.15, or 1/5 of the total length). Along the shell length, there are 498 sampling points. By means of zero padding, a 2048 point Fourier transform is performed.

The forward going acoustic wave trace matches the shear and the compressional waves, making the forward membrane waves mainly forced waves. In the backward direction, the acoustic wave vanishes and the three elastic waves are all free waves.

The loci of the elastic waves in the empty shell is shown in subplot (a) of Fig. C-6. I overlay the loci of the equivalent infinite cylindrical shell submerged in water over plot (a) and the result is shown in subplot (b) of Fig. C-6, in contour format.

I observe that the elastic wave loci in the empty shell are not different from that in an infinitely long cylinder, which is well expected.

Fig. C-7 overlay the dispersions of the ringed shell with that from the infinitely long shell. The center of the flexural wave dispersion loci is not different from the infinitely long shell case. It is difficult to compare the dispersion loci of the membrane waves.

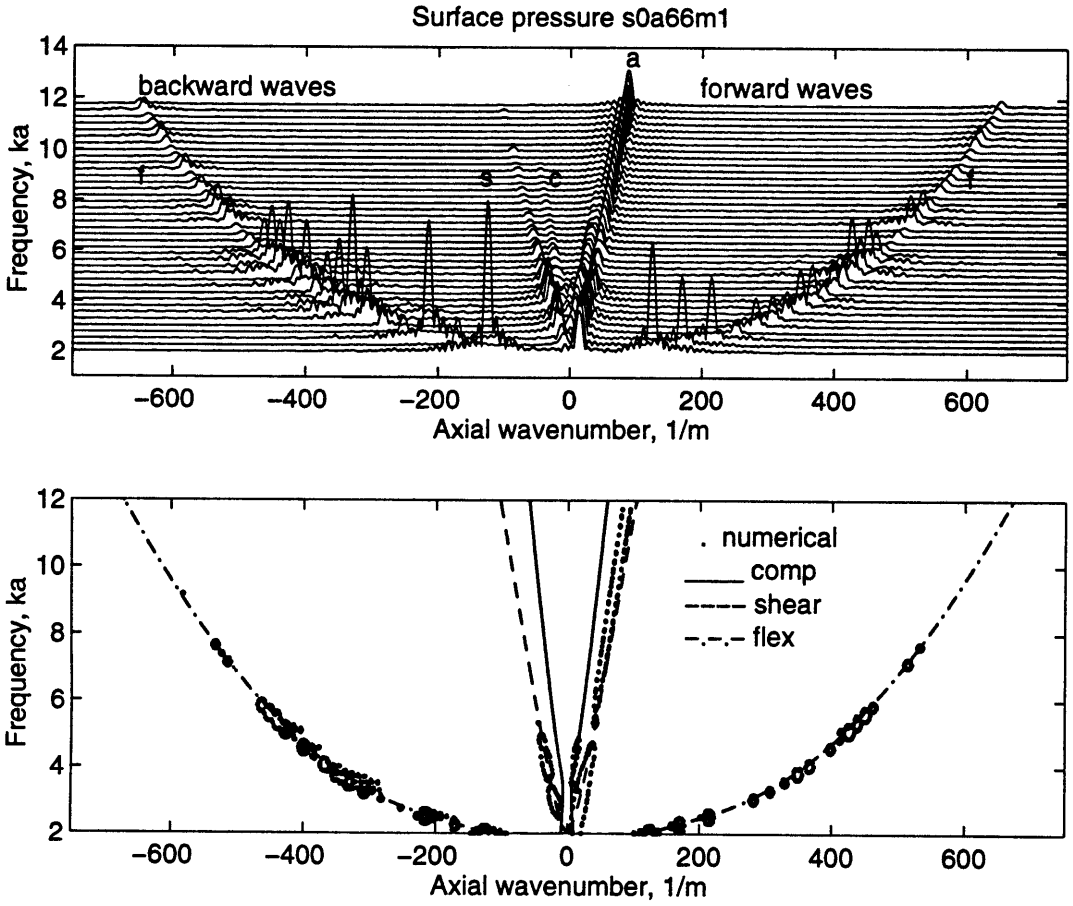

Figure C-6: Frequency - axial wavenumber display of surface pressure of the empty shell under 66° incidence in waterfall. Circumferential order $n = 1$. Positive axial wavenumber represents forward going waves. The acoustic wave, shear, compressional and flexural waves are labeled by the initials a,s,c and f respectively. (a) waterfall plot; (b) contour plot, overlayed by dispersion curves from an infinitely long shell in water.

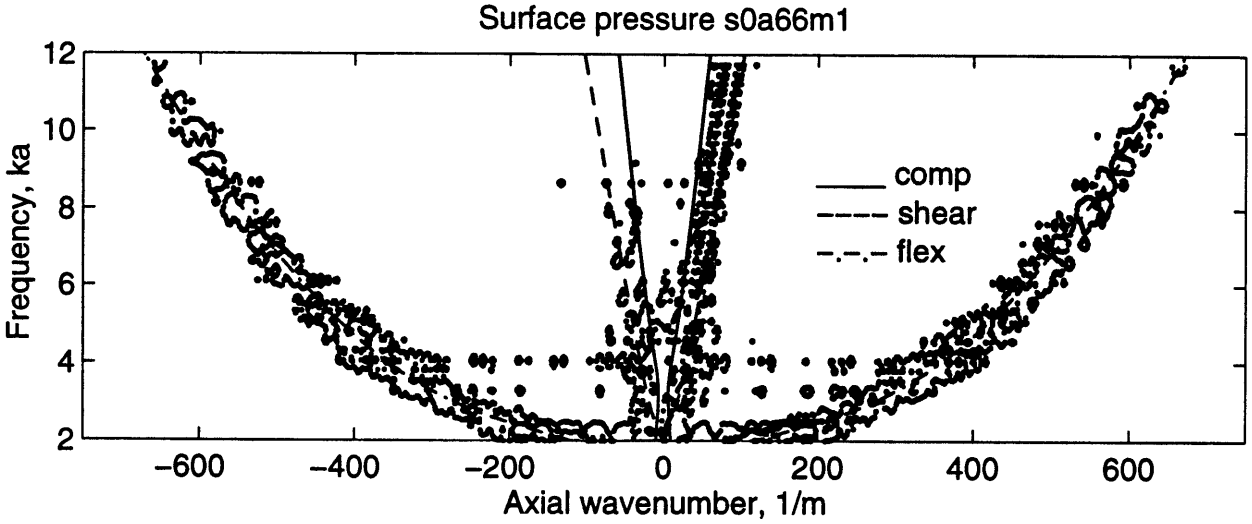

Figure C-7: Overlay the dispersion loci of the equivalent infinite cylindrical shell to that of the ringed shell under 66° incidence in waterfall. Circumferential order $n = 1$.

I observe some new features in the wave patterns for the ringed shell. The rings increase the width of the flexural wave dispersion loci and create many sidelobes.

In the following, I take a close look at the elastic waves surface pressure and the velocities in the two shells for a particular case: sound incident at 66° and mode $n = 1$. Fig. C-6 illustrates surface pressure in $ka - k_x$, for sound incident at 66° on the empty shell. Fig. C-8 displays the surface pressure and normal velocity of the empty shell and Fig. C-9 displays the circumferential and axial velocities respectively. Similar presentations of the ringed shell surface response can be found in Fig. C-10 and C-11 respectively. In the four color contour plots, all the shell responses are scaled by the incident pressure, and all have MKS units.

I make the following observations about the empty shell.

- The shell membrane wave response is concentrated mostly at the low frequencies, $2.5 < ka < 5.5$, consistent with the half-power bandwidth of trace matching region $3 < ka < 4.7$ displayed in Fig. 2-7.

- The in-plane motion (see Fig. C-9) is dominated by the membrane waves, while the out-of-plane motion, together with the surface pressure (Fig. C-8), is contributed to by both the flexural and membrane waves.

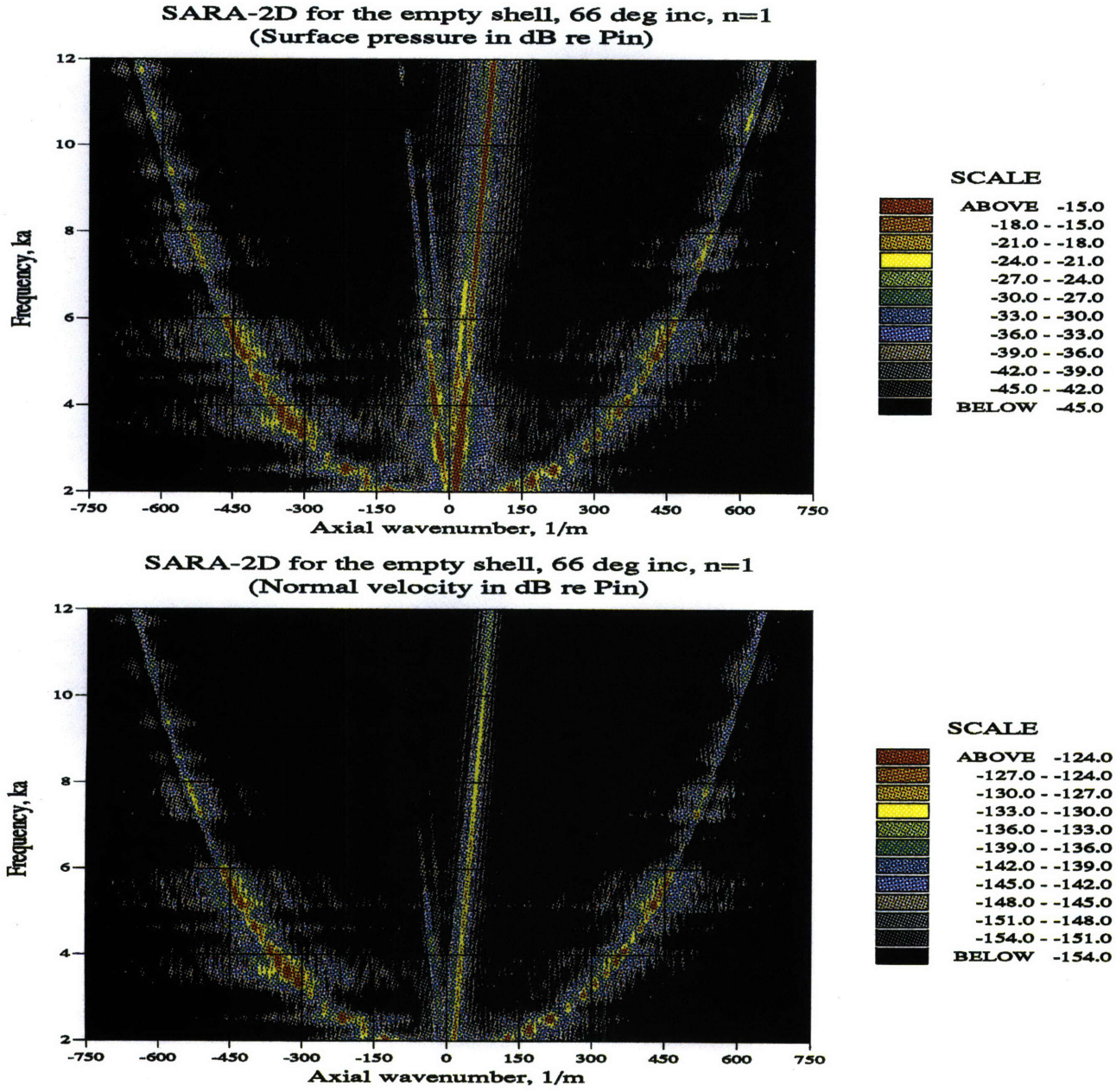

Figure C-8: Surface pressure (upper) and radial velocity (lower) of the empty shell due to sound incidence at $\theta = 66°$. $n = 1$.

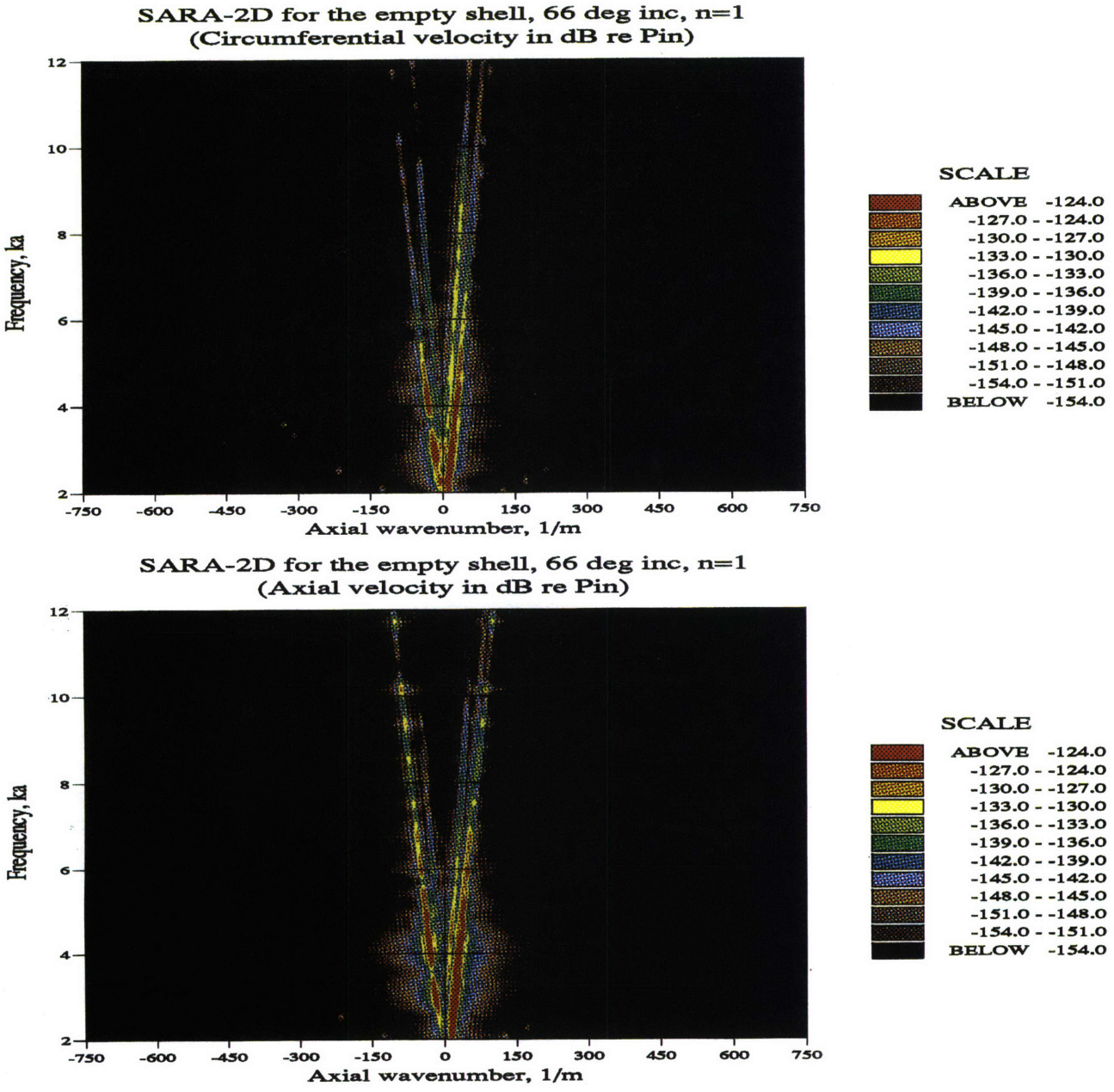

Figure C-9: (upper) Circumferential velocity (lower) axial velocity of the empty shell due to sound incidence at $\theta = 66°$, $n = 1$.

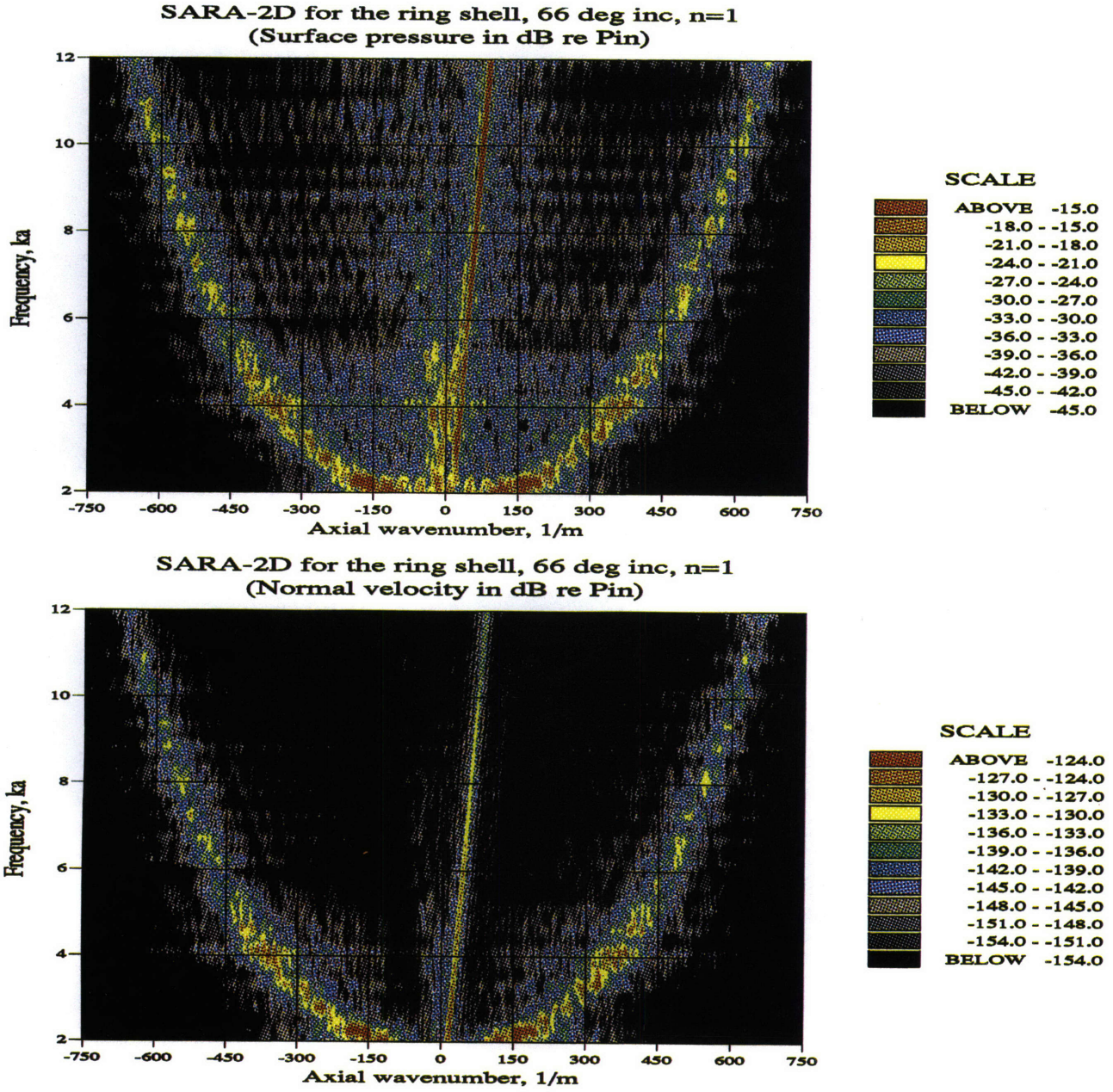

Figure C-10: (a) Surface pressure (b) radial velocity of the ringed shell due to sound incidence at $\theta = 66°$. $n = 1$.

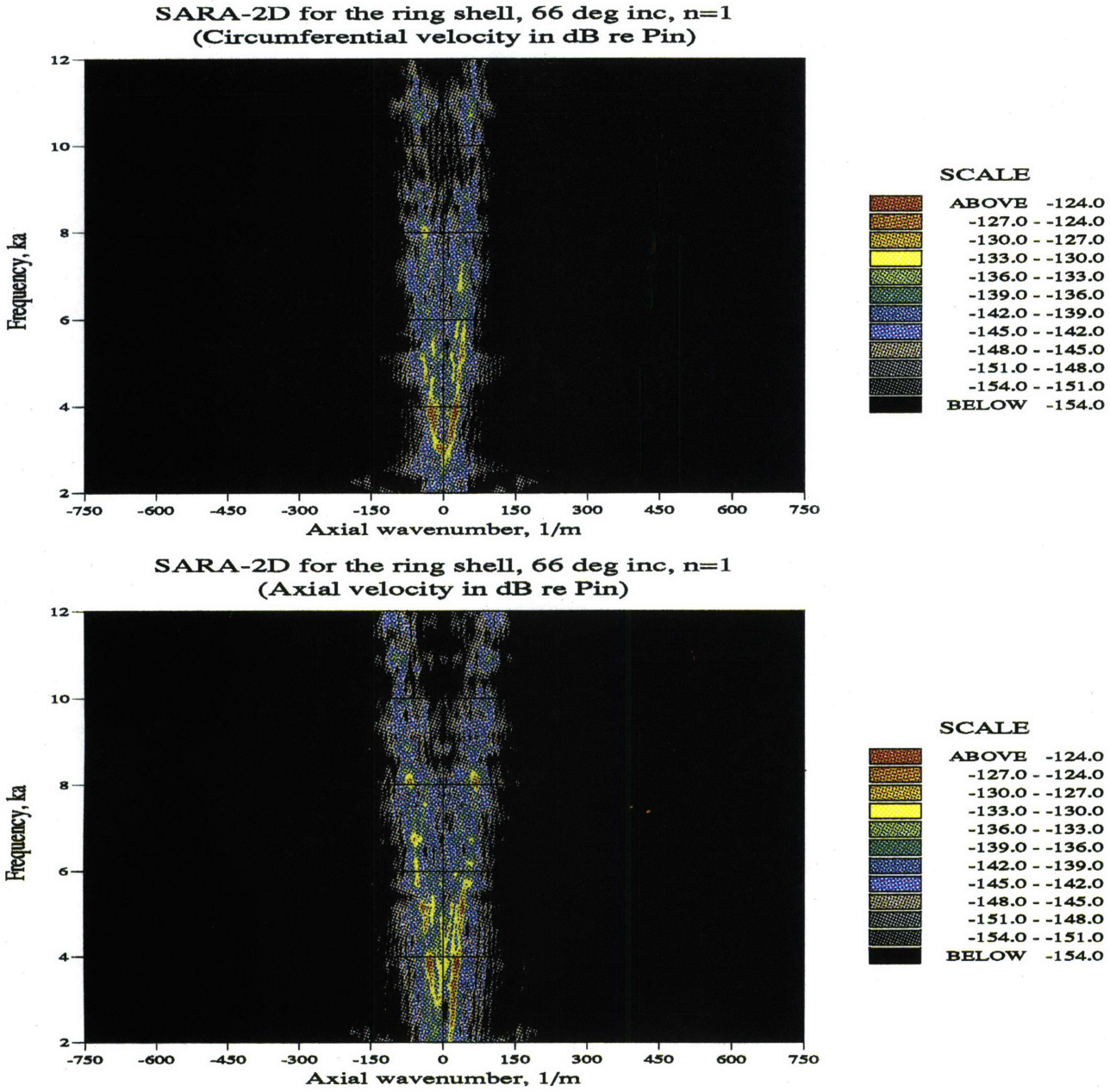

Figure C-11: (a) Circumferential velocity (b) axial velocity of the ringed shell due to sound incidence at $\theta = 66°$. $n = 1$.

Similarly I make observations about the ringed shell, with emphasis on the comparison with the empty shell.

- Although smeared out to certain degree in the wavenumber domain, the membrane waves can still be identified, especially in the in-plane response.
- In comparison with the empty shell, the flexural waves are significantly smeared out. The broader width of the flexural wave dispersion loci indicates that the flexural waves are confined within the ring bays, consistent with the observation in Fig. 4-2.
- The ring stiffeners create side-lobe-like responses in the $ka-k_x$ plane. No strong modulation pattern is observed because because the rings are unequally placed. The energy of the 'side-lobe' responses velocities is insignificant relative to the response near the eigen-wavenumbers and are neglected.
- The 'side-lobe' response is absent at wavenumbers greater than the eigen-wavenumber of the flexural waves. This indicates that the ring discontinuities are not abrupt, so that a direct spatial Fourier transform is justified across the rings for the whole length of the ring shell.

What I learn from the above analysis confirms the plausibility of identifying the elastic wave and evaluating them in the wavenumber domain, even at the presence of the ring discontinuities.

The spatially averaged mean squared velocity $< \hat{v}_n^2 >$ can be obtained from the wavenumber spectral density S_{vn},

$$< \hat{v}_n^2 >= \int_{-\infty}^{+\infty} S_{vn} dk_x \approx \int_{k_{x1}}^{k_{x2}} S_{vn} dk_x \ . \tag{C.5}$$

The approximated wavenumber band $[k_{x1}, k_{x2}]$ is centered at the 'eigen' axial wavenumber of the corresponding wave type. The bandwidth is chosen to include most contributions from the expected wave type while exclude the contributions from the unwanted wave types. Since the flexural wave loci are well separated from that

of the membrane waves, the band for the flexural wave is chosen to be $8\pi/L$. The averaging band for the shear and the compressional waves is chosen to be $1.75\pi/L$.

Appendix D

Elastic wave conversion at a line joint

Elastic wave transmission through plate slope discontinuity (bending angle) is studied, for the purpose of estimating wave transmission from cylindrical shell to the endcaps. The estimation is meaningful at least for high frequency where the shell curvature effect is small. As shown in Fig. D-1, plate 1 and 2 are joined in vacuum with an angle 26.5° and have same material (Young's Modulus E_Y, Poisson ratio σ, and density ρ) and thickness h as the MIT shell models.

The wave motion potential in the plates is governed by the following equations, corresponding to the compressional, shear and flexural waves respectively.

$$\begin{aligned} \nabla^2\Phi + k_p^2\Phi &= 0; \\ \nabla^2\Psi + k_s^2\Psi &= 0; \\ \nabla^4\Theta + k_b^4\Theta &= 0. \end{aligned} \tag{D.1}$$

where wavenumbers denote

$$k_p^2 = \omega^2/c_p^2$$

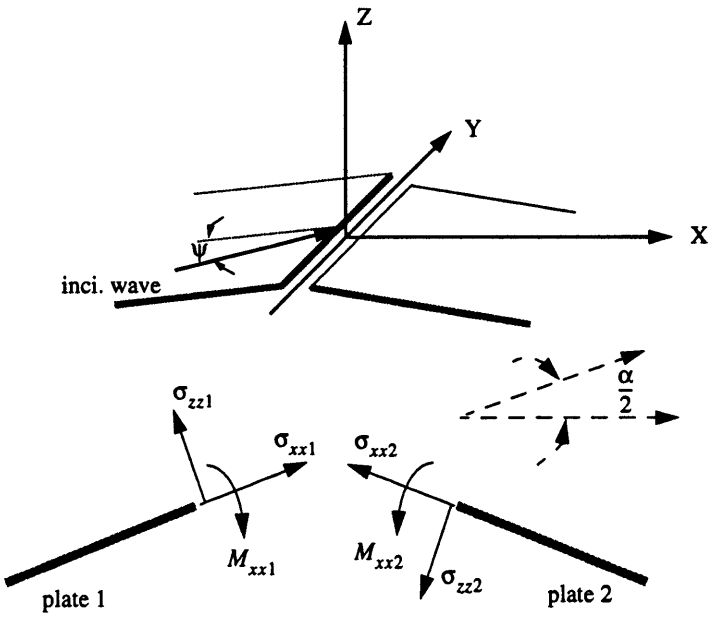

Figure D-1: Sketch of wave coupling at plate junction. The global coordinate is represented by (X, Y, Z). The local coordinate x, y, z (not shown) is so arranged that when plate bending angle α vanishes, (x, y, z) coincides with (X, Y, Z).

$$k_s^2 = \omega^2/c_s^2$$
$$k_b^4 = 12\rho\omega^2/E_Y h^2 \,. \tag{D.2}$$

and $e^{(-i\omega t)}$ is assumed and is compressed in the formulation.

The wave incidence is oblique so that the trace wavenumber along the junction k_y is the same for all waves, both reflected and transmitted. If the Fourier transform $e^{(ik_y y)}$ is used to represent y dependence, the 2-dimensional wave equations in Eq. D.1 become separated in 1-dimensional form.

$$\frac{\partial \Phi}{\partial x} + (k_p^2 - k_y^2)\Phi = 0;$$
$$\frac{\partial \Psi}{\partial x} + (k_s^2 - k_y^2)\Psi = 0;$$
$$\frac{\partial^4 \Theta}{\partial^4 x} + (k_b^4 - k_y^4)\Theta = 0. \tag{D.3}$$

Considering wave incidence onto the junction from plate 1, the field in plate 1

consists of both incidence waves and reflected waves and the field in plate 2 consists of the transmitted waves only.

$$\begin{aligned}
\Phi_1(x,k_y) &= A_1^+ e^{iax} + A_1^- e^{-iax};\\
\Psi_1(x,k_y) &= C_1^+ e^{icx} + C_1^- e^{-icx};\\
\Theta_1(x,k_y) &= B_1^+ e^{ibx} + B_1^- e^{-ibx}; + B_{1j} e^{bx};\\
\Phi_2(x,k_y) &= A_2^+ e^{iax};\\
\Psi_2(x,k_y) &= C_2^+ e^{icx};\\
\Theta_2(x,k_y) &= B_2^+ e^{ibx} + B_{2j} e^{-bx}.
\end{aligned} \tag{D.4}$$

where a, b and c denote wavenumber in x direction, and subnote 1 and 2 index plate 1 and 2 respectively.

$$\begin{aligned}
a &= \sqrt{k_p^2 - k_y^2};\\
b &= \sqrt{k_b^2 - k_y^2};\\
c &= \sqrt{k_c^2 - k_y^2}.
\end{aligned} \tag{D.5}$$

There are 11 variables in Eq. D.4 and three of them are known. The incident wave strength vector $\mathbf{A} = [A_1^+ \;\; B_1^+ \;\; C_1^+]$ are given in advance. For instance, the incidence of compressional, shear and flexural waves can be conveniently given as $\mathbf{A} = [1\ 0\ 0]$, $\mathbf{A} = [0\ 0\ 1]$ and $\mathbf{A} = [0\ 1\ 0]$ respectively. The 8 unknowns represent the reflection and transmission coefficients correspondingly.

The 8 unknowns can be solved by matching boundary conditions across the junction. First, the displacements in x,y and z directions have to be continuous. In addition, the corresponding forces(stresses) have to be continuous. Finally, the rotation angle and momentum cross the junction have to be continuous as well.

Denoting displacements by u, v, w in x, y, z directions, the corresponding stresses

by σ_{xx}, τ_{xy}, σ_{xx} and the momentum by M, the boundary conditions are listed in the following:

$$
\begin{aligned}
u_1 cos\alpha - w_1 sin\alpha &= u_2 cos\alpha + w_2 sin\alpha; \\
v_1 &= v_2; \\
u_1 sin\alpha + w_1 cos\alpha &= u_2 sin\alpha + w_2 cos\alpha; \\
\sigma_{xx1} cos\alpha + \sigma_{zz1} sin\alpha &= \sigma_{xx2} cos\alpha - \sigma_{zz2} sin\alpha; \\
\tau_{xy1} &= \tau_{xy2}; \\
\sigma_{xx1} sin\alpha - \sigma_{zz1} cos\alpha &= -\sigma_{xx2} sin\alpha - \sigma_{zz2} cos\alpha; \\
\partial w_1/\partial x &= \partial w_2/\partial x; \\
\partial^2 w_1/\partial^2 x &= \partial^2 w_2/\partial^2 x \, .
\end{aligned}
\tag{D.6}
$$

The displacements and stresses are derived from the potential field in Eq. D.4.

$$
\begin{aligned}
u &= \frac{\partial \Phi}{\partial x} - \frac{\partial \Psi}{\partial y}; \\
v &= \frac{\partial \Phi}{\partial y} + \frac{\partial \Psi}{\partial x}; \\
w &= \frac{\partial \Theta}{\partial x}; \\
\sigma_{xx} &= \lambda \nabla^2 \Phi + 2\mu \left(\frac{\partial \Phi}{\partial x} + \frac{\partial^2 \Psi}{\partial x \partial y} \right); \\
\tau_{xy} &= \mu \left[\nabla^2 \Psi + 2 \left(\frac{\partial^2 \Phi}{\partial x \partial y} - \frac{\partial \Psi}{\partial x} \right) \right] .
\end{aligned}
\tag{D.7}
$$

where λ and μ are Lame's constants,

$$
\lambda = \frac{E_Y \sigma}{(1+\sigma)(1-2\sigma)} \quad , \quad \mu = G = \frac{E_Y}{2(1+\sigma)} \quad . \tag{D.8}
$$

The unknown coefficient vector $\mathbf{R} = [A_1^- \; C_1^- \; B_1^- \; B_{1j} \; A_2^+ \; C_2^+ \; B_2^+ \; B_{2j}]$ can be solved by linear equations in the matrix format:

$$[\mathbf{G}] \cdot [\mathbf{R}] = [\mathbf{Q}] , \quad [\mathbf{R}] = [\mathbf{G}]^{-1} \cdot [\mathbf{Q}] , \tag{D.9}$$

where the nonzero elements of 8×8 matrix $\mathbf{G}$ and 8×1 matrix $\mathbf{Q}$ are given in the following.

$$g11 = -ia\,cos\alpha; \quad g12 = -ik_y\,cos\alpha; \quad g13 = -ib\,sin\alpha; \quad g14 = -b\,sin\alpha;$$
$$g15 = -ia\,cos\alpha; \quad g16 = ik_y\,cos\alpha; \quad g17 = -ib\,sin\alpha; \quad g18 = b\,sin\alpha;$$
$$g21 = ik_y; \quad g22 = -ic; \quad g25 = -ik_y; \quad g26 = -ic;$$
$$g31 = -ia\,sin\alpha; \quad g32 = -ik_y\,sin\alpha; \quad g33 = -ib\,cos\alpha; \quad g34 = b\,cos\alpha;$$
$$g35 = ia\,sin\alpha; \quad g36 = -ik_y\,sin\alpha; \quad g37 = -ib\,cos\alpha; \quad g38 = b\,cos\alpha;$$
$$g41 = -\{\lambda(a^2 + k_y^2) + 2\mu a^2\}\,cos\alpha; \quad g42 = 2\mu c k_y\,cos\alpha;$$
$$g43 = (b^4 + k_y^2 b^2)h^2\,sin\alpha/12; \quad g44 = (b^4 - k_y^2 b^2)h^2\,sin\alpha/12;$$
$$g45 = \{\lambda(a^2 + k_y^2) + 2\mu a^2\}\,cos\alpha; \quad g46 = 2\mu c k_y\,cos\alpha;$$
$$g47 = (b^4 + k_y^2 b^2)h^2\,cos\alpha/12; \quad g48 = (b^4 - k_y^2 b^2)h^2\,cos\alpha/12;$$
$$g51 = -\{\lambda(a^2 + k_y^2) + 2\mu a^2\}\,sin\alpha; \quad g52 = 2\mu c k_y\,sin\alpha;$$
$$g53 = (b^4 + k_y^2 b^2)h^2\,cos\alpha/12; \quad g54 = -(b^4 - k_y^2 b^2)h^2\,sin\alpha/12;$$
$$g55 = -\{\lambda(a^2 + k_y^2) + 2\mu a^2\}\,sin\alpha; \quad g56 = -2\mu c k_y\,sin\alpha;$$
$$g57 = (b^4 + k_y^2 b^2)h^2\,cos\alpha/12; \quad g58 = (b^4 - k_y^2 b^2)h^2\,cos\alpha/12;$$
$$g61 = 2ak_y; \quad g62 = c^2 - k_y^2; \quad g65 = 2ak_y; \quad g66 = -c^2 + k_y^2;$$
$$g73 = -1; \quad g74 = 1; \quad g77 = 1; \quad g78 = -1;$$
$$g83 = i(b^3 - \sigma k_y^3); \quad g84 = (b^3 - i\sigma k_y^3); \quad g87 = i(b^3 + \sigma k_y^3); \quad g88 = (b^3 + i\sigma k_y^3);$$
$$q1 = -ia\,cos\alpha\,A_1^+ + ik_y\,cos\alpha\,C_1^+ + ib\,sin\alpha\,B_1^+;$$
$$q2 = -ik_y\,A_1^+ - ic\,C_1^+;$$
$$q3 = -ia\,sin\alpha\,A_1^+ + ik_y\,sin\alpha\,C_1^+ - ib\,cos\alpha\,B_1^+;$$
$$q4 = \{\lambda(a^2 + k_y^2) + 2\mu a^2\}\,cos\alpha\,A_1^+ + 2 * mu * ck_y\,cos\alpha\,C_1^+ - (b^4 + k_y^2 b^2)h^2\,sin\alpha\,B_1^+/12;$$
$$q5 = \{\lambda(a^2 + k_y^2) + 2\mu a^2\}\,sin\alpha\,A_1^+ + 2 * mu * ck_y\,sin\alpha\,C_1^+ + (b^4 + k_y^2 b^2)h^2\,cos\alpha\,B_1^+/12;$$
$$q6 = 2ak_y\,A_1^+ + (k_y^2 - c^2)\,C_1^+;$$

$$q7 = B_1^+; \quad q8 = i(b^3 + \sigma k_y^3)B_1^+ \text{ (D.10)}$$

From wave transmission coefficients, one can derive the wave power transmissibility, which is the ratio of incoming wave power to the transmitted wave power. In the example of compressional wave, the intensity is expressed as

$$I_c = \frac{1}{2}\rho c_p |v_c|^2 = \frac{1}{2}\rho\omega k_p |\Phi|^2 \tag{D.11}$$

In oblique incidence, the projected intensity on the junction has to be scaled by $cos\psi$. Notice that $k\,cos\psi$ is the wavenumber component in x direction, the transmissibility of compressional wave from plate 1 to elastic waves in plate 2 can be calculated.

$$\tau_{cc} = |\Phi|^2 , \quad \tau_{sc} = \frac{c}{a}|\Psi|^2 , \quad \tau_{bc} = \frac{2b}{a}|\Theta|^2 . \tag{D.12}$$

In Eq. D.12, factor 2 in flexural wave transmissibility is caused by real energy work from force on displacement as well as from moment on rotation. Since two plates are identical, the elastic wave transmissibilities to compressional wave should be the same as compressional wave transmissibility to the elastic waves, according to reciprocal principle.

Appendix E

Formulation for a 1D bar with M-K subsystems

An elastic bar of density ρ, length L, cross-section area S and wave speed c_x is studied, which is attached by N identical mass-spring $(M-K)$ subsystems having mass M and stiffness K. The $M-K$ subsystems are randomly distributed in the bar. Fig. E-1 shows the sketch of the bar system. The wave velocity field in the bar between the nth and the $(n+1)$th subsystems is assumed to be in the following general form

$$v(x) = A_n^+ e^{ik_x x} + A_n^- e^{-ik_x x}\ ,\quad x_n \le x \le x_{n+1}\ ,\quad n = 0, 1...N-1 \qquad \text{(E.1)}$$

where two waves of wavenumber k_x propagate in the forward and the backward directions, with the magnitude A_n^+ and A_n^- respectively.

Note that the wave velocity at the attachment point of the nth subsystem is continuous, so that

$$A_n^+ e^{ik_x x_n} + A_n^- e^{-ik_x x_n} = A_{n+1}^+ e^{ik_x x_{n+1}} + A_{n+1}^- e^{-ik_x x_{n+1}}\ . \qquad \text{(E.2)}$$

Similarly, the force across the attachment is continuous as well;

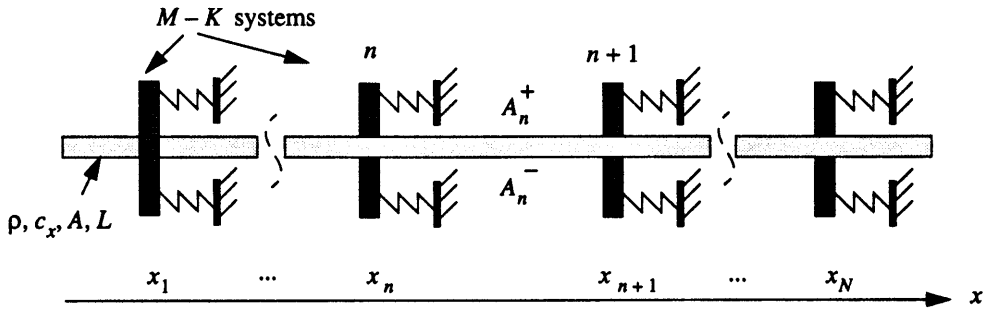

Figure E-1: An elastic bar with random distributed mass-spring subsystems.

$$Z\left[A_n^+ e^{ik_x x_n} - A_n^- e^{-ik_x x_n}\right] - Z\left[A_{n+1}^+ e^{ik_x x_{n+1}} - A_{n+1}^- e^{-ik_x x_{n+1}} = Z_{MK}\left[A_{n+1}^+ e^{ik_x x_{n+1}} - A_{n+1}^- e^{-ik_x x_{n+1}}\right], \quad \text{(E.3)}$$

where Z is the axial wave impedance of the bar, $Z = \rho c_x S$; Z_{MK} is the impedance of the $M-K$ system, $Z_{MK} = j\omega M + K/(j\omega)$; ω is the operating frequency, $\omega = k_x c_x$.

Eq. E.2 and Eq. E.3 provide a transfer matrix which helps to solve the chain system in Fig. E-1 'globally'. In solving the global matrix, I assume unit incident wave magnitude, $A_0^+ = 1$, and no wave reflection at the bar ends, A_N^-=0.

The forward wave field in the bar can be then derived using the forward wave magnitude A_n^+. By measuring the slope of the unwrapped propagation phase of the forward wave field, one can obtain the modified wavenumber.

List of Tables

List of Figures

List of Symbols

a	shell radius
a, c, r	subscripts identifying variables for axial, circumferential and radial directions
A	cross-section area
A_p	surface area of plate
b	average separation of two adjacent rings
c	sound speed in fluid (water)
c_ϕ, c_g	phase speed and group speed, respectively
$\bar{c}_g$	group speed averaged over frequency band $\Delta\omega$
c_p, c_s	wave speed of compressional and shear waves, respectively
c_x	axial phase speed
c, s, f	subscripts identifying variables for compressional, shear and flexural waves, respectively
C_n	pressure coefficient
d	mean free path
f	frequency in Hz
f_c	coincident frequency
e	subscript identifying elastic wave types (Chap.5)
E_Y	Young's modulus
E	energy
$\mathcal{E}$	energy density (per unit length)
G	shear modulus
G_w	Green's function
H_n	nth order Hankel function
i	$\sqrt{-1}$
J_n	nth order Bessel function
k	wavenumber, $k = \omega/c$
k_x	axial wavenumber, $k = \omega/c_x$
k_r	radial wavenumber, $k = \sqrt{k^2 - k_x^2}$
m, m'	subscript identifying the two membrane waves
h	shell thickness
L	length of a shell, or a bar (Sec.4.2.1)

$\mathbf{L}$, $\mathbf{U}$, $\mathbf{F}$	Operator, displacement and force matrices of constitute equations for coupled shell-fluid system
n	mode order
N_n	number of axial modes for each mode n
$\mathbf{n_0}$	normal directional vector
p_0	incident sound pressure on shell surface
p_i	incident sound pressure
p_s	scattered pressure
$\mathbf{r}$	position vector locating a field point
$\mathbf{r_0}$	position vector locating a source point
R	spatial separation between source and receiver
S_{vn}	wavenumber spectral density of shell surface velocity of mode n
t	time
$\bar{TS}$	logarithmic mean target strength over frequency region $3 < ka < 10$ and angular region $60° < \theta < 120°$
u, ϑ, w	shell displacement in axial, circumferential and radial directions
$\hat{u}$, $\hat{\vartheta}$, $\hat{w}$	Spatial Fourier transform of shell displacement in axial, circumferential and radial directions
$\mathcal{W}_0$	incident sound wave power; used to normalize elastic wave power
$\mathcal{W}_n$	elastic wave power equipartitioned among the elastic waves
$\mathcal{W}_{nm}$	elastic wave power for a membrane wave
$\mathcal{W}_{nm}^{in}$	sound power injected into the membrane waves
x	axial coordinate
Z	wave impedance or mechanical impedance
α	decay rate
β	ratio of radial velocity to total velocity
β_b	flexural bending parameter, $h^2/12a^2$
β_{bc}	correction factor of boundary influence for radiation coefficient σ_{rad}
δ_n	attenuation of the compressional wave at the conical endcaps, from Guo's analysis [26].
$\Delta_{1/2}$	half-power bandwidth along axial wavenumber
γ	angle between surface normal and observation direction
Γ	perimeter

η	loss factor
η_{diss}, η_{coup}	wave loss factor and coupling loss factor, respectively
θ	Sound incidence (and observation) direction measured respect to the shell axis.
ϑ	circumferential displacement
λ_x	axial wavelength
ν	wave interaction rate
Π	Power flow
ρ	density of acoustic medium
ρ_r, ρ_s	density of ring, and shell respectively
σ	Poisson's ratio
σ_{rad}	radiation coefficient
τ, τ'	wave transmissibility and reflectivity, respectively
ϕ	azimuthal angle
Φ	phase of a complex variable
ψ	helical angle. Wave is axial for $\psi = 0°$ and circumferential for $\psi = 90°$
ω	radian frequency
Ω	$\omega a/c_p$
$< >$	spatial average

Bibliography

[1] J.E. Cole, M.C. Junger, and M.R. Lamberton. Bistatic predictions from monostatic data. *NSWC Report U-2319-381.41*, (From Professor Dyer's handout for MIT course 13.851, App.5.2, Spring 1996).

[2] M.C. Junger and D. Feit. *Sound, Structures and Their Interaction.* M.I.T Press, Cambridge, MA, (1986).

[3] G. Maze and J. Ripoche. Visualization of acoustic scattering by elastic cylinders at low ka. *J. Acoust. Soc. Am.*, 73:41–41, (1983).

[4] G. Maze, F. Lecroq, D. Decultot, J. Ripoche, S.K. Numrich, and H. Uberall. Acoustic scattering from finite cylindrical elastic objects. *J. Acoust. Soc. Am.*, 90:3271–3278, (1991).

[5] J.M. Ho. Geometrical theory of acoustic scattering by thin elastic shells. *Submitted to J. Acoust. Soc. Am.*, (1993).

[6] A.N. Norris and D.A. Rebinsky. Acoustic coupling to membrane waves on elastic shells. *Submitted to J. Acoust. Soc. Am.*, (1993).

[7] A.N. Norris and N. Vasudevan. Acoustic wave scattering from thin shell structures. *J. Acoust. Soc. Am.*, 92:3320–3336, (1992).

[8] P.L. Marston. Gtd for backscattering from elastic spheres and cylinders in water and the coupling of surface elastic waves with the acoustic field. *J. Acoust. Soc. Am.*, 88:25–37, (1988).

[9] S.-H. Choi, T. Igusa, and J.D. Achenbach. Acoustic radiation from a cylindrical shell with substrctures subjected to an impulsive load. *Wave Motion*, 22:259–277, (1995).

[10] R.L. Weaver. Diffuse radiation from submerged thin shells. *ASME Winter Annual Meeting*, 93-WA/NCA-18, (1993).

[11] A.D. Pierce. Fundamental structural-acoustic idealizations for structures with fuzzy internals. *ASME Journal of Vibration and Acoustics*, 117:339–348, (1995).

[12] C. Soize. A modal and numerical method in the medium frequency range for vibroacoustic predictions using the theory of structural fuzzy. *J. Acoust. Soc. Am.*, 94:849–65, (1993).

[13] S.A. Rybak. Waves in a plate containing random inhomogeneities. *Soviet Physics-Acoustics*, 17:345–349, (1972).

[14] S.A. Rybak. Randomly coupled flexurall and longitudinal vibrations of plates. *Soviet Physics-Acoustics*, 18:76–79, (1972).

[15] R.H. Lyon. Progressive phase in multi-degree-of-freedom systems. *J. Acoust. Soc. Am.*, 73:1223–1228, (1983).

[16] R.H. Lyon. Range and frequency dependence of transfer function phase. *J. Acoust. Soc. Am.*, 76:1435–1437, (1984).

[17] R.H. Lyon M. Tohyama and T. Koike. Reverberant phase in a room and zeros in the complex frequency plane. *J. Acoust. Soc. Am.*, 89:1701–1707, (1991).

[18] H. He and R.H. Lyon. Group delay in resonant scattering. *J. Acoust. Soc. Am.*, 99:1465–1474, (1996).

[19] C.N. Corrado. *Mid-Frequency Acoustic Backscattering from Finite Cylindrical Shells and the Influence of Helical Membrane Waves.* PhD thesis, Massachusetts Institute of Technology, January 1993.

[20] J. E. Bondaryk. *Array Processing and Forward Modeling Methods for the Analysis of Stiffened, Fluid-Loaded Cylindrical Shells.* PhD thesis, Massachusetts Institute of Technology, May 1994.

[21] M. Conti. *Mid-frequency Acoustic Scattering from Finite Internally-loaded Cylindrical Shells Near Axial Incidence.* PhD thesis, Massachusetts Institute of Technology, May 1995.

[22] S. Park. Sound wave scattering by cylindrical shells with internal structures. Master's thesis, Massachusetts Institute of Technology, February 1995.

[23] D.P. Mackovjak. Array measurements of backscattered data from internally loaded cylindrical shells. Master's thesis, Massachusetts Institute of Technology, February 1993.

[24] D.C. Ricks. *Globally stable infinite cylindrical shell model.* PhD thesis, Massachusetts Institute of Technology, May 1994.

[25] Y.P. Guo. Normal modes propagation on a conical shell. *J. Acoust. Soc. Am.*, (1994).

[26] Y.P. Guo. Fluid loading effects on waves on conical shells. *J. Acoust. Soc. Am.*, 97:1061–1066, (1995).

[27] Y.P. Guo. Sound scattering from cylindrical shells with internal elastic plates. *J. Acoust. Soc. Am.*, (1993).

[28] Y.P. Guo. Flexural wave transmission through angled structural joints. *Submitted to J. Acoust. Soc. Am.*, (1993).

[29] Y.P. Guo. Acoustic radiation from cylindrical shells due to internal forcing. *J. Acoust. Soc. Am.*, 99:1495–1505, (1996).

[30] R.H. Lyon and R.G. DeJong. *Theory and Application of Statistical Energy Analysis.* Butterworth-Heinemann, Newton, MA, (1994).

[31] H. Allik, R. Dees, S. Moore, and D. Pan. *SARA-2D User's Manual.* BBN Systems And Technologies, New London, CT, (1994).

[32] The basic version of the SARA-2D input code used in this study is kindly provided by Dr. Liu and Dr. Vasudevan in NSWC (in Maryland). (1995).

[33] A. Leissa. *Vibration of Shells.* Acoustical Society of America, New York, (1993).

[34] Private conversation with Professor Ira Dyer. (1996).

[35] R.H. Lyon. *Machinery Noise and Diagnostics.* Butterworth, Boston, MA, (1987).

[36] P.W. Smith. Structural wave scattering from the endcap on a cylindrical shell (a paean to matlab). *Handout in a seminar presented at Boston University,* (1995).

[37] M. C. Junger. Scattering enhancement by supersonic resonances of cylindrical shells. *J. Acoust. Soc. Am.*, 93:1743–1746, (1993).

[38] Leon Brillouin. *Wave Propagation and Group Velocity.* Academic Press, Inc., first edition, 1960.

[39] M. L. Rumerman. Contribution of membrane wave reradiation to scattering from finite cylindrical shells in water. *J. Acoust. Soc. Am.*, 93:55–65, (1993).

[40] M. Klausbruckner. Theoretical and experimental investigation of the acoustic behavior of visco-elastically damped cylindrical shells. Master's thesis, Massachusetts Institute of Technology, August 1995.

[41] L. Cremer, M. Heckl, and translated and revised by E.E. Ungar. *Structure-Borne Sound.* Springer-Verlag, Berlin, Germany, 1988.

[42] F.B. Jensen W.A. Kuperman M.B. Porter and H.S. Schmidt. *Computational Ocean Acoustics.* American Institute of Physics, New York, (1994).